Microscopic Models for Ultrarelativistic Heavy Ion Collisions

S. A. Bass, M. Belkacem, M. Bleicher, M. Brandstetter, L. Bravina, C. Ernst, L. Gerland, M. Hofmann, S. Hofmann, J. Konopka, G. Mao, L. Neise, S. Soff, C. Spieles, H. Weber, L. A. Winckelmann, H. Stöcker and W. Greiner

Institut für Theoretische Physik

Robert-Mayer-Strasse 10

Johann Wolfgang Goethe - Universität

D-60054 Frankfurt am Main

Ch. Hartnack and J. Aichelin

SUBATECH, Ecole des Mines

4, rue Alfred Kastler

La Chantrerie

F-44070 Nantes, Cedex 03, France

N. Amelin

Joint Institute for Nuclear Research (JINR) Dubna

141980 Moscow region

Russia

April 13, 2005

Contents

Chapter 1

Introduction

The investigation of nuclear matter under extreme conditions is one of the major research topics of nuclear and high energy physics (a short and necessarily incomplete overview may be obtained in refs. [1, 2, 3, 4, 5, 6, 7, 8, 9, 10, 11, 12]). The motivation for this is the unique opportunity to investigate the equation of state of nuclear matter and the search for phase transitions (such as the liquid gas or the quark gluon plasma (QGP) phase transition) and the possible restoration of chiral symmetry. Also the general understanding of the dynamics of heavy ion collisions over a vast energy range from the Coulomb barrier (several MeV per nucleon) to the highest energies currently available or planned for the future is interesting in itself. Here one can check the current understanding of the theory of strong interactions (QCD) and different effective theories based on hadronic/quark degrees of freedom. The intriguing role of color coherence phenomena (transparency and opacity) for fluctuations, stopping and charmonium production can be studied best at these energies.

The measurements above several hundreds of AMeV are done at experimental heavy-ion facilities in three energy regimes: *i*) at about 1 AGeV at BEVALAC in Berkeley or SIS (SchwerIonenSynchrotron) at GSI-Darmstadt; *ii*) the AGS (Alternating Gradient Synchrotron, in Brookhaven) energy regime at about 2-15 AGeV; *iii*) and the SPS (Super Proton Synchrotron, at CERN) energy regime of 40-200 AGeV. Much higher energies will be available in the future with the Relativistic Heavy Ion Collider (RHIC) in Brookhaven ($\sqrt{s} \approx 200$ AGeV) and the Large Hadron Collider (LHC) at CERN ($\sqrt{s} \approx 6$ ATeV).

Unfortunately, there exists presently no theoretical model that provides a **consistent** understanding of the reaction dynamics of heavy ion collisions over the whole energy range. One has to deal with quite different reaction mechanisms from compound nucleus formation and deep inelastic scattering at the Coulomb barrier over particle and resonance production at intermediate energies up to string-excitation and -fragmentation or parton scattering at (ultra-)relativistic energies. While at low and intermediate energies, descriptions in terms of hadrons (resonances) are appropriate, at high energies the quark and gluon degrees of freedom enter the game.

One aim of this paper is the description of a theoretical model that incorporates these different reaction mechanisms and that is able to yield observables. The model is dubbed UrQMD. Such a microscopic model is based on a phase space description of the reaction. It contains a lot of unknown parameters, which will have to be checked and fixed by experimental data or by further model assumptions. This theoretical approach allows to pin down physical ingredients that determine the values of certain observables like particle abundances, collective flow of hadrons, rapidity distributions, cluster formation, etc. Thus certain experimental observables can either be uniquely traced to a physical parameter or if they are described equally well by different physical assumptions. This is of utmost importance if one wants to find evidence for new physical phenomena like the phase transition to the quark gluon plasma. It must be clarified whether

the measured data could also be understood in terms of a purely hadronic scenario or by assuming only a partial dynamical deconfinement, which is not accompanied by complete equilibration. One example is the vividly discussed suppression of J/Ψ or Ψ' production in Pb+Pb collisions as compared to p+p or p+A collisions, which can be explained in different physical scenarios.

It is one of the main tasks of theoretical heavy ion physics to link experimental observables to the different phases and manifestations of nuclear or – in more general terms – hadronic matter. For this, a detailed understanding of the dynamics of heavy ion reactions is essential. Transport theory has played an important role in the interpretation of experimental results and in predicting new interesting effects in relativistic heavy ion reactions. It is particularly well suited for the non-equilibrium situation, rapid time-dependence of the system (even the use of the term "state" seems questionable), finite size effects, non-homogeneity, N-body phase space, particle/resonance production and freeze-out as well as collective dynamics. Microscopic and macroscopic (hydrodynamical) transport models attempt to describe the full time-evolution from the initial state of the heavy ion reaction (i.e. the two colliding nuclei) up to the freeze-out of all initial and produced particles after the reaction. Simplified thermal equilibrium models neglect most of these dynamical effects, but make physical assumptions on the initial part of the reaction, e.g. thermalization or plasma creation.

It should be kept in mind that notions like 'phase transition' are in principle restricted to equilibrated systems in the thermodynamic limit ($N, V \to \infty, N/V$ =const.). However, in heavy ion collisions we have to deal with finite, dynamical systems, which makes the applicability of thermodynamic models doubtful, even though they might successfully describe some global observables like particle abundances. Nevertheless, thermodynamic concepts are quite useful for a global characterization of the hot and compressed hadronic matter. In figure 1.1 we therefore present a conjectural phase diagram of nuclear matter where only the point at T=0, $\rho_0 = 0.16$ fm^{-3}, realized in nuclei, is well known. For low excitation energies (low densities $\rho < \rho_0$ and low temperatures $T < T_C \sim 15$ MeV), one expects a phase transition from a hadronic gas to liquefied nuclei. This possibility results from the resemblance of the nuclear interaction to that of atoms in gases. Both exhibit a short range repulsion and a long range attraction. There are indications that this phase transition may have been recently observed [13].

At higher densities (2-3 ρ_0) the possible existence of density isomers was proposed [14, 2]. At even higher densities and/or temperatures, one expects a phase transition or even a smooth cross over to the QGP. However, neither the exact critical density and temperature are known, nor the order of the transition. The latter is important, since a coexistence region of plasma (strongly interacting quarks and gluons not confined to well separated hadrons) and hadron gas might lead to observable effects in the flow excitation function [15, 7, 16, 17, 18] and other observables.

Figure 1.1 shows the generalization of the phase diagram to net-strangeness and net-antibaryon. Hypermatter and antimatter can only be produced in energetic heavy ion collisions. The production of (multi-)strange nuclei containing one or more Λ-particles [19, 20, 21, 22], as well as the production of anti-nuclei (anti-matter cluster) have been measured [23, 24]. Furthermore, the possibility of metastable exotic multi strange objects (MEMOS) [25, 26] and strangelets [27, 28, 29, 30, 31, 32, 33] might serve as observables for deconfinement during heavy ion collisions. Ultra-relativistic heavy ion collisions offer the unique opportunity to probe these different states of highly excited hot and dense nuclear matter under controlled laboratory conditions. The dashed lines in figure 1.1 visualize how different regions in the phase diagram may be probed simultaneously in the course of one heavy ion collision event, due to distillation and local fluctuations [34].

Note that in a hot and compressed hadron gas at high excitation energies we deal not only with nucleons but with many different baryon (> 50) and meson (> 30) species. With increasing mass, these particles are often unstable – the width of the resonances increases. Many of the presently available microscopic models

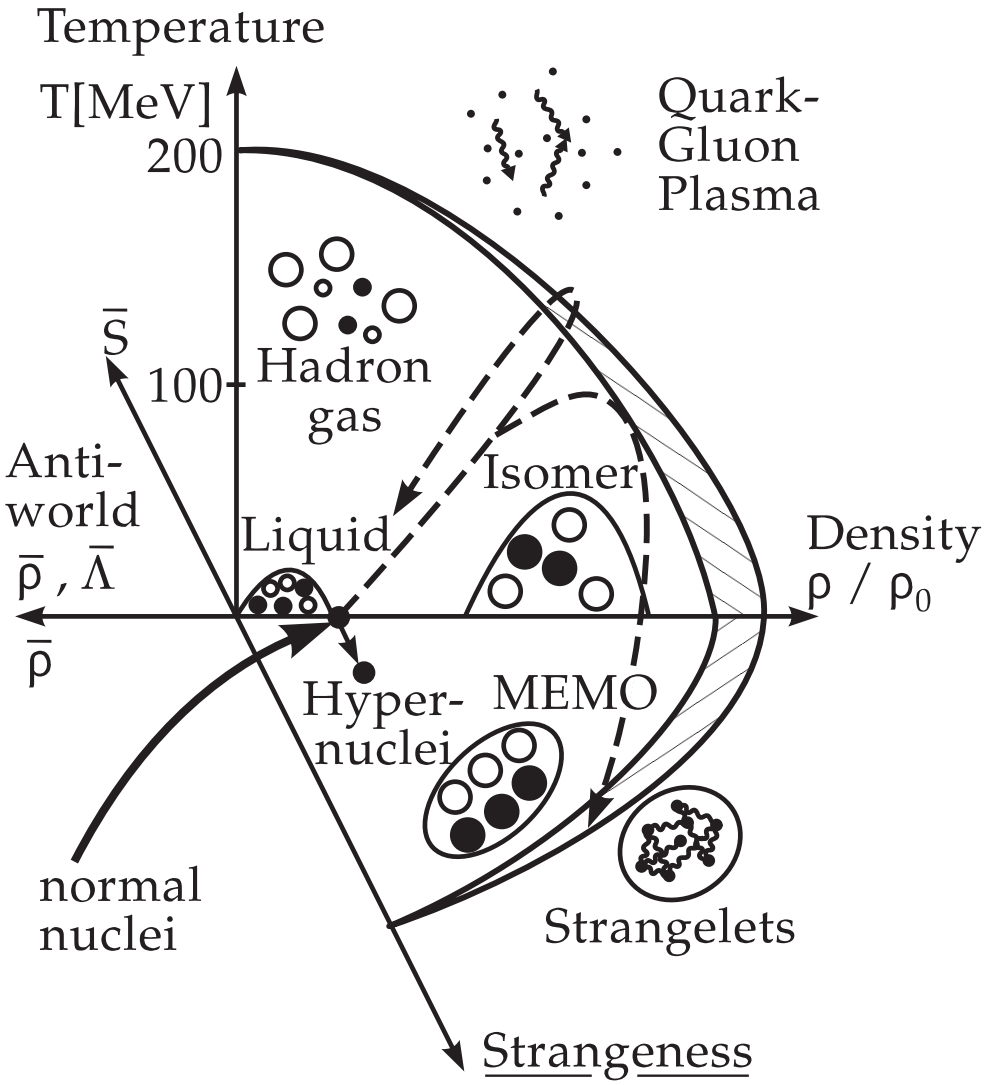

Figure 1.1: Phase diagram of hadronic matter: Only the point at ground state density is well known; the dashed lines show areas probed in the course of heavy ion reactions.

treat resonances as quasi-particles which propagate and scatter during their lifetime and then decay into other resonances or stable hadrons (with respect to strong interactions). This concept becomes doubtful when the width of the resonances is so large that no well defined quasi particle state (i.e. width/mass ≈ 1) exists. However, the resonances turn out to be important for the microscopic description of heavy ion collisions at bombarding energies above 1 GeV per nucleon. On the other hand, the concept of resonances cannot be used for internal excitation energies above 2 GeV. Here the quark degrees of freedom must be explicitly taken into account. Therefore some of the models presently available, including the UrQMD model presented in detail in this review, replace the resonances by continuous string excitations for higher energies.

A microscopic dynamics description of heavy ion collisions is usually based on transport theory. Here a sequence of propagations of particles is simulated numerically (representing baryons (resonances) and mesons with or without interaction with a potential and subsequent scattering processes or decays). The main ingredients in this description of heavy-ion collisions are the cross sections, the two-body potentials and decay widths. It is obvious that – at least in principal – these models should be obtained consistently

from an underlying theory. Since the particles propagate in a hot and dense and even not equilibrated medium of highly excited hadrons, the properties of the particles might change significantly. Consequently, properties like effective masses, effective momenta, in-medium cross sections and decay widths should be calculated for the actual local situation in which the particle propagates. Unfortunately this is very complicated and from the numerical point of view also very time consuming, so that in most of the models drastic approximations are made.

Furthermore, the basic requirements for the applicability of transport theoretical models might not be fulfilled in certain realistic situations. First of all the quasi particle limit, i.e. on shell propagation between subsequent scatterings, can be a bad approximation in strongly interacting, dense matter. Between two subsequent scatterings of a particle with time difference Δt, the energy of the state of the particle can only be fixed up to $\Delta E = \hbar/\Delta t$. For short collision times this uncertainty can become rather large ($\Delta t = 1$ fm/c $\rightarrow \Delta E = 200$ MeV). Even without collisional broadening the quasi particles acquire a finite life time, which requires the introduction of nontrivial spectral functions. Consequently one needs to introduce the energy of the quasi particles as an additional independent variable, i.e. the full 8-dimensional phase space description of transport theory is required. Secondly, transport theory relies on the description of the dynamics of the system as a Markovian process. This means the particles completely 'forget' about their critical state before each scattering. At least in the energy regime of several GeV per nucleon the so called memory effect does not seem to be negligible [35]. Moreover, pure transport models describe the system by the one body phase space distribution function, which does not contain any information about correlations of the particles. These are, however, the most important for the description of fragment or cluster formation (hypernuclei, antinuclei, etc.). Such clusters can be obtained from the one body phase space distributions only with the help of a statistical coalescence model. In the UrQMD model described below, this shortcoming is avoided, since the particles can interact by individual two body forces at least at low energies.

Unfortunately, the generalization of such two body forces to the relativistic region is not a simple task and is not incorporated in the present UrQMD model. In principle, the interaction must be mediated by fields, which are propagated according to wave equations or one must make use of the so called constraint Hamiltonian dynamics [36, 37]. Many other models avoid the propagation of fields using local density approximation.

Finally, we would like to mention an additional problem arising from the practical realization of transport models: Even though the underlying transport equations are relativistically invariant, the actual realization by a sequence of propagations, scatterings and decays is not (see section 3.3.1). This leads to a frame dependence of the observables which contributes to the systematic errors of the respective model predictions.

This review is organized as follows: Chapter 2 contains a brief introduction into the many-body theory of nuclear collisions. In chapter 3 we discuss in great detail one specific microscopic transport model, the Ultra-relativistic Quantum Molecular Dynamics (UrQMD) model. Chapter 4 focuses on the exploration of hot and dense nuclear matter with microscopic transport approaches. Different effects and observables are discussed and dependencies to model parameters are pointed out. The main focus lies on baryon stopping, collective flow and particle production. A brief summary and conclusions are found in chapter 5.

Chapter 2

Transport theory of nuclear collisions

2.1 Non-relativistic transport theory

The ultimate goal of a theoretical description of heavy ion collisions is a derivation and solution of equations of motion for the elementary degrees of freedom, the quarks and gluons. Since non perturbative dynamical solutions of QCD are not possible yet, one is forced to separate the description into two parts: The low energy part ($\sqrt{s} <$ several GeV), where a description in terms of QCD-quasi particles (hadrons) is possible and a high energy part where the quark and gluon degrees of freedom are treated explicitly. For the low energy part one can derive solvable equations of motion from phenomenological effective Lagrangians, if strong but controllable approximations are made. This means that at least in principle one knows what has been neglected in the approximation scheme as long as one accepts an effective Lagrangian with baryons and mesons as degrees of freedom as a starting point. One example is the $\sigma - \omega -$ model [38, 39], where the interaction of nucleons is described by the exchange of a scalar and a vector meson. While the ω-meson has a clear physical significance, it is not quite clear if the σ-meson can be interpreted as a real physical particle or rather must be taken as an effective description of the interaction. This model must be extended to include other baryonic and mesonic degrees of freedom (e.g. Δ, N^*, π, K, ρ etc.) since already at moderate energies of several hundred MeV per nucleon a significant production of new particles sets in (mainly pions but also other (pseudo-)scalar and (pseudo-)vector mesons as well as a lot of baryon resonances and even anti-baryons). The general theoretical framework for the derivation of practically solvable equations of motion based on effective Lagrangians is transport theory. The basic approximation which is made here is the description of the dynamics in terms of a semi-classical single particle phase space distribution instead of N-body non-equilibrium Green's functions.

In order to sketch the corresponding approximation scheme, we start with a simple non-relativistic potential model for nucleons and then later on simply write down the proper relativistic generalizations. The Hamilton operator shall be given by

$$\begin{aligned} H &= \int \mathrm{d}^3\boldsymbol{x}\; \psi_H^\dagger(\boldsymbol{x}_1\,,t)\left(-\frac{\hbar^2}{2m}\Delta_1\right)\psi_H(\boldsymbol{x}_1\,,t) + \frac{1}{2}\int \mathrm{d}^3\boldsymbol{x}_1\;\mathrm{d}^3\boldsymbol{x}_2\;\mathrm{d}^3\boldsymbol{x}_1'\;\mathrm{d}^3\boldsymbol{x}_2' \\ &\quad \langle \boldsymbol{x}_1\,,\,\boldsymbol{x}_2 \mid V \mid \boldsymbol{x}_1'\,,\,\boldsymbol{x}_2'\rangle\, \psi_H^\dagger(\boldsymbol{x}_1\,,t)\psi_H^\dagger(\boldsymbol{x}_2\,,t)\psi_H(\boldsymbol{x}_2'\,,t)\psi_H(\boldsymbol{x}_1'\,,t)\,, \end{aligned} \tag{2.1}$$

where the nucleon field operator $\psi_H^\dagger(\boldsymbol{x}_1, t)$ and $\psi_H(\boldsymbol{x}_1\,, t)$ are given in the Heisenberg representation. For simplicity we neglect here the complications introduced by a spin or isospin dependent interaction as well as three body forces, since we only want to review the principle steps of the derivation. For details we will refer to the corresponding literature as well as to the derivations in the relativistic case. The

non-relativistic non-equilibrium Green's functions (g^c, g^a) and correlation functions ($g^>$,$g^<$) are defined by:

$$\begin{aligned} g^c(\mathbf{1},\mathbf{1'}) &= \frac{1}{\mathrm{i}\hbar}\langle T^c \psi_H(\mathbf{1})\,\psi_H^\dagger(\mathbf{1'})\rangle\,, \\ g^a(\mathbf{1},\mathbf{1'}) &= \frac{1}{\mathrm{i}\hbar}\langle T^a \psi_H(\mathbf{1})\,\psi_H^\dagger(\mathbf{1'})\rangle\,, \\ g^>(\mathbf{1},\mathbf{1'}) &= \frac{1}{\mathrm{i}\hbar}\langle \psi_H(\mathbf{1})\,\psi_H^\dagger(\mathbf{1'})\rangle\,, \\ g^<(\mathbf{1},\mathbf{1'}) &= -\frac{1}{\mathrm{i}\hbar}\langle \psi_H^\dagger(\mathbf{1'})\,\psi_H(\mathbf{1})\rangle\,, \end{aligned} \tag{2.2}$$

with $\mathbf{1}$ a short hand notation for $(\boldsymbol{x_1}, t_1)$ and/or spin or isospin indices and T^c, T^a are the chronological and anti-chronological time ordering operators. In the relativistic case $\psi^\dagger$ must be replaced by $\bar{\psi}$. The four two point functions can be written in a more compact form as a path ordered Green's function (2×2 matrix denoted by the underline)

$$\underline{G}(\mathbf{1},\mathbf{1'}) = \frac{1}{\mathrm{i}\hbar}\langle P\,\psi(\mathbf{1})\,\psi^\dagger(\mathbf{1'})\rangle. \tag{2.3}$$

Here, additionally to the times $t_1, t_{1'}$, one has to specify if these times are on the upper or lower branch of the integration contour, which yields the four combinations given in Eq. (2.2). Originally, the theory was formulated by Schwinger [40] and the first application to transport problems is due to Kadanoff and Baym [41]. For an introduction to the formalism of path ordered non equilibrium Green's functions we refer the reader to the works of Danielewicz [42] and Botermans and Malfliet [43]. To some extent we will follow their work and notations. From the equations of motion for the Heisenberg field operators one can derive equations of motion for the Green's functions. However these equations for the one body Green's functions couple to the two body Green's functions and so on. This set of coupled equations of motion is usually called the Martin Schwinger hierarchy [44]. In order to solve the problem completely one has to solve the whole set of coupled equations for all n-body Green's functions. However, one can replace in the equation for the one body Green's function the unknown two body Green's function by the also unknown self-energy. This leads to the Dyson equation in differential form:

$$s(\mathbf{1})\,\underline{G}(\mathbf{1},\mathbf{1'}) \;=\; \underline{\delta}(\mathbf{1}-\mathbf{1'}) + \int\limits_C \mathrm{d}\mathbf{1''}\,\underline{\Sigma}(\mathbf{1},\mathbf{1''})\,\underline{G}(\mathbf{1''},\mathbf{1'}) \tag{2.4}$$

here $s(\mathbf{1})$ is the differential operator

$$s(\mathbf{1}) \;=\; \mathrm{i}\hbar\partial_{t_1} + \frac{\hbar^2}{2m}\Delta_{x_1} \quad . \tag{2.5}$$

The δ-function is generalized to the integration contour

$$\int\limits_C \mathrm{d}\mathbf{1} \;=\; \int\limits_{-\infty}^{\infty} \mathrm{d}\mathbf{1}\,(\text{upper}) - \int\limits_{-\infty}^{\infty} \mathrm{d}\mathbf{1}\,(\text{lower}) \tag{2.6}$$

such that $\int\limits_C \mathrm{d}\mathbf{1'}\,\underline{\delta}(\mathbf{1}-\mathbf{1'})\,\underline{F}(\mathbf{1'}) = \underline{F}(\mathbf{1})$, namely:

$$\underline{\delta}(t_1-t_2) = \begin{cases} \delta(t_1-t_2) & \text{both } t_1 \text{ and } t_2 \text{ on the upper branch} \\ -\delta(t_1-t_2) & \text{both } t_1 \text{ and } t_2 \text{ on the lower branch} \\ 0 & \text{otherwise} \end{cases} \quad . \tag{2.7}$$

Of course the proper self-energy $\underline{\Sigma}(\mathbf{1},\mathbf{1'})$ is also a two by two matrix defined on the contour. In more detail, equation (2.4) has four components:

$$\begin{aligned}
s(\mathbf{1})g^c(\mathbf{1},\mathbf{1'}) &= \delta(\mathbf{1}-\mathbf{1'}) + \int d\mathbf{1''}\,[\Sigma^c(\mathbf{1}\ ,\ \mathbf{1''})\,g^c(\mathbf{1''},\mathbf{1'}) - \Sigma^<(\mathbf{1},\mathbf{1''})\,g^>(\mathbf{1''},\mathbf{1'})]\ , \\
s(\mathbf{1})g^a(\mathbf{1},\mathbf{1'}) &= -\delta(\mathbf{1}-\mathbf{1'}) + \int d\mathbf{1''}\,[\Sigma^>(\mathbf{1}\ ,\ \mathbf{1''})\,g^<(\mathbf{1''},\mathbf{1'}) - \Sigma^a(\mathbf{1},\mathbf{1''})\,g^a(\mathbf{1''},\mathbf{1'})]\ , \\
s(\mathbf{1})g^>(\mathbf{1},\mathbf{1'}) &= \int d\mathbf{1''}\,[\Sigma^>(\mathbf{1}\ ,\ \mathbf{1''})\,g^c(\mathbf{1''},\mathbf{1'}) - \Sigma^a(\mathbf{1},\mathbf{1''})\,g^>(\mathbf{1''},\mathbf{1'})]\ , \\
s(\mathbf{1})g^<(\mathbf{1},\mathbf{1'}) &= \int d\mathbf{1''}\,[\Sigma^c(\mathbf{1}\ ,\ \mathbf{1''})\,g^<(\mathbf{1''},\mathbf{1'}) - \Sigma^<(\mathbf{1},\mathbf{1''})\,g^a(\mathbf{1''},\mathbf{1'})]\ , \qquad (2.8)
\end{aligned}$$

which are known as Kadanoff-Baym equations [41]. In integral form equation (2.4) is the Dyson equation on the contour

$$\underline{G}(\mathbf{1},\mathbf{1'}) = \underline{G_0}(\mathbf{1},\mathbf{1'}) + \int\limits_C \mathrm{d}\mathbf{1''} \int\limits_C \mathrm{d}\mathbf{1'''}\,\underline{G_0}(\mathbf{1},\mathbf{1'''})\,\underline{\Sigma}(\mathbf{1'''},\mathbf{1''})\underline{G}(\mathbf{1''},\mathbf{1}) \qquad (2.9)$$

where the zeroth order Green's function inverts $s(\mathbf{1})$

$$s(\mathbf{1})\,\underline{G_0}(\mathbf{1},\mathbf{1'}) = \underline{\delta}(\mathbf{1}-\mathbf{1'}) \quad . \qquad (2.10)$$

The equations of motion (2.4) or (2.8), respectively, contain in principle the unknown self energies which have to be calculated by an appropriate approximation scheme, e.g. in perturbation theory or in T- or G-matrix approximation. However, the corresponding expressions will in turn contain the unknown Green's functions, such that one obtains a coupled set of equations for the $\underline{G}$'s and $\underline{\Sigma}$'s. E.g. in the T- or G-matrix approximation one calculates the self energies from

$$\underline{\Sigma}(\mathbf{1},\mathbf{1'}) = -\mathrm{i}\hbar \int\limits_C \mathrm{d}\mathbf{2} \int\limits_C \mathrm{d}\mathbf{2'}\ (\,\langle \mathbf{1}\,\mathbf{2}|\underline{T}|\mathbf{1'}\,\mathbf{2'}\rangle - \langle \mathbf{1}\,\mathbf{2}|\underline{T}|\mathbf{2''}\,\mathbf{1'}\rangle\,)\ \underline{G}(\mathbf{2''},\mathbf{2}^+) \qquad (2.11)$$

where the T-matrix is defined by the integral equation:

$$\begin{aligned}
\langle \mathbf{1}\,\mathbf{2}|\underline{T}|\mathbf{1'}\,\mathbf{2'}\rangle &= \langle \mathbf{1}\,\mathbf{2}|\underline{V}|\mathbf{1'}\,\mathbf{2'}\rangle \\
&+ \mathrm{i}\hbar \int\limits_C \mathrm{d}\mathbf{1''}\,\mathrm{d}\mathbf{2''}\mathrm{d}\mathbf{1'''}\,\mathrm{d}\mathbf{2'''}\,\langle \mathbf{1}\,\mathbf{2}|\underline{V}|\mathbf{1'''}\,\mathbf{2'''}\rangle\,\underline{G}(\mathbf{1''},\mathbf{1'''})\,\underline{G}(\mathbf{2''},\mathbf{2'''})\,\langle \mathbf{1'''}\,\mathbf{2'''}|\underline{T}|\mathbf{1'}\,\mathbf{2'}\rangle \qquad (2.12)
\end{aligned}$$

For the effective interaction in nuclear matter (G-matrix), one has additionally to incorporate the Pauli blocking of the intermediate states where the two particles or holes propagate from $\mathbf{2'''}$ to $\mathbf{2''}$ and from $\mathbf{1'''}$ to $\mathbf{1''}$, respectively. For details, we refer the reader to [43, 45]. In the dynamical situation of heavy-ion collisions, the problem is more difficult. At the beginning of the reaction, one does not have a single Fermi sphere at zero temperature as for nuclear matter in the ground state, but rather one has to deal with two Fermi spheres separated by the beam momentum. Calculations of the G-matrix for colliding nuclear matter have so far not been carried out. However, the effects of the dynamical situation on the mean-fields (real part of the self-energy) have been estimated by the Munich group [46]. Only a few attempts have been made to include realistic G-matrices into a transport description, see e.g. the work of the Tübingen group [47]. In many other cases, free or in medium corrected cross sections are used together with parameterizations of the mean-field (e.g. different versions of the QMD approach) or the latter is calculated in local density approximation (see below). In order to avoid confusion with the propagator $\underline{G}(\mathbf{1},\mathbf{1'})$, we use the term T-matrix or T instead of G-matrix or G.

Equation (2.12) corresponds to a resummation of all the ladder diagrams for the effective interaction (T-matrix) in the medium, which is an appropriate approximation for interactions with hard core, like the nucleon-nucleon interaction. However, polarization insertions are neglected in this approximation. This will be of some importance for the relativistic generalization, where pions (in general mesons), nucleons and resonances appear (see below). Unfortunately the coupled equations (2.9), (2.11) and (2.12) form a very complicated set of integral equations in an 8-dimensional coordinate space. They might be visualized in a comprehensive way by Feynman diagrams in figure 2.1.

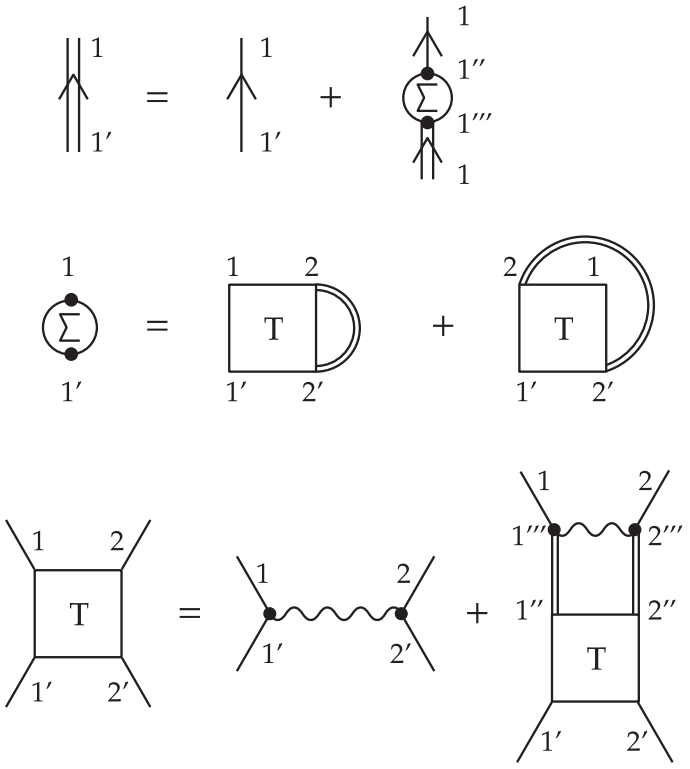

Figure 2.1: Feynman diagrams for the T-matrix approximation

Here the double (single) line denotes the interacting (non-interacting) Green's function in the T-matrix approximation, while the wiggled line is the bare nucleon-nucleon interaction. Σ and T represent the proper self-energy (two point function) and effective interaction or T-matrix (four point function), respectively. Even in equilibrium nuclear matter calculations one usually has to make further approximations to come to solvable equations. E.g. one approximates the two interacting propagators in the T-matrix equation neglecting the hole contributions and/or one treats the self-consistency only on the average etc.. Then one obtains e.g. the Brueckner-Hartree-Fock equations (in equilibrium!) or in the relativistic version the Dirac-Brueckner equation (see e.g. [45]).

One important requirement for all kinds of approximations for the dynamical problem is the preservation of the basic conservation laws of the underlying theory. It has been shown that the above mentioned T-matrix approximation leads to energy, momentum and particle number conserving transport equations [43]. Furthermore it has also been shown *loc. cit.* that the T-matrix approximation follows from boundary conditions for the two body Green's function which correspond to Boltzmann's assumption of molecular chaos. This means that the two body Green's function should factorize for times in the infinite past, representing two non-interacting free particles. In order to come to solvable approximations one can e.g. approximate the T-matrix by the bare interaction alone ($T \approx V$). This leads to the time dependent

Hartree-Fock approach which will be discussed below. In this approach the particles interact only via a time dependent mean field generated by all particles. Direct interactions (correlations) are neglected (see graphs in figure 2.2).

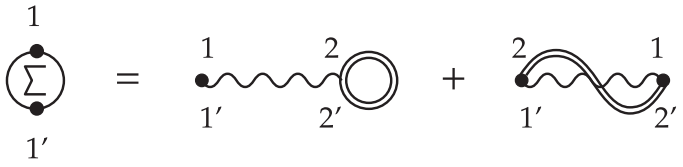

Figure 2.2: Feynman diagrams for the Hartree-Fock approximation

The self-consistency is still preserved, since the full Green's function in Hartree-Fock approximation appears. One can give up the self-consistency to some extent but include higher orders in the interactions. The Born approximation is obtained via the graphs in figure 2.3, which leads to the self-energy as sketched in figure 2.4.

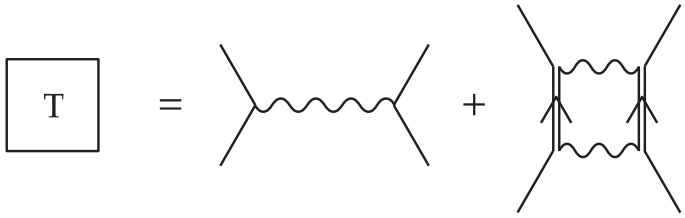

Figure 2.3: Feynman diagrams for the Born approximation

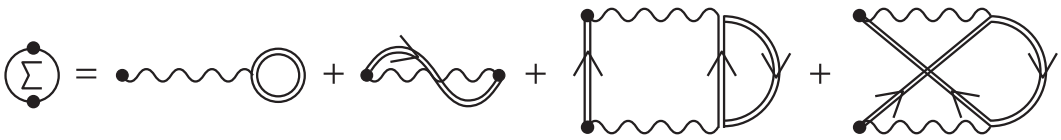

Figure 2.4: Feynman diagrams for the self-energy in the Born approximation

However, in most cases the self consistent propagator has to be replaced by some further approximations for practical reasons. One can use e.g. a propagator calculated for a local equilibrium situation, i.e. replacing essentially the bare mass of the particle (here nucleons) by an effective mass or effective dispersion relation, respectively, which is calculated for an equilibrium system. Usually this is called dressing the propagator. In this way one can take also polarization insertions into account, which are important for the relativistic generalization. An analogous approximation can also be applied to the self-energy itself. I.e. in the dynamical theory one uses the self-energy calculated from equilibrium theory (in T-matrix approximation) [47]. In this approach self-consistency is still preserved in the equilibrium calculation of the effective interaction, but then this interaction is also used for the non equilibrium situation.

Only a few attempts have been made to take the non equilibrium situation at the beginning of a high energy nucleus nucleus collision at least in a stationary approximation into account, e.g. for two streams of nucleons inter-penetrating each other [46, 48]. It should be kept in mind, however, that in most works the approximations mentioned above are combined with a gradient and quasi particle approximation which then leads to transport equations for the dynamical problem. In order to summarize the necessary steps

to derive a transport theory, we do not need to specify a certain approximation scheme for the self-energy, but rather take this quantity as calculable and therefore known.

We introduce the retarded and advanced Green's functions by

$$\begin{aligned} g^+ &= g^c - g^< = g^> - g^a \,, \\ g^- &= g^c - g^> = g^< - g^a \,, \end{aligned} \tag{2.13}$$

and analogous equations for the retarded and advanced self energies. The advantage of these quantities is that the real part of the retarded self-energy can be interpreted as the (in general non local) mean field while the imaginary part describes the absorption or finite life time of the quasi particles (dressed nucleons).

If the (anti)chronological quantities are eliminated from equation (2.8) one obtains in obvious operator notation for the two point functions

$$s(\mathbf{1})\, g^{\gtrless} = \Sigma^+ g^{\gtrless} + \Sigma^{\gtrless}\, g^- \,, \tag{2.14}$$

$$s(\mathbf{1})\, g^{\pm} = 1 + \Sigma^{\pm} g^{\pm} \,. \tag{2.15}$$

If one adds or subtracts the corresponding hermitian conjugate equations one can separate the real and imaginary parts of these equations, e.g.

$$\begin{aligned} (s(\mathbf{1}) - s^*(\mathbf{1'}))\; g^{\gtrless} &= \left[Re\,\Sigma^+ \,,\, g^{\gtrless} \right]_- + \left[\Sigma^{\gtrless} \,,\, Re\, g^+ \right]_- \\ &\quad + \frac{1}{2} \left[\Sigma^> \,,\, g^< \right]_+ - \frac{1}{2} \left[\Sigma^< \,,\, g^> \right]_+ \end{aligned} \tag{2.16}$$

$$\begin{aligned} (s(\mathbf{1}) + s^*(\mathbf{1'}))\; g^{\gtrless} &= \left[Re\,\Sigma^+ \,,\, g^{\gtrless} \right]_+ + \left[\Sigma^{\gtrless} \,,\, Re\, g^+ \right]_+ \\ &\quad + \frac{1}{2} \left[\Sigma^> \,,\, g^< \right]_- - \frac{1}{2} \left[\Sigma^< \,,\, g^> \right]_- \end{aligned} \tag{2.17}$$

where the brackets, $[A\,,\,B]_\pm$, denote (anti) commutators of the operators.

Those equations for two point functions $A(\mathbf{1}, \mathbf{1'})$ are now transformed into phase space by the Wigner transform defined by

$$A_W(R\,,\,p) = \int d^4y\, e^{\mathrm{i}p\cdot y/\hbar}\, A\left(R + \frac{1}{2}y \,,\, R - \frac{1}{2}y \right) \quad . \tag{2.18}$$

The main advantage of this transformation is that functions sharply peaked with respect to the relative variable y and smooth with respect to R translate into smooth phase space functions with respect to both arguments, R and p. In this way local operators have momentum independent Wigner transforms etc.. To perform the Wigner transformations, equations (2.16) and (2.17) are rewritten in terms of the new variables R and y and the operation $\int \mathrm{d}^4y \exp(\mathrm{i}p\cdot y/\hbar)$ is then applied to the equations. Derivatives with respect to y can be expressed by multiplications with p by partial integration.

$$\begin{aligned} \mathrm{i}\hbar \left[\frac{\partial}{\partial T} + \frac{\boldsymbol{p}}{m} \cdot \boldsymbol{\nabla}_R \right] g^{\gtrless}_W &= \left[Re\,\Sigma^+ \,,\, g^{\gtrless} \right]_{-,W} + \left[\Sigma^{\gtrless} \,,\, Re\, g^+ \right]_{-,W} \\ &\quad + \frac{1}{2} \left[\Sigma^> \,,\, g^< \right]_{+,W} - \frac{1}{2} \left[\Sigma^< \,,\, g^> \right]_{+,W} \,, \end{aligned} \tag{2.19}$$

$$\begin{aligned} 2 \left[\omega - \frac{\boldsymbol{p}^2}{2m} + \frac{1}{4}\frac{\hbar^2}{2m}\Delta_R \right] g^{\gtrless}_W &= \left[Re\,\Sigma^+ \,,\, g^{\gtrless} \right]_{+,W} + \left[\Sigma^{\gtrless} \,,\, Re\, g^+ \right]_{+,W} \\ &\quad + \frac{1}{2} \left[\Sigma^> \,,\, g^< \right]_{-,W} - \frac{1}{2} \left[\Sigma^< \,,\, g^> \right]_{-,W} \,. \end{aligned} \tag{2.20}$$

Here the subscript W at the (anti-) commutators denote the Wigner transforms of the whole quantity. In order to express the right hand side in terms of Wigner transforms, we need the Wigner transform of Operator products, which is in general given by

$$(AB)_W(R\,,\,p) \;=\; A_W(R\,,\,p)\exp\left\{\frac{\mathrm{i}\hbar}{2}\overleftrightarrow{\Lambda}\right\}B_W(R\,,\,p) \quad . \tag{2.21}$$

The differential operator, $\overleftrightarrow{\Lambda}$, in the exponent is given by $\overleftarrow{\partial}_p\cdot\overrightarrow{\partial}_R - \overleftarrow{\partial}_R\cdot\overrightarrow{\partial}_p$ in four vector notation and where the arrows indicate the direction into which the partial derivatives act.

The essential simplification is now to neglect higher than first order derivatives. More precisely: we require quantities of the form

$$\left|\frac{\mathrm{i}\hbar}{2}\,\frac{\partial_p A_W\cdot\partial_R B_W}{A_W B_W}\right| \ll 1 \qquad \text{and} \qquad \left|\frac{\mathrm{i}\hbar}{2}\,\frac{\partial_R A_W\cdot\partial_p B_W}{A_W B_W}\right| \ll 1 \tag{2.22}$$

to be small every where in phase space i.e. that the operators are sufficiently diagonal (local) in space-time representation and slowly varying with $R=(x+x')/2$, and that higher order derivatives can be omitted. It should be mentioned that the smoothness of the Wigner transformed quantities in phase space can be enforced to some extent by averaging them over a sufficiently large region in phase space (of volume larger than $\hbar$), what usually is called coarse graining. Of course in doing this some of the information contained in the exact Wigner transforms is lost, but one gains in simplicity of the dynamical description and in the case of heavy ion collisions this is the only theoretical approximation which leads to (numerically) solvable dynamical equations. Other approaches like the Quantum Molecular Dynamics model are motivated by the form of these equations but up to now these models are lacking a strict theoretical derivation. Now in a gradient expansion up to first order derivatives the Wigner transforms of the (anti) commutators, $[A\,,\,B]_{\pm,W}$, can be expressed by simple products or Poisson brackets of the Wigner transformed operators by

$$[A\,,\,B]_{+,W} = 2\,A_W\,B_W \tag{2.23}$$

$$[A\,,\,B]_{-,W} = \mathrm{i}\hbar\{A_W\,,\,B_W\} \equiv \mathrm{i}\hbar(\partial_p A_W\cdot\partial_R B_W - \partial_R A_W\cdot\partial_p B_W) \tag{2.24}$$

Furthermore the left hand side of Eq. (2.19) can also be expressed by a Poisson bracket namely $\mathrm{i}\hbar\{\omega - \frac{p^2}{2m}\,,\,g^{\gtrless}_W\}$, where ω denotes the zero component of the momentum four vector, while the derivative on the left hand side of Eq. (2.20) is of second order and consequently should be neglected in a gradient expansion up to first order. We arrive at

$$\mathrm{i}\hbar\left\{\omega - \frac{\boldsymbol{p}^2}{2m} - Re\,\Sigma^+\,,\,g^{\gtrless}\right\} - \mathrm{i}\hbar\left\{\Sigma^{\gtrless}\,,\,Re\,g^+\right\} \;=\; \Sigma^{>}g^{<} \,-\, \Sigma^{<}g^{>}\,, \tag{2.25}$$

$$\left[\omega - \frac{\boldsymbol{p}^2}{2m} - Re\,\Sigma^+\right]g^{\gtrless} \,-\Sigma^{\gtrless}\,Re\,g^+ \;=\; \frac{\mathrm{i}\hbar}{4}\,\{\Sigma^{>}\,,\,g^{<}\} \,-\, \frac{\mathrm{i}\hbar}{4}\,\{\Sigma^{<}\,,\,g^{>}\}\,, \tag{2.26}$$

where we dropped the index W for the Wigner transformed quantities. These are of course just c-number functions in phase space and the above equations of motion are therefore local, in contrast to the exact equations. The analogous equations for the retarded Green's functions are

$$\mathrm{i}\hbar\left\{\omega - \frac{p^2}{2m} - \Sigma^{\pm}\,,\,g^{\pm}\right\} \;=\; 0\,, \tag{2.27}$$

$$\left[\omega - \frac{p^2}{2m} - \Sigma^{\pm}\right] g^{\pm} \;=\; 1\,. \tag{2.28}$$

The right hand side of Eq. (2.25) is the collision term, with the rate of loss minus the rate of gain (note an over all minus sign implicitly contained in the Green's functions).

Especially the self energies $\Sigma^{>,<}$ can be interpreted as the rate of scattering out (in) per occupied (empty) state respectively. The correlation functions $g^{>,<}$ are connected to the local occupation number, $f(R,p)$, and the local spectral function, $a(R,p)$, via the definitions of a and f,

$$g^{>} \;=\; \frac{1}{\mathrm{i}\hbar} a(1-f)\,, \qquad\qquad g^{<} \;=\; -\frac{1}{\mathrm{i}\hbar} af\,. \tag{2.29}$$

such that $a = \mathrm{i}\hbar(g^{>} - g^{<}) = \mathrm{i}\hbar(g^{+} - g^{-})$. The interpretation of a and f is motivated by the solutions for $g^{>,<}$ in a non interacting equilibrium system of fermions, where $a(R,p) \sim \delta(\omega - \frac{p^2}{2m})$ (independent of R) and $f(R,p)$ is the Fermi distribution. In this case the energy of the particles is fixed to their mass shell value. On the left hand side of (2.25), the first Poisson bracket describes the motion of the phase space points propagated by a semi-classical Hamiltonian given by $p^2/2m + \Re\,\Sigma^{+}$. The real part of the retarded self-energy can therefore be interpreted as a space and momentum dependent potential. The difference to a completely classical motion is of course again the possibility of energies off the mass shell. The second Poisson bracket on the left hand side of (2.25) reflects the kinetic effects of the collisions, e.g. the effects of the energy and momentum change in collisions on the effective mass etc. In contrast to the transport equations (2.25), equations (2.26) which should be simultaneously fulfilled are not studied in great detail. The reason is that the possibility of off shell propagation ($\omega \neq \frac{p^2}{2m} + \Re\Sigma^{+}$) in between collisions makes practical solutions rather difficult. Therefore one usually neglects all terms except the first one in equation (2.26), which is called the quasi particle approximation. In this approximation the energy of the particles is fixed to their mass shell value and therefore the energy is no independent variable anymore. In order to see when this is justified we solve equation (2.28) for the retarded and advanced Green's function

$$g^{\pm} \;=\; \frac{1}{\omega - \frac{p^2}{2m} - \Sigma^{\pm} \pm \mathrm{i}\epsilon}\,. \tag{2.30}$$

The $\mathrm{i}\epsilon$ prescription is only needed if the imaginary part of the self energy vanishes or is neglected. If this solution is put into (2.27) the latter equation is automatically fulfilled. Subtracting the two equations (2.27) from each other and doing the same with (2.28) we obtain two equations for the spectral function:

$$\{\omega - E\,,\, a\} \;=\; \{\Gamma\,,\, \Re\, g^{+}\}\,, \tag{2.31}$$

$$(\omega - E)a \;=\; \Gamma\,\Re\, g^{+}\,. \tag{2.32}$$

Here we introduced

$$\Gamma \;=\; \mathrm{i}\hbar(\Sigma^{>} \,-\, \Sigma^{<}) = \mathrm{i}\hbar(\Sigma^{+} \,-\, \Sigma^{-}) = -2\hbar\Im\,\Sigma^{+} \tag{2.33}$$

in analogy to the spectral function and the abbreviation, E, for $E(R,p) = \frac{p^2}{2m} + \Re\,\Sigma^{+}(R,p)$. Observing that from Eq. (2.30) it follows that

$$\Re\, g^{+} \;=\; \frac{\omega - E}{(\omega - E)^2 + \left(\frac{\Gamma}{2\hbar}\right)^2} \;=\; \frac{\omega - E}{(\omega - E)^2 + \gamma^2}\,, \tag{2.34}$$

with $\gamma = \Gamma/2\hbar$, one can solve the algebraic equation (2.32) for a with the result

$$a \;=\; \frac{\Gamma}{(\omega - E)^2 + \left(\frac{\Gamma}{2\hbar}\right)^2} \;=\; 2\hbar\frac{\gamma}{(\omega - E)^2 + \gamma^2}\,. \tag{2.35}$$

The spectral function is therefore (formally) a Lorentzian with the width $\gamma = -\Im\,\Sigma^+$ around the mass shell $E = \frac{p^2}{2m} + \Re\,\Sigma^+$. It can easily be shown that the solution (2.35) of (2.32) is also a solution of (2.31). The quasi particle approximation is valid if the Lorentzian becomes a δ-function in the limit $\Gamma/E \ll 1$. The imaginary part of the retarded self-energy varies from -10 MeV at $E = 125$ MeV to -25 MeV at $E = 325$ MeV so that the fraction Γ/E seems to be sufficiently small for nonrelativistic energies. However, it should be kept in mind that off shell propagation can cause changes in the order of more than 10% in the scattering rates since in the collision term foldings of four spectral functions occur, which increases the effective width by a factor of $2-4$. However, if we adopt the quasi particle approximation and if we neglect the momentum dependence of the real part of the retarded self-energy in the collision term, one immediately obtains the so called Vlasov-Uehling-Uhlenbeck equation (VUU, sometimes also called Boltzmann-Uehling-Uhlenbeck BUU):

$$\begin{aligned}\left[\frac{\partial}{\partial t} \;+\; \left(\frac{\boldsymbol{p}_1}{m} + \boldsymbol{\nabla}_{p_1}\Re\Sigma^+\right)\cdot\boldsymbol{\nabla}_{r_1} - \boldsymbol{\nabla}_{r_1}\Re\Sigma^+\cdot\boldsymbol{\nabla}_{p_1}\right] f_1(\boldsymbol{r}_1,\boldsymbol{p}_1,t) \\ = \;\frac{2g}{m^2(2\pi\hbar)^3}\int \mathrm{d}^3\boldsymbol{p}_2\int \mathrm{d}^3\boldsymbol{p}_1'\int \mathrm{d}^3\boldsymbol{p}_2'\,\delta^4(p_1+p_2-p_1'-p_2')\frac{\mathrm{d}\sigma}{\mathrm{d}\Omega} \\ \times\,[f_1'f_2'(1-f_1)(1-f_2) - f_1f_2(1-f_1')(1-f_2')] \qquad (2.36)\end{aligned}$$

which especially in its relativistic version (see below) is a starting point for many practical simulations of heavy ion collisions ($g = 4$ denotes the nucleon degeneracy factor). If the r.h.s of Eq. (2.36), the collision integral, is neglected one obtains the Vlasov equation [49]. On the other hand, if the real part of the retarded self-energy $\Re\Sigma^+$ is neglected and if the so called Pauli blocking factors $(1-f)$ in the collision integral are approximated by 1, one obtains the famous Boltzmann equation. The modification of Boltzmann's collision integral by the Pauli blocking factors, which take into account the Pauli principle for the final state of the two-body collisions, was first introduced by Nordheim [50], and latter worked out by Uehling and Uhlenbeck [51, 52]. Examples for the application of Eq. (2.36) to heavy ion collisions can be found e.g. in [53, 54, 55, 56, 57, 58]. It should be noted that the momentum dependence of the self-energy causes some practical problems in the collision term, since scatterings change the momenta of the particles and therefore also the potential energy. In principle this is correctly incorporated in equation (2.25) where the energy $E = \boldsymbol{p}^2/2m + \Re\Sigma^+$ occurs in the spectral function (δ-function in quasi particle limit) and from this one can derive more general transport equations than (2.36). However, then additional factors (Z-factors) appear in the collision integral which make the practical solution more difficult [41, 59]. Such collision terms are standard in other fields [60, 61]. In equation (2.36), only the free on shell energy $\boldsymbol{p}^0 = \boldsymbol{p}^2/2m$ appears in the energy conserving δ-function. Therefore in some practical computer simulations the momentum or the energy respectively must be rescaled to guarantee the conservation laws if the potential is momentum dependent.

The basic ingredients of transport equations like (2.36) are the real part of the retarded self-energy (the potential energy) and the cross sections which both should be calculated consistently from the same basic interaction e.g. in G-matrix approximation, etc. Then the cross section and the G-matrix are connected by

$$|\langle \boldsymbol{p}_1\,\boldsymbol{p}_2|G|\boldsymbol{p}_1'\,\boldsymbol{p}_2'\rangle^{a.s.}|^2 \;=\; 4g\,\frac{(2\pi)^5\hbar^7}{m^2V^3}\,\frac{\mathrm{d}\sigma}{\mathrm{d}\Omega}(\boldsymbol{p}_1'-\boldsymbol{p}_1)\delta^3(\boldsymbol{p}_1+\boldsymbol{p}_2-\boldsymbol{p}_1'-\boldsymbol{p}_2') \qquad (2.37)$$

where the plane waves are normalized to the volume V [47].

In practice one solves equations like (2.36) by Monte-Carlo methods. First practical solutions of the Boltzmann equation (no self-energies, no Pauli blocking) were done in the late 70's for hadron induced and heavy-ion reactions [62, 63, 64, 65, 66, 67]. Later, the BUU simulations with test-particle methods were the

first to include mean potentials and Pauli blocking [53, 54, 55, 56, 57]. The phase space distributions can be represented by the density of test particles. The latter are propagated classically with the Hamiltonian $E(R,p) = \boldsymbol{p}^2/2m + \Re\Sigma^+(R,p)$ which yields a solution of the Vlasov part (l.h.s. $= 0$) of the transport equation. At the point of closest approach of two particles one performs a random scattering process, if the distance at that point is smaller than $\sqrt{\sigma_{tot}/\pi}$. The angular distribution for the scattering is obtained from $\mathrm{d}\sigma/\mathrm{d}\Omega$.

Up to now there is no stringent proof that this procedure really yields a solution of the full transport equation, but it can be shown numerically that this prescription yields the correct asymptotic approach to equilibrium, which can be deduced from the Boltzmann equation, i.e. equation (2.36), without potential and without the $(1-f)$ Pauli-blocking factors [68].

However, a deficiency of all transport equations for the single particle phase space distribution is that clusters or fragments in heavy ion collisions can only be constructed in a statistical way, e.g. with the help of a coalescence model. The reason is that in transport theory bound states of many nucleons cannot be described directly. This can be avoided if one combines the fully classical equations of motion with the random scatterings of transport theory. The classical many body theory with two body forces allows for bound states of the particles but completely ignores any quantum effects. Especially the hard core of the nucleon-nucleon interaction would lead to a completely different classical behavior as compared to quantum mechanical scattering. Therefore in models like QMD, RQMD etc. one translates the soft (long range) part of the effective interaction in the medium ($\mathrm{Re}\Sigma^+$) into a classical but density and possibly momentum dependent two body interaction. However this must be supplemented by random scatterings to account for the short range part of the interaction and the other quantum effects like Pauli blocking. Unfortunately this procedure can only in part be justified from first principles [69], but it can be shown that this model yields quite similar results as the transport model as long as one body observables are concerned [70, 71, 72]. They are different though for many body observables like fragments.

2.2 Relativistic transport theory

We now proceed to generalize the approximation scheme outlined above to the relativistic case. Here one should start from an effective Lagrangian with baryons and mesons as elementary degrees of freedom. Since the well known $\sigma-\omega-$model has been proven to describe static properties of finite nuclei very well [73, 74] it seems to be reasonable to start with this model also for the description of the dynamics of heavy ion collisions. It is known that the linear energy dependence of the real part of the self-energy is too strong as compared to the measured logarithmic behavior. However, this can be remedied by an effective (energy and density dependent) coupling strength [75].

We start from a Lagrangian density for nucleons, deltas and a nucleon resonance like the N^*_{1440} plus the σ and ω and π meson, for details cf. [76]. The free part reads:

$$\begin{aligned}\mathcal{L}_{\mathrm{F}} &= \bar{\psi}[\mathrm{i}\gamma_\mu\partial^\mu - M_N]\psi + \bar{\psi}^*[\mathrm{i}\gamma_\mu\partial^\mu - M_{N^*}]\psi^* \\ &\quad +\bar{\psi}_{\Delta\nu}[\mathrm{i}\gamma_\mu\partial^\mu - M_\Delta]\psi^\nu_\Delta + \frac{1}{2}\partial_\mu\sigma\partial^\mu\sigma - U(\sigma) \\ &\quad -\frac{1}{4}\omega_{\mu\nu}\omega^{\mu\nu} + U(\omega) + \frac{1}{2}(\partial_\mu\boldsymbol{\pi}\partial^\mu\boldsymbol{\pi} - m_\pi^2\boldsymbol{\pi}^2) \qquad (2.38)\end{aligned}$$

and U(σ), U(ω) are the self-interaction part of the scalar field [77] and vector field [78]

$$U(\sigma) = \frac{1}{2}m_\sigma^2\sigma^2 + \frac{1}{3}b(\mathrm{g}^\sigma_{NN}\sigma)^3 + \frac{1}{4}c(\mathrm{g}^\sigma_{NN}\sigma)^4, \qquad (2.39)$$

$$U(\omega) = \frac{1}{2} m_\omega^2 \omega_\mu \omega^\mu (1 + \frac{(\mathrm{g}_{NN}^\omega)^2}{2} \frac{\omega_\mu \omega^\mu}{Z^2}), \tag{2.40}$$

respectively. $\mathcal{L}_I$ is the interaction Lagrangian density

$$\begin{aligned}
\mathcal{L}_I &= \mathcal{L}_{NN} + \mathcal{L}_{N^*N^*} + \mathcal{L}_{\Delta\Delta} + \mathcal{L}_{NN^*} + \mathcal{L}_{\Delta N} + \mathcal{L}_{\Delta N^*} \\
&= \mathrm{g}_{NN}^\sigma \bar\psi(x)\psi(x)\sigma(x) - \mathrm{g}_{NN}^\omega \bar\psi(x)\gamma_\mu\psi(x)\omega^\mu(x) + \mathrm{g}_{NN}^\pi \bar\psi(x)\gamma_\mu\gamma_5 \boldsymbol{\tau}\cdot\psi(x)\partial^\mu\boldsymbol{\pi}(x) \\
&\quad + \mathrm{g}_{N^*N^*}^\sigma \bar\psi^*(x)\psi^*(x)\sigma(x) - \mathrm{g}_{N^*N^*}^\omega \bar\psi^*(x)\gamma_\mu\psi^*(x)\omega^\mu(x) + \mathrm{g}_{N^*N^*}^\pi \bar\psi^*(x)\gamma_\mu\gamma_5 \boldsymbol{\tau}\cdot\psi^*(x)\partial^\mu\boldsymbol{\pi}(x) \\
&\quad + \mathrm{g}_{\Delta\Delta}^\sigma \bar\psi_{\Delta\nu}(x)\psi_\Delta^\nu(x)\sigma(x) - \mathrm{g}_{\Delta\Delta}^\omega \bar\psi_{\Delta\nu}(x)\gamma_\mu\psi_\Delta^\nu(x)\omega^\mu(x) + \mathrm{g}_{\Delta\Delta}^\pi \bar\psi_{\Delta\nu}(x)\gamma_\mu\gamma_5 \mathbf{T}\cdot\psi_\Delta^\nu(x)\partial^\mu\boldsymbol{\pi}(x) \\
&\quad + [\mathrm{g}_{NN^*}^\sigma \bar\psi^*(x)\psi(x)\sigma(x) - \mathrm{g}_{NN^*}^\omega \bar\psi^*(x)\gamma_\mu\psi(x)\omega^\mu(x) + \mathrm{g}_{NN^*}^\pi \bar\psi^*(x)\gamma_\mu\gamma_5 \boldsymbol{\tau}\cdot\psi(x)\partial^\mu\boldsymbol{\pi}(x) \\
&\quad - \mathrm{g}_{\Delta N}^\pi \bar\psi_{\Delta\mu}(x)\partial^\mu\boldsymbol{\pi}(x)\cdot\mathbf{S}^+\psi(x) - \mathrm{g}_{\Delta N^*}^\pi \bar\psi_{\Delta\mu}(x)\partial^\mu\boldsymbol{\pi}(x)\cdot\mathbf{S}^+\psi^*(x) + H.c.] \\
&= \mathrm{g}_{NN}^A \bar\psi(x)\Gamma_A^N\psi(x)\Phi_A(x) + \mathrm{g}_{N^*N^*}^A \bar\psi^*(x)\Gamma_A^{N^*}\psi^*(x)\Phi_A(x) + \mathrm{g}_{\Delta\Delta}^A \bar\psi_{\Delta\nu}(x)\Gamma_A^\Delta\psi_\Delta^\nu(x)\Phi_A(x) \\
&\quad + [\mathrm{g}_{NN^*}^A \bar\psi^*(x)\Gamma_A^{N^*}\psi(x)\Phi_A(x) - \mathrm{g}_{\Delta N}^\pi \bar\psi_{\Delta\mu}(x)\partial^\mu\boldsymbol{\pi}(x)\cdot\mathbf{S}^+\psi(x) \\
&\quad - \mathrm{g}_{\Delta N^*}^\pi \bar\psi_{\Delta\mu}(x)\partial^\mu\boldsymbol{\pi}(x)\cdot\mathbf{S}^+\psi^*(x) + h.\,c.]
\end{aligned} \tag{2.41}$$

Here, ψ, ψ^* are the Dirac spinors of the nucleon and $N^*(1440)$, and $\psi_{\Delta\mu}$ is the Rarita-Schwinger spinor of the Δ-baryon. $\boldsymbol{\tau}$ is the isospin operator of the nucleon and N^* (1440), $\mathbf{T}$ is the isospin operator of the Δ, and $\mathbf{S}^+$ is the isospin transition operator between the isospin 1/2 and 3/2 fields. $\mathrm{g}_{NN}^\pi = f_\pi/m_\pi$, $\mathrm{g}_{\Delta N}^\pi = f^*/m_\pi$; $\Gamma_A^N = \Gamma_A^{N^*} = \gamma_A\tau_A$, $\Gamma_A^\Delta = \gamma_A T_A$, A=$\sigma$, ω, π, the symbols and notation are defined in table 2.1.

In the closed time path formalism one obtains quite analogous Dyson equations for the different particle species from which one obtains in turn transport equations for nucleons, N^*_{1440} and Δ_{1232} [75, 76, 79]. However, in the relativistic case, even more difficulties arise as for the nonrelativistic tranport equations. T- or G-matrix calculations starting from a Lagrangian like (2.41) are very cumbersome even for the static equilibrium situation. Also the non-locality of the Fock term in the mean-field approximation, leads to a non-trivial momentum dependence of the self-energy. The same is true for the Born approximation, therefore one usually takes only the Hartree or the mean-field approximation for the Vlasov part in the transport equation. Effective masses and momenta enter both the Vlasov part and the collision term where the cross section has to be calculated in some approximation. As a qualitative guideline, one can calculate cross sections from Lagrangians as (2.41) in the Born approximation. However, in medium dressed propagators should be used for the internal lines, taking into account effective mass and momentum in Hartree approximation. For a more rigorous derivation, we refer to the work of Cassing *et al.* [10, 80]. How the cross sections are determined in the UrQMD model can be found in section 3.3.2.

One then usually uses the propagators of non-interacting systems of particles with effective mass, e.g. for the nucleon and the N^*_{1440}

$$g^{c,a}(x,p) = (\not{p} + m^*_{N^*}) \left[\frac{\pm 1}{p^2 - m^{*2}_{N^*} \pm \mathrm{i}\epsilon} + \frac{\pi\mathrm{i}}{E(p)} \delta(p_0 - E(p)) f_{N^*}(x,p) \right], \tag{2.42}$$

$$g^{>}(x,p) = -\frac{\pi\mathrm{i}}{E(p)} \delta(p_0 - E(p))[1 - f_{N^*}(x,p)](\not{p} + m^*_{N^*}) \tag{2.43}$$

$$g^{<}(x,p) = \frac{\pi\mathrm{i}}{E(p)} \delta(p_0 - E(p)) f_{N^*}(x,p)(\not{p} + m^*_{N^*}). \tag{2.44}$$

where $E(p) = \sqrt{\boldsymbol{p}^2 + M^2_{N^*}}$. The effective mass and momentum of e.g. the N^*_{1440} are defined as

$$m^*_{N^*}(x) = M_{N^*} + \Sigma^S_{N^*}(x) \tag{2.45}$$

$$p^\mu(x) = P^\mu - \Sigma^\mu_{N^*}(x). \tag{2.46}$$

A	m_A	g^A_{NN}	$g^A_{N^*N^*}$	$g^A_{\Delta\Delta}$	$g^A_{NN^*}$	γ_A	τ_A	T_A	$\Phi_A(x)$	D^μ_A	D^i_A
σ	m_σ	g^σ_{NN}	$g^\sigma_{N^*N^*}$	$g^\sigma_{\Delta\Delta}$	$g^\sigma_{NN^*}$	1	1	1	$\sigma(x)$	1	1
ω	m_ω	$-\ g^\omega_{NN}$	$-\ g^\omega_{N^*N^*}$	$-\ g^\omega_{\Delta\Delta}$	$-\ g^\omega_{NN^*}$	γ_μ	1	1	$\omega^\mu(x)$	$-\ g^{\mu\nu}$	1
π	m_π	g^π_{NN}	$g^\pi_{N^*N^*}$	$g^\pi_{\Delta\Delta}$	$g^\pi_{NN^*}$	$\not{\gamma}_5$	$\boldsymbol{\tau}$	$\mathbf{T}$	$\boldsymbol{\pi}$(x)	1	δ_{ij}

Table 2.1: Symbol and notation definitions.

The self-energies are taken here in Hartree Fock approximation only. Herewith one assumes that the contribution of the Born diagrams to the real part of the self-energy is small. Furthermore one often also neglects the Fock part of the self-energy for the same reason. The self energies in Hartree approximation for the N^*_{1440} for example are given by

$$\Sigma^S_{N^*}(x) = -\frac{g^\sigma_{N^*N^*}}{m^2_\sigma}[g^\sigma_{NN}\rho_S(N) + g^\sigma_{N^*N^*}\rho_S(N^*) + g^\sigma_{\Delta\Delta}\rho_S(\Delta)], \tag{2.47}$$

$$\Sigma^\mu_{N^*}(x) = \frac{g^\omega_{N^*N^*}}{m^2_\omega}[g^\omega_{NN}\rho^\mu_V(N) + g^\omega_{N^*N^*}\rho^\mu_V(N^*) + g^\omega_{\Delta\Delta}\rho^\mu_V(\Delta)]. \tag{2.48}$$

where $\rho_S(i)$ and $\rho^\mu_V(i)$ are the scalar and vector densities of particle species i and analogous expressions for N and Δ_{1232}. Furthermore one usually makes use of the so called local density approximation. This means that the mean σ and ω fields are determined from the local scalar and vector densities alone, neglecting retarded contributions from other space time regions, i.e. in the Klein-Gordon equation for the σ (and analogous for the ω):

$$(\Box + m^2_\sigma)\sigma + b(g^\sigma_{NN})^3\,\sigma^2 + c(g^\sigma_{NN})^4\,\sigma^3 \;=\; g^\sigma_{NN}\rho_S(N) + g^\sigma_{N^*N^*}\rho_S(N^*) + g^\sigma_{\Delta\Delta}\rho_S(\Delta) \tag{2.49}$$

One neglects the dynamical contributions of the $\Box$-operator. This should be a good approximation as long as there are no rapid field oscillations on the scale of the (small) inverse mass of σ and ω meson. However, the retardation of the interaction should not be neglected for all energies from non-relativistic up to the ultra-relativistic energy regime. It is not clear up to now if one should take related phenomena like σ, ω Bremsstrahlung seriously [81]. Moreover, it has been shown that for intermediate energies of several hundred MeV per nucleon the above approximation is acceptable [82].

As an example, the RBUU equation e.g. for the N^*_{1440} distribution function now reads:

$$\begin{aligned}&\{p_\mu[\partial^\mu_x - \partial^\mu_x\Sigma^\nu_{N^*}(x)\partial^p_\nu + \partial^\nu_x\Sigma^\mu_{N^*}(x)\partial^p_\nu] + m^*_{N^*}\partial^\nu_x\Sigma^S_{N^*}(x)\partial^p_\nu\}\frac{f_{N^*}(\mathbf{x},\mathbf{p},t)}{E^*_{N^*}(p)}\\ &= C^{N^*}(x,p).\end{aligned} \tag{2.50}$$

and analogous equations for the nucleon and the Δ_{1232}. A practical solution of the relativistic Vlasov equation (l.h.s. of equation (2.50) = 0) can be found in [83]. Attempts have been made also to solve the corresponding quantum mechanical problem in terms of the time-dependent Dirac equation with mean fields [84]. Realizations of the full relativistic Boltzmann Uehling Uhlenbeck model (RBUU) can be found in [82, 85].

The collision term on the r.h.s. can be written as

$$\begin{aligned}C^{N^*}(x,p) \;&=\; \frac{1}{2}\int\frac{d^3p_2}{(2\pi)^3}\int\frac{d^3p_3}{(2\pi)^3}\int\frac{d^3p_4}{(2\pi)^3}(2\pi)^4\delta^{(4)}(p+p_2-p_3-p_4)\\ &\quad\times W^{N^*}(p,\,p_2,\,p_3,\,p_4)(F_2-F_1),\end{aligned} \tag{2.51}$$

where F_2, F_1 are the Uehling-Uhlenbeck factors :

$$F_2 = [1 - f_{N^*}(\mathbf{x}, \mathbf{p}, t)][1 - f_{B_2}(\mathbf{x}, \mathbf{p}_2, t)] f_{B_3}(\mathbf{x}, \mathbf{p}_3, t) f_{B_4}(\mathbf{x}, \mathbf{p}_4, t), \tag{2.52}$$

$$F_1 = f_{N^*}(\mathbf{x}, \mathbf{p}, t) f_{B_2}(\mathbf{x}, \mathbf{p}_2, t)[1 - f_{B_3}(\mathbf{x}, \mathbf{p}_3, t)][1 - f_{B_4}(\mathbf{x}, \mathbf{p}_4, t)], \tag{2.53}$$

B_2, B_3, B_4 can be N, Δ and $N^*(1440)$ and possibly many other resonances. $W^{N^*}(p,\, p_2,\, p_3,\, p_4)$ is the transition probability of different channels, which has the form (for details see ref. [76])

$$W^{N^*}(p,\, p_2,\, p_3\, , p_4) = \frac{1}{16 E^*_{N^*}(p) E^*_{B_2}(p_2) E^*_{B_3}(p_3) E^*_{B_4}(p_4)} \sum_{AB} (T_D \Phi_D - T_E \Phi_E) + p_3 \longleftrightarrow p_4. \tag{2.54}$$

Here T_D, T_E are the isospin matrices and Φ_D, Φ_E are the spin matrices, respectively. D denotes the contribution of the direct diagrams and E is that of the exchange diagrams. A, $B = \sigma$, ω, π represent the contributions of different mesons. The exchange of p_3 and p_4 is only for the case of identical particles in the final state. The two-body scattering reactions relevant to the $N^*(1440)$ in the N, Δ and $N^*(1440)$ system are as follows:

(1) Elastic reactions:

$NN^* \longrightarrow NN^*$, $\quad \Delta N^* \longrightarrow \Delta N^*$, $\quad N^*N^* \longrightarrow N^*N^*$.

(2) Inelastic reactions:

$NN \longleftrightarrow NN^*$, $\quad N\Delta \longleftrightarrow NN^*$, $\quad \Delta\Delta \longleftrightarrow NN^*$,
$NN^* \longleftrightarrow \Delta N^*$, $\quad NN^* \longleftrightarrow N^*N^*$, $\quad NN \longleftrightarrow \Delta N^*$,
$N\Delta \longleftrightarrow \Delta N^*$, $\quad \Delta\Delta \longleftrightarrow \Delta N^*$, $\quad N^*N^* \longleftrightarrow \Delta N^*$,
$NN \longleftrightarrow N^*N^*$, $\quad N\Delta \longleftrightarrow N^*N^*$, $\quad \Delta\Delta \longleftrightarrow N^*N^*$.

In principle one also obtains resonance formation and decay terms which are not given here. From this it becomes clear that for higher energies (above several GeV per nucleon), where dozens of baryon and meson resonances come into play, the number of reaction channels increases tremendously. Even for comparatively low energies higher resonances contribute significantly to (subthreshold) particle production (see section 4.2.1). Most of the corresponding coupling constants are not known and instead one directly parameterizes the cross sections and potentials and decay widths. Furthermore the resonances have a spectral function (mass distribution) of finite width which is neglected in the quasi particle approximation. These spectral functions might change (width and the position of the pole) in the hot and dense nuclear medium, which has caused much interest during the last years [86, 87, 88, 89, 90, 91].

However, we would like to stress that a shift of the resonance mass distribution to lower masses is not necessarily connected to chiral symmetry restoration ($m^* \to 0$), since such a shift could also be obtained in a model without chiral symmetry in the high energy limit.

In a pragmatic way one can incorporate the mass distributions of resonances by folding the collision terms with appropriate mass distributions of the involved resonances [92] (see also section 3.3.2). In the actual numerical implementations this is usually taken into account by choosing the actual resonance mass (mass of the test-particles) according to a probability distribution, which might depend on the local density and temperature.

However, the basic concept of well established quasi particles becomes meaningless for energies beyond several GeV (baryons), where there is no pronounced resonance structure on the corresponding cross section anymore. For these energies one must incorporate a mechanism for continuous excitations of mesons and baryons. Since for such high energies also the internal quark and gluon degrees of freedom become more and more important one usually supplements the actual resonances by continuous string excitations above a (model dependent) energy threshold. These excited strings can then fragment into pre-hadrons by string fragmentation algorithms, which have been proven to be successful as long as rescatterings of newly

produced hadrons can be neglected [93]. A well known example is the FRITIOF model [94, 95], which however does not incorporate a complete phase space picture but rather works only in momentum space so that rescatterings are difficult to be included. Perturbative QCD effects like multiple minijets have been included in the PYTHIA model [96].

In the UrQMD model, to be discussed in more detail in the following chapter, a string excitation and fragmentation scheme is combined with the transport theoretical approach. Other models working along the same line are the RQMD (Relativistic Quantum Molecular Dynamics) model [37] or the HSD (Hadron String Dynamics) [97]. Some other models are based mainly on the dynamics of strings like VENUS [98] and QGSM [17] or partons like the parton cascade model PCM [99, 100] or the dual parton model [101, 102].

Since parton cascades are mainly based on the cross sections from perturbative QCD, a basic requirement is that the typical momentum transfer $\sqrt{Q^2}$ in parton scatterings is larger than ~ 10 GeV so that running coupling constants become sufficiently small. Even if this is fulfilled in first collisions, secondary interactions are much softer and require a non-perturbative treatment. Therefore these models have to be supplemented by hadronization prescriptions like the parton-hadron conversion model HIJING [103] and prescriptions for rescattering of newly produced hadrons like the hadron cascade HIJET [104].

A common problem for all models involving a transition from the string or parton picture to hadrons is the so called formation time. This is the time after which newly produced quarks and anti-quarks can be considered to be in a well established hadronic state (meson or baryon) that can interact again with other particles. Not much is known from the theoretical side how such a parameter can be calculated or how an appropriate model prescription could be derived. For the prescription used in the UrQMD model, we refer to section 3.3.5.

Even though models like RQMD or VENUS are impressively fine tuned for CERN SPS data the price to be paid are additional mechanisms or model assumptions like string droplets in VENUS [105] or color ropes in RQMD [106]. Furthermore, many of these models are not designed to work over a broad energy range (e.g. the relativistic cascade ARC [107] is only designed for AGS energies and models such as QMD/IQMD [71, 108, 109, 110, 111] or BUU [55, 56, 112] may only be applied to the BEVALAC/SIS energy domain). On the other hand the search for the quark gluon plasma in high energetic heavy ion collisions will require a systematic study of the excitation functions of observables over the broad energy range from SIS ($\sim$ 1 AGeV) up to SPS ($\sim$ 200 AGeV) or even higher energies in colliders like RHIC ($\sqrt{s} = 20$ AGeV) or LHC ($\sqrt{s} > 1000$ AGeV).

A general problem of hadron or parton cascades or transport models is the geometric interpretation of the cross section in most of the actual model implementations. Even though the underlying theory or model is usually Lorentz invariant the practical realization might not be [113]. This is due to the fact that the sequence of collisions according to a specific collision criterion can be reference frame dependent. The reason is that points of closest approach of several particles in space and time might be interchanged in the time sequence after a Lorentz transformation, such that in different reference frames one obtains different results for the sequence of scatterings. In the UrQMD model this problem has been minimized by the choice of the collision criterion (see section 3.3.1) such that the frame dependence of the observables (going from the CM to the target rest frame) is only in the order of $\sim 5\%$ at CERN/SPS energies.

2.3 The Quantum Molecular Dynamics approach

In the following we discuss an approach which goes beyond the one-body descriptions as discussed above, which is the Quantum Molecular Dynamics (QMD) model [69, 108, 109, 110]. The QMD model is a

N-body theory which simulates heavy ion reactions at intermediate energies on an event by event basis. Taking into account all fluctuations and correlations has basically two advantages: i) many-body processes, in particular the formation of complex fragments are explicitly treated and ii) the model allows for an event-by-event analysis of heavy ion reactions similar to the methods which are used for the analysis of exclusive high acceptance data.

The major aspects of the formulation of QMD will now be discussed briefly. For a more detailed description we refer to ref. [69]. The particular realization of the UrQMD model will be discussed later.

2.3.1 Formal derivation of the transport equation

In QMD each nucleon is represented by a coherent state of the form (we set $\hbar, c = 1$)

$$\phi_i(\boldsymbol{x}; \boldsymbol{q}_i, \boldsymbol{p}_i, t) = \left(\frac{2}{L\pi}\right)^{3/4} \exp\left\{-\frac{2}{L}(\boldsymbol{x} - \boldsymbol{q}_i(t))^2 + \frac{1}{\hbar}\mathrm{i}\boldsymbol{p}_i(t)\boldsymbol{x}\right\} \tag{2.55}$$

which is characterized by 6 time-dependent parameters, $\boldsymbol{q}_i$ and $\boldsymbol{p}_i$, respectively. The parameter L, which is related to the extension of the wave packet in phase space, is fixed. The total n-body wave function is assumed to be the direct product of coherent states (2.55)

$$\Phi = \prod_i \phi_i(\boldsymbol{x}, \boldsymbol{q_i}, \boldsymbol{p_i}, t) \tag{2.56}$$

Note that we do not use a Slater determinant and thus neglect antisymmetrization. The computational time scales like $(A_p + A_t)^4$ in the case of a Slater determinant, while in QMD it is like $(A_p + A_t)^2$. First successful attempts to simulate heavy ion reactions with antisymmetrized states have been performed for small systems [114, 115], for a recent review see Ref. [116]. A consistent derivation of the QMD equations of motion for the wave function under the influence of both, the real and the imaginary part of the G-matrix, however, has not yet been achieved. Therefore we will add the imaginary part as a cross section and treat them as in the cascade approach. How to incorporate cross sections into an antisymmetrized molecular dynamics is not yet known. This limits its applicability to very low beam energies.

The initial values of the parameters are chosen in a way that the ensemble of $A_T + A_P$ nucleons gives a proper density distribution as well as a proper momentum distribution of projectile and target nuclei.

The equations of motion of the many-body system is calculated by means of a generalized variational principle: we start out from the action

$$S = \int_{t_1}^{t_2} \mathcal{L}[\Phi, \Phi^*]dt \tag{2.57}$$

with the Lagrange functional $\mathcal{L}$

$$\mathcal{L} = \left\langle \Phi \left| \mathrm{i}\hbar\frac{d}{dt} - H \right| \Phi \right\rangle \tag{2.58}$$

where the total time derivative includes the derivation with respect to the parameters. The Hamiltonian H contains a kinetic term and mutual interactions V_{ij}, which can be interpreted as the real part of the Brueckner G-matrix supplemented by the Coulomb interaction. We will later on describe the components of H in detail. The time evolution of the parameters is obtained by the requirement that the action is stationary under the allowed variation of the wave function. This yields an Euler-Lagrange equation for each parameter.

If the true solution of the Schrödinger equation is contained in the restricted set of wave functions $\phi_i(\boldsymbol{x}; \boldsymbol{q}_i, \boldsymbol{p}_i, t)$ this variation of the action gives the exact solution of the Schrödinger equation. If the

parameter space is too restricted we obtain that wave function in the restricted parameter space which comes closest to the solution of the Schrödinger equation. Note that the set of wave functions which can be covered with special parameterizations is not necessarily a subspace of Hilbert-space, thus the superposition principle does not hold.

For the coherent states and a Hamiltonian of the form $H = \sum_i T_i + \frac{1}{2}\sum_{ij} V_{ij}$ (T_i= kinetic energy, V_{ij} = potential energy) the Lagrangian and the variation can easily be calculated and we obtain:

$$\mathcal{L} = \sum_i \Big[-\dot{\boldsymbol{q}}_i \boldsymbol{p}_i - T_i - \frac{1}{2}\sum_{j\neq i}\langle V_{ik}\rangle - \frac{3}{2Lm}\Big] \tag{2.59}$$

$$\dot{\boldsymbol{q}}_i = \frac{\boldsymbol{p}_i}{m} + \nabla_{\boldsymbol{p}_i}\sum_j \langle V_{ij}\rangle = \nabla_{\boldsymbol{p}_i}\langle H\rangle \tag{2.60}$$

$$\dot{\boldsymbol{p}}_i = -\nabla_{\boldsymbol{q}_i}\sum_{j\neq i}\langle V_{ij}\rangle = -\nabla_{\boldsymbol{q}_i}\langle H\rangle \tag{2.61}$$

with $\langle V_{ij}\rangle = \int d^3x_1\, d^3x_2\, \phi_i^*\phi_j^* V(x_1,x_2)\phi_i\phi_j$. These are the time evolution equations which are solved numerically. Thus the variational principle reduces the time evolution of the n-body Schrödinger equation to the time evolution equations of $6\cdot(A_P + A_T)$ parameters to which a physical meaning can be attributed. The equations of motion for the parameters $\boldsymbol{p}_i$ and $\boldsymbol{q}_i$ read

$$\dot{\boldsymbol{p}}_i = -\frac{\partial\langle H\rangle}{\partial \boldsymbol{q}_i} \quad \text{and} \quad \dot{\boldsymbol{q}}_i = \frac{\partial\langle H\rangle}{\partial \boldsymbol{p}_i}\,, \tag{2.62}$$

and show the same structure as the classical Hamilton equations. The numerical solution can be treated in a similar manner as it is done in classical molecular dynamics [53, 117, 118, 119, 120]. Using trial wave functions other than Gaussians in Eq. (2.55) yields more complex equations of motion and hence the analogy to classical molecular dynamics is lost. If $\langle H\rangle$ has no explicit time dependence, QMD conserves energy and momentum by construction.

2.3.2 Inclusion of collisions

As stated above the imaginary part of the G-matrix acts like a collision term. In the QMD simulation we restrict ourselves to binary collisions (two-body level). The collisions are performed in a point-particle sense in a similar way as in VUU or cascade [65]: Two particles collide if their minimum distance d, i.e. the minimum relative distance of the centroids of the Gaussians during their motion, in their CM frame fulfills the requirement:

$$d \leq d_0 = \sqrt{\frac{\sigma_{\text{tot}}}{\pi}}, \qquad \sigma_{\text{tot}} = \sigma(\sqrt{s},\ \text{type}). \tag{2.63}$$

where the cross section is assumed to be the free cross section of the regarded collision type ($N-N$, $N-\Delta$, ...).

Beside the parameters describing the N–N potential, the cross sections constitute another major part of the model. In principle, both quantities are connected and can be deduced from Brueckner theory. QMD-calculations using consistently derived cross-sections and potentials from the local phase space distributions have been discussed e.g. in [47]. Such simulations are time-consuming since the cross-sections and potentials do explicitly depend on the local phase space population.

Within the framework of using free cross section one may parameterize the cross section of the processes to fit to the experimental data if available. For unknown cross sections isospin symmetry and time reversibility is assumed.

2.3.3 Pauli blocking due to Fermi statistics

The cross section is reduced to an effective cross section by the Pauli-blocking. For each collision the phase space densities in the final states are checked in order to assure that the final distribution in phase space is in agreement with the Pauli principle ($f \leq 1$). Phase space in QMD is not discretized into elementary cells as in one-body models like VUU. In order to obtain smooth distribution functions the following procedure is applied: The phase space density f_i' at the final states $1'$ and $2'$ is measured and interpreted as a blocking probability. Thus, the collision is only allowed with a probability of $(1 - f_1')(1 - f_2')$. If the collision is not allowed the particles remain at their original momenta.

2.3.4 The Relativistic Quantum Molecular Dynamics approach

The Relativistic Quantum Molecular Dynamics (RQMD) approach has been developed to extend the QMD model up to relativistic energies (AGS and CERN/SPS domain) [37]. Its main improvements compared to the standard QMD model [69, 72, 109, 108, 110, 111, 121] are

1. covariant dynamics

2. an improved and extended collision term containing heavy baryon-resonances, strange particles and string-excitation for high energy hadron-hadron interactions

In this section we will focus on the first item – the covariant dynamics – since the description of the UrQMD collision term in the following chapter will cover in great detail all the techniques which have also been employed in the RQMD model.

The Relativistic Quantum Molecular Dynamics model describes the time-evolution of a many-body system using classical covariant equations of motion. The system propagates in a $8N$-dimensional phase space with $6N$ degrees of freedom representing the classical configuration- and momentum-space. The remaining $2N$ degrees of freedom contain the eigentime and energy of each particle.

The necessity of employing an $8N$-dimensional phase-space is based on the *no-interaction theorem* (NIT) by Curri, Sudarshan and Mukunda [36]: In a $6N + 1$-dimensional phase-space a Lagrangian for a Poincaré-invariant dynamics can only be formulated in the case of non-interacting free particles. In order to reduce the $8N$-dimensional phase-space to the commonly used $6N + 1$ dimensions, Lorentz-covariant constraints have to be introduced. These constraints have to yield reasonable equations of motion in the non-relativistic limit of a dilute gas. These constraints impose a time-ordering on the dynamics of the system. They consist of N mass-shell constraints:

$$H_i = \boldsymbol{p}_i^2 - m_i^2 - V_i \; = \; 0 \quad i = 1, \ldots, N \tag{2.64}$$

and $N - 1$ constraints which connect the relative times of the particles

$$\chi_i = \sum_{j \neq i} g_{ij} \boldsymbol{p}_{ij} \boldsymbol{q}_{ij} \; = \; 0 \qquad i = 1, \ldots, N \tag{2.65}$$

with

$$\boldsymbol{q}_{ij} = \boldsymbol{q}_i - \boldsymbol{q}_j \,, \quad \boldsymbol{p}_{ij} = \boldsymbol{p}_i + \boldsymbol{p}_j \,, \quad g_{ij} = \frac{\exp(\boldsymbol{q}_{ij}^2 / L)}{\boldsymbol{q}_{ij}^2} \tag{2.66}$$

The Nth constraint then serves to attach the individual eigentimes to a common time-evolution parameter τ.

In the case of finite range interactions, acausalities may occur. The constraints (2.65), however, suppress correlations of particles with strongly differing eigentimes.

Furthermore a time-ordering for binary collisions must be imposed (via the time-evolution parameter τ). This time-ordering, unfortunately, depends on the reference frame. One has to assume that the number of collisions is large enough for the dynamics of a single binary collision not to influence macroscopic properties of the system.

The Hamiltonian is defined as linear combination of all Poincaré-invariant constraints:

$$H = \sum_{i=1}^{N} \lambda_i H_i + \sum_{i=1}^{N-1} \delta\mu_i \chi_i \tag{2.67}$$

The canonical equations of motion are then given as

$$\frac{d\boldsymbol{q}_j}{d\tau} = \frac{\partial H}{\partial \boldsymbol{p}_j} = 2\lambda_j \boldsymbol{p}_j - \sum_{i=1}^{N} \lambda_i \frac{\partial V_i}{\partial \boldsymbol{p}_j} \qquad j = 1, \ldots, N \tag{2.68}$$

$$\frac{d\boldsymbol{p}_j}{d\tau} = -\frac{\partial H}{\partial \boldsymbol{q}_j} = \sum_{i=1}^{N} \lambda_i \frac{\partial V_i}{\partial \boldsymbol{q}_j} \tag{2.69}$$

with the coefficients λ_i:

$$\lambda_i \approx -\frac{\partial \chi_N}{\partial \tau} S_{Ni} \qquad i = 1, \ldots, N \tag{2.70}$$

The Nth constraint χ_N connects the eigentimes of the individual particles to the time-evolution parameter τ. Although this parameter is used to describe the time-evolution of the system, it should, however, not be interpreted as the system time. The matrix S_{ij} is then given by:

$$(S^{-1})_{ij} \equiv \{H_i, \chi_j\} \qquad i, j = 1, \ldots, N \tag{2.71}$$

Here, the main drawback of the RQMD ansatz appears: In order to solve the equations of motion one needs to calculate the coefficients λ_i. For their calculation the matrix S^{-1} must be inverted. Since the number of elements of S^{-1} is quadratic in the number of particles N, the inversion of S^{-1} (which can only be done numerically) is very time-consuming, especially for heavy collision systems at CERN/SPS energies.

Chapter 3

The UrQMD-Model

3.1 Initialization

This section describes the initialization of projectile and target nuclei in the UrQMD model. Projectile and target are modeled according to the Fermi-gas ansatz. The nucleons are represented by Gaussian shaped density distributions:

$$\varphi_j(\boldsymbol{x}_j, t) \;=\; \left(\frac{2\alpha}{\pi}\right)^{\frac{3}{4}} \exp\left\{-\alpha(\boldsymbol{x}_j - \boldsymbol{r}_j(t))^2 + \frac{\mathrm{i}}{\hbar}\boldsymbol{p}_j(t)\boldsymbol{x}_j\right\} \quad . \tag{3.1}$$

The wave-function of the nucleus is defined as the product wave-function of the single nucleon Gaussians:

$$\Phi \;=\; \prod_j \varphi_j(\boldsymbol{x_i}, \boldsymbol{p_i}, t) \quad . \tag{3.2}$$

Each initialized nucleus must meet the following constraints:

- $\sum_i \boldsymbol{q}_i = \boldsymbol{0}$, i.e. it is centered in configuration space around $\boldsymbol{0}$,
- $\sum_i \boldsymbol{v}_i = \boldsymbol{0}$, i.e. the nucleus is at rest
- its binding energy should correspond to the value given by the Bethe-Weizsäcker formula,
- the radius should yield the following mass dependence

$$R(A) \;\sim\; r_0 \cdot A^{\frac{1}{3}} \tag{3.3}$$

  and have a reasonable surface-thickness,

- in its center, the nucleus should have nuclear matter ground-state density.

In configuration space the centroids of the Gaussians are randomly distributed within a sphere. The finite width of Gaussians results in a surface region beyond the radius of that sphere. Therefore its radius is reduced by half a layer of nucleons from the original nuclear radius of equation (3.3):

$$R(A) \;=\; r_0 \left(\frac{1}{2}\left[A + \left(A^{\frac{1}{3}} - 1\right)^3\right]\right)^{\frac{1}{3}} \quad . \tag{3.4}$$

The parameter r_0 is a function of the nuclear matter ground state density ρ_0 used in the UrQMD model:

$$r_0 = \left(\frac{3}{4\pi\rho_0}\right)^{\frac{1}{3}} . \tag{3.5}$$

The relatively small number of nucleons to be distributed over the volume of the nucleus may result in large fluctuations in the mean density of the nucleus. Therefore the phase-space density at the location of each nucleon is evaluated after its placement. If the phase-space density is too high (i.e. the respective area of the nucleus is already occupied by other nucleons), then the location of that nucleon is rejected and a new location is randomly chosen.

The initial momenta of the nucleons are randomly chosen between 0 and the local Thomas-Fermi-momentum:

$$p_F^{max} = \hbar c \left(3\pi^2\rho\right)^{\frac{1}{3}} , \tag{3.6}$$

with ρ being the corresponding local proton- or neutron-density.

A principal disadvantage of this type of initialization is that the initialized nuclei are not really in their ground-state with respect to the Hamiltonian used for their propagation. The parameters of the Hamiltonian (see section 3.2) are tuned to the equation of state of infinite nuclear matter and to properties of finite nuclei (such as their binding energy and their root mean square radius). If, however, the energy of the nucleons within the nucleus is minimized according to the Hamiltonian in a self-consistent fashion, then the nucleus would collapse to a single point in momentum space because the Pauli-principle has not been taken into account in the Hamiltonian.

A viable solution to this problem is the inclusion of fermionic properties of the nucleons via the antisymmetrization of the wave-function of the nucleus. This ansatz has first been implemented in the framework of the Fermionic Molecular Dynamics (FMD) [114]. The FMD equations of motion are computationally very expensive – it has therefore not been possible so far, to calculate systems heavier than Ca+Ca in the framework of FMD [116].

An alternative recipe is the use of a so-called Pauli-Potential [118] in the Hamiltonian. This potential, which is repulsive in configuration and momentum space, allows to maintain the product ansatz for the wave-function of the nucleus. A self-consistent minimization (e.g. via a Metropolis-algorithm [122]) of the energy of the nucleus results in a reasonable ground-state due to the Pauli-Potential mimicking the fermionic properties of the nucleons. A drawback of the Pauli-Potential is, however, that the kinetic momenta of the nucleons are not anymore equivalent to their canonic momenta, i.e. the nucleons carry the correct Fermi-momentum, but their velocity is zero. Furthermore, the Pauli-Potential leads to a wrong specific heat and changes the dynamics of fragment formation. A big advantage of the Pauli-Potential is that the initialized nuclei remain absolutely stable whereas in the *conventional* initialization and propagation without the Pauli-Potential the nuclei start evaporating single nucleons after approximately 20 - 30 fm/c.

3.2 Equations of motion

This section describes the real part of the nucleon-nucleon interaction as it is implemented into the UrQMD model [123]. The interaction is based on a non-relativistic density-dependent Skyrme-type equation of state with additional Yukawa- and Coulomb potentials. Momentum dependent potentials are not used – a Pauli-potential, however, may be included optionally.

The nucleon- or baryon-density can be obtained from the Gaussian (3.1):

$$\varrho_j(\boldsymbol{x}_j,t) \;=\; \left(\frac{2\alpha}{\pi}\right)^{\frac{3}{2}} \exp\left\{-2\alpha(\boldsymbol{x}_j-\boldsymbol{r}_j(t))^2\right\}. \tag{3.7}$$

where $\boldsymbol{x}_j$ denotes the quantum mechanical position variable, while $\boldsymbol{r}_j(t)$ is the classical parameter of the Gaussian. The Skyrme-Potential (momentum-dependence and spin-exchange has been neglected) has the form:

$$V^{Sk} \;=\; \frac{1}{2!}t_1 {\sum_{j,k}}'\delta(\boldsymbol{x}_j-\boldsymbol{x}_k) + \frac{1}{3!}t_2 {\sum_{j,k,l}}'\delta(\boldsymbol{x}_j-\boldsymbol{x}_k)\delta(\boldsymbol{x}_j-\boldsymbol{x}_l) \quad , \tag{3.8}$$

where in order to avoid self-interactions, all terms where at least two indices are identical are discarded in the primed sum. This potential consists of a sum of two- and a three-body interaction terms. The two-body term, which has a linear density-dependence models the long range attractive component of the nucleon-nucleon interaction, whereas the three-body term with its quadratic density-dependence is responsible for the short range repulsive part of the interaction. Using the Gaussian (3.1) as the wave-function of the nucleon we obtain for the two-body Skyrme potential of particle j:

$$\begin{aligned} V_j^{\mathrm{Sk2}} &= {\sum_{k}^{N}}' \int \mathrm{d}\boldsymbol{x}_j\,\mathrm{d}\boldsymbol{x}_k\,\varphi_j^*(\boldsymbol{x}_j)\,\varphi_k^*(\boldsymbol{x}_k)\,t_1\delta(\boldsymbol{x}_j-\boldsymbol{x}_k)\,\varphi_j(\boldsymbol{x}_j)\,\varphi_k(\boldsymbol{x}_k) \\ &= t_1 {\sum_{k}^{N}}' \left(\frac{\alpha}{\pi}\right)^{\frac{3}{2}} \exp\left\{-\alpha(\boldsymbol{r}_j-\boldsymbol{r}_k)^2\right\} \\ &= t_1\varrho_j^{\mathrm{int}}(\boldsymbol{r}_j) \quad . \end{aligned} \tag{3.9}$$

In the last line the interaction density was introduced. This density has the same form as the nucleon density (3.7) obtained from the Wigner-transform of the Gaussian (3.1), but omits the nucleon at the location j and its Gaussian has twice the width of that used in equation (3.7). The three-body potential for particle j can be derived in an analogous fashion:

$$\begin{aligned} V_j^{\mathrm{Sk3}} &= \frac{1}{2!}{\sum_{kl}^{N}}' \int \mathrm{d}\boldsymbol{x}_j\,\mathrm{d}\boldsymbol{x}_k\,\mathrm{d}\boldsymbol{x}_l\,\varphi_j^*(\boldsymbol{x}_j)\,\varphi_k^*(\boldsymbol{x}_k)\,\varphi_l^*(\boldsymbol{x}_l) \\ &\qquad \times t_2\delta(\boldsymbol{x}_j-\boldsymbol{x}_k)\delta(\boldsymbol{x}_j-\boldsymbol{x}_l)\,\varphi_j(\boldsymbol{x}_j)\,\varphi_k(\boldsymbol{x}_k)\,\varphi_l(\boldsymbol{x}_l) \\ &= t_2\frac{1}{2!}{\sum_{kl}^{N}}' \left(\frac{4\alpha^2}{3\pi^2}\right)^{\frac{3}{2}} \exp\left\{-\frac{2}{3}\alpha\left((\boldsymbol{r}_j-\boldsymbol{r}_k)^2+(\boldsymbol{r}_k-\boldsymbol{r}_l)^2+(\boldsymbol{r}_l-\boldsymbol{r}_j)^2\right)\right\} \quad . \end{aligned} \tag{3.10}$$

In the case of infinite nuclear matter the individual relative distances should be close to their average value. Therefore the relative distance between particle k and l may be substituted by the average of the other two relative distances:

$$V_j^{\mathrm{Sk3}} \;\approx\; \frac{1}{2!}t_2 {\sum_{kl}^{N}}' \left(\frac{4\alpha^2}{3\pi^2}\right)^{\frac{3}{2}} \exp\left\{-\alpha\left((\boldsymbol{r}_j-\boldsymbol{r}_k)^2+(\boldsymbol{r}_j-\boldsymbol{r}_l)^2\right)\right\} \quad . \tag{3.11}$$

Using the definition of the interaction-density given in equation (3.9), the quadratic density dependence of the three particle term (3.11) may be generalized to arbitrary exponents for the density. This is of great importance for the implementation of a so-called *soft* equation of state. Then, however, the interpretation of V_j^{Sk3} as three particle interaction is no longer valid:

$$V_j^{\mathrm{Sk3}} \;\approx\; t_2 3^{-\frac{3}{2}}(\varrho_j^{\mathrm{int}})^2 \to t_\gamma(\gamma+1)^{-\frac{3}{2}}(\varrho_j^{\mathrm{int}})^\gamma \quad . \tag{3.12}$$

In the UrQMD model expression (3.12) is always used, even for the case $\gamma = 2$.

The Yukawa-, Coulomb- and (optional) Pauli-potentials may be written in the form of two-particle interactions:

$$V_{\rm Yuk}^{ij} = V_0^{\rm Yuk} \frac{\exp\{-|\boldsymbol{r}_i - \boldsymbol{r}_j|/\gamma_Y\}}{|\boldsymbol{r}_i - \boldsymbol{r}_j|} \tag{3.13}$$

$$V_{\rm Coul}^{ij} = \frac{Z_i Z_j e^2}{|\boldsymbol{r}_i - \boldsymbol{r}_j|} \tag{3.14}$$

$$V_{\rm Pau}^{ij} = V_{\rm Pau}^0 \left(\frac{\hbar}{q_0 p_0}\right)^3 \exp\left\{-\frac{|\boldsymbol{r}_i - \boldsymbol{r}_j|^2}{2q_0^2} - \frac{|\boldsymbol{p}_i - \boldsymbol{p}_j|^2}{2p_0^2}\right\} \delta_{\tau_i \tau_j} \delta_{\sigma_i \sigma_j} \tag{3.15}$$

σ_j and τ_j denote the spin and isospin of particle j and Z_j represents its charge.

In infinite nuclear matter the contribution of the Yukawa-potential to the total energy has a linear density-dependence, just like the two-body Skyrme-contribution. Therefore all parameter sets which satisfy the following relation for the parameter t_1 yield the same equation of state in infinite nuclear matter:

$$\frac{1}{2} t_1 + 2\pi V_0^{\rm Yuk} \gamma_Y^2 = \text{const.} \tag{3.16}$$

In finite nuclei the usage of a Yukawa-potential has the advantage that the parameters can be tuned to the proper surface properties of the nuclei without changing the equation of state.

parameter	**without Pauli-potential**	**with Pauli-potential**
α (fm^{-2})	0.25	0.1152
t_1 (MeV fm^3)	-7264.04	-84.5
t_γ (MeV fm^6)	87.65	188.2
γ	1.676	1.46
$V_0^{\rm Yuk}$ (MeV fm)	-0.498	-85.1
γ_Y (fm)	1.4	1.0
V_0^{Pauli} (MeV)	–	98.95
q_0 (fm)	–	2.16
p_0 (MeV/c)	–	120

Table 3.1: Parameters of the hard equation of state implemented in the UrQMD model, with and without Pauli-potential.

The classical UrQMD Hamiltonian which governs the motion of the parameters $\boldsymbol{r}_j$ and $\boldsymbol{p}_j$ of the wave-functions is thus given by:

$$\begin{aligned} H_{\rm UrQMD} = \sum_{j=1}^{N} E_j^{\rm kin} &+ \frac{1}{2} \sum_{j=1}^{N} \sum_{k=1}^{N} \left(E_{jk}^{\rm Sk2} + E_{jk}^{\rm Yukawa} + E_{jk}^{\rm Coulomb} + E_{jk}^{\rm Pauli}\right) \\ &+ \frac{1}{6} \sum_{j=1}^{N} \sum_{k=1}^{N} \sum_{l=1}^{N} E_{jkl}^{\rm Sk3} \end{aligned} \tag{3.17}$$

The individual contributions are defined as:

$$E_j^{\mathrm{kin}} = \sqrt{p_j^2 + m_j^2} \quad , \tag{3.18}$$

$$E_{jk}^{\mathrm{Sk2}} = t_1 \left(\frac{\alpha}{\pi}\right)^{\frac{3}{2}} \exp\left\{-\alpha r_{jk}^2\right\} \quad , \tag{3.19}$$

$$E_{jkl}^{\mathrm{Sk3}} = t_\gamma \left(\frac{4\alpha^2}{3\pi^2}\right)^{\frac{3}{2}} \exp\left\{-\alpha(r_{jk}^2 + r_{jl}^2)\right\} \quad , \tag{3.20}$$

$$\begin{aligned} E_{jk}^{\mathrm{Yukawa}} = {} & V_0^{\mathrm{Yuk}} \frac{1}{2r_{jk}} \exp\left\{\frac{1}{4\alpha\gamma_Y^2}\right\} \left[\exp\left\{-\frac{r_{jk}}{\gamma_Y}\right\} \left(1 - \mathrm{erf}\left(\frac{1}{2\gamma_Y\sqrt{\alpha}} - \sqrt{\alpha} r_{jk}\right)\right)\right. \\ & \left. - \exp\left\{\frac{r_{jk}}{\gamma_Y}\right\} \left(1 - \mathrm{erf}\left(\frac{1}{2\gamma_Y\sqrt{\alpha}} + \sqrt{\alpha} r_{jk}\right)\right)\right] \quad , \end{aligned} \tag{3.21}$$

$$E_{jk}^{\mathrm{Coulomb}} = \frac{Z_i Z_j \mathrm{e}^2}{r_{jk}} \mathrm{erf}\left(\sqrt{\alpha} r_{jk}\right) \quad , \tag{3.22}$$

$$\begin{aligned} E_{jk}^{\mathrm{Pauli}} = {} & V_0^{\mathrm{Pau}} \left(\frac{\hbar}{p_0 q_0}\right)^3 \left(1 + \frac{1}{2\alpha q_0^2}\right)^{-\frac{3}{2}} \\ & \times \exp\left\{-\frac{\alpha r_{jk}^2}{2\alpha q_0^2 + 1} - \frac{p_{jk}^2}{2p_0^2}\right\} \delta_{\tau_j \tau_k} \delta_{\sigma_j \sigma_k} \quad , \end{aligned} \tag{3.23}$$

with

$$r_{jk} = |\boldsymbol{r}_j - \boldsymbol{r}_k| \qquad \text{and} \quad p_{jk} = |\boldsymbol{p}_j - \boldsymbol{p}_k| \quad . \tag{3.24}$$

So far, only a hard equation of state has been implemented into the UrQMD model. The respective parameters are listed in table 3.1.

Unfortunately, the generalization of such two body forces to the relativistic region is not a simple task and is not incorporated in the present UrQMD model. In principle, the interaction must be mediated by fields, which are propagated according to wave equations or one must make use of the so called constraint Hamiltonian dynamics [36, 37]. Many other models avoid the propagation of fields using local density approximation. Above 2 AGeV, we therefore resort to a cluster decomposition in phase space, i.e. potential interactions are only enforced for particles with relative momenta smaller than 2 GeV/c.

3.3 The collision term

The UrQMD collision term contains 55 different baryon species (including nucleon, delta and hyperon resonances with masses up to 2.25 GeV/c^2) and 32 different meson species (including strange meson resonances), which are supplemented by their corresponding anti-particle and all isospin-projected states. The baryons and baryon-resonances which can be populated in UrQMD are listed in table 3.2, the respective mesons in table 3.3. The states listed can either be produced in string decays, s-channel collisions or resonance decays. For excitations with higher masses than 2 GeV/c^2 a string picture is used. Full baryon/antibaryon symmetry is included: The number of implemented baryons therefore defines the number of antibaryons in the model and the antibaryon-antibaryon interaction is defined via the baryon-baryon interaction cross sections.

Elementary cross sections are fitted to available proton-proton or pion-proton data. Isospin symmetry is used when possible in order to reduce the number of individual cross sections which have to be parameterized or tabulated.

nucleon	delta	lambda	sigma	xi	omega
N_{938}	Δ_{1232}	Λ_{1116}	Σ_{1192}	Ξ_{1315}	Ω_{1672}
N_{1440}	Δ_{1600}	Λ_{1405}	Σ_{1385}	Ξ_{1530}	
N_{1520}	Δ_{1620}	Λ_{1520}	Σ_{1660}	Ξ_{1690}	
N_{1535}	Δ_{1700}	Λ_{1600}	Σ_{1670}	Ξ_{1820}	
N_{1650}	Δ_{1900}	Λ_{1670}	Σ_{1750}	Ξ_{1950}	
N_{1675}	Δ_{1905}	Λ_{1690}	Σ_{1775}	Ξ_{2030}	
N_{1680}	Δ_{1910}	Λ_{1800}	Σ_{1915}		
N_{1700}	Δ_{1920}	Λ_{1810}	Σ_{1940}		
N_{1710}	Δ_{1930}	Λ_{1820}	Σ_{2030}		
N_{1720}	Δ_{1950}	Λ_{1830}			
N_{1900}		Λ_{1890}			
N_{1990}		Λ_{2100}			
N_{2080}		Λ_{2110}			
N_{2190}					
N_{2200}					
N_{2250}					

Table 3.2: Baryons and baryon-resonances included into the UrQMD model. Through baryon-antibaryon symmetry the respective antibaryon states are included as well.

0^{-+}	1^{--}	0^{++}	1^{++}	1^{+-}	2^{++}	$(1^{--})^{*}$	$(1^{--})^{**}$
π	ρ	a_0	a_1	b_1	a_2	ρ_{1450}	ρ_{1700}
K	K^*	K_0^*	K_1^*	K_1	K_2^*	K_{1410}^*	K_{1680}^*
η	ω	f_0	f_1	h_1	f_2	ω_{1420}	ω_{1662}
η'	ϕ	f_0^*	f_1'	h_1'	f_2'	ϕ_{1680}	ϕ_{1900}

Table 3.3: Mesons and meson-resonances, sorted with respect to spin and parity, included into the UrQMD model.

3.3.1 The collision criterion

In the UrQMD model hadron-hadron collisions are performed stochastically, in a similar way as in the original cascade models [65]. The cross section is interpreted geometrically as an area. Two particles collide if their distance d_{trans} fulfills the relation:

$$d_{\text{trans}} \leq d_0 = \sqrt{\frac{\sigma_{\text{tot}}}{\pi}}, \qquad \sigma_{\text{tot}} = \sigma(\sqrt{s}, \text{type}) \quad . \tag{3.25}$$

The total cross section σ_{tot} depends on the c.m. energy $\sqrt{s}$ and on the species and quantum numbers of the incoming particles. d_{trans} is the relative distance between the two colliding particles (in three dimensional configuration space). At the point of closest approach this distance is purely transverse with regard to the relative velocity vector of the particles.

During the calculation each particle is checked at the beginning of each time step whether it will collide according to criterion (3.25) within that time step. After each binary collision or decay the outgoing particles are checked for further collisions within the respective time step. This procedure assumes that all particles have the same clock, i.e. that a $6N + 1$ dimensional phase-space is used.

In relativistic heavy ion collisions, however, the relative distance between the particles depends on the reference-frame of the calculation. Therefore the time-order of the binary collisions and their cross sections also depend on the reference frame. One possible ansatz to overcome this unphysical frame-dependence is the use of a $8N$ dimensional phase-space [37], although even here the time-order of the collisions is not unique. In $8N$ dimensional phase space each particle has its own eigentime. The connection between a time-evolution parameter τ (the system clock) and the individual eigentimes is constructed via $2N - 1$ Lorentz-covariant constraints, which reduce the $8N$ dimensional phase-space to a $6N + 1$ dimensional phase-space. The particles move in Minkowsky-space along 4-dimensional curved trajectories. At the beginning of each time step (in units of τ) criterion (3.25) is applied to scan for collisions. Now, however, d_{trans} is defined as the covariant relative distance:

$$d_{\text{trans}} = \sqrt{\left(\frac{(q_n - q_m)^\nu (p_m + p_n)_\nu}{(p_n + p_m)^2} (p_n + p_m)^\mu - (q_n - q_m)^\mu \right)^2} \quad , \tag{3.26}$$

using 4-vectors for the locations q_ν and momenta p_ν of the particles.

In the UrQMD model a $6N + 1$ dimensional phase-space has been used. We therefore use a different ansatz to minimize the frame-dependence of the collisions: The impact parameter of two colliding particles – here also called d_{trans} – is well defined in the local rest-frame of the two particles. It corresponds to the relative distance between the two particles at the time of closest approach. In order to compute the time of closest approach of the two particles one always transforms into the local rest-frame of the two particles (using a $6N + 1$ dimensional phase space – this implies that no time-coordinates are transformed). With $\boldsymbol{q}_i$ being the locations and $\boldsymbol{p'}_i$ the momenta in the local rest-frame one obtains for the squared impact parameter d^2_{trans}:

$$d^2_{\text{trans}} = \boldsymbol{d}^2 - \boldsymbol{d}^2_{\parallel} = (\boldsymbol{q}_1 - \boldsymbol{q}_2)^2 - \frac{((\boldsymbol{q}_1 - \boldsymbol{q}_2) \cdot (\boldsymbol{p'}_1 - \boldsymbol{p'}_2))^2}{(\boldsymbol{p'}_1 - \boldsymbol{p'}_2)^2} \quad , \tag{3.27}$$

The constraint of always using the local rest-frame of the colliding particles ensures that the cross section of the two particles is always calculated in the same fashion and does not depend on the reference frame of the nucleus-nucleus collision.

The time of closest approach τ_{coll} (i.e. the collision time), however, still depends on the reference-frame of the nucleus-nucleus reaction. This dependence cannot be avoided since the system clock is linked to

that reference-frame. Therefore the time-order of the individual binary collisions strongly varies with the respective reference-frame [124]. Using the locations $\boldsymbol{r}_i$ and the momenta $\boldsymbol{p}_i$ in the reference frame of the nucleus-nucleus collision one obtains for the time of closest approach for the two colliding particles:

$$\tau_{\mathrm{coll}} \;=\; -\frac{(\boldsymbol{r}_1-\boldsymbol{r}_2)\cdot(\boldsymbol{p}_1/E_1-\boldsymbol{p}_2/E_2)}{(\boldsymbol{p}_1/E_1-\boldsymbol{p}_2/E_2)^2} \quad . \tag{3.28}$$

We have studied the computational frame dependence in the system S+S at 200 GeV/nucleon: using the above described algorithm, particle multiplicities and collision numbers vary by less than 3% between the laboratory frame and the CM frame.

The frame-independent definition of the cross section (via the impact parameter in the two-particle rest frame) is an important factor in ensuring the approximate reference-frame independence.

3.3.2 Cross sections

Nucleon-nucleon interactions

In UrQMD cross sections are a function of the incoming and outgoing particle types, their isospins and their c.m. energy. They may either be tabulated, parameterized according to an algebraic function or extracted from other cross sections via general principles, such as detailed balance or the additive quark model.

The total and elastic proton-proton and proton-neutron cross sections are well known [125]. Since their functional dependence on $\sqrt{s}$ shows at low energies a complicated shape, UrQMD uses a table-lookup for those cross sections. Figure 3.1 shows the comparison between measurements for the proton-proton elastic and total cross sections and the respective UrQMD table lookup. The same comparison for the proton-neutron case is shown in figure 3.2. At low energies large differences are visible between the proton-proton and the proton-neutron cross sections. Therefore the proper treatment of isospin – especially at low energies – is of major importance; simple averaged nucleon-nucleon cross sections should not be used. The neutron-neutron cross section is treated as equal to the proton-proton cross section (isospin-symmetry). In the high energy limit ($\sqrt{s} \geq 5$ GeV) the CERN/HERA parameterization for the proton-proton cross section is used [125].

Particle production in UrQMD either takes place via the decay of a meson- or baryon-resonance or via a string excitation and fragmentation. Up to incident beam energies of 8–10 GeV/nucleon particle production is dominated by resonance decays. Production cross sections for the excitation of individual resonances can be calculated in the framework of OPE or OBE models [126]. Regarding the number of implemented resonances in UrQMD and considering the limited applicable energy-range for cross sections calculated within OPE and OBE models the calculation of all implemented resonance excitation cross sections in the framework of these models is not practical. We therefore employ in UrQMD an effective parameterization based on simple phase space considerations; free parameters are tuned to experimental measurements. The cross section has the general form:

$$\sigma_{1,2\to3,4}(\sqrt{s}) \;\sim (2S_3+1)(2S_4+1)\frac{\langle p_{3,4}\rangle}{\langle p_{1,2}\rangle}\,\frac{1}{(\sqrt{s})^2}\,|\mathcal{M}(m_3,m_4)|^2\,. \tag{3.29}$$

The matrix element $|\mathcal{M}(m_3,m_4)|^2$ is assumed to have no spin-dependence but may depend on the masses of the outgoing particles. The cross section depends also on the momenta of the in- and outgoing particles in the two-particle rest-frame $\langle p_{i,j}\rangle$. If the outgoing particles are stable particles with a well-defined mass,

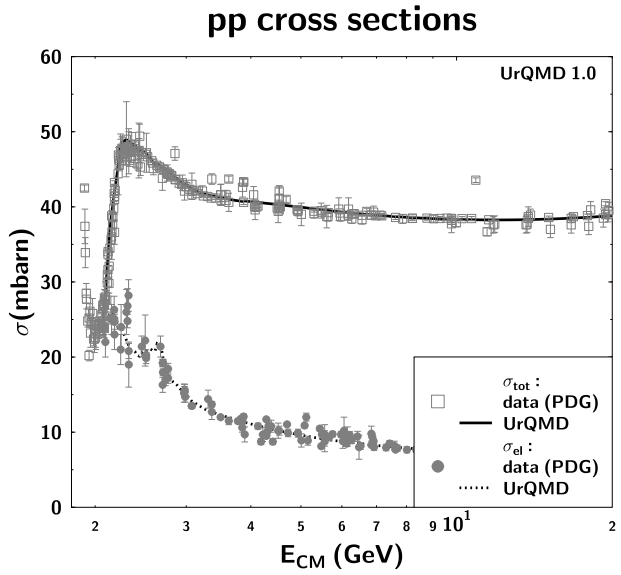

Figure 3.1: UrQMD parameterization of the total and elastic proton-proton cross section. The data has been taken from [125]. A table-lookup has been used at low energies to properly describe the data.

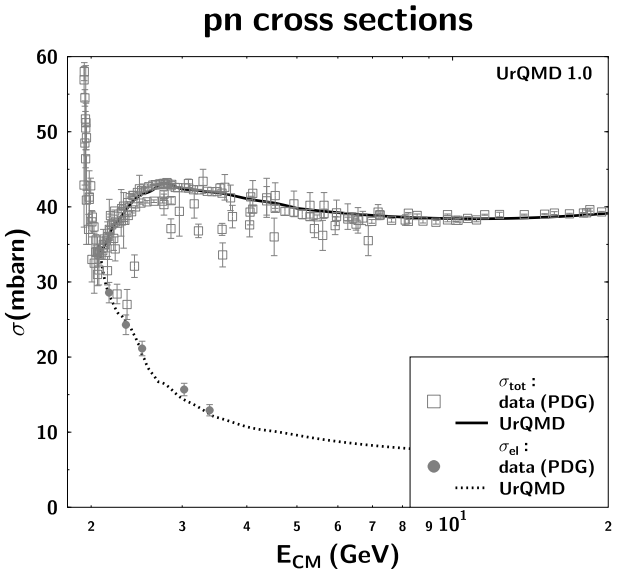

Figure 3.2: UrQMD parameterization of the total and elastic proton-neutron cross section. The data has been taken from [125]. A table-lookup has been used at low energies to properly describe the data. Note the large differences between the proton-proton and the proton-neutron data which emphasize the importance of correct isospin treatment

$\langle p_{3,4} \rangle$ is defined as:

$$\langle p_{3,4}(\sqrt{s}) \rangle \;=\; p_{CMS}(\sqrt{s}) \;=\; \frac{1}{2\sqrt{s}} \sqrt{(s-(m_3+m_4)^2)\,(s-(m_3-m_4)^2)} \quad . \tag{3.30}$$

($\langle p_{1,2} \rangle$ is defined as above exchanging m_3, m_4 by m_1, m_2, respectively). If, however, 3 or 4 are resonances, the width of their mass distribution must be taken into account. Then relation (3.30) must be modified by an integral over the mass distribution $A_r(m)$ of the respective resonance (in the case both are resonances):

$$\langle p_{3,4}(\sqrt{s}) \rangle \;=\; \int\int p_{CMS}(\sqrt{s}, m_3, m_4)\, A_3(m_3)\, A_4(m_4)\, \mathrm{d}m_3\, \mathrm{d}m_4 \,. \tag{3.31}$$

The mass distribution $A_r(m)$ is normalized to unity. The upper and lower boundaries for the integration in equation (3.31) are determined by the production thresholds for the respective resonances (e.g. in UrQMD this threshold is $m_N + m_\pi = 1.07$ GeV for non-strange baryon resonances) and the maximum available energy (e.g. in the case of $pp \to p\Delta$ the maximum available energy is $\sqrt{s} - m_N$). For the solution of this integral we assume the mass distribution to have the shape of a free Breit-Wigner distribution with a mass-dependent width:

$$A_r(m) \;=\; \frac{1}{N} \frac{\Gamma(m)}{(m_r - m)^2 + \Gamma(m)^2/4} \qquad \text{with} \quad \lim_{\Gamma \to 0} A_r(m) = \delta(m_r - m)\,, \tag{3.32}$$

with the normalization constant

$$N = \int_{-\infty}^{\infty} \frac{\Gamma(m)}{(m_r - m)^2 + \Gamma(m)^2/4} \, \mathrm{d}m \, . \tag{3.33}$$

Alternatively one can also choose a Breit-Wigner distribution with a fixed width, the normalization constant then has the value $N = 2\pi$.

In UrQMD, the excitation of non-strange resonances is subdivided into 6 classes: $NN \to N\Delta_{1232}$, $NN \to NN^*$, $NN \to N\Delta^*$, $NN \to \Delta_{1232}\Delta_{1232}$, $NN \to \Delta_{1232}N^*$ and $NN \to \Delta_{1232}\Delta^*$. Here the Δ_{1232} is explicitly listed, whereas higher excitations of the Δ resonance have been denoted as Δ^*. For each of these classes specific assumptions are made with regard to the form of the matrix-element $|\mathcal{M}(m_3, m_4)|^2$. Free parameters are tuned to experimental measurements, when available. We make the following assumptions for the matrix elements:

1. $NN \to N\Delta_{1232}$ excitation:

$$|\mathcal{M}(\sqrt{s}, m_3, m_4)|^2 = A \frac{m_\Delta^2 \Gamma_\Delta^2}{\left((\sqrt{s})^2 - m_\Delta^2\right)^2 + m_\Delta^2 \Gamma_\Delta^2} \quad , \tag{3.34}$$

   with $m_\Delta = 1.232$ GeV, $\Gamma_\Delta = 0.115$ GeV and $A = 40000$. Note that this form of the matrix element has been adjusted to fit the data shown in figure 3.4.

2. $NN \to NN^*$, $NN \to N\Delta^*$, $NN \to \Delta_{1232}N^*$ and $NN \to \Delta_{1232}\Delta^*$ excitation:

$$|\mathcal{M}(m_3, m_4)|^2 = A \frac{1}{(m_4 - m_3)^2 \, (m_4 + m_3)^2} \quad , \tag{3.35}$$

   with $A = 6.3$ for $NN \to NN^*$, $A = 12$ for $NN \to N\Delta^*$ and $A = 3.5$ for $NN \to \Delta_{1232}N^*$. In the case of $NN \to \Delta_{1232}\Delta^*$ there are insufficient data available, therefore we use the same matrix element and parameters as in the case of $NN \to \Delta_{1232}N^*$. Since $m_3 \neq m_4$ is valid for all above cases, the matrix element cannot diverge.

3. $NN \to \Delta\Delta$ excitation:

$$|\mathcal{M}(m_3, m_4)|^2 = A \quad , \tag{3.36}$$

   with $A = 2.8$.

E. g. the total cross section for the excitation of a N^* resonance can be obtained by summing equation (3.29) over all N^* resonances implemented in the UrQMD model. Figure 3.3 shows the total cross sections for the excitation of the different resonance classes $NN \to N\Delta_{1232}$, $NN \to NN^*$, $NN \to N\Delta^*$, $NN \to \Delta_{1232}\Delta_{1232}$, $NN \to \Delta_{1232}N^*$ and $NN \to \Delta_{1232}\Delta^*$. Also plotted is the cross section for the excitation of a string which is defined as the difference between total inelastic cross section and the sum of all the resonance excitation cross sections: $\sigma_{\mathrm{string}} = \sigma_{\mathrm{tot}} - \sigma_{\mathrm{el}} - \sum \sigma^i_{\mathrm{inel}}$. For $\sqrt{s} \geq 6$ GeV the string excitation cross section yields the strongest contribution to the total inelastic cross section.

Figure 3.4 shows the fit of the UrQMD $pp \to N\Delta_{1232}$ cross section to experimental measurements [127]. The measurements refer to the $\Delta^+ + n$ exit channel and have been rescaled to match the full isospin-summed cross section. In the case of the exclusive Δ_{1232} cross section the quality of the data and thus also the quality of the resulting fit is very good. For higher resonance excitations this is unfortunately no longer the case and additional measurements are needed to clarify the situation. One has to keep in

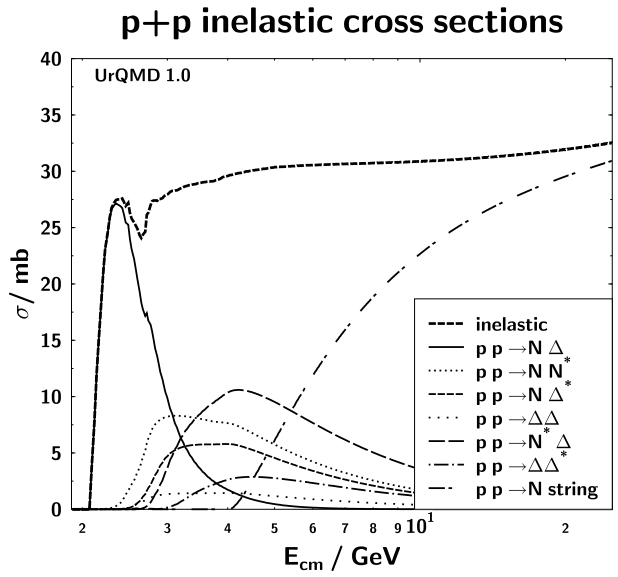

Figure 3.3: Inelastic proton-proton cross section in UrQMD, subdivided into the classes $NN \rightarrow N\Delta_{1232}$, $NN \rightarrow NN^*$, $NN \rightarrow N\Delta^*$, $NN \rightarrow \Delta_{1232}\Delta_{1232}$, $NN \rightarrow \Delta_{1232}N^*$, $NN \rightarrow \Delta_{1232}\Delta^*$ and $NN \rightarrow Nstring$. For high energies, string-excitation is dominant.

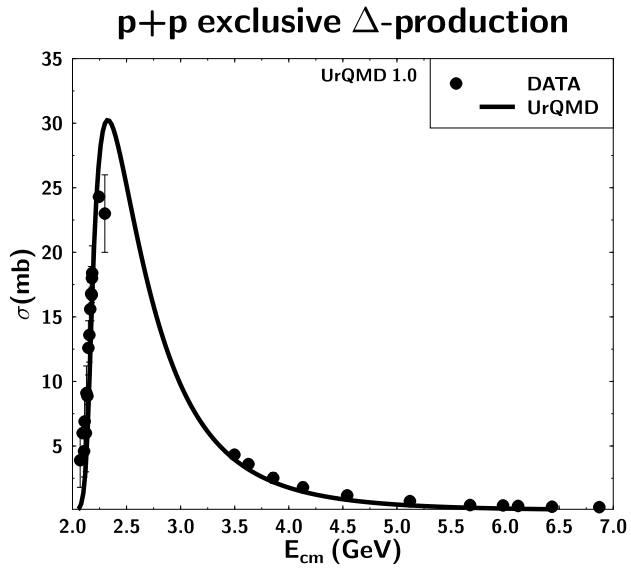

Figure 3.4: UrQMD fit for the exclusive Δ_{1232} production in proton-proton reactions compared to data [127].

mind, however, that the experimental extraction of exclusive resonance production cross sections is only possible via two- or three-particle correlations (e.g. a pion-nucleon correlation in the case of the Δ) which introduces large systematic errors, especially for broad resonances.

In figure 3.5 the UrQMD cross sections for the processes $pp \rightarrow pp^*_{1440}$, $pp \rightarrow pp^*_{1520}$ $pp \rightarrow pp^*_{1680}$ and $pp \rightarrow pp^*_{1700}$ are compared to data [127]. One single parameter has been used to fit all four cross sections. The data situation is not as good as in the case of the Δ_{1232} resonance, some ambiguities are visible which results in the quality of the fit being not as good as in the previous case. The parameters for the other classes are fitted in the same fashion.

After the species of the excited resonance has been assigned, its mass must be determined: This happens stochastically between the minimum allowed mass for the resonance and the maximum available free energy according to the mass distribution (3.32).

In the UrQMD model, the full decay width $\Gamma_{tot}(M)$ of a resonance is defined as the sum of all partial decay widths and depends on the mass of the excited resonance:

$$\Gamma_{tot}(M) \; = \; \sum_{br=\{i,j\}}^{N_{br}} \Gamma_{i,j}(M) \quad . \tag{3.37}$$

The partial decay widths $\Gamma_{i,j}(M)$ for the decay into the exit channel with particles i and j is given by:

$$\Gamma_{i,j}(M) \; = \; \Gamma_R^{i,j} \frac{M_R}{M} \left(\frac{\langle p_{i,j}(M) \rangle}{\langle p_{i,j}(M_R) \rangle} \right)^{2l+1} \frac{1.2}{1 + 0.2 \left(\frac{\langle p_{i,j}(M) \rangle}{\langle p_{i,j}(M_R) \rangle} \right)^{2l}} \quad , \tag{3.38}$$

here M_R denotes the pole mass of the resonance, $\Gamma_R^{i,j}$ its partial decay width into the channel i and j at the pole and l the decay angular momentum of the exit channel. All pole masses and partial decay widths

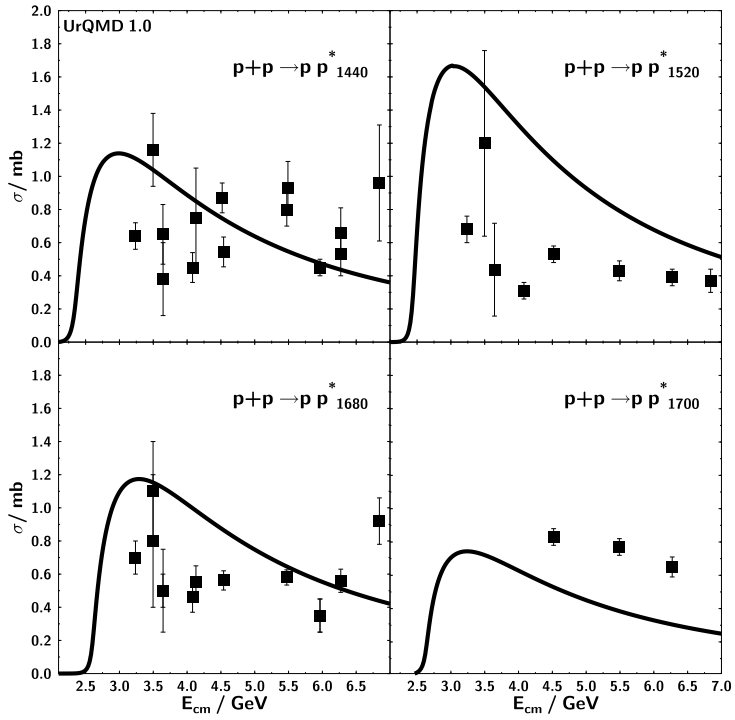

Figure 3.5: UrQMD parameterization for exclusive pp^* cross sections. Only one parameter was used to describe all available cross section data [127].

at the pole are taken from the Review of Particle Properties [125]. $\Gamma_{i,j}(M)$ is constructed in such a way that $\Gamma_{i,j}(M_R) = \Gamma_R^{i,j}$ is fulfilled at the pole. In many cases only crude estimates for $\Gamma_R^{i,j}$ are given in [125] – the partial decay widths must then be fixed by studying exclusive particle production in elementary proton-proton and pion-proton reactions.

All masses, full widths and decay probabilities used in UrQMD are listed in table 3.4 for non-strange baryon-resonances, in table 3.5 for single-strange baryon-resonances, in table 3.6 for double-strange baryon-resonances, and in tables 3.7 and 3.8 for meson-resonances. Due to experimental uncertainties there frequently exists a large interval in which the respective parameters may be tuned. Therefore the given set of parameters is not unique. However, the known uncertainties have been exploited to gain an optimized fit to the available inclusive and exclusive meson production data.

An important component in the computation of mass-dependent decay widths is the momentum of the decay products in the rest frame of the resonance, $\langle p_{i,j}(M) \rangle$, which has been defined in equations (3.30) and (3.31). In order to avoid recursion (the full decay width as defined in (3.37) is needed for the evaluation of (3.31)), the full and partial decay widths are evaluated at the beginning of the calculation using a mass distribution $A_r(M)$ with a fixed mass-independent width and then tabulated for further use.

resonance	mass	width	$N\gamma$	$N\pi$	$N\eta$	$N\omega$	$N\varrho$	$N\pi\pi$	$\Delta_{1232}\pi$	$N^*_{1440}\pi$	ΛK
N^*_{1440}	1.440	200		0.70				0.05	0.25		
N^*_{1520}	1.520	125		0.60				0.15	0.25		
N^*_{1535}	1.535	150	0.001	0.55	0.35			0.05		0.05	
N^*_{1650}	1.650	150		0.65	0.05			0.05	0.10	0.05	0.10
N^*_{1675}	1.675	140		0.45					0.55		
N^*_{1680}	1.680	120		0.65				0.20	0.15		
N^*_{1700}	1.700	100		0.10	0.05		0.05	0.45	0.35		
N^*_{1710}	1.710	110		0.15	0.20		0.05	0.20	0.20	0.10	0.10
N^*_{1720}	1.720	150		0.15			0.25	0.45	0.10		0.05
N^*_{1900}	1.870	500		0.35		0.55	0.05		0.05		
N^*_{1990}	1.990	550		0.05			0.15	0.25	0.30	0.15	0.10
N^*_{2080}	2.040	250		0.60	0.05		0.25	0.05	0.05		
N^*_{2190}	2.190	550		0.35			0.30	0.15	0.15	0.05	
N^*_{2220}	2.220	550		0.35			0.25	0.20	0.20		
N^*_{2250}	2.250	470		0.30			0.25	0.20	0.20	0.05	
Δ_{1232}	1.232	115.	0.01	1.00							
Δ^*_{1600}	1.700	200		0.15					0.55	0.30	
Δ^*_{1620}	1.675	180		0.25					0.60	0.15	
Δ^*_{1700}	1.750	300		0.20			0.10		0.55	0.15	
Δ^*_{1900}	1.850	240		0.30			0.15		0.30	0.25	
Δ^*_{1905}	1.880	280		0.20			0.60		0.10	0.10	
Δ^*_{1910}	1.900	250		0.35			0.40		0.15	0.10	
Δ^*_{1920}	1.920	150		0.15			0.30		0.30	0.25	
Δ^*_{1930}	1.930	250		0.20			0.25		0.25	0.30	
Δ^*_{1950}	1.950	250	0.01	0.45			0.15		0.20	0.20	

Table 3.4: Masses, widths and branching ratios for non-strange baryon-resonances in UrQMD. Masses are given in GeV and the widths in MeV. All parameters are within the range given by the Review of Particle Properties [125] and have been tuned to exclusive particle production channels.

Figure 3.6 shows the total and partial decay-widths of the N^*_{1535} resonance as a function of its mass. This resonance is particularly interesting since it dominates the production of the η meson at SIS-energies. The grey-shaded area represents the experimental uncertainty of the full width at the resonance pole [125]. The opening of the $N\eta$ decay-channel at its threshold energy is clearly visible. Figure 3.7 shows the respective probabilities for the different decay channels. Here, the grey-shaded area depicts the Breit-Wigner mass-distribution of the N^*_{1535} resonance. Obviously the resonance can also be easily populated below the η production threshold – due to limited phase-space in a heavy-ion reaction the integrated decay-probability of a N^*_{1535} into a nucleon and an η meson may lie well below the free branching ratio given in the Review of Particle Properties [125].

Unfortunately, equation (3.38) cannot be easily extended to include three- or four-body decay channels. In order to treat all decay channels on an equal footing in UrQMD, the outgoing particles of a three- or four-body decay are combined into two "effective" particles which are used to compute the respective partial decay-widths. N-body phase-space, however, is treated explicitly.

All resonances decay isotropically in their rest frame. For a two-particle exit channel the momenta are given by equation (3.30). If a resonance is among the outgoing particles, its mass must first be determined according to a Breit-Wigner mass-distribution. If the exit channel contains three or four particles, then the respective N-body phase-space must be taken into account for their momenta [128].

resonance	mass	width	$N\bar{K}$	$N\bar{K}^*_{892}$	$\Sigma\pi$	$\Sigma^*\pi$	$\Lambda\gamma$	$\Lambda\eta$	$\Lambda\omega$	$\Lambda\pi$	$\Sigma\eta$	$\Lambda^*\pi$	$\Delta\bar{K}$
Λ^*_{1405}	1.407	50			1.00								
Λ^*_{1520}	1.520	16	0.45		0.43	0.11	0.01						
Λ^*_{1600}	1.600	150	0.35		0.65								
Λ^*_{1670}	1.670	35	0.20		0.50			0.30					
Λ^*_{1690}	1.690	60	0.25		0.45	0.30							
Λ^*_{1800}	1.800	300	0.40	0.20	0.20	0.20							
Λ^*_{1810}	1.810	150	0.35	0.45	0.15	0.05							
Λ^*_{1820}	1.820	80	0.73		0.16	0.11							
Λ^*_{1830}	1.830	95	0.10		0.70	0.20							
Λ^*_{1890}	1.890	100	0.37	0.21	0.11	0.31							
Λ^*_{2100}	2.100	200	0.35	0.20	0.05	0.30		0.02	0.08				
Λ^*_{2110}	2.110	200	0.25	0.45	0.30								
Σ^*_{1385}	1.384	36			0.12					0.88			
Σ^*_{1660}	1.660	100	0.30		0.35					0.35			
Σ^*_{1670}	1.670	60	0.15		0.70					0.15			
Σ^*_{1750}	1.750	90	0.40		0.05						0.55		
Σ^*_{1775}	1.775	120	0.40		0.04	0.10				0.23		0.23	
Σ^*_{1915}	1.915	120	0.15		0.40	0.05				0.40			
Σ^*_{1940}	1.940	220	0.10	0.15	0.15	0.15				0.15		0.15	0.15
Σ^*_{2030}	2.030	180	0.20	0.04	0.10	0.10				0.20		0.18	0.18

Table 3.5: Masses, widths and branching ratios for single-strange baryon-resonances in UrQMD. Masses are given in GeV and the widths in MeV. All parameters are within the range given by the Review of Particle Properties [125] and have been tuned to exclusive particle production channels and to the total kaon-nucleon cross section.

resonance	mass	width	$\Xi\pi$	$\Xi\gamma$	$\Lambda\bar{K}$	$\Sigma\bar{K}$
Ξ^*_{1530}	1.532	9	0.98	0.02		
Ξ^*_{1690}	1.700	50	0.10		0.70	0.20
Ξ^*_{1820}	1.823	24	0.15		0.70	0.15
Ξ^*_{1950}	1.950	60	0.25		0.50	0.25
Ξ^*_{2030}	2.025	20	0.10		0.20	0.70

Table 3.6: Masses, widths and branching ratios for double-strange baryon-resonances in UrQMD. Masses are given in GeV and the widths in MeV. All parameters are within the range given by the Review of Particle Properties [125] and have been tuned to exclusive particle production channels.

meson	**mass**	**width**	$\gamma\pi$	$\gamma\rho$	$\gamma\omega$	$\gamma\eta$	γK	$\pi\pi$	$\pi\rho$	3π	$\pi\eta$	4π	$K\bar{K}^*$	$\bar{K}K^*$
ω	0.782	8	0.09					0.02		0.89				
ρ	0.769	151						1.00						
$f_0(980)$	0.980	100						0.70						
η'	0.958	0.2		0.30	0.05									
K^*	0.893	50												
ϕ	1.019	4				0.01			0.13	0.02				
K_0^*	1.429	287												
a_0	0.984	100									0.90			
$f_0(1370)$	1.370	200						0.10				0.70		
$K_1(1270)$	1.273	90												
a_1	1.230	400	0.10						0.90					
f_1	1.282	24		0.07								0.20		
$f_1(1510)$	1.512	350											0.50	0.50
$K_2(1430)$	1.430	100												
$a_2(1320)$	1.318	107							0.70		0.14			
$f_2(1270)$	1.275	185						0.50				0.30		
$f_2'(1525)$	1.525	76						0.01						
$K_1(1400)$	1.400	174												
$b_1(1235)$	1.235	142												
$h_1(1170)$	1.170	360							0.90	0.10				
$h_1'(1380)$	1.380	80											0.50	0.50
$K^*(1410)$	1.410	227												
$\rho(1465)$	1.465	310						0.50				0.50		
$\omega(1419)$	1.419	174							1.00					
$\phi(1680)$	1.680	150											0.40	0.40
$K^*(1680)$	1.680	323												
$\rho(1700)$	1.700	235						0.10				0.20		
$\omega(1662)$	1.662	280							0.50					
$\phi(1900)$	1.900	400											0.40	0.40

Table 3.7: Masses, widths and branching ratios for meson-resonances in UrQMD, part I. Masses are given in GeV and the widths in MeV. All parameters are within the range given by the Review of Particle Properties [125]. Additional branching ratios can be found in table 3.8.

meson	**mass**	**width**	$\eta\pi\pi$	$\eta\rho$	$\rho\pi\pi$	$\omega\pi\pi$	$\eta\eta$	$K\bar{K}$	$K\bar{K}\pi$	$K\pi$	$K^*\pi$	$K\rho$	$K\omega$	$K^*\pi\pi$	$\omega\pi$
ω	0.782	8													
ρ	0.769	151													
$f_0(980)$	0.980	100						0.30							
η'	0.958	0	0.65												
K^*	0.893	50								1.00					
ϕ	1.019	4						0.84							
K_0^*	1.429	287								1.00					
a_0	0.984	100						0.10							
$f_0(1370)$	1.370	200						0.20							
$K_1(1270)$	1.273	90									0.47	0.42	0.11		
a_1	1.230	400													
f_1	1.282	24	0.54		0.10				0.09						
$f_1(1510)$	1.512	350													
$K_2(1430$	1.430	100								0.50	0.25	0.09	0.03	0.13	
$a_2(1320)$	1.318	107				0.11		0.05							
$f_2(1270$	1.275	185						0.20							
$f_2'(1525)$	1.525	76					0.10	0.89							
$K_1(1400)$	1.400	174									0.96	0.03	0.01		
$b_1(1235)$	1.235	142		0.10											0.90
$h_1(1170)$	1.170	360													
$h_1'(1380)$	1.380	80													
$K^*(1410)$	1.410	227								0.30	0.65	0.05			
$\rho(1465)$	1.465	310													
$\omega(1419)$	1.419	174													
$\phi(1680)$	1.680	150						0.10	0.10						
$K^*(1680)$	1.680	323								0.40	0.30	0.30			
$\rho(1700)$	1.700	235			0.70										
$\omega(1662)$	1.662	280				0.50									
$\phi(1900)$	1.900	400						0.10	0.10						

Table 3.8: Masses, widths and branching ratios for meson-resonances in UrQMD, part II. Masses are given in GeV and the widths in MeV. All parameters are within the range given by the Review of Particle Properties [125].

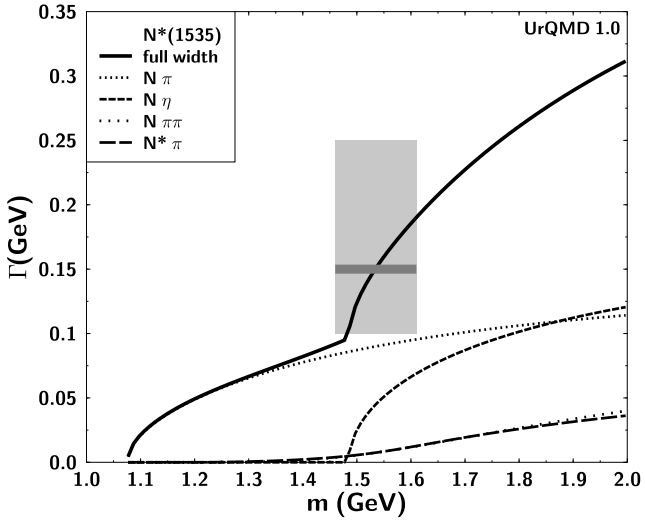

Figure 3.6: Total and partial mass-dependent decay widths of the N^*_{1535} resonance. The grey-shaded area marks the size of the error-bar for the total decay-widths according to [125]. The opening of the $N\eta$ decay-branch above its energetic threshold is clearly visible.

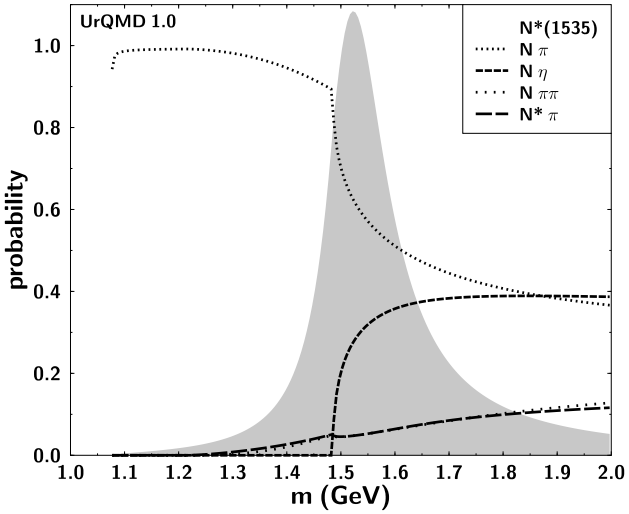

Figure 3.7: Mass-dependent branching ratios for the different exit-channels of a N^*_{1535} decay. The grey-shaded area symbolizes the Breit-Wigner mass-distribution of the resonance. The resonance may also be populated in a mass-range in which the η-production is strongly suppressed or even energetically impossible.

The implementation of the resonances and their inelastic production cross sections can be evaluated by studying exclusive meson production in proton-proton reactions: Figure 3.8 shows a comparison for exclusive π^0 production in proton-proton reactions between the UrQMD model and data [127]. Especially at low energies close to the production threshold, such exclusive cross sections are very sensitive to the partial decay width and pole mass of the resonances from which the respective particle emerges. Above $\sqrt{s} \approx 5$ GeV all inclusive particle production cross sections are dominated by string decays, which, however, have no influence on the exclusive $p + p \rightarrow p + p + \pi^0$ channel.

Baryon-antibaryon annihilation

The physics of baryon-antibaryon annihilation is still a subject of active research and not yet fully understood. A number of different models exist – for an overview we refer to [129, 130]. In UrQMD the elementary annihilation cross section is fitted to the available data: Figure 3.9 shows the UrQMD parameterization in comparison to data for the antiproton-proton total, elastic and annihilation cross section [125, 127].

For the annihilation cross section we employ a parameterization first suggested by Koch and Dover [131]:

$$\sigma^{\bar{p}p}_{\mathrm{ann}} \;=\; \sigma_0^N \, \frac{s_0}{s} \left[\frac{\mathrm{A}^2 s_0}{(s - s_0)^2 + \mathrm{A}^2 s_0} + \mathrm{B} \right] \quad , \tag{3.39}$$

with $\sigma_0^N = 120$ mb, $s_0 = 4m_N^2$, A = 50 MeV and B= 0.6.

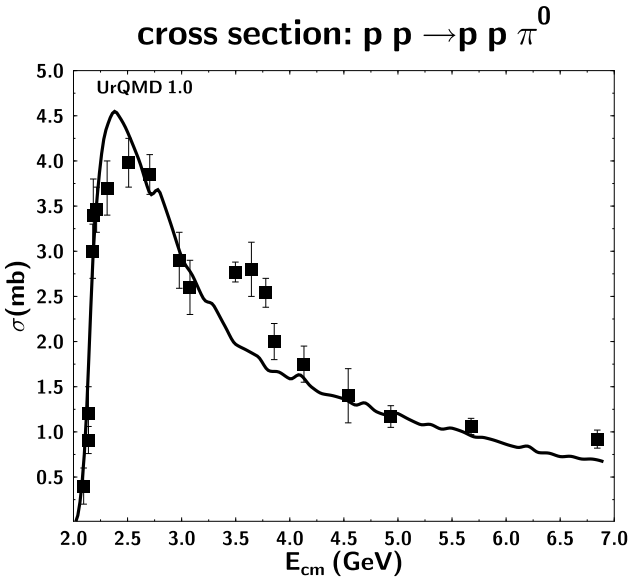

Figure 3.8: Exclusive π^0 production cross section in proton-proton reactions within the UrQMD model (solid line) compared to data (solid squares) [127]. The comparison allows to evaluate the implementation of baryon-resonances into the UrQMD model.

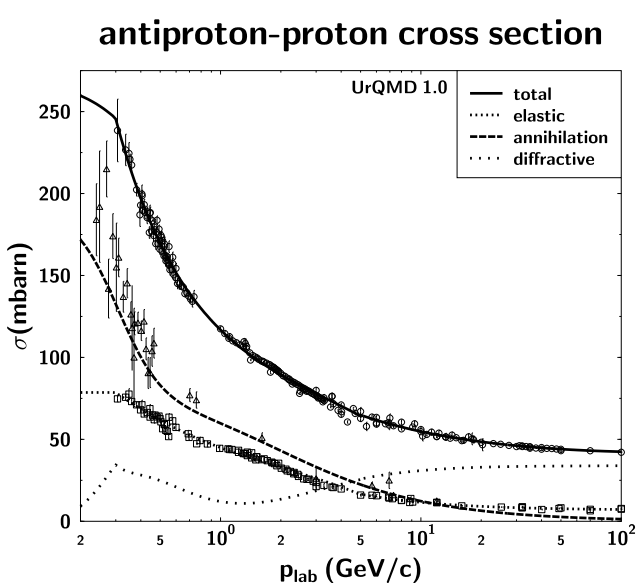

Figure 3.9: Parameterization of antiproton-proton cross sections in UrQMD compared to data [125]. The "diffractive" cross section is the difference between the total cross section and the sum of elastic and annihilation cross sections.

The antiproton-neutron annihilation cross section is very similar to the antiproton-proton annihilation cross section [132] and is therefore treated identically.

The total and elastic proton-antiproton cross sections are treated according to the CERN/HERA parameterization:

$$\sigma(p) \;=\; \mathrm{A} + \mathrm{B}\, p^n + \mathrm{C}\ln^2(p) + \mathrm{D}\ln(p)\,, \tag{3.40}$$

with the laboratory-momentum p in GeV/c. The respective parameters are listed in table 3.9.

	A	B	n	C	D
σ_{tot}	38.4	77.6	-0.64	0.26	-1.2
σ_{el}	10.2	52.7	-1.16	0.125	-1.28

Table 3.9: Parameters for the CERN/HERA parameterization for the total and elastic proton-antiproton cross sections. This parameterization is used in UrQMD for momenta $p_{lab} > 5$ GeV/c.

For momenta $p_{lab} < 5$ GeV/c, UrQMD uses another parameterization to obtain a good fit to the data:

$$\sigma_{\mathrm{tot}}(p) = \begin{cases} 75.0 + 43.1p^{-1} + 2.6p^{-2} - 3.9p & : \quad 0.3 < p < 5 \\ 271.6\exp(-1.1\,p^2) & : \quad p < 0.3 \end{cases} \tag{3.41}$$

$$\sigma_{\mathrm{el}} = \begin{cases} 31.6 + 18.3p^{-1} - 1.1p^{-2} - 3.8p & : \quad 0.3 < p < 5 \\ 78.6 & : \quad p < 0.3 \end{cases} \tag{3.42}$$

For low lab-momenta the annihilation cross section is dominant. The sum of annihilation and elastic cross section, however, is smaller than the total cross section:

$$\Delta\sigma = \sigma_{\mathrm{tot}} - \sigma_{\mathrm{el}} - \sigma_{\mathrm{ann}} \tag{3.43}$$

This difference is called "diffractive" cross section in UrQMD, $\sigma_{\mathrm{diff}} = \Delta\sigma$, and is used to excite one (or both) of the collision partners to a resonance or to a string. In the string case the same excitation scheme as for proton-proton reactions is used. For high energies the "diffractive" cross section is the dominant contribution to the total antiproton-proton cross section.

The extrapolation from nucleon-antinucleon annihilation to generic baryon-antibaryon annihilation poses a large problem since the respective cross sections have not been measured and the overall uncertainties in the understanding of the basic annihilation mechanism leave ample room for speculation. Due to different masses and quark-contents, modifications to the nucleon-antinucleon cross sections are inevitable.

Assuming a weak t-dependence of the matrix-element, a phase-space correction analogous to that for exchange reactions was suggested in [133], which leads to the following rescaling of the nucleon-antinucleon cross section:

$$\sigma_{\bar{\mathrm{B}}\mathrm{B}} \sim \frac{p_{\bar{\mathrm{N}}\mathrm{N}}}{p_{\bar{\mathrm{B}}\mathrm{B}}} \sigma_{\bar{\mathrm{N}}\mathrm{N}} \,. \tag{3.44}$$

A disadvantage of this ansatz is that the cross section diverges for low energies.

The same $\sqrt{s}$-dependence is used in UrQMD for all baryon-antibaryon cross sections (i.e. the parameterization of the proton-antiproton cross section). The different quark-content of the colliding (anti-)baryons is taken into account by rescaling the cross section with the ratio of the total baryon-baryon and nucleon-nucleon cross sections as obtained from the Additive Quark Model (AQM, see also the following section):

$$\sigma_{\bar{\mathrm{B}}\mathrm{B}}(\sqrt{s}) = \frac{\sigma_{\mathrm{BB}}^{\mathrm{AQM}}}{\sigma_{\mathrm{N}\bar{\mathrm{N}}}^{\mathrm{AQM}}} \, \sigma_{\bar{\mathrm{N}}\mathrm{N}}(\sqrt{s}) \,. \tag{3.45}$$

By scaling the cross section with the ratio of the respective AQM cross sections, the strangeness content of the colliding baryons is taken into account.

The final state of a baryon-antibaryon annihilation is generated via the formation of two meson-strings. The available c.m. energy of the reaction is distributed in equal parts to the two strings which decay in the rest frame of the reaction. On the quark level this procedure implies the annihilation of a quark-antiquark pair and the reordering of the remaining constituent quarks into newly produced hadrons (additionally taking sea-quarks into account). This model for the baryon-antibaryon annihilation thus follows the topology of a *rearrangement*-graph. Another possibility would be the annihilation of a diquark-antidiquark with the subsequent fragmentation of a single meson-string. This ansatz, which is being used in RQMD [37] follows the topology of an *annihilation*-graph.

Details in the treatment of the baryon-antibaryon annihilation cross section may have a large influence on the final yield of antiprotons and antihyperons: If the baryon-antibaryon annihilation cross section is parameterized as the proton-antiproton annihilation cross section but then rescaled to equivalent relative momenta in the incoming channel, changes in the order of 50% – 300% may occur. At CERN/SPS energies the $\bar{\Xi}$ yield in central Pb+Pb reactions at 160 GeV/nucleon would decrease by a factor of 3. The $\bar{p}$ and $\bar{Y}$ yields would then be diminished by 50% and 25%, respectively.

Additive Quark Model

For all interactions for which no experimental data exist (e.g. hyperon-baryon resonance scattering) *ad hoc* assumptions must be made. Ignoring all unknown cross sections and setting them to zero would contradict the experimentally observed hadron universality, which states that particle production in highly energetic jets does not strongly depend on the incoming collision partners (taking all conservation laws into account). A relatively simple prescription for obtaining unknown hadron-hadron cross sections is the Additive Quark Model: In this model the cross section only depends on the quark-content of the colliding hadrons [134]:

$$\sigma_{tot} = 40 \cdot \left(\frac{2}{3}\right)^{n_{\mathrm{M}}} \cdot (1 - 0.4x_1^s) \cdot (1 - 0.4x_2^s) \tag{3.46}$$

$$\sigma_{el} = 0.039 \cdot \sigma_{tot}^{2/3} \,. \tag{3.47}$$

Here n_{M} is the number of colliding mesons and x_i^s is the ratio of strange quarks to non-strange quarks in the i-th hadron. Both relations are phenomenological and do not contain any energy- or momentum-dependence. For high energies they agree well with experimentally known hadron-hadron cross sections. The missing momentum- or energy-dependence, however, leads to a breakdown of this prescription for cross sections close to threshold.

Detailed Balance

The principle of detailed balance is based on the time-reversal invariance of the matrix element of the reaction. It is most commonly found in text books in the form:

$$\sigma_{f\to i} = \frac{\boldsymbol{p}_i^2}{\boldsymbol{p}_f^2}\frac{g_i}{g_f}\sigma_{i\to f} \quad , \tag{3.48}$$

with g denoting the spin-isospin degeneracy factors. UrQMD applies the general principle of detailed balance to the following two process classes:

1. Resonant meson-meson and meson-baryon interactions: Each resonance created via a meson-baryon or a meson-meson annihilation may again decay into the two hadron species which originally formed it. This symmetry is only violated in the case of three- or four-body decays and string fragmentations, since N-body collisions with (N$>$ 2) are not implemented in UrQMD.

2. Resonance-nucleon or resonance-resonance interactions: the excitation of baryon-resonances in UrQMD is handled via parameterized cross sections which have been tuned to data. The reverse reactions usually have not been measured - here the principle of detailed balance is applied. Inelastic baryon-resonance deexcitation is the only method in UrQMD to absorb mesons (which are *bound* in the resonance). Therefore the application of the detailed balance principle is of crucial importance for heavy nucleus-nucleus collisions.

Equation (3.48), however, is only valid in the case of stable particles with well-defined masses. Since in UrQMD detailed balance is applied to reactions involving resonances with finite lifetimes and broad mass distributions, equation (3.48) has to be modified accordingly. For the case of one incoming resonance the respective modified detailed balance relation has been derived in [92]. Here, we generalize this expression for up to two resonances in both, the incoming and the outgoing channels.

The differential cross section for the reaction $(1\,,\,2) \rightarrow (3\,,\,4)$ is given by:

$$\mathrm{d}\sigma_{12}^{34} \;=\; \frac{|\mathcal{M}|^2}{64\pi^2 s}\,\frac{p_{34}}{p_{12}}\,\mathrm{d}\Omega\,\prod_{i=3}^{4}\delta(p_i^2 - M_i^2)\mathrm{d}p_i^2 \quad , \tag{3.49}$$

here the p_i in the δ-function denote four-momenta. The δ-function ensures that the particles are on mass-shell, i.e. their masses are well-defined. If the particle, however, has a broad mass distribution, then the δ-function must be substituted by the respective mass distribution (including an integration over the mass):

$$\mathrm{d}\sigma_{12}^{34} \;=\; \frac{|\mathcal{M}|^2}{64\pi^2 s}\,\frac{1}{p_{12}}\,\mathrm{d}\Omega\,\prod_{i=3}^{4} p_{34}\cdot\frac{\Gamma}{\left(m - M_i\right)^2 + \Gamma^2/4}\frac{\mathrm{d}m}{2\pi}\,. \tag{3.50}$$

Incorporating these modifications into equation (3.48) and neglecting a possible mass-dependence of the matrix element we obtain:

$$\frac{\mathrm{d}\sigma_{34}^{12}}{\mathrm{d}\Omega} = \frac{\langle p_{12}^2\rangle}{\langle p_{34}^2\rangle}\,\frac{(2S_1+1)(2S_1+1)}{(2S_3+1)(2S_4+1)}\,\sum_{J=J_-}^{J_+}\langle j_1 m_1 j_2 m_2 \| JM\rangle\,\frac{\mathrm{d}\sigma_{12}^{34}}{\mathrm{d}\Omega}\,. \tag{3.51}$$

Here, S_i indicates the spin of particle i and the summation of the Clebsch-Gordan-coefficients is for the isospin of the outgoing channel only. For the incoming channel, isospin is treated explicitly. The summation limits are given by:

$$J_- \;=\; \max\left(|j_1 - j_2|, |j_3 - j_4|\right) \tag{3.52}$$

$$J_+ \;=\; \min\left(j_1 + j_2, j_3 + j_4\right) \quad . \tag{3.53}$$

The integration over the mass distributions of the resonances in equation (3.51) has been denoted by the brackets $\langle\rangle$, e.g.

$$p_{3,4}^2 \;\Rightarrow\; \langle p_{3,4}^2\rangle \;=\; \int\int p_{CMS}^2(\sqrt{s}, m_3, m_4)\,A_3(m_3)\,A_4(m_4)\,\mathrm{d}m_3\,\mathrm{d}m_4 \quad ,$$

which is identical to equation (3.31). Correspondingly, the mass distribution $A_r(m)$ is given by equation (3.32).

The most frequent applications of equation (3.51) in UrQMD are the processes $\Delta_{1232}\,N \rightarrow N\,N$ and $\Delta_{1232}\,\Delta_{1232} \rightarrow N\,N$.

Meson-baryon and meson-meson interactions

Due to the large pion-nucleon cross section at low c.m. energies, resonant meson-baryon and meson-meson cross sections are among the most important in UrQMD. Up to c.m. energies of 2.2 GeV meson-baryon and meson-meson interactions in UrQMD are dominated by resonance scattering, i.e. the formation of an intermediate resonance. For example, the total meson-baryon cross section for non-strange particles is given by

$$\begin{aligned}\sigma_{tot}^{MB}(\sqrt{s}) \;&=\; \sum_{R=\Delta,N^*}\langle j_B, m_B, j_M, m_M \| J_R, M_R\rangle\,\frac{2S_R+1}{(2S_B+1)(2S_M+1)} \\ &\quad\times\frac{\pi}{p_{CMS}^2}\,\frac{\Gamma_{R\rightarrow MB}\Gamma_{tot}}{(M_R - \sqrt{s})^2 + \frac{\Gamma_{tot}^2}{4}}\end{aligned} \tag{3.54}$$

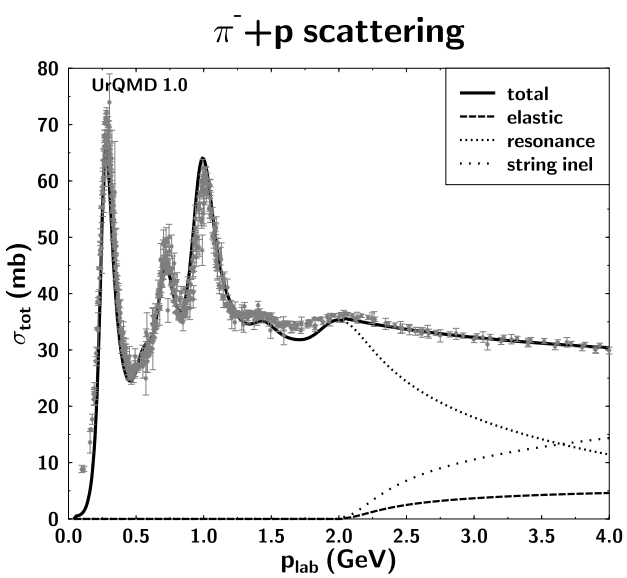

Figure 3.10: Total $\pi^- p$ cross section in UrQMD, compared to data [125]. Up to $p_{lab} = 2$ GeV the total cross section consists solely of resonance scattering. For higher momenta elastic scattering and string excitation are employed to fill the total cross section.

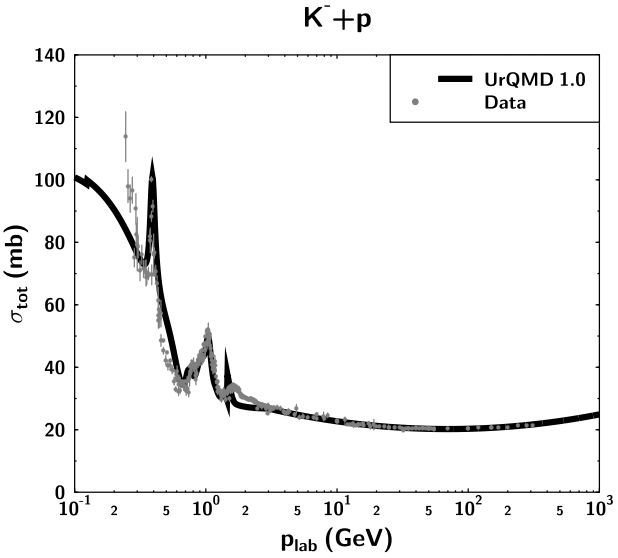

Figure 3.11: Total $K^- p$ cross section in UrQMD. The data is from [125]. Resonant $K^- p$ scattering is only possible via Λ and Σ resonances, whereas in the case $\pi^- p$ only non-strange resonances contribute.

with the total and partial $\sqrt{s}$-dependent decay widths Γ_{tot} and $\Gamma_{R \to MB}$ (see equations (3.37) and (3.38)). Therefore, the total pion-nucleon cross section depends on all pole masses, widths and branching ratios of all N^* and Δ^* resonances listed in table 3.4.

Figure 3.10 compares the total $\pi^- p$ cross section of UrQMD to data [125]. Up to $p_{lab} = 2$ GeV the total cross section is very well described by resonance scattering. For higher momenta the resonance description breaks down and the total cross section is described as a superposition of elastic scattering and inelastic string excitation. A comparison between the total $\pi^- p$ and the total $K^- p$ cross sections (see figures 3.10 and 3.11) is of particular interest: In the first case only N^*- and Δ-resonances contribute to the cross section, whereas in the latter case only hyperon resonances may be excited.

The same basic principles apply in the meson-meson case: Figure 3.12 shows the total $\pi^+ \pi^-$ cross section, which is dominated by the ρ-resonance. However, in the case of meson-meson scattering a constant elastic cross section of 5 mb is added in order to fully reproduce the measured cross section.

The cross section for an exclusive exit channel $M\,B \to R \to M'\,B'$ may be obtained by replacing the total width Γ_{tot} in equation (3.54) by the respective partial decay-width $\Gamma_{R \to M'B'}$. Figure 3.13 shows the cross section for the process $\pi^- p \to \eta n$ compared to data. Such exclusive processes allow for the fine-tuning of the resonance parameters listed in table 3.4, which is very important since the parameters given in [125] often are only crude estimates. η-production is a rather selective probe: Apart from the N^*_{1535} resonance, also the N^*_{1650}, the N^*_{1710}, the N^*_{1710} and the N^*_{2080} contribute to this cross section.

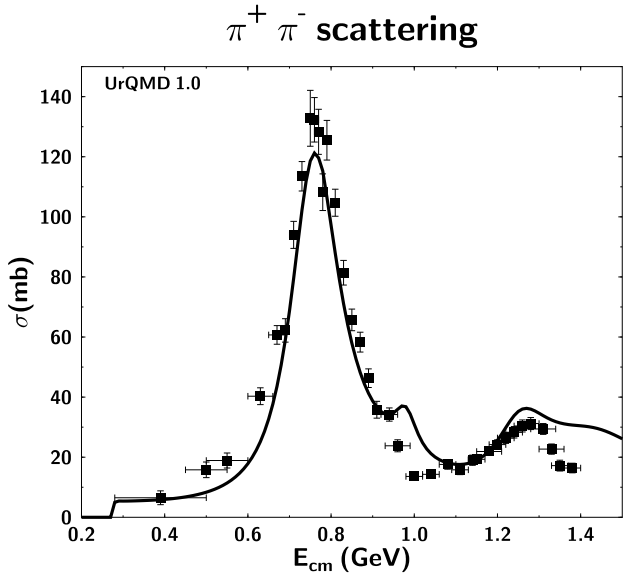

Figure 3.12: Total $\pi^+\pi^-$ cross section in UrQMD compared to data [127]. The cross section is dominated by the ρ-resonance.

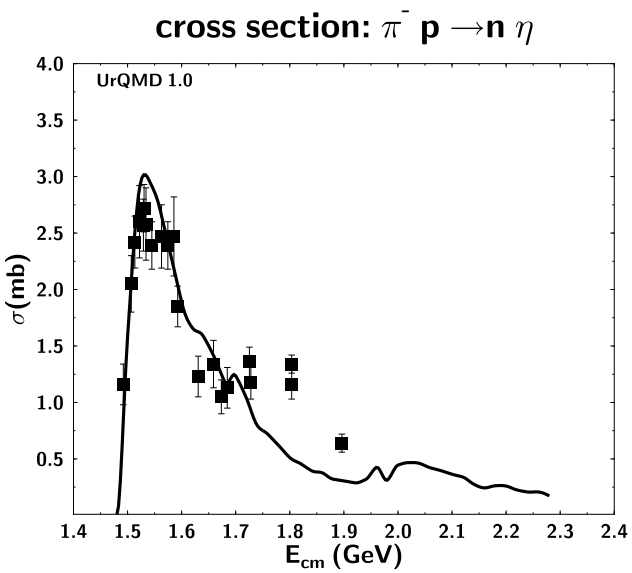

Figure 3.13: Exclusive pion-induced η production in UrQMD compared to data [127]: Apart from the N^*_{1535} resonance, also the N^*_{1650}, the N^*_{1700}, the N^*_{1710} and the N^*_{2080} contribute to the cross section.

3.3.3 Angular distributions

The UrQMD approach uses an analytical expression for the differential cross-section of in-medium NN elastic scattering derived from the collision term of the RBUU equation [135, 76] to determine the scattering angles between the outgoing partners of all elementary hadron-hadron collisions. Here it is assumed that the angular distributions for all relevant two-body processes are similar and can be described approximately by the differential cross-section of in-medium NN elastic scattering. This cross section is

$$\sigma_{NN\to NN}(s,t) = \frac{1}{(2\pi)^2 s}[D(s,t) + E(s,t) + (s,t \longleftrightarrow u)], \tag{3.55}$$

$$\begin{aligned}
D(s,t) &= \frac{(g^{\sigma}_{NN})^4}{2(t-m_\sigma^2)^2}(t-4m^{*2})^2 + \frac{(g^{\omega}_{NN})^4}{(t-m_\omega^2)^2}(2s^2+2st+t^2-8m^{*2}s+8m^{*4}) \\
&\quad + \frac{24(g^{\pi}_{NN})^4}{(t-m_\pi^2)^2}m^{*4}t^2 - \frac{4(g^{\sigma}_{NN}g^{\omega}_{NN})^2}{(t-m_\sigma^2)(t-m_\omega^2)}(2s+t-4m^{*2})m^{*2}, \qquad (3.56) \\
E(s,t) &= -\frac{(g^{\sigma}_{NN})^4}{8(t-m_\sigma^2)(u-m_\sigma^2)}[t(t+s)+4m^{*2}(s-t)] + \frac{(g^{\omega}_{NN})^4}{2(t-m_\omega^2)(u-m_\omega^2)}(s-2m^{*2}) \\
&\quad \times(s-6m^{*2}) - \frac{6(g^{\pi}_{NN})^4}{(t-m_\pi^2)(u-m_\pi^2)}(4m^{*2}-s-t)m^{*4}t \\
&\quad + (g^{\sigma}_{NN}g^{\omega}_{NN})^2[\frac{t^2-4m^{*2}s-10m^{*2}t+24m^{*4}}{4(t-m_\sigma^2)(u-m_\omega^2)} + \frac{(t+s)^2-2m^{*2}s+2m^{*2}t}{4(t-m_\omega^2)(u-m_\sigma^2)}] \\
&\quad + (g^{\sigma}_{NN}g^{\pi}_{NN})^2[\frac{3m^{*2}(4m^{*2}-s-t)(4m^{*2}-t)}{2(t-m_\sigma^2)(u-m_\pi^2)} + \frac{3t(t+s)m^{*2}}{2(t-m_\pi^2)(u-m_\sigma^2)}]
\end{aligned}$$

$$+(\mathrm{g}^{\omega}_{NN}\mathrm{g}^{\pi}_{NN})^2[\frac{3m^{*2}(t+s-4m^{*2})(t+s-2m^{*2})}{(t-m^2_{\omega})(u-m^2_{\pi})}+\frac{3m^{*2}(t^2-2m^{*2}t)}{(t-m^2_{\pi})(u-m^2_{\omega})}], \tag{3.57}$$

where the function D represents the contribution of the direct term and E is the exchange term. The coupling strengths are $\mathrm{g}^{\sigma}_{NN} = 6.9$, $\mathrm{g}^{\omega}_{NN} = 7.54$ and $\mathrm{g}^{\pi}_{NN} = 1.434$ and Mandelstam variables are given by:

$$s = (p+p_2)^2 = [E^*(p)+E^*(p_2)]^2 - (\mathbf{p}+\mathbf{p}_2)^2, \tag{3.58}$$

$$t = (p-p_3)^2 = \frac{1}{2}(s-4m^{*2})(\cos\theta - 1), \tag{3.59}$$

$$u = (p-p_4)^2 = 4m^{*2} - s - t, \tag{3.60}$$

with θ denoting the scattering angle in the c.m. system. The in-medium single-particle energy is given by

$$E^*(p) = \sqrt{\mathbf{p}^2 + m^{*2}}\ . \tag{3.61}$$

The formula for the differential cross section of in-medium NN elastic scattering can be extended to all elementary hadron-hadron collisions if it is scaled by the replacement

$$s \rightarrow s - (m^*_1 + m^*_2)^2 + 4m^{*^2}\ , \tag{3.62}$$

where m^*_1 and m^*_2 denote the effective masses of the incoming hadrons. Furthermore, we take into account the effects stemming from the finite size of hadrons and a part of the short range correlation by introducing a phenomenological form factor at each vertex. For the nucleon-nucleon-meson vertex we take the commonly used form

$$F_{NNA} = \frac{\Lambda^2_A}{\Lambda^2_A - t}\ . \tag{3.63}$$

Here Λ_A is the cut-off mass of the meson A. These cut-off masses are Λ_σ =1200 MeV, Λ_ω =808 MeV and Λ_π =500 MeV.
The total energy and the masses of the incoming hadrons serve as an input for calculating the angular distribution.

Since at the current stage UrQMD only uses free cross sections and free on-shell particles the effective in-medium quantities E^* and m^* are replaced by the respective free quantities E and m.

It is worth to stress again that equation (3.55) is only used for the angular distributions of all elementary two-body processes but not for the corresponding total cross sections.

3.3.4 Resonance lifetimes

Recently, the treatment of resonance lifetimes in microscopic transport calculations has received much attention [136]. The standard approach to resonance lifetimes τ_R in transport calculations is the application of $\tau_R = 1/\Gamma_R$ in conjunction with a Monte-Carlo sampling of the exponential decay law. The total decay width of the resonance Γ_R is either taken to be constant or mass dependent (see e.g. figure 3.6). The resulting lifetimes in the case of the Δ_{1232} resonance can be seen in the left frame of figure 3.14.

However, this treatment is highly questionable. Time delays and resonance lifetimes in the context of semi-classical transport calculations can be investigated via the scattering of an incident wave packet on a spherical volume. The details of this investigation are presented in the work of Danielewicz and Pratt (DP) [136]. Here, only a brief summary with emphasis on its application in a microscopic transport model is given.

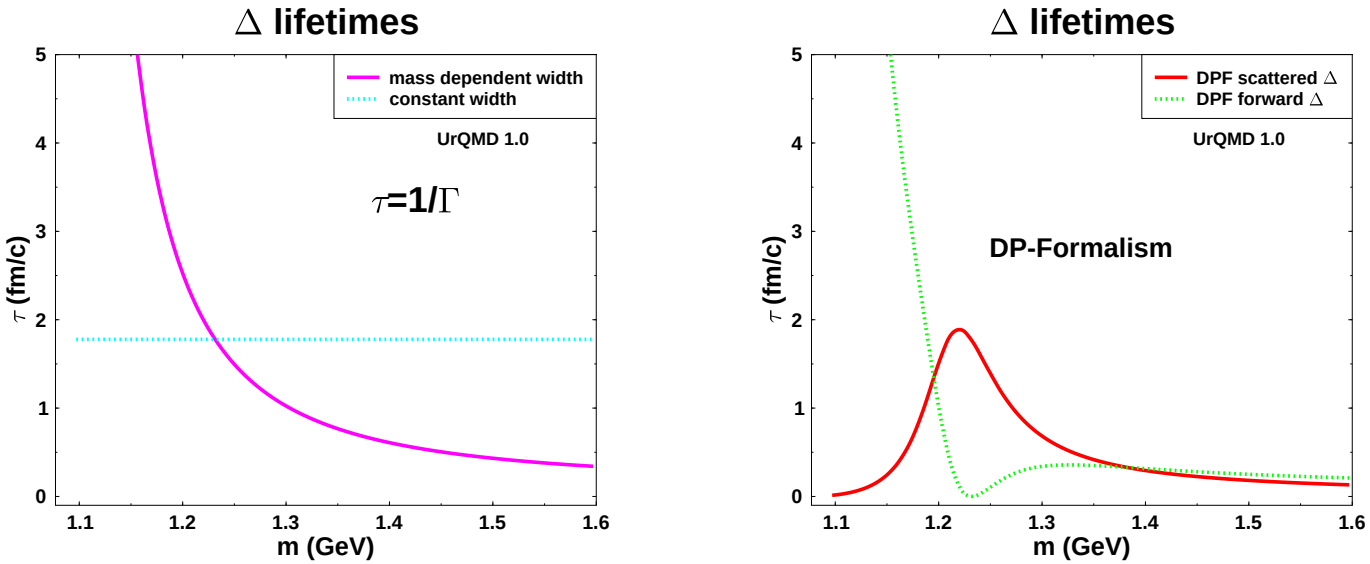

Figure 3.14: Mass-dependent lifetime of the $\Delta(1232)$ resonance as used in transport model calculations. The current prescription of the lifetime computed as inverse (optionally mass-dependent) width is shown on the left. The r.h.s. displays lifetimes according to Danielewicz and Pratt [136].

As a result of the scattering, both, the forward going and the scattered part of the wave packet suffer time delays. In terms of phase shifts they are given by:

$$\Delta\tau_S = \frac{\mathrm{d}\delta_l}{\mathrm{d}E} \quad ; \qquad \Delta\tau_F = \frac{(2l+1)\,2\cos(2\delta_l)}{\sum_l (2l+1)(1-4\sin^2(\delta_l))}\frac{\mathrm{d}\delta_l}{\mathrm{d}E} \tag{3.64}$$

If one is only interested in the thermodynamic quantities of the system, one can define an ergodic constraint which relates the time delays to its densities of state. The investigation of this system, which in the context of transport model calculations may be thought of as a "thermal" or infinite matter limit yields the following results:

- $\Delta\tau_F$ is consistent with the motion of particle through a mean field:
  $U = \rho \cdot \mathrm{Re}\,\mathcal{F}(0)$ (impulse approximation)

- all interaction effects (to lowest non-trivial order in density) can either be absorbed into a mean field or into a modified scattering delay $\Delta\tau'_S$

$$\Delta\tau'_S = \frac{1}{2\sin^2(\delta_l)}\frac{\mathrm{d}\delta_l}{\mathrm{d}E} \tag{3.65}$$

Transport model calculations dominantly treat resonances as Breit-Winger resonances. In that case the form of the phase shift δ_l is well known and the application of the formalism yields:

$$\Delta\tau_S = \frac{\Gamma/2}{(E-E_R)^2+\Gamma^2/4} \tag{3.66}$$

$$\Delta\tau_F = \frac{\sigma_R}{\sum_l (2l+1)\frac{\pi}{k^2}}\frac{(E-E_R)^2-\Gamma^2/4}{\Gamma\left((E-E_R)^2+\Gamma^2/4\right)} \tag{3.67}$$

$$\Delta\tau_S' = 1/\Gamma_R \quad (\text{“thermal” or infinite matter limit}) \tag{3.68}$$

During these delay-times, particle identity should change to ensure the correct density of states. However, $\Delta\tau_F$ is negative near E_R. When treating the forward time delay as a mean field interaction this negative time delay corresponds to an acceleration of the respective particle. If, on the other hand, the time delay is treated as such with the scattered particle in a resonance state during that time-span, then $\Delta\tau_F$ and (in order to remain consistent) $\Delta\tau_S$ must be rewritten in a way that no negative delays occur:

$$\Delta\tau_S^{\text{UrQMD}} = \frac{\Gamma/4}{(E-E_R)^2+\Gamma^2/4} \tag{3.69}$$

$$\Delta\tau_F^{\text{UrQMD}} = \frac{\sigma_R}{\sigma_F}\frac{(E-E_R)^2}{\Gamma\left((E-E_R)^2+\Gamma^2/4\right)} \tag{3.70}$$

These time delays are plotted in the right frame of figure 3.14. The $1/\Gamma(E)$ divergence of $\Delta\tau_F$ should not pose a serious problem since it appears at an energy far off the pole at which the cross section for resonance production usually vanishes. It can therefore be omitted through the proper energy dependence of the ratio σ_R/σ_F. However, the determination of the cross section σ_F is not straightforward[1], since it is experimentally not directly observable via $\frac{\mathrm{d}\sigma}{\mathrm{d}\Omega}$. For the application in a transport model one can attempt to determine the strength of σ_F via the infinite matter limit: an infinite matter calculation employing $\Delta\tau_S$ and $\Delta\tau_F$ with their respective cross sections must yield the same result as a calculation with $\Delta\tau_S'$ and the scattering cross section alone – if the forward cross section has been chosen properly. This approach does of course not yield a unique choice for σ_F but provides a range of σ_F parameterizations which are consistent with the well known “thermal” or infinite matter limit.

Different ansatzes for σ_F are currently under investigation in the framework of UrQMD. Apart from this novel approach it is also possible to perform calculations with $\tau_R = 1/\Gamma_R$, both, for fixed and mass-dependent widths.

3.3.5 String-excitation and -fragmentation

The strong interactions of hadrons and nuclei are described by Quantum Chromodynamics. Due to asymptotic freedom of QCD the coupling constant $\alpha_s(Q^2)$ becomes small at small distances or large Q^2. It gives a possibility to apply the perturbation theory to the processes with large momentum transfer. On the other hand at large distances ($\approx 1/\Lambda_{QCD}$) the coupling constant is not small and non perturbative effects, which are responsible for the confinement should be important. This large distance dynamics is very essential for understanding the processes with small momentum transfer, which give a dominant contribution to the high energy hadronic interaction.

If one considers the hadrons as bubbles in QCD vacuum liquid with the chromodynamical fields of quarks which do not penetrate in the vacuum medium, then the interactions of such bubbles at high energies leads to the production of new objects - color tubes, or strings. The interaction between such objects can take place with color transfer when quarks from different hadrons are interacting and without color transfer when hadrons are interacting only by exchange of the momenta. In both cases it leads to increase of energy and at some moment it will be energetically favorable to break the color tube by producing $q\bar{q}$-pair from the vacuum. This process repeats until many white bubbles - hadrons will be produced. According to the uncertainty principle the time needed for production of a hadron with

[1]Note that when following the mean field approach for the forward time delay, the form of the mean field can directly be determined from the experimentally accessible forward scattering amplitude $\mathcal{F}(0)$

momentum p is $\tau \approx p/m^2$, so in the c.m. system the last will be produced the fastest hadrons containing the spectator quarks (inside-outside cascade). Each produced q and $\bar{q}$ have small relative momenta in their rest frame or small rapidity distances. As a result due to Lorentz invariance of the picture, finally produced hadrons at high energies will be uniformly distributed in rapidity and will have limited transverse momenta.

Hereby for high energy reactions we use a similar picture corresponding to the case when two hadrons are interacting only by momentum transfer. It imitates the processes with the double and single diffraction. In baryon-baryon (meson-meson) interaction strings between quark q_v and diquark qq_v (antiquark $\bar{q}_v$) from the same hadron are produced. The hadron-hadron interactions at high energies are simulated in 3 stages. According to the cross sections the type of interaction is defined: elastic, inelastic, antibaryon-baryon annihilation etc. In the case of inelastic collision with string excitation the kinematical characteristics of strings are modeled in the following way: The hadron momentum transfer p_T is simulated according to a Gaussian distribution

$$f(\boldsymbol{p_T}) \propto \frac{1}{\sqrt{\pi\sigma^2}} \exp(-p_T^2/\sigma^2) \tag{3.71}$$

where $\sigma = 1.6$ GeV/c. The other interacting hadron gets the same momentum transfer but in the opposite direction. The excited strings have the continuous mass distribution $f(M) \propto 1/M^2$ with the masses M, limited by the total collision energy $\sqrt{s}$: $M_1 + M_2 \leq \sqrt{s}$. The rest of the $\sqrt{s}$ is equally distributed between the longitudinal momenta of two produced strings: $\boldsymbol{p_{1\parallel}} = -\boldsymbol{p_{2\parallel}}$. The energy of the ith string E_i is defined by the longitudinal momentum of the string $\boldsymbol{p_{i\parallel}}$, momentum transfer p_T and the mass of the string M_i:

$$E_i^2 = p_{i\parallel}^2 + p_T^2 + M_i^2, \quad i = 1, 2 \tag{3.72}$$

$$E_1 + E_2 = \sqrt{s}. \tag{3.73}$$

The longitudinal momenta of the constituent quarks are chosen according to the structure functions of hadrons:

$$f(x_q) = f_0(x_q)^{\alpha-1}(1 - x_q)^{\beta-1} \tag{3.74}$$

with $\alpha = 0.5$ and $\beta = 2.5$ for valence quark in nucleons.

The transverse distribution of the constituent quarks was generated according to the same Gaussian distribution as for the momentum transfer Eq. (3.71). The diquark transverse momentum is equal in magnitude, but of opposite direction.

The second stage of h-h interactions is connected with **string fragmentation**. UrQMD uses the Field-Feynman fragmentation procedure when the strings decay independently from both ends. It includes energy, momentum and quantum number conservation laws and the possibility of converting diquarks into mesons via diquark breaking.

Figure 3.15 schematically sketches the fragmentation excitation of a baryon-string: Two quark-antiquark pairs are created (a $\bar{u}u$ and an $\bar{s}s$ pair). The leading diquark combines with a newly produced s quark to form a hyperon, the newly produced $\bar{s}$ quark combines with a newly produced u quark to form a kaon and the newly produced $\bar{u}$ quark forms together with the leading quark a pion. In order to produce baryon-antibaryon pairs in a string-excitation, also the creation of diquark-antidiquark pairs from the Dirac-sea must be possible. The suppression factor for the flavors of the quark-antiquark pair produced in string decays can be defined by a Schwinger-like formula [137]:

$$|\mathcal{M}|^2 \sim \exp\left(-\frac{\pi m^2}{\kappa}\right) \quad , \tag{3.75}$$

Figure 3.15: Particle production in a string-excitation. Two quark-antiquark pairs are spontaneously created in the color flux-tube between the constituent diquark and the constituent quark.

where $\mathcal{M}$ gives the matrix-element for the production of a quark-antiquark pair. The string-tension κ is ($\kappa \approx 1$ GeV/fm) and m is the mass of the quark-antiquark pair [93, 138, 139].

The suppression factors can also be tuned to the production probabilities for certain meson- and baryon-species in elementary proton-proton collisions: The s-quark suppression factor is very sensitive with regard to kaon-production, whereas the diquark suppression factor plays an important role for the antinucleon production. The strange diquark suppression factor can be tuned by studying antihyperon production. The standard values for the different suppression factors in UrQMD are:

$$u : d : s : qq \; = \; 1 : 1 : 0.35 : 0.1 \quad . \tag{3.76}$$

In the UrQMD string-excitation scheme it is not only possible to excite the ground-states of baryons and mesons, but also their excited states, which have the same quark-content. If for baryons, the quark-content does not determine whether the state belongs to the lowest octet or to the lowest decuplet, then octet or decuplet are chosen with equal probability. The probabilities for the higher excited multiplets are tuned to multiplicities measured in proton-proton reactions. In the case of mesons the multiplet must also be determined before a species can be assigned. The probability of choosing a certain multiplet depends on the spin of the multiplet and its average mass:

$$P_{J^{PC}} \sim \frac{2S+1}{\langle m \rangle_{J^{PC}}} \quad . \tag{3.77}$$

The respective values for the meson multiplets implemented in UrQMD are listed in table 3.10.

multiplet J^{PC}	0^{-+}	1^{--}	0^{++}	1^{++}	2^{++}	1^{+-}	1^{--*}	1^{--**}
probability	0.102	0.190	0.056	0.124	0.197	0.127	0.110	0.095

Table 3.10: Excitation probabilities for the different meson-multiplets in UrQMD. The probabilities depend on spin and average mass of the multiplet.

The excitation and fragmentation of a string follows an iterative scheme:

$$\text{string} \Longrightarrow \text{hadron} + \text{new string} \quad ,$$

i.e. a quark-antiquark (or a diquark-antidiquark) pair is created and placed between leading constituent quark-antiquark (or diquark-quark) pair. Then a hadron is formed randomly on one of the end-points of the string. The quark content of the hadron determines its species and charge. In case of resonances the mass is determined according to a Breit-Wigner distribution. Finally, the energy-fraction of the string which is assigned to the newly created hadron must be determined: After the hadron has been stochastically assigned a transverse momentum, the fraction of longitudinal momentum transferred from the string to the hadron is determined by the fragmentation function.

For the following discussion, it is convenient to introduce light-cone variables in configuration space ($z^{\pm}$) and in momentum space ($p^{\pm}$). They depend on space-time (t,z) and energy-momentum (E,p) coordinates and are defined as:

$$z^{\pm} = t \pm z \quad \text{and} \quad p^{\pm} = E \pm p \quad . \tag{3.78}$$

where For the stochastic fragmentation of a string one defines the Lorentz-invariant quantities:

$$x^{\pm} = \frac{p^{\pm}_{\text{hadron}}}{p^{\pm}_{\text{total}}} \quad (0 \leq x^{\pm} \leq 1) \quad , \tag{3.79}$$

which represent the longitudinal momentum-fraction of the string which is transferred to the new hadron. As examples we show a meson string fragmenting from the r.h.s.:

$$p^+ \underbrace{(q\,\bar{q}q\,\bar{q})}_{\text{string}} = x^+p^+ \underbrace{(q\bar{q})}_{\text{meson}} + (p^+ - x^+p^+) \underbrace{q\bar{q}}_{\text{string}} \quad , \tag{3.80}$$

and a baryon string fragmenting from the l.h.s:

$$p^- \underbrace{(qq\,q\bar{q}\,q)}_{\text{string}} = x^-p^- \underbrace{(qqq)}_{\text{baryon}} + (p^- - x^-p^-) \underbrace{\bar{q}q}_{\text{string}} \quad . \tag{3.81}$$

This iterative fragmentation process is repeated until the remaining energy of the string gets too small for a further fragmentation.

The fragmentation function $f(x, m_t)$ represents the probability distribution for hadrons with the transverse mass m_t to acquire the longitudinal momentum fraction x from the fragmenting string. One of the most common fragmentation functions is the one used in the LUND model [139]:

$$f(x, m_t) \sim \frac{1}{x}(1-x)^a \exp\left(-b \cdot m_t^2/x\right). \tag{3.82}$$

In UrQMD, different fragmentation functions are used for leading nucleons and newly produced particles, respectively (see figure 3.16):

$$f(x)_{\text{nuc}} = \exp\left(-\frac{(x-B)^2}{2\,A^2}\right) \quad \text{for leading nucleons} \tag{3.83}$$

$$f(x)_{\text{prod}} = (1-x)^2 \quad \text{for produced particles} \tag{3.84}$$

with $A = 0.275$ and $B = 0.42$. The fragmentation function $f(x)_{\text{prod}}$, used for newly produced particles, is the well-known Field-Feynman fragmentation function [140, 141]. At string break-up, $q\bar{q}$-pairs have zero transverse momentum in the string frame, but the transverse momenta of a single quark, $\boldsymbol{p_t}$, and the corresponding antiquark, $-\boldsymbol{p_t}$, is taken according to eq. (3.71).

The main criteria for the selection of the fragmentation functions and the fine-tuning of their parameters is that the particle multiplicities and momentum distributions in elementary proton-proton reactions must match the data.

Figure 3.17 shows the Feynman-x ($x_f = 2p_{lab}/\sqrt{s}$) distributions for emitted protons and lambdas in proton-proton reactions at $E_{lab} \approx 200$ GeV. UrQMD fits quite well the data [142], which is important for the predictive power with regard to stopping and particle production in nucleus-nucleus collisions. The UrQMD estimate of particle multiplicities in comparison to data is shown for proton-proton reactions at 200 GeV in table 3.11, and in figure 3.18 at $\sqrt{s} = 27$ GeV. The overall agreement is very good, however,

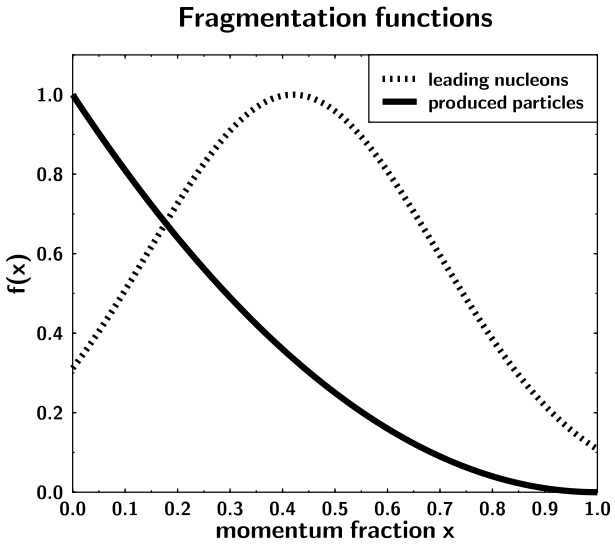

Figure 3.16: UrQMD fragmentation functions: nucleons containing leading constituent quarks have a Gaussian fragmentation function whereas a Field-Feynman fragmentation function is used for newly produced particles.

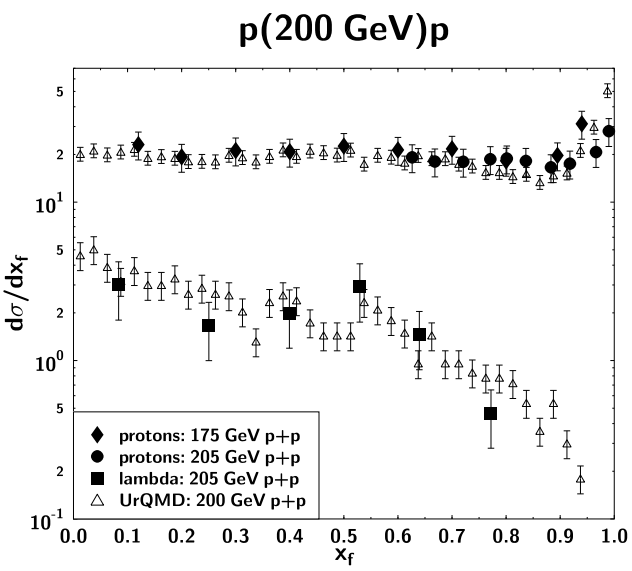

Figure 3.17: Comparison of the Feynman-x distribution for lambdas and protons between UrQMD and data [142] in proton-proton reactions at $\approx$ 200 GeV.

currently the ϕ-meson production is underestimated by almost a factor of 2 and (anti-)lambda and Σ^0 production is overestimated by 50%. Also shown in Fig. 3.19 is the excitation function of anti-proton multiplicities in inelastic proton-proton collisions.

The last central issue to be discussed in this section is the definition of the formation time: The formation time of a hadron is the time the constituent quarks of the respective hadron need in order to bind together and form the hadron and to tunnel out of the vacuum. For composed particles, there are two possibilities to define the formation point: *i*) "constituent" formation point has the coordinates of the string break-up points; *ii*) "yo-yo" formation point has the coordinates of the quark trajectories intersection. In UrQMD, the "yo-yo" formation time definition is used. The formation time depends on the momentum and energy of the created hadron.

Figure 3.20 schematically shows the fragmentation of a meson string into several mesons. At the vertices V_n and V_{n-1} quark-antiquark pairs are created. The antiquark of vertex V_n then forms a new meson together with the quark of vertex V_{n-1}. Configuration space (as depicted in figure 3.20) and momentum space are linked by the following relations [93]:

$$E_n = \kappa\,(z_{n-1} - z_n) \tag{3.85}$$
$$p_n = \kappa\,(t_{n-1} - t_n) \quad . \tag{3.86}$$

and for the light-cone variables:

$$p_n^+ = \kappa\,(z_{n-1}^+ - z_n^+) \tag{3.87}$$
$$p_n^- = \kappa\,(z_n^- - z_{n-1}^-) \quad . \tag{3.88}$$

particle	data	UrQMD
π^-	2.62 ± 0.06	2.47
π^+	3.22 ± 0.12	3.07
π^0	3.34 ± 0.24	3.01
K^+	0.28 ± 0.06	0.23
K^-	0.18 ± 0.05	0.13
K^0_S	0.17 ± 0.01	0.18
$\Lambda + \Sigma^0$	0.096 ± 0.01	0.17
$\bar{\Lambda} + \bar{\Sigma}^0$	0.013 ± 0.004	0.03
p	1.34 ± 0.15	1.32
$\bar{p}$	0.05 ± 0.02	0.05

Table 3.11: UrQMD particle multiplicities compared to data [143] for proton-proton reactions at 200 GeV.

The formation point and time of the hadron is defined as the point in space-time where the quark trajectories of the quark-antiquark pair forming the hadron meet for the first time. In figure 3.20 this point is denoted as P_f. The formation time is then given by:

$$t_{f,n} \;=\; \frac{1}{2}(t_{n-1} \;+\; t_n + z_{n-1} - z_n) \;=\; \frac{1}{2}(z^+_{n-1} + z^-_n) \tag{3.89}$$

If the momenta of the produced particles are numbered consecutively from right to left, one obtains in momentum space:

$$t_{f,n} \;=\; \frac{1}{2\kappa}\left(M + E_n - p_n - 2\sum_{j=0}^{n-1} p_j\right) \quad , \tag{3.90}$$

with $L = M/\kappa$ and $T = 2L = 2M/\kappa$.

Depending on the hadron-species, formation times are in the order of 1 – 2 fm/c. During the formation time, the cross sections of the leading hadrons containing leading constituent quarks are reduced since prior to the formation of the hadron only the constituent quark part of the cross section is present:

$$\begin{aligned} \sigma_{\mathrm{qh}} &\approx \frac{1}{3}\sigma_{\mathrm{Bh}} \quad \text{for baryons} \quad , \\ \sigma_{\mathrm{qqh}} &\approx \frac{2}{3}\sigma_{\mathrm{Bh}} \quad \text{for baryons} \quad , \\ \sigma_{\mathrm{qh}} &\approx \frac{1}{2}\sigma_{\mathrm{Mh}} \quad \text{for mesons} \quad . \end{aligned} \tag{3.91}$$

Newly created hadrons without any leading constituent quarks of the initial hadron have zero interaction cross section during their formation time.

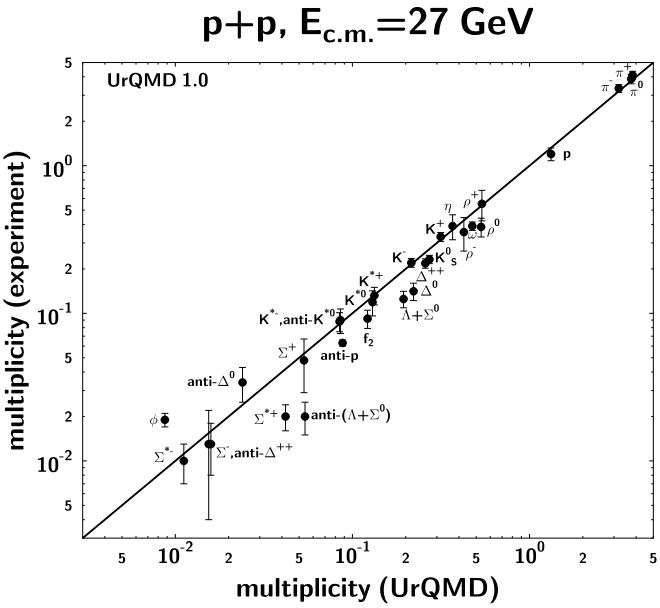

Figure 3.18: Data [144, 145, 146] vs. UrQMD particle multiplicities in proton-proton reactions at a c.m. energy of 27 GeV.

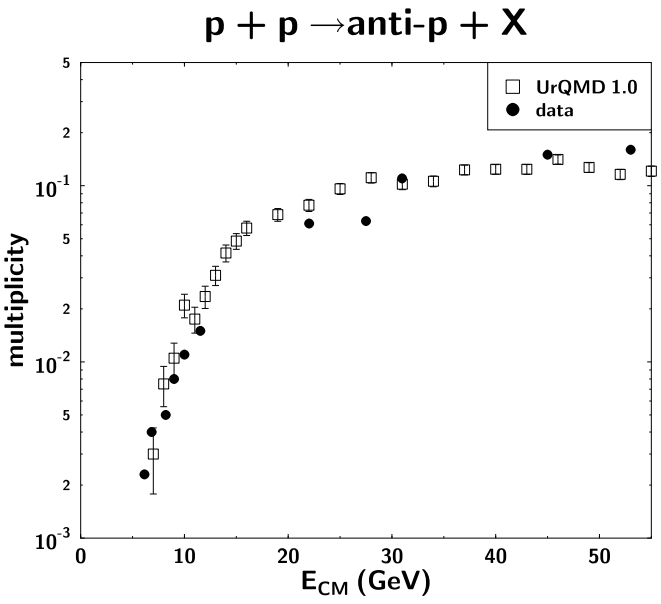

Figure 3.19: Proton-proton excitation function of anti-proton multiplicities as obtained in UrQMD. The experimental data are taken from [147]

3.3.6 Color fluctuations, color opacity and transparency

Quantum Chromodynamics (QCD) has important - and so far not considered - implications on high energy processes [148]:

- Hadrons consist of configurations of very different spatial size;
- At high energies, hadronic quark-gluon configurations can be considered frozen. Due to the long coherence length at these energies geometrical color optics can be applied;
- Small object have reduced interactions;
- Small objects will expand at high energies;
- Large-size objects can be captured in the central zone of a heavy ion collision.

These effects have diverse consequences. One of them is color transparency: Suppose a small sized object is created; this object does not interact very much due to color screening. At sufficiently high energies, it can pass through an entire nucleus without fluctuating into a large configuration. Thus it does not interact - the nucleus is transparent. Nucleus-Nucleus collisions provide a tool to investigate the effects of color transparency e.g. in the production of J/Ψ [149]. However, the complementary color opacity effect (large size configurations) can cause stronger stopping and significant fluctuations in the transverse energy for central reactions.

A first step to investigate these QCD effects within a microscopic transport model can be made by using fluctuations in the elementary hadron hadron reactions. Thus one needs the probability $P(\sigma)$ for different sized configurations. It is convenient to consider moments of the distribution:

$$< \sigma^0 >= \int \mathrm{d}\sigma \overline{\sigma}^0 P(\sigma) = 1 \quad , \tag{3.92}$$

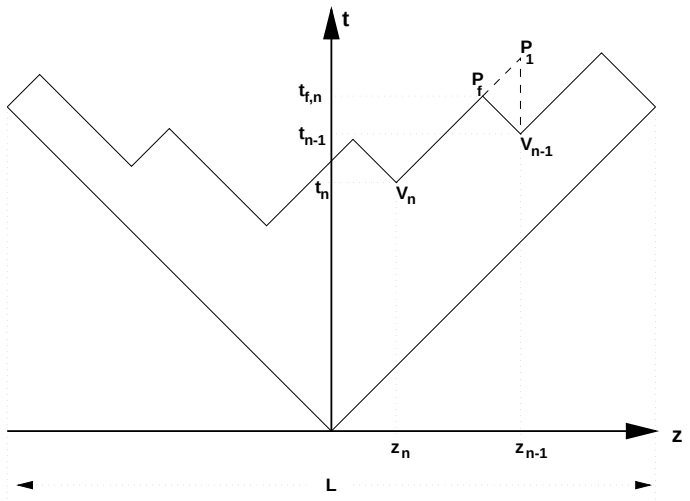

Figure 3.20: Schematic picture of a fragmenting meson string in configuration space. The first newly produced meson on the r.h.s. forms at the point P_f at which the quark lines first meet.

$$< \sigma^1 >= \int \mathrm{d}\sigma \overline{\sigma}^1 P(\sigma) = \overline{\sigma} \quad , \tag{3.93}$$

$$\vdots \tag{3.94}$$

where $\overline{\sigma}$ denotes the average cross section, and $P(\sigma)$ the probability of a certain cross section. The second moment $< \sigma^2 >$can be determined from diffractive dissociation experiments. In addition further information can be obtained from QCD, which implies:

$$P(\sigma) \propto \sigma^{N_q - 2} \quad , \tag{3.95}$$

for $\sigma \to 0$, with N_q being the number of valence quarks. Thus, we get for the nucleon and pion distributions:

$$P_N(\sigma) \propto \sigma \quad \text{nucleon} \quad , \tag{3.96}$$

$$P_N(\sigma) \propto \text{const.} \quad \text{pion} \quad . \tag{3.97}$$

from these arguments, we can construct $P(\sigma)$. As shown in Fig.3.21, one gets a broad distribution for proton projectiles and an even broader one for pions.

By exploring these color coherent phenomena, we have an effective new method to investigate QCD and the nuclear structure. This helps to disentangle and select distinct properties of interacting hadronic systems. This has been so far neglected in microscopic calculations of heavy ion collisions.

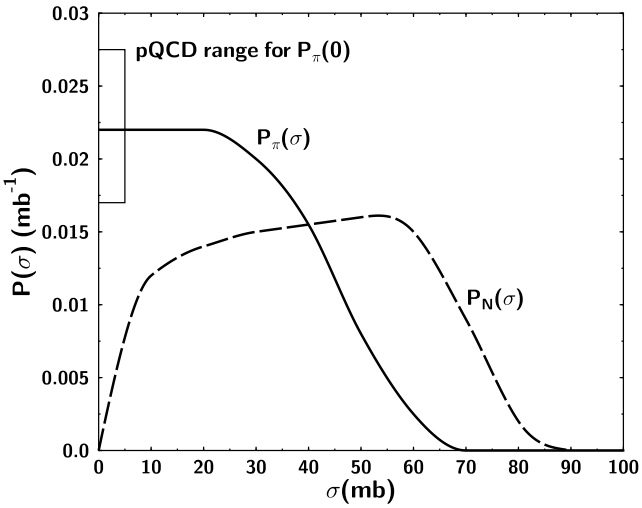

Figure 3.21: Cross-section probability for pions $P_\pi(\sigma)$ and nucleons $P_N(\sigma)$ as extracted from experimental data. $P_\pi(\sigma = 0)$ is compared with the perturbative QCD prediction. (Figure taken from [148]).

Chapter 4

Probing hot and dense nuclear matter with relativistic heavy ion collisions

4.1 Baryon stopping

Head-on collisions of two nuclei can be used to create highly excited nuclear matter [2, 1]. In the course of the reaction, a part of the respective longitudinal momenta is converted into transverse momentum and secondary particles. This causes the creation of a zone of high energy density. Nuclear shock waves have been suggested as a primary mechanism of creating high energy densities in such collisions [2, 1, 150].

The term *nuclear stopping power* [151] characterizes the degree of stopping which an incident nucleon suffers when it collides with the nuclear matter of another nucleus. It can be studied by measuring the rapidity distribution of the net-baryons present in the reaction. Obviously, the average collision number per baryon increases with the mass number of the colliding nuclei. Thus, the heaviest systems available, such as Pb+Pb or Au+Au, are best suited for the creation of strongly stopped matter and high energy densities.

The shape of the baryon rapidity distribution can give clear indications on the onset of critical phenomena: Due to the strong dependence of the baryon rapidity distribution on the baryon–baryon cross section [152, 153, 154], a rapid change in the shape of the scaled $dN/d(y/y_p)$ distribution with varying incident beam energy is a clear signal for new degrees of freedom entering the reaction (i.e. deconfinement) or for phenomena such as critical scattering [155]. The width of the $dN/d(y/y_p)$ distribution for baryons is inversely proportional to their cross section. In [156] it was pointed out that at energies $E \geq 200$ GeV/nucleon large fluctuations of size in the nucleon wave function, leading to the color-transparency or color-opacity effect, respectively, should be observed.

The degree of stopping can furthermore be used to estimate the achieved energy density in the course of the collision. One often assumes that particles produced at $y = y_{CM}$ originate from the central reaction zone at $z = 0$ and the initial proper time τ_0. The rapidity distribution of these produced particles can then be used to estimate the initial energy density in the central reaction zone [4]:

$$\epsilon_0 = \frac{m_T}{\tau_0 A} \left.\frac{dN}{dy}\right|_{y=y_{CM}} . \tag{4.1}$$

Here A is the transverse overlapping region area in the collision and m_T the transverse mass of the produced particles. The proper production time is estimated to be of the order of 1 fm/c. Estimates for the CERN/SPS energy region were in the order of 1 to 10 GeV/fm^3 [4].

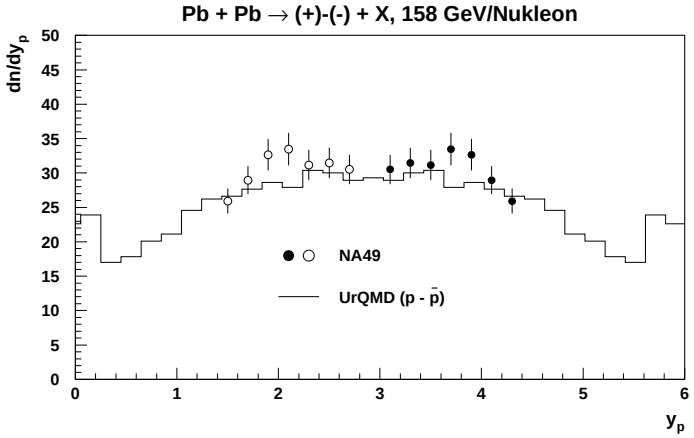

Figure 4.1: Rapidity distributions of net-protons for Pb+Pb collisions at the SPS (160 AGeV) in comparison to preliminary NA49 data [157].

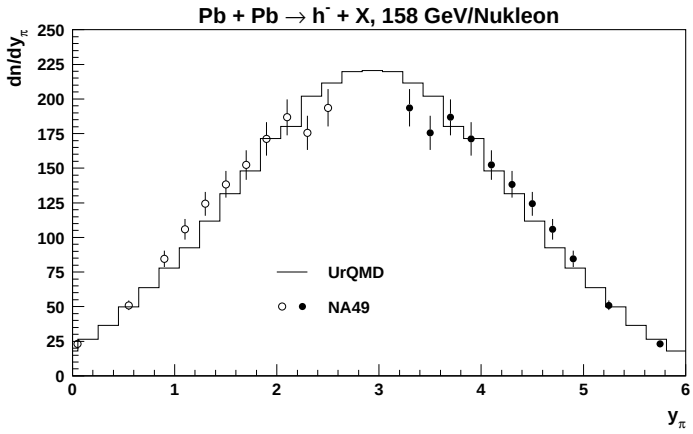

Figure 4.2: Rapidity distributions of negatively charged hadrons (i.e. π^-, K^- and $\overline{p}$) for Pb+Pb collisions at the SPS (160 AGeV) in comparison to preliminary NA49 data [157].

Hadronic transport models are well able to predict or reproduce the measured rapidity distributions over a vast energy range, if baryon and meson rescattering and particle production via string decay [107, 159, 160, 161] are incorporated. The VENUS model including possible formation and decay of multi–quark clusters [162] seems to give similar results. A simple "first collision model" without rescattering [98, 163, 164, 165] does not suffice to reproduce the data. However, it has been shown recently that a simple geometrical model of nucleus-nucleus collisions (LEXUS) [166] describes rather well the rapidity and transverse momentum distributions of protons at SPS energies. It is based on linear extrapolations of nucleon-nucleon collisions, following the concepts of Glauber [167] and the rows-on-rows model of Hüfner and Knoll [168]. LEXUS ignores rescattering of secondary particles or any other collective effect completely. This is visible in the resulting numbers of produced (anti-)strange particles which differ strongly from experimental values. Similar in spirit are investigations, where the final state of nucleus-nucleus collisions is described as a superposition of isotropically decaying fireballs [169]. Here, the longitudinal motion is extrapolated from p+p data while the transverse motion is due to random walk collisions, fitted to p+A reactions. Like in [166] the model is designed to serve as a baseline for further analyses. Unfortunately some genuine collective effects which arise in AA collisions may counteract themselves, leaving the discussed observables unchanged. With respect to the net-baryon distribution, these studies show that gross features alone are not necessarily decisive signatures of new physics.

Let us first explore the stopping behavior of UrQMD in central Pb+Pb collisions at the SPS (160 AGeV) as depicted in Fig. 4.1 in comparison to recently measured data by the NA49 collaboration [157]. Overall good agreement is observed. A large amount of longitudinal momentum has been deposited, leading to excessive particle production at central rapidities in line with preliminary data from NA49 [157] (cf. Fig. 4.2).

Figure 4.3 shows a UrQMD calculation of the proton rapidity distribution for three presently used heavy ion accelerators. In all cases, a system as heavy as Au+Au or Pb+Pb exhibits a central pile-up at mid-rapidity. However, the physical processes associated are different: The average longitudinal momentum loss in the SIS energy regime is mainly due to the creation of transverse momentum whereas at the AGS/SPS energies abundant particle production eats up a considerable amount of the incident beam energy. The form of the distributions change from a Gaussian at SIS energies to a plateau at AGS

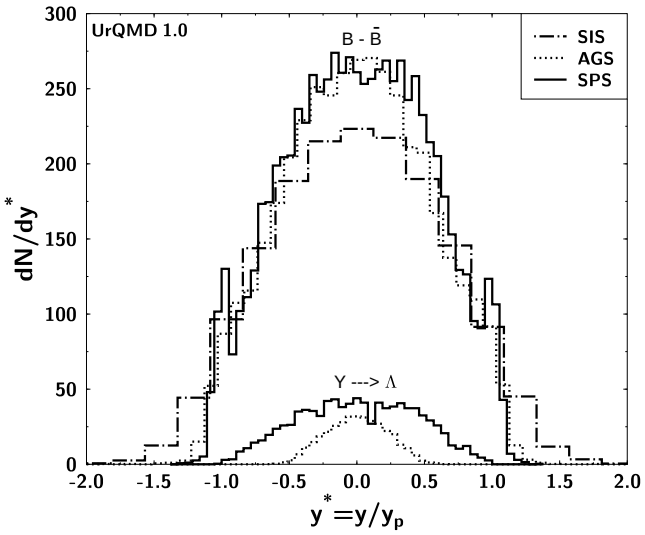

Figure 4.3: Rapidity distributions of net-baryons for Au+Au collisions at SIS (1 GeV/nucleon), AGS (10.6 GeV/nucleon) and CERN/SPS energies (160 GeV/nucleon) calculated with the UrQMD model (higher curves). All distributions have been normalized to the projectile rapidity in the center of mass frame. We have also plotted rapidity distributions of strange baryons decaying into Λ (lower curves).

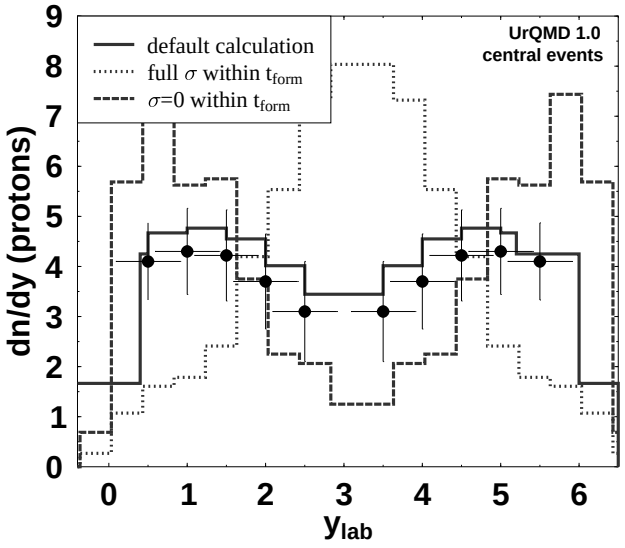

Figure 4.4: Formation time dependence of stopping power for the reaction S+S at 200 GeV/nucleon. Solid dots represent experimental data from [158]. The cross sections of particles within their formation time introduce large uncertainties for their rapidity distribution.

and finally to a slight two-bump structure at CERN energies.

At CERN/SPS energies baryon stopping is dominated not only by rescattering effects but also by the formation time after hard collisions in which strings are excited. Within their formation time, baryons originating from a leading (di)quark interact with (2/3) 1/3 of their free cross section and mesons with 1/2 of their free cross sections. The influence of the formation time is shown in figure 4.4 for the system S+S at 200 GeV/nucleon. The default calculation (including formation time) reproduces the data [158] fairly well whereas the calculation with zero formation time (dotted line) exhibits total stopping. A calculation with zero cross section within the formation time, however, exhibits transparency.

In order to study this effect more closely, the $\sqrt{s}$ distributions of elementary baryon-baryon collisions are analyzed for Au+Au collisions at AGS and S+S collisions at SPS energies. Figure 4.5 shows the respective distribution for Au+Au. The collision spectrum is dominated by BB collisions with full cross sections and exhibits a maximum at low energies. Approximately 20% of the collisions involve a diquark, i.e. a baryon originating from a string decay whose cross section is reduced to 2/3 of its full cross section.

In figure 4.6, the same analysis is performed for S+S at 200 GeV/nucleon. In contrast to the heavy system at AGS the collision spectrum exhibits two pronounced peaks dominated by full BB collisions, one in the beam energy range and one in the low (thermal) energy range. Approximately 50% of the collisions, most of them at intermediate $\sqrt{s}$ values, involve baryons stemming from string excitations whose cross sections are reduced by factors of 2/3 (referred to as *diquarks*) or 1/3 (referred to as *quarks*). The peak at high $\sqrt{s}$ values stems from the initial hard collisions whereas the peak at low energies is related to the

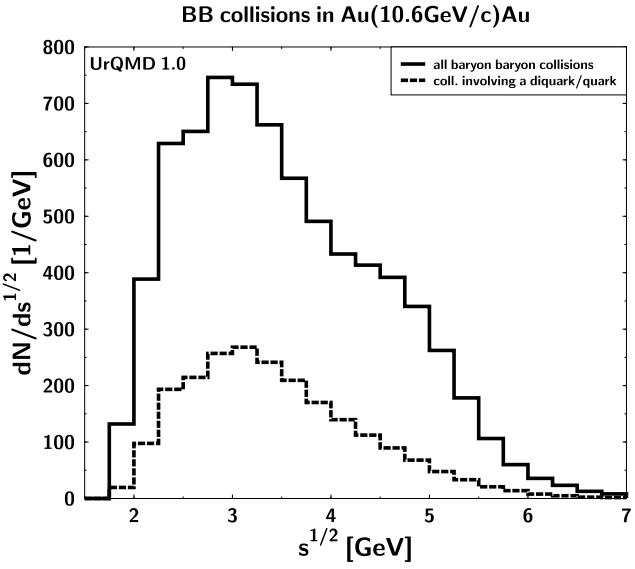

Figure 4.5: E_{CM}^{coll} distribution for baryon baryon collisions in a central Au+Au reaction at the AGS.

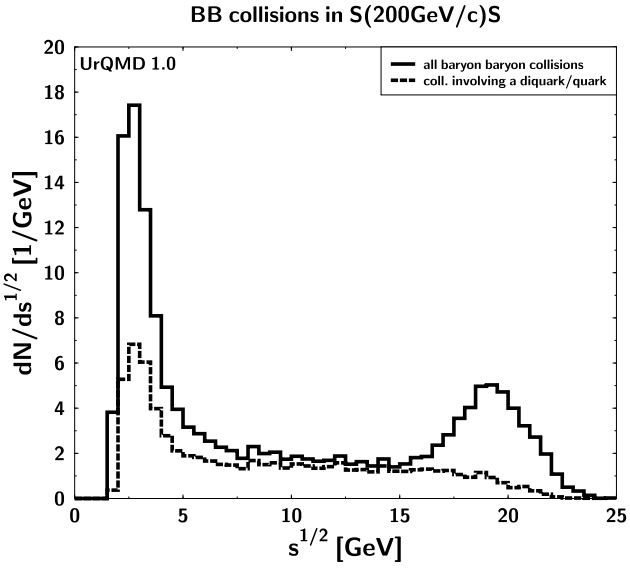

Figure 4.6: E_{CM}^{coll} distribution for baryon baryon collisions in a central S+S reaction at SPS energies.

late, thermal stages of the reaction.

Figure 4.7 shows the importance of fluctuations of the net-baryon distribution in a single event for highest energies. Although the average net-baryon $\mathrm{d}N/\mathrm{d}y$ is less than 5 at mid-rapidity, regions of high positive or negative net-baryon density occur stochastically in a limited region of phase space.

4.2 Particle production

4.2.1 Subthreshold particle production from resonance matter

Subthreshold particle production is kinematically forbidden in first nucleon-nucleon collisions. Therefore it provides a good tool to extract information about collective effects and the high density phase.

As an example, we consider in the following the subthreshold production of antiprotons: The process has first been observed experimentally for Si+Si at BEVALAC [170]. Experimental studies have also been done recently with a 2.0 GeV/u and 1.8 GeV/u Ne beam from the heavy ion synchrotron (SIS) at GSI [171, 172].

Since the antiproton yields cannot be described in terms of a first collision model [173], various mechanisms of antibaryon enrichment have been proposed, e.g. hadronic multi-step processes [131, 174, 175, 176], strong mean field effects [177] and meson-meson interaction like $\rho\rho \rightarrow p\bar{p}$ [178].

Subthreshold antiproton production has been investigated with respect to a reduction of the effective nucleon mass in the framework of RBUU [179, 180], QMD [181] and RVUU [182]. The important contribution of high lying baryon resonances without consideration of in-medium masses has also been studied[183]. This we will discuss in the following. Note that the threshold behavior of $\bar{p}$-production in NN-reactions for $\sqrt{s} - 4m > 1$ GeV is not experimentally determined, so any model calculation depends on extrapolations.

Schematically there are three different energy regions in hadron-hadron interactions: the (quasi-)elastic scattering, the region of resonance production and formation and the high energy region characterized by

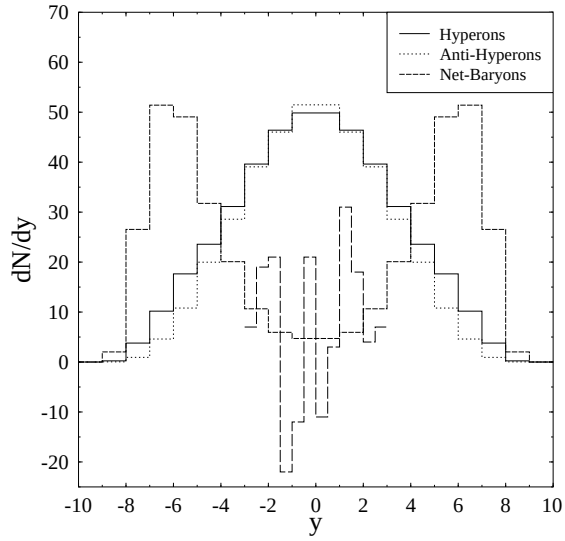

Figure 4.7: Event-averaged rapidity density of net-baryons, hyperons and anti-hyperons in collisions of $Pb + Pb$ at 6.5 TeV and $b = 0$, calculated with Fritiof 7.02. For the mid-rapidity range, the net-baryon distribution of one single event is also depicted (figure taken from [34]).

abundant production of particles. In the resonance region the kinetic energy of the reaction partners is sufficient to form excited states of the ingoing hadrons which subsequently decay again into the stable hadrons. The most prominent examples are

$$\begin{array}{rcl} \pi N & \longrightarrow & \Delta_{1232} \\ \pi\pi & \longrightarrow & \varrho(770) \\ NN & \longrightarrow & N\Delta_{1232} \end{array} \tag{4.2}$$

The formation of resonances influences the particle production rates and their momentum distributions, e.g. the p_t spectra. The particle chemistry may change, too, distorting signatures from earlier reaction stages, e.g. due to reactions like

$$\begin{array}{ccccc} \pi Y & \longleftrightarrow & Y^\star & \longleftrightarrow & \bar{K}N \\ \pi\pi & \longleftrightarrow & f_0(980) & \longleftrightarrow & K\bar{K} \end{array} \tag{4.3}$$

Any of these secondary interactions can be of utmost importance for particle production as discussed in [160, 174, 175, 184], the dominant process being the annihilation of produced mesons on baryons which leads to the formation of s channel resonances or strings. Those resonances formed are not only responsible for strangeness enrichment at the AGS [184, 185], but they may be further excited in a subsequent collision to a mass larger than $3m_N$ which allows for $\bar{N}N$ creation.

If the projectile nucleon gets excited in the first collision, but does not lose momentum for target excitation (which may happen in a subset of cases), a further excitation in a subsequent collision then may help to bring the projectile beyond the $\bar{B}$ creation threshold.

On the one hand, the larger the mass of the incoming hadrons, the better the chance to overcome the $\bar{B}$ creation threshold in a subsequent collision, because the second step of excitation can be smaller. On

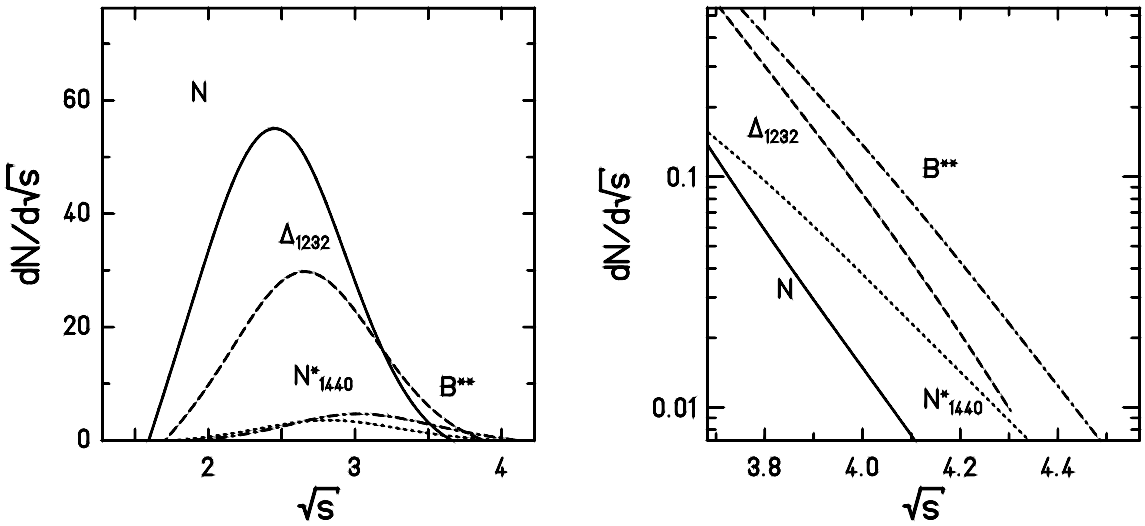

Figure 4.8: RQMD calculation of the collision spectrum for the reaction $Ni+Ni$ at 2 GeV/u (min. bias). The contributions are classified according to the heaviest baryon involved: N (solid line), Δ_{1232} (dashed line), N^*_{1440} (dotted line) and all higher resonances (dashed-dotted line). Shown is the total spectrum (left) and the tails above the $\bar{p}$-production threshold (right).

the other hand, the life time goes down with increasing mass reducing the chance to hit another target nucleon. Therefore the multi-step process of $\bar{p}$ production has to be viewed as a complicated interplay between excitation and decay processes.

Calculations in the framework of RQMD [186] exhibit a scenario of cumulative scattering of participants and secondaries, a multi-step process of successive binary collisions like πN, ρN, ηN^*, etc, as well as $\Delta\Delta$, etc. Baryons and mesons get more and more excited and decay or rescatter subsequently. Possibly, the invariant mass of a single resonance-resonance collision exceeds the threshold for antiproton production. The collision spectra of AA-reactions at 2 GeV/u show that meson-baryon-interactions play a decisive role for the excitation of these high masses. We do not find evidence for any antiproton production via the meson-meson channel (especially $\rho\rho$) at SIS-energies.

According to RQMD, BUU and IQMD calculations, the enrichment of nuclear matter with Δ resonances is only about 15% for medium systems at SIS energies [187, 188, 189], higher resonances are even less populated. Nevertheless, they turn out to be most important for the production of heavy particles, since the collisions at high center of mass energy preferentially involve these highly excited baryons. Fig. 4.8 shows the baryon-baryon collision spectrum of the reaction Ni+Ni at 2 GeV/u. Above $\sqrt{s} = 4 \cdot m_{\mathrm{N}}$ only 1/3 of the BB-reactions are NN-, $N\Delta_{1232}$- or $\Delta_{1232}\Delta_{1232}$-collisions. 50% involve resonances higher than N^*_{1440}. They act as energy depots and dominate the $\bar{p}$-production.

In the other microscopic models mentioned above the contribution of high mass resonances are neglected, but the antiproton production is strongly enhanced due to a reduced effective mass. In particular the $\bar{p}$ annihilation probability differs drastically between the models [183]. This question might be resolved by the measurements of anti-flow, as was suggested in [190]. Thus, different microscopic models give totally incompatible scenarios (see also section 4.2.6).

4.2.2 Temperatures and single particle spectra

The hot and dense reaction zone consists of incident nucleons and produced particles. The *fireball* model considers the hadrons as a gas in thermodynamic equilibrium. For temperatures above 50 MeV, Fermi-Dirac and Bose-Einstein distribution functions for baryons and mesons may be approximated by a Maxwell-Boltzmann distribution [191, 192], with the temperature T as parameter. Equilibration is thought to be visible predominantly in the transverse degrees of freedom; therefore, transverse momentum or transverse mass distributions are used to extract temperatures.

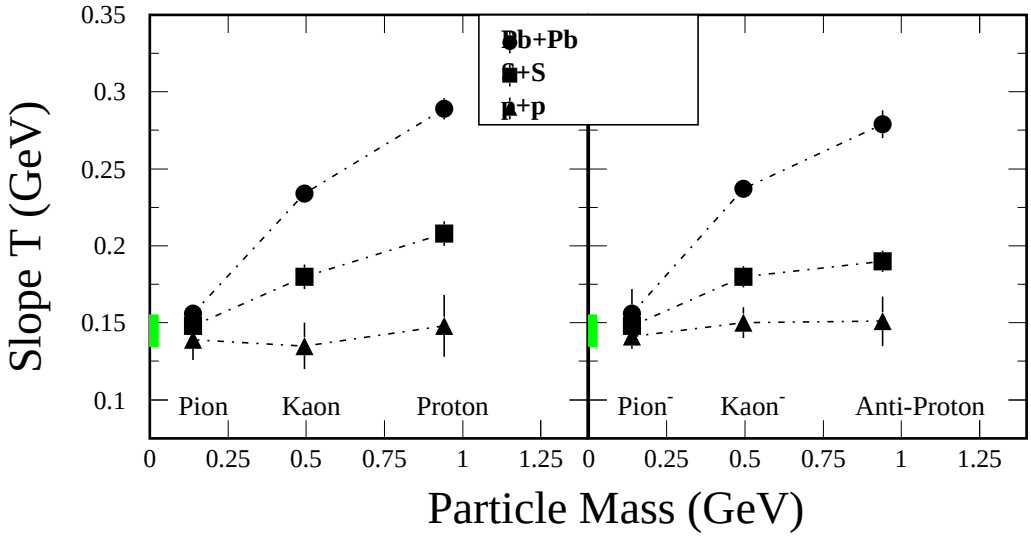

Figure 4.9: Mass and collision system dependence of the inverse slope parameter T measured by the NA44 collaboration [193].

The inverse slope T is obtained from a fit to the transverse mass m_T spectrum using

$$\frac{1}{m_T}\frac{dN}{dm_T} \propto \mathrm{e}^{m_T/T} \quad . \tag{4.4}$$

Heavy ion collisions at the AGS and, even more at the SPS, exhibit an intricate scenario. Here, typical MB collision energies are in the range of 2-10 GeV in a baryon rich regime. Thus two problems have to be addressed: The influence of the modeling of meson baryon scattering as well as the creation of collective transverse flow (first measured at the SPS from the NA44 collaboration, see Fig. 4.9) which lead to increasing apparent temperatures "T". To study these aspects, the UrQMD model was used in two different modes:

1. A complete downward extrapolation of the high energy longitudinal color flux picture to $\sqrt{s} = 2$ GeV (referred to as forward-backward peaked (f-b) variant).

2. An upward extrapolation of the resonance behavior, i.e. an isotropic angular distribution of all outgoing particles in MB reactions (indicated as (iso)).

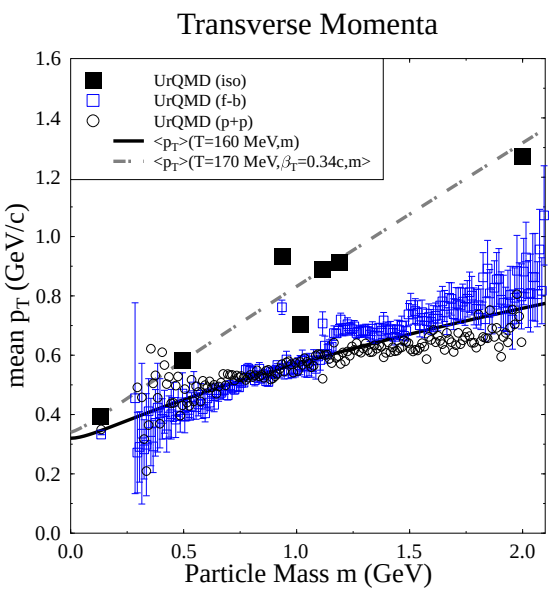

Figure 4.10: Mean p_t at midrapidity ($|y| < 0.5$) as a function of particle mass in central Pb(160GeV)+Pb reactions. Figure taken from [194].

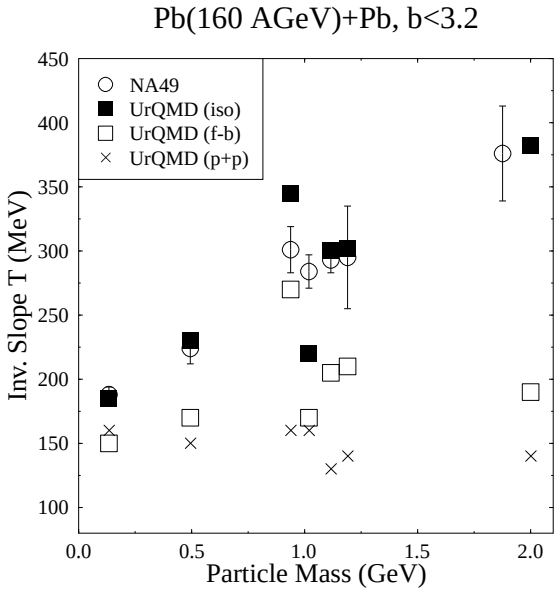

Figure 4.11: Mass and collision system dependence of the inverse slope parameter T in comparison to measured NA49 data [195]. Figure taken from [194].

To gain insight into the creation of transverse flow, Fig. 4.10 discusses mean transverse momenta of particles for different mass bins at $|y| < 0.5$ in central Pb+Pb collisions at the SPS. Circles show the p(160 AGeV)+p events, open squares indicate the (f-b) Pb+Pb events and the full black squares show the isotropic model (iso). In addition, we fit the resulting mass spectra with a simple fireball plus flow model. The full black line is the mean transverse momentum $< p_T(m, T_0, \beta_T) >$ for different masses m calculated from a thermal distribution with temperature $T_0 = 160$ MeV without any additional flow ($\beta_T = 0$). The grey dashed line shows the $< p_T(m, T_0, \beta_T) >$ from an expanding thermal source ($T_0 = 170$ MeV) with an additional transverse flow velocity of $\beta_T = 0.34c$. This yields in the saddle point approximation a rough value for the *apparent* temperature T[196]:

$$T \approx T_0 + m\beta_T^2 \quad . \tag{4.5}$$

The proton proton reactions and the f-b scenario show no significant difference in mean p_T to a non expanding thermal source. Only the isotropic model produces a transversally expanding hadronic source with significant additional transverse flow velocity of $0.34c$. Note that the statistical error bars are only stated for the (f-b) Pb+Pb reaction, in the (iso) and p+p case they are of approximately the same order.

This behavior of the (iso) prescription is also seen if we study the apparent temperatures (inverse slopes) at midrapidity ($|y| < 0.5$) as a function of particle mass m as depicted in Fig.4.11. Proton proton collisions (crosses) show about the same freeze-out temperature for all particles from 130 MeV mass (pions) to 2 GeV mass. This is mostly the same in the forward backward scenario (high energy limit extrapolated downwards) in Pb+Pb. The inverse slopes increase only slightly with particle mass. Only the isotropic treatment of intermediate energy meson baryon collisions in line with the resonance picture yields an increasing apparent temperature with the particle mass as indicated by the preliminary NA49 data[195].

The mass dependence of the apparent temperature is sensitive to the detailed modeling of the meson baryon rescattering process above the resonance region and below the high energy domain. Strong transverse expansion only builds up in the 'resonance model' in contrast to the high energy model which creates much less transverse flow.

Thus, collective (radial) flow [197, 198] as well as feeding from resonances, strongly influences the shape of particle spectra [199, 200]. For light composite particles, the influence of collective flow is visible in a strong shoulder-arm shape of transverse momentum spectra. This can be seen in figure 4.12. In order to account for flow effects, the spectra have to be fitted with a thermal distribution including collective flow. The temperature T and the transverse flow velocity β_t are the fit-parameters. The shapes of the flow velocity profile and density profile at freeze out enter as additional degrees of freedom in the analysis. Usually a box shaped density profile and a linearly increasing transverse velocity profile are assumed.

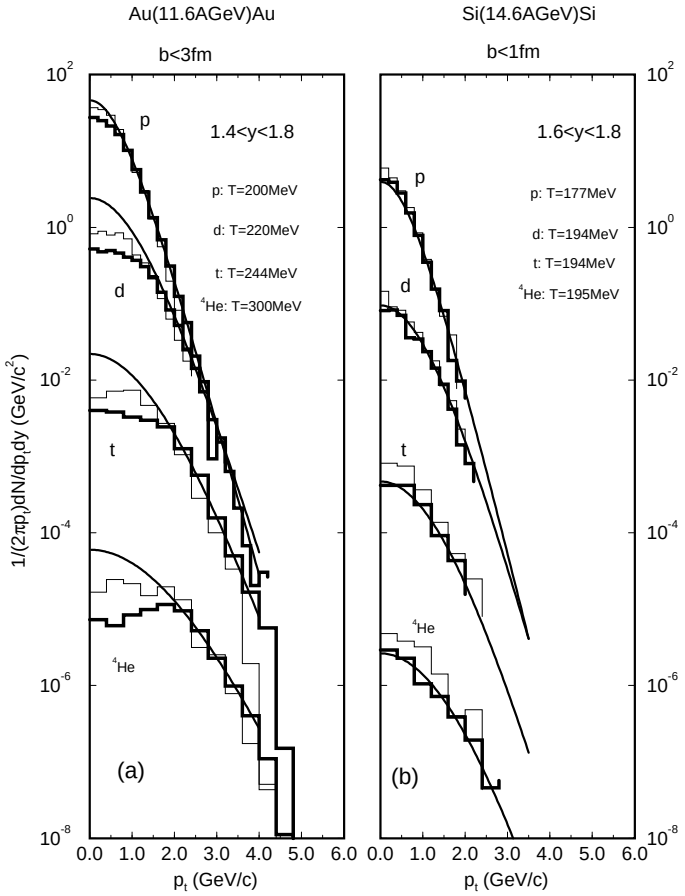

Figure 4.12: RQMD prediction of transverse momentum spectra at mid-rapidity for protons and light composite particles in central Si and Au collisions at the AGS. The bold solid histogram is a calculation with potentials, the thin histogram the respective calculation without potentials and the smooth solid line depicts a Boltzmann parameterization adjusted to the high momentum part of the spectra. The strong shoulder arm structure is due to collective flow. The figure has been taken from [201].

In microscopic calculations, temperatures and flow velocities can also be extracted by subdividing the system into cells and analyzing the local transverse and longitudinal velocity distributions. Temperatures extracted via a global two parameter fit are more than a factor of two higher than temperatures obtained from such a microscopic analysis, at least at beam energies in the 100 MeV/nucleon to 10 GeV/nucleon regime [123].

The reason for this discrepancy lies in the assumed shape of the freeze out density and velocity profiles. Analyses based on microscopic transport calculations show an extreme sensitivity of the extracted values of β_t and T on the shapes of the profiles [123, 201]. Whereas a linearly increasing transverse freeze-out velocity profile seems a tolerable assumption the shape of the freeze-out density profile has a rather Gaussian shape (centered at $r_t = 0$), far from the usually assumed box-like distribution. When using realistic density and velocity profiles one finds the high m_t components of the particle spectra dominated by large collective effects (i.e. the high expansion velocity). This results in a lower value for the temperature T. A microscopic analysis of spectra of protons and light composite particles at AGS energies showed β_t and T depending on the mass of the particle [201].

Spectra of light secondary particles, such as pions, at SIS and low AGS energies are dominated by resonance decays: Here we will use pion spectra in Au+Au reactions at 1 GeV/nucleon as example for the importance of resonances. They show how the shape of the spectra and the origin of the spectra can be explained in a fully dynamical and non-thermal scenario:

Figure 4.13 shows a comparison of inclusive π^0 spectra for Au+Au and Ca+Ca (minimum bias and $y_{c.m.} \pm 0.16$) between the IQMD model [111, 202] and data published by the TAPS collaboration [203]. The data have been rescaled by a factor of 0.6 in oder to obtain a minimum bias distribution from the measurement. The IQMD model overpredicts the yield for the heavy system Au+Au by approximately 20% which is consistent with the findings of the KaoS collaboration for charged pions (a comparison has been published in ref. [111]). However, the π^0 yield of the light system Ca+Ca is overpredicted by almost a factor of 2. For both systems IQMD calculations fail to reproduce the high transverse momentum tails.

Newer transport models perform much better when compared to the data [112, 204]. Figure 4.14 shows a comparison to the same data with the UrQMD model. Note that the slopes agree extremely well with the experiment and the yield for the system Ca+Ca deviates less than 20% from the data. However, the yield for the heavy Au+Au system is underpredicted for low transverse momenta. A reason for this may lie in the strength of the $\Delta_{1232} - N$ absorption cross section, which is calculated via the principle detailed balance from the $NN \rightarrow N\Delta_{1232}$ cross section (see figure 3.4). The UrQMD fit to the Δ_{1232} is very good. The absorption channel, however, diverges for low energies (due to the detailed balance principle) and is therefore extremely sensitive to even the minutest changes in the cross section parameterization. A reparameterization of the exclusive Δ_{1232} production cross section (within the constraints given by the data) may therefore improve the pion yield in heavy collision systems.

The importance of higher baryon resonances can be seen when comparing the IQMD[1] pion spectrum at 1 GeV/nucleon, figure 4.13, with the respective spectrum generated by the UrQMD model in figure 4.14. The enhancement at high p_t in the UrQMD calculation – which is due to the incorporation of higher baryon resonances [205] – is clearly visible and UrQMD agrees with the data even at the highest momenta.

Especially the measurement of those high energy pions is of great interest. They correlate directly to early freeze out times and heavy resonances [206]:

Transverse momenta p_t of pions in semi-central Au+Au collisions at 1 GeV/nucleon are shown in figure 4.15 as a contour plot versus their freeze out time (the time of their final interaction in the heavy ion collision): High p_t pions are produced almost exclusively in the early reaction phase with freeze out

[1]Note that the IQMD model includes only the Δ_{1232} and no other resonances are considered.

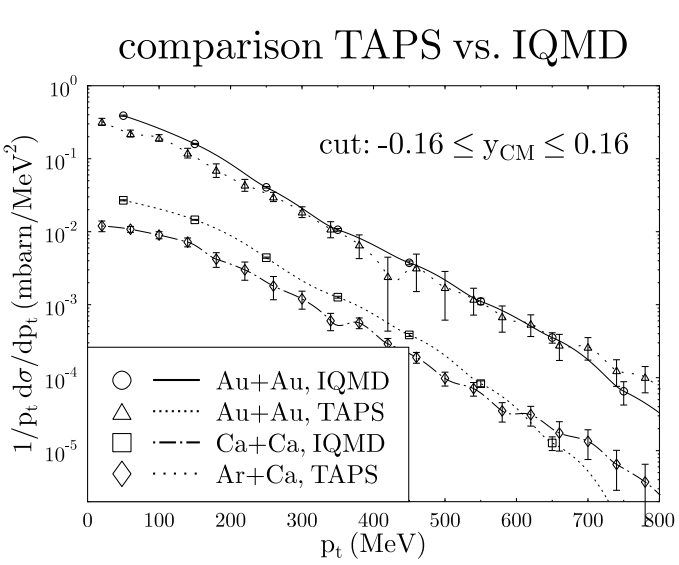

Figure 4.13: Comparison of inclusive π^0 spectra $\frac{d\sigma}{p_t dp_t}$ for Au+Au and Ca+Ca (minimum bias) collisions between the IQMD model and data measured by the TAPS collaboration. A hard EoS including momentum dependence is used. Figure taken from [111].

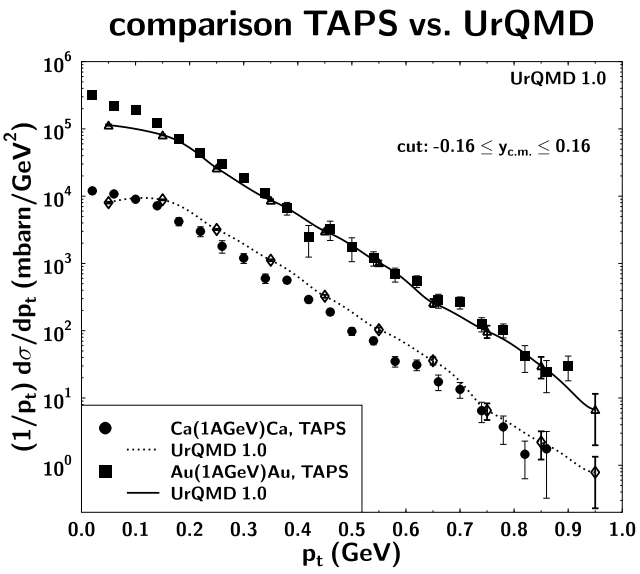

Figure 4.14: Same analysis as in figure 4.13, but with the UrQMD model: The influence of higher resonances on the high energy part of the spectrum is clearly visible.

times smaller than 20 fm/c, well in the high density phase of the reaction. The scaling of the contour lines in figure 4.15 is linear, far higher transverse momenta are obtained than depicted by the contour lines. We can establish a correlation between high p_t pions, early freeze out times and the hot and dense reaction phase. A correlation between high energy pions and early freeze out times has also been observed in BUU calculations of La+La collisions at 1.35 GeV/nucleon [207, 208]. However, the global, fixed event averaged time cut of 20 fm/c for La+La at 1.35 GeV/nucl. employed in ref. [207, 208] is a rough estimate of the **nucleonic** freeze out time (while in our approach the actual time (event by event) for **pion** freeze out is employed): The densities in the collision center are then already far lower than ground state density.

The average freeze out density for all pions lies well below nuclear ground state density; this is well known and has severely diminished the usefulness of pions as probes for the hot and dense reaction phase [58, 209, 210]. High p_t pions, however, freeze out at far higher densities: Their average freeze out density lies between 1.2 and 1.5 ρ/ρ_0 with some of them even freezing out at densities near the maximum density obtained in the collision.

Figure 4.16 shows the transverse mass spectrum of π^+ in Au+Au collisions at 1 GeV/nucleon within the IQMD model [206]. The spectrum has been decomposed into contributions of light ($m_\Delta \leq 1172$ MeV), medium (1172 MeV $\leq m_\Delta \leq$ 1292 MeV) and heavy ($m_\Delta \geq 1292$ MeV) Δ resonances. The correlation between high m_t pions and heavy resonances is obvious. Note that since the IQMD model is limited to the Δ_{1232} resonance and the inelastic nucleon nucleon cross section is projected onto the excitation of this particular resonance this statement has to be interpreted in a more general manner: at high transverse masses heavy resonances such as the N^*_{1440}, N^*_{1520} and N^*_{1535} should be substituted for the heavy $\Delta(1232)$ resonances of the IQMD model and contribute strongly to the transverse momentum or mass spectrum.

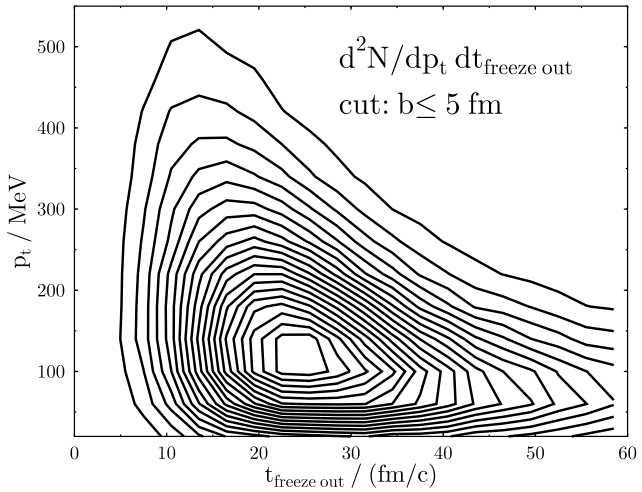

Figure 4.15: Transverse momentum versus freeze out time for pions in semi-central Au+Au collisions at 1 GeV/nucl. in the IQMD model [206]. High p_t pions freeze out predominantly in the hot and dense reaction phase. The scaling of the contour lines is linear; far higher transverse momenta occur than is depicted by the contour lines.

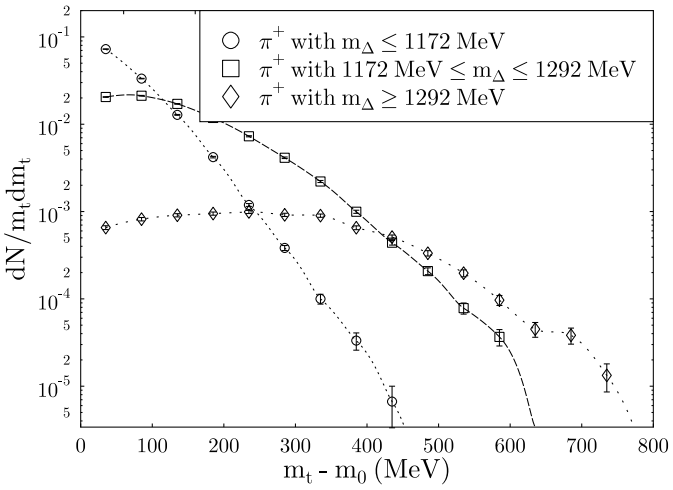

Figure 4.16: Transverse mass m_t distribution of freeze out π^+ with cuts on the mass of the emitting Δ resonance. The calculation are done for Au+Au collisions at 1 GeV/nucleon within the IQMD model. The connection between high m_t and large resonance mass is obvious: The production of freeze out pions with high m_t is dominated by the decay of heavy Δ resonances.

4.2.3 Hadrochemistry: multiplicities and ratios

Hadron abundances and ratios have been suggested as possible signatures for exotic states and phase transitions in dense nuclear matter. In addition they have been applied to study the degree of chemical equilibration in a relativistic heavy-ion reaction. Bulk properties like temperatures, entropies and chemical potentials of highly excited hadronic matter have been extracted assuming thermal and chemical equilibrium [14, 7, 144, 211, 212, 213, 6, 214, 215, 216, 217, 218, 219, 220, 221]. Recent SPS data on hadron yields and ratios have been fit either in the framework of a hadronizing QGP droplet [211, 222, 223, 224] or of a hadron gas in thermal and chemical equilibrium [221] (including elementary proton-proton interactions [144]). It has been shown that the thermodynamic parameters T and μ_B imply that these systems have been either very close to or even above the critical T, μ_B line for QGP formation [225, 211]. However, a UrQMD calculation [226] agrees with many of the data (π/p, d/p, $\bar{p}/p$, $\bar{\Lambda}/\Lambda$, $\bar{\Xi}/\bar{\Lambda}$ etc.) without assuming thermal and chemical equilibrium. Large discrepancies to the data (> 50 %) are only found for the K^0_S/Λ and Ω/Ξ ratios (see figure 4.17). The microscopic transport model calculation shows that secondary interactions significantly change the primordial hadronic cocktail of the system. The ratios exhibit a strong dependence on rapidity [226].

The assumption of global thermal and chemical equilibrium – as being employed by the static thermal models – is not justified: Both, the discovery of directed collective flow of baryons and anti-flow of mesons in Au+Au reactions at 10.6 GeV/nucleon [239] and Pb+Pb reactions at 160 GeV/nucleon energies [240] (see also section 4.3) as well as transport model analyses presented in section 4.2.7, which show distinctly different freeze-out times and radii for different hadron species, indicate that the yields and ratios result

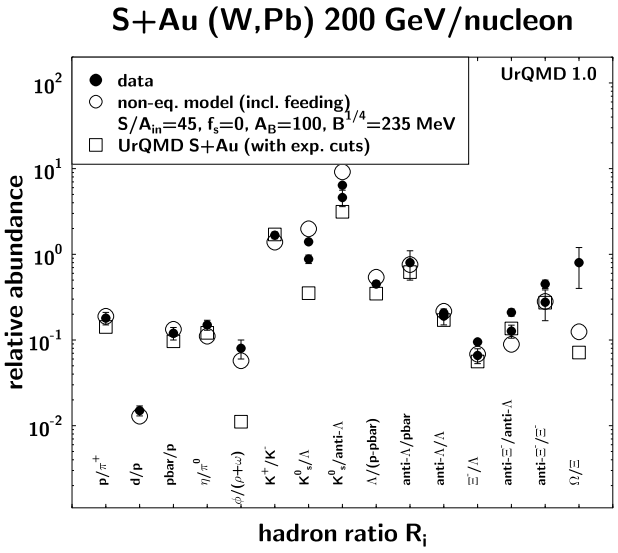

Figure 4.17: comparison between the UrQMD model and data for the system S+Au(W,Pb) at 200 GeV/nucleon. Also shown is a fit by a simple hadronization model [211]. Both models agree quite well with the data compilation [221]. The original data are from [227, 228, 229, 230, 231, 232, 233, 234, 235, 236, 237, 238]

.

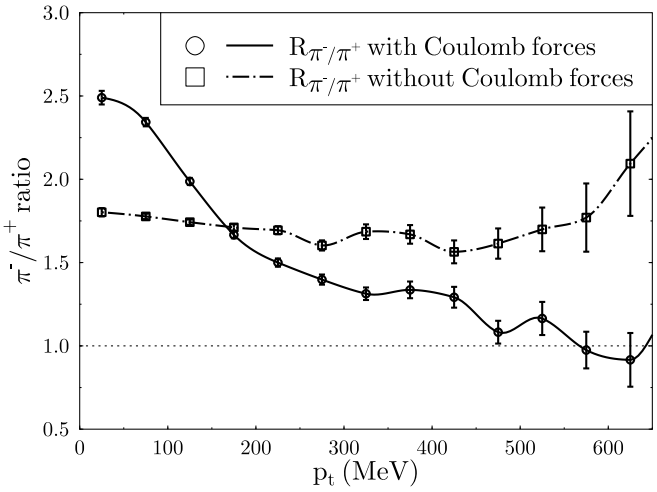

Figure 4.18: IQMD prediction for the π^- to π^+ ratio versus transverse momentum p_t in Au+Au collisions (minimum bias) at 1 GeV/nucl. with a hard EoS and momentum dependence [111]. The solid line shows the full calculation including Coulomb forces. The dashed-dotted line shows a calculation without Coulomb forces acting upon the pions.

from a complex non-equilibrium time evolution of the hadronic system. A thermal model fit may therefore not seem meaningful.

On the other hand, particle ratios also contain valuable information about the time-evolution and the dynamics of the collision system: The inclusion of Coulomb forces and energy dependent cross sections is also important in the domain of particle production. Figure 4.18 demonstrates this by showing the IQMD prediction [111] for the π^- to π^+ ratio versus transverse momentum p_t for Au+Au at 1 GeV/nucleon. The solid line shows a full calculation including Coulomb forces. For high p_t the π^-/π^+ ratio decreases towards 1, whereas for low p_t it increases to 2.5 – considerably higher than the value of 1.9 predicted by the Δ-isobar model. The dashed line shows a calculation without Coulomb forces. This ratio remains constant at ≈ 1.9. The (small) remaining variations might be due to the different energy dependence of the $\pi^+ - p$ and $\pi^- - p$ inelastic cross sections. The IQMD prediction is compatible to recent measurements by the KaoS collaboration [241]. A detailed comparison of the data to the UrQMD model has yet to be performed.

Note that the p_t-integrated values agree very well with the Δ-isobar model and thus hide any further information possibly contained in the p_t dependent ratio. The Δ-isobar model [242] was originally developed to describe p-wave pion-nucleon scattering and is based on considering the Δ_{1232} as an independent baryon species. Here it is applied in a statistical limit, i.e. it is the basis for the assumption that all pions are produced via the Δ_{1232} and the resulting multiplicity ratios only depend on the number of incident protons and neutrons and can be calculated via combinatorics applying the respective Clebsch-Gordan coefficients for the Δ_{1232} excitation and the subsequent decay into pions.

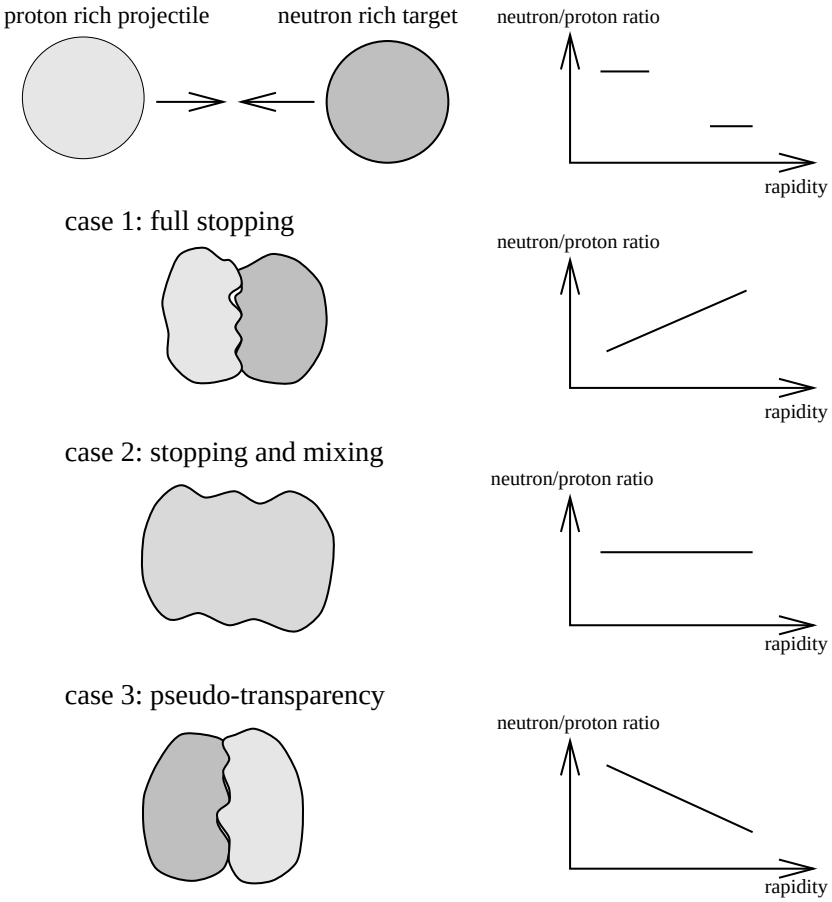

Figure 4.19: By using projectile and target with different isospin content, the mechanism of stopping, i.e. the amount of penetration between projectile and target nucleons, can be measured by plotting the neutron to proton ratio (or related quantities) versus the rapidity. Three possible scenarios are schematically depicted in the figure together with their respective signature.

Particle ratios like the proton to neutron or the experimentally accessible ^{3}He to triton ratio may also be used to gain experimental information on the mechanism of stopping (i. e. the amount of inter-penetration between projectile and target nucleons). So far the analysis of the stopping mechanism has only been accessible to transport model calculations. We propose an experiment with which regions in rapidity dominated by projectile or target nucleons can be identified (even at central collisions!) and with which therefore the question of the stopping mechanism can be investigated. If projectile and target have a large difference in their total isospin (i.e. they differ strongly in their neutron to proton ratio) then the comparison of the neutron to proton ratio vs. rapidity **before** the reaction with the respective ratio **after** the reaction yields direct information on the degree of penetration between projectile and target nucleons. Figure 4.19 depicts three extreme cases: (a) full stopping, (b) complete mixing of projectile and target nucleons and (c) transparency. Note that the configuration in momentum space is opposite to that in coordinate space.

We have used the QMD/IQMD model in order to test the feasibility of the suggested observable. As a test system we selected ^{50}Cr+^{48}Ca which has a large difference in the neutron to proton ratio at almost identical mass. The calculations were performed with impact parameters b$\leq$ 2 fm.

Figure 4.20a shows the neutron to proton asymmetry vs. rapidity for ^{50}Cr+^{48}Ca and the symmetric

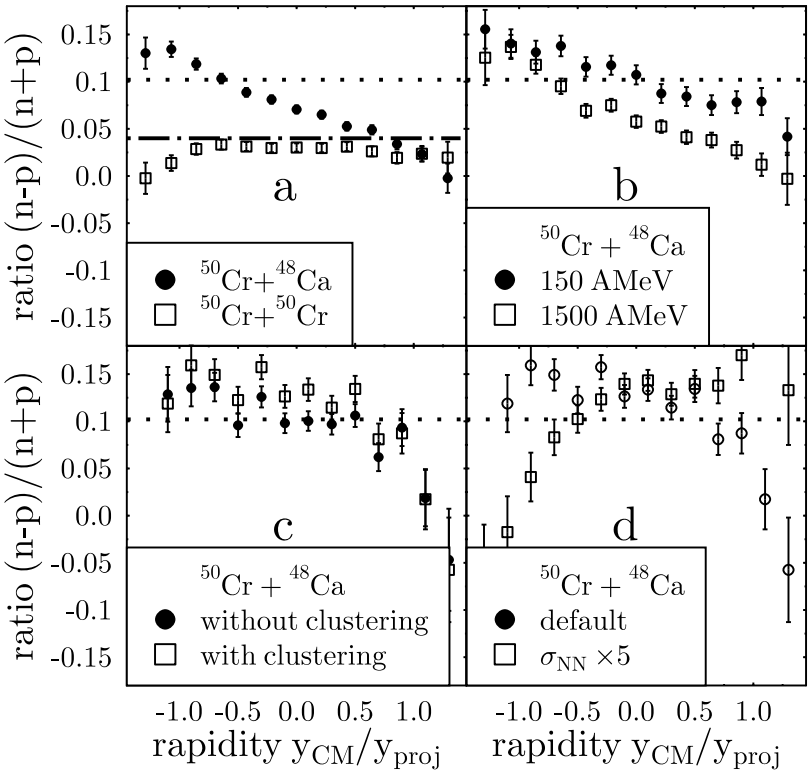

Figure 4.20: Neutron to proton asymmetry as obtained in IQMD model for ^{50}Cr+^{48}Ca and ^{50}Cr+^{50}Cr at 1 GeV/nucl. (a), for ^{50}Cr+^{48}Ca at 150 MeV/nucl. vs. 1.5 GeV/nucl. (b), for the same system without vs. with cluster subtraction (c) and with an enhanced (factor 5) cross section (d).

system ^{50}Cr+^{50}Cr, both at 1 GeV/nucleon. The horizontal lines mark the values expected for case (2) of fig. 4.19 for the isospin asymmetric (dotted) and symmetric system (dash-dotted). The calculations clearly indicate that projectile and target move through each other although the nucleon rapidity distribution (which usually characterizes stopping) shows a peak at c.m. rapidity. Figure 4.20b shows the energy dependence of the asymmetry. At 1.5 GeV/nucl. the transparency is far more pronounced than at 150 MeV/nucl. (which is within error bars almost compatible with case (2) of Fig. 4.19). However, Figs. (a) and (b) only show nucleons without taking clusterization into account. Fig. 4.20c compares an analysis based on (all) nucleons with the respective analysis in which clusters were subtracted (250 MeV/nucl. incident beam energy). The qualitative trends remain unchanged. In order to investigate the sensitivity of the asymmetry to the stopping power we have performed a calculation with a 5 times higher nucleon-nucleon cross section. Fig. 4.20d shows the respective calculation at 250 MeV/nucl. and compares it with the default calculation. A sign reversal in the slope of the asymmetry is visible.

Experimentally it may be easier to study the ^{3}He to triton ratio instead of the neutron to proton ratio. At beam energies above 1.5 GeV/nucl. the isospin content of the system is transferred to pionic degrees of freedom and the neutron to proton ratio looses its effectiveness.

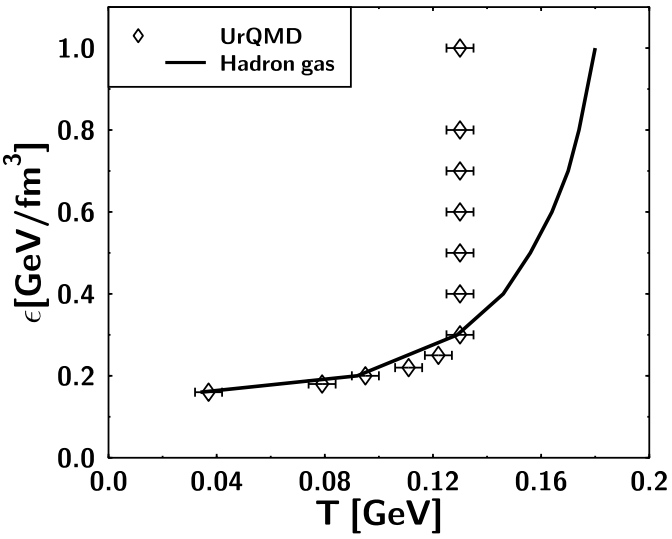

Figure 4.21: Equation of State $\epsilon = \epsilon(T)$ obtained in UrQMD box calculations (squares) and in ideal hadron gas (solid line) at normal nuclear matter density and zero strangeness.

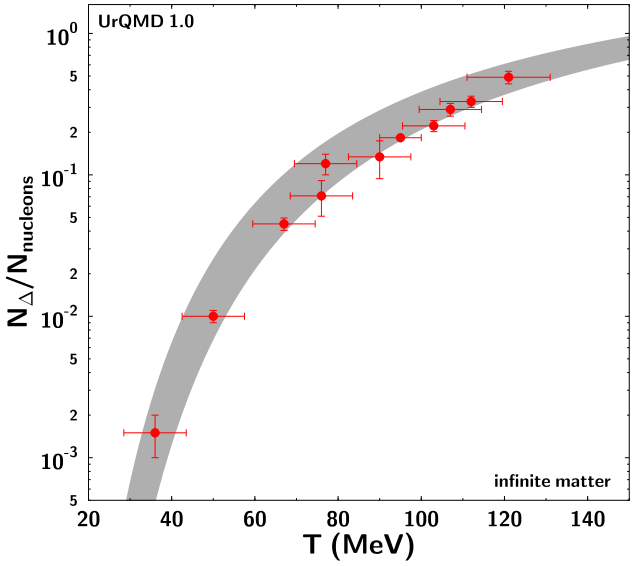

Figure 4.22: The delta to nucleon ratio vs. temperature as obtained in UrQMD infinite matter calculation. The gray dashed area shows the delta to nucleon ratio calculated from the law of mass action in a Boltzmann approximation, taking fluctuations in the delta mass into account.

4.2.4 Equilibrium properties of hadronic matter

The possibility of thermal and chemical equilibration of hadronic matter is studied using UrQMD box calculations with periodic boundary conditions for normal baryonic density and zero strangeness at different energy densities from $\epsilon = 0.2$ to 2.0 GeV/fm^3. Starting from a state of pure nucleons with random momentum distribution, one observes that particle multiplicities equilibrate after some time. At low energy density ϵ, equilibration times for strange particles are much larger than for non-strange particles, but this difference decreases with growing ϵ. In equilibrium, the energy spectra of the different hadronic species are nicely fitted by a Boltzmann distribution $\exp(-E/T)$ with the same temperature T. Figure 4.21 shows the variation of the temperature T versus energy density ϵ at $\rho_B = \rho_0$ and $\rho_S = 0$, obtained in UrQMD. The solid line shows the results of an ideal gas model including the same hadrons as UrQMD (tables 3.2 and 3.3). The UrQMD Equation of State shows a Hagedorn-like shape with a limiting temperature $T \approx 130$ MeV, while the hadron gas EoS shows a continuous rise of the temperature with ϵ. Both models are however in good agreement at low energy densities $\epsilon \leq 0.3$-0.35 GeV/fm^3. Because the UrQMD model uses a stochastic collision term, and no hard core repulsion is considered for the different particles (cascade mode), excluded volume correction is not included in the ideal gas formulation. This correction, however, could be significant [243] and could be treated in the Chappman-Enskog approximation.

In particular, the delta to nucleon ratio is consistent with the theoretical expectation of a hadron gas. This can be seen in figure 4.22 which displays the delta to nucleon ratio obtained at various energy densities ranging from 0.16 to 0.3 GeV/fm^3. The gray shaded area shows the delta to nucleon ratio calculated from the law of mass action in a Boltzmann approximation, taking fluctuations in the delta mass into account. At higher energy densities, despite the smaller temperature in UrQMD compared to ideal gas, the number of pions and other mesons is larger than in the Ideal Gas. The difference between the two models resides

in the string degrees of freedom included in UrQMD [244]. At high energy densities, they keep a large fraction of the system energy. Moreover, the inclusion of strings in UrQMD leads to a violation of the detailed balance at high energies, assumed in statistical model. Box calculations in a simplified version where no strings and no many-body decays were included, show a very good agreement with the ideal gas. They nicely reproduce both temperature slopes and different hadronic multiplicities [244].

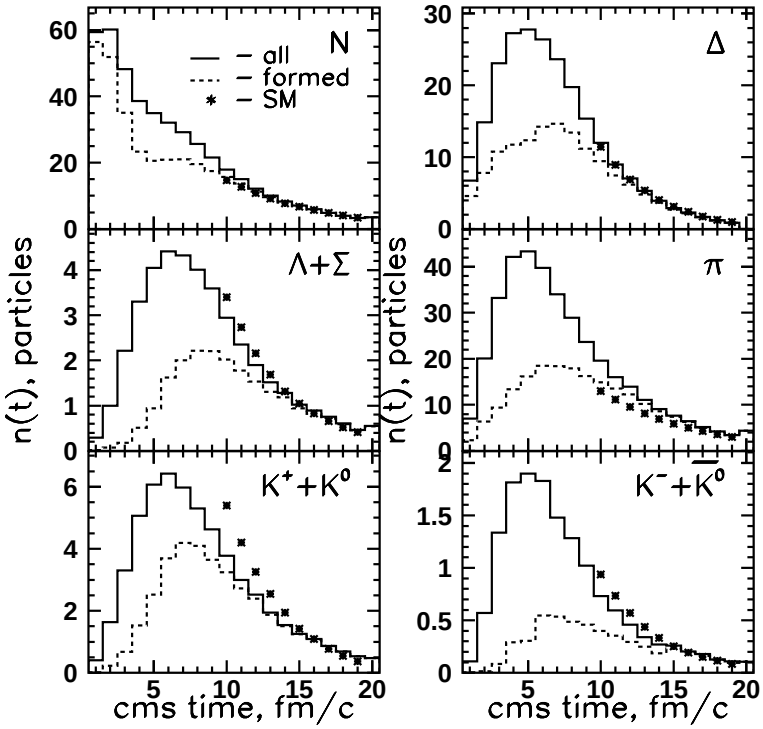

Figure 4.23: Number of particles as a function of cms time, obtained in the central zone ($5 \times 5 \times 5$ fm^3) of central (b =0) Au+Au collisions at 10.7 AGeV. Solid lines correspond to all hadrons in the zone, dashed lines - to only formed hadrons. Points are the predictions of ideal gas calculated at the same energy, baryonic and strangeness densities as in UrQMD full sample in the zone.

The possibility of local equilibration in Au+Au collisions at AGS energies (10.7 AGeV) is studied by analyzing the time evolution of hadronic matter in the central reaction zone [245]. It is found that between t_{cm} = 10 and 20 fm/c, there is an isotropic velocity distribution of hadrons in the central region. In this time interval, there are practically no strings left in this zone. Figure 4.23 shows the time evolution of different particle multiplicities in the central region. The solid lines correspond to the total number of particles for the different species, whereas the dashed lines show the multiplicities of only already formed particles (cf. section 3.3.5). The dots depict the results of the statistical model, obtained at the same ϵ, ρ_B and ρ_S as in the central zone of UrQMD calculation.

Baryonic density ρ_B drops from $\approx 2\rho_0$ at t_{cm} =10 fm/c to 0.5 ρ_0 at t_{cm} =15 fm/c. Energy spectra of the different species are nicely reproduced by Boltzmann distributions with the temperature predicted by the statistical model (fig. 4.24). The statistical model reproduces also the multiplicities of baryons and mesons obtained in UrQMD (fig. 4.25). One can see from fig. 4.21 that for the energy densities reached in the central zone of Au+Au collisions at AGS at these times (e.g. ϵ = 293 MeV/fm^3, $\rho_B = \rho_0$ and $\rho_S \approx 0$ for

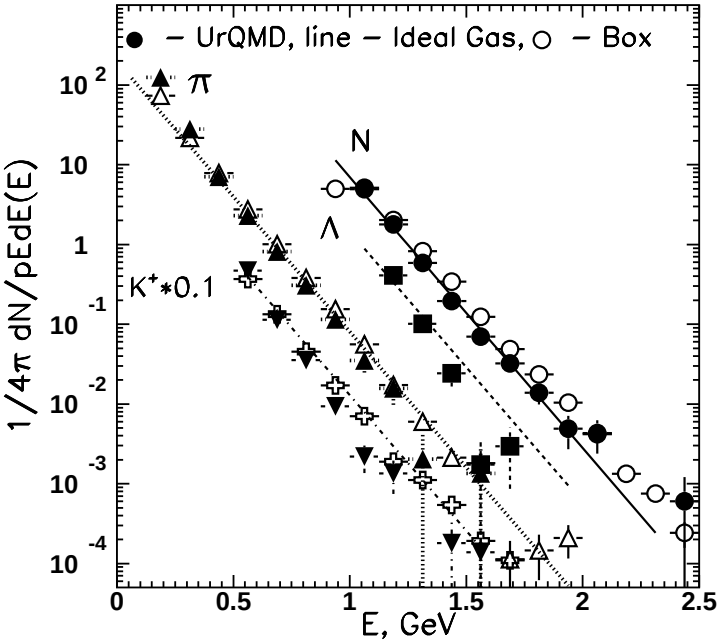

Figure 4.24: Energy spectra of N (•), Λ (□), π (△) and K^+ ($\bigtriangledown$) in central zone of Au+Au collisions at 10.7 AGeV at t_{cm}=13 fm/c fitted by Boltzmann distributions with parameters T=128 MeV, μ_B=534 MeV, μ_S = 112 MeV, predicted by the statistical model (lines) and obtained in UrQMD box calculations (open symbols).

t_{cm} =13 fm/c) the equation of state of the UrQMD model agrees quite well with that of the ideal resonance gas. The comparison with the equilibrated state obtained in box calculations at the same ϵ, ρ_B and ρ_S (fig. 4.24-4.25) also indicates that in the central zone of Au+Au collisions, one probably reaches local chemical and thermal equilibrium. However, the existence of collective flow [239, 246] as well the analysis of the freeze-out properties of nucleons, hyperons and various meson species in section 4.2.7 indicate that the final state does not originate from an equilibrium configuration. One therefore has to be very careful when trying to draw conclusions from the existence of a local zone of hadrochemical equilibrium to the final state of the reaction.

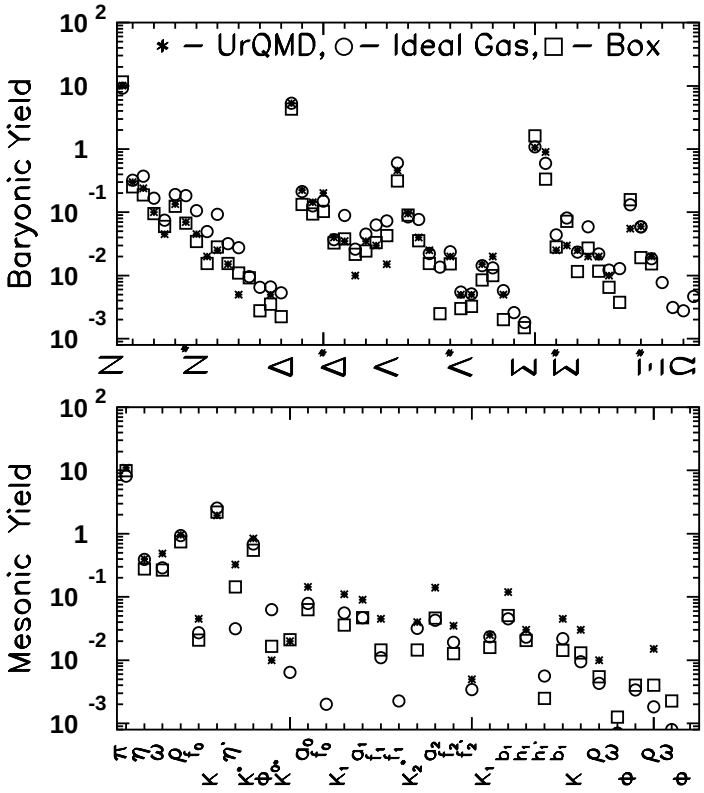

Figure 4.25: Yields of hadrons obtained in central zone of Au+Au collisions at t_{cm}=13 fm/c (*), in statistical model (◯) and in UrQMD box calculations (□).

4.2.5 Resonance matter

The possibility of producing Δ-*matter* (or in more general terms: *resonance matter*) and density isomers has been already discussed early on [14, 2]. Recently this topic has received renewed attention [247, 248, 249, 250, 251, 252, 253]: At beam energies above a few hundred MeV/nucleon, the nucleons can be excited into Δ-resonances. If the density of these resonances is as high as the nuclear matter ground state density, then a new state of matter, Δ-*matter*, has been created. One of the potential signals for the presence of Δ-*matter* is the creation of pions as decay products of the Δ-resonance.

How can Δ-*matter* be produced? In order to address this question we first limit ourselves to Au+Au collisions at 1 GeV/nucleon. In that case the hadrochemistry is well described by a simple closed system of nucleons, pions and the Δ_{1232} resonance:

Figure 4.26 shows the pion – nucleon cycle in the IQMD model, which is limited to nucleons, pions and the Δ_{1232} resonance. The scheme describes (for impact parameters b $\leq$ 5 fm and averaged over 60 fm/c possible processes linked to the creation of Δ-*matter*. The probabilities in the boxes always refer to the vertices they are directly connected with. Δ-resonances are initially produced via inelastic nucleon nucleon scattering. The produced resonances can either be reabsorbed via inelastic scattering or decay by emitting a pion. The pion can then either *freeze out* or interact with a nucleon to form a Δ again. In case the Δ has been absorbed the corresponding high energetic nucleon might have a second chance of becoming a Δ by inelastic scattering. It could also transfer energy via elastic scattering onto another nucleon which then could scatter inelastically and form a new Δ. A nucleon interacts in the average about three times before it freezes out. This value fluctuates considerably, depending on whether the nucleon was in the participant zone (geometrical overlap of the colliding heavy ions) or in the spectator zone of the collision.

Unfortunately, the probability for a nucleon to undergo inelastic scattering and to form a Δ during the heavy ion collision at 1 GeV/nucleon is as low as 10%. The main process for sustaining Δ-*matter* is the $\Delta \rightarrow N\pi \rightarrow \Delta$ loop, which, however, first has to be fueled by the $NN \rightarrow \Delta N$ process. The average pion passes approximately three times through this loop (it has been created by the decay of a *hard* Δ). However, 30% pass more than 6 times through the loop. For nucleons the probability of forming a *soft* Δ i.e. via $\pi N \rightarrow \Delta$ is almost twice as high (Δ-*matter pump*) than the probability of forming a *hard* Δ via $NN \rightarrow N\Delta$. This picture is however much more complicated when going towards higher energies and higher resonances are considered. We show for example in fig. 4.27, the N^*_{1535}-pump (time integrated) as obtained in UrQMD calculations for Ni + Ni collisions at 2 GeV/nucleon. One sees from the figure that only half of η-mesons produced at this energy are coming from N^*_{1535} decays. The other half comes mainly from meson-baryon collisions like $N\pi \longrightarrow \Delta\eta$ or from other resonances like the N^*_{1710}.

Figure 4.28a shows the IQMD time evolution of the total baryon, nucleon and Δ densities in units of ρ/ρ_0 for Au+Au collisions at 1 GeV/nucleon. The densities are calculated in a sphere of 2 fm radius around the collision center. Between 5 and 20 fm/c more than 20 Δ-resonances can be found in the whole system: This time interval coincides with the hot and dense reaction phase. At 10 fm/c up to 55 resonances are present in the *total* reaction volume (keep in mind this is *not* in the 2 fm test sphere). A Δ multiplicity of > 40 can be sustained for an interval of 10 fm/c, 6 times longer than the lifetime of a free Δ-resonance. However, this is not pure Δ-*matter*: in the small *test* volume shown in figure 4.28a the resonance *density* is 0.5 ρ_0 and the nucleon density is 2.2 ρ_0: the Δ-contribution is 20% in the test volume which contains, as a matter of fact, only 2.5 resonances. The total multiplicity of Δ resonances is just about 10% of the total nucleon multiplicity.

However, it is obvious that the other Δs can be distributed all over the reaction volume. Figure 4.28b shows the Δ density distribution as experienced by the Δ's in the system at 5, 10 and 20 fm/c.

The densities were calculated by summing over all contributing Gaussians of all Δs in the system at the locations of the respective Δs. We would like to point out that the mean Δ-density experienced by the Δs is about 0.25 ρ_0. Less than 1% of the Δs experience Δ densities around 0.5 ρ_0. Δs show *collective flow* in the reaction plane. Its measurable signature (the pion $\boldsymbol{p_x}(y)$ distribution in central collisions) is discussed in section 4.3.1.

At AGS energies, however, RQMD calculations predict an excited state of baryonic matter, dominated by the Δ_{1232} resonance. Analysis show a long apparent lifetime ($>$ 10 fm/c) and a rather large volume (several 100 fm^3) for this Δ matter state in central Au+Au collisions at the AGS [254] (see figure 4.29). At higher energies (SPS), UrQMD calculations shown in fig. 4.30, indicate that in the early stages of the reaction, about 75% of baryons are excited resonances (among which 55% are nucleon and delta resonances and 20% are hyperons). This fraction is even higher at mid-rapidity (about 85%). The excited hyperons are created in the first 3 fm/c and remain almost constant for the whole propagation. This fast strangeness equilibration is different from the time scales for strangeness equilibration predicted by UrQMD box calculations at an energy density equivalent to that obtained in the central region of a Au+Au collision at 160 GeV/nucleon [255]. Because of the large fraction of hyperons during the whole propagation, there is a finite probability for the formation of hyperon clusters (hyperon-matter).

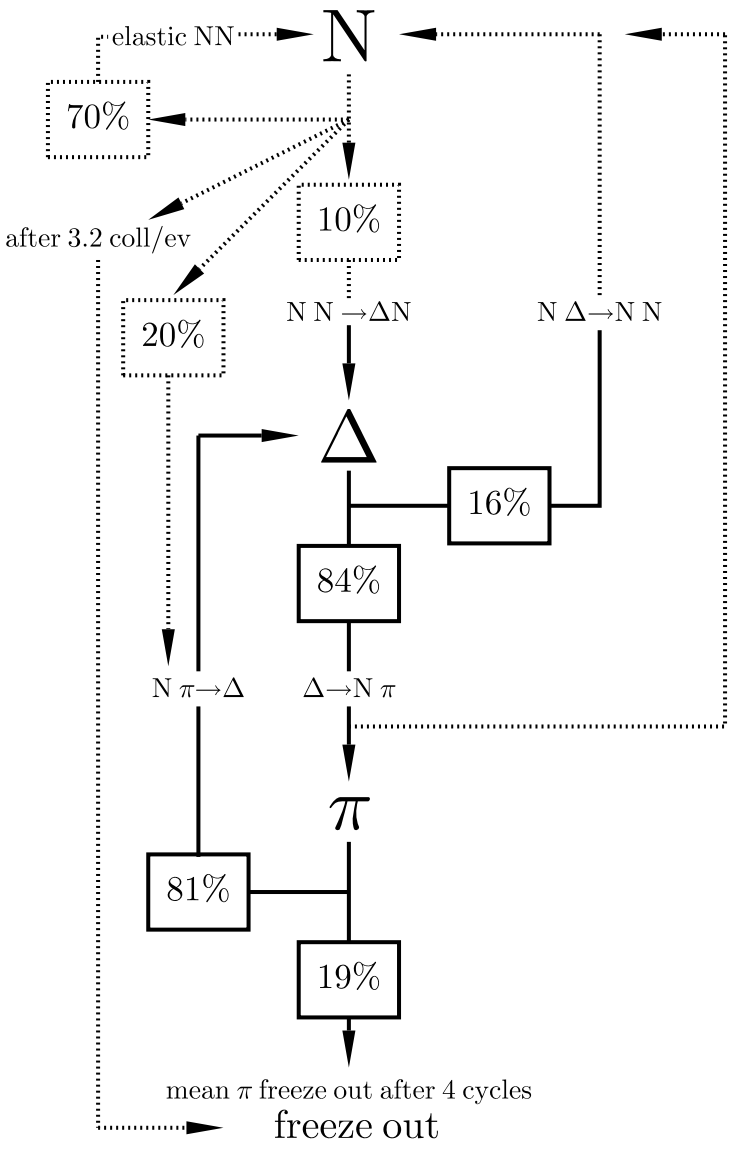

Figure 4.26: Pion - nucleon cycle in the IQMD model for Au+Au collisions at 1 GeV/nucleon. The scheme describes (for b $\leq$ 5 fm and time-averaged) all possible processes (in the IQMD model) linked to the creation of Δ-*matter*. The probabilities in the boxes always refer to the vertices they are directly connected with. The main process for sustaining Δ-*matter* is the $\Delta \rightarrow N\pi \rightarrow \Delta$ loop, which, however,first has to be fueled by the $NN \rightarrow \Delta N$ process.

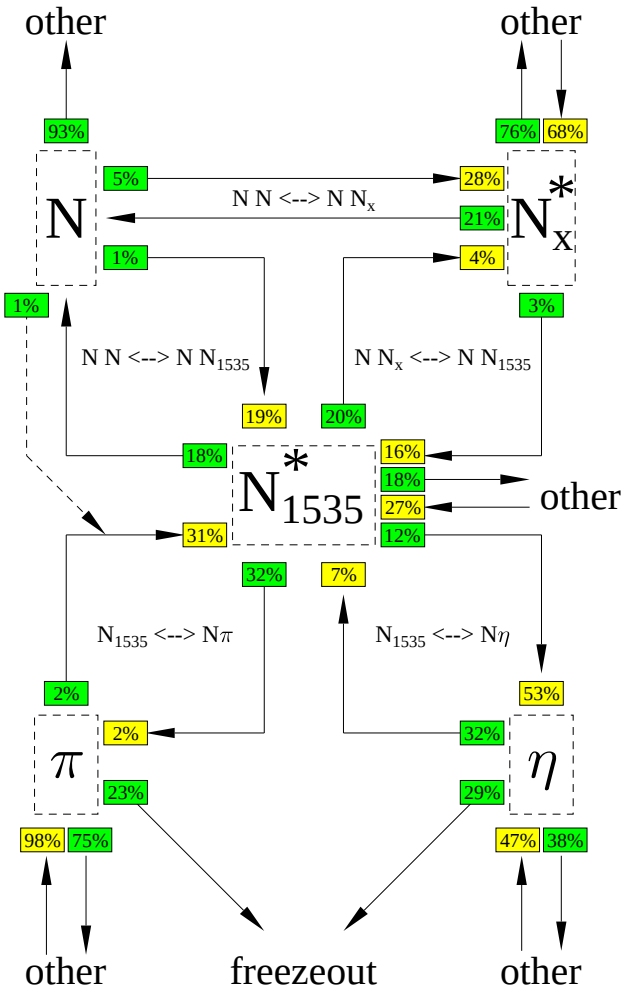

Figure 4.27: N^*_{1535}-pump as obtained in UrQMD calculations for Ni + Ni collisions at 2 GeV/nucleon. The scheme describes (for b $\leq$ 5 fm and time-averaged) all possible processes linked to the creation of N^*_{1535}. The probabilities in the boxes always refer to the vertices they are directly connected with.

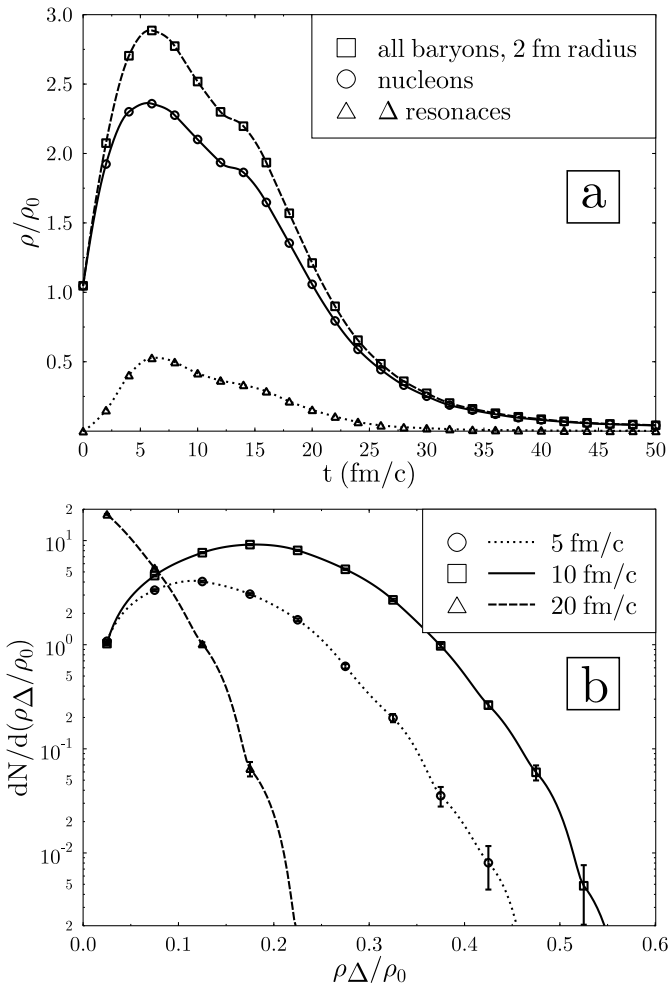

Figure 4.28: IQMD time evolution of the total baryon, nucleon and Δ-resonance density in units of ρ/ρ_0 (a) and Δ density distribution the respective Δs experience for 5, 10 and 20 fm/c (b) for Au+Au collisions at 1 GeV/nucleon. The densities in the upper frame (a) are calculated in a sphere of 2 fm radius around the collision center. The densities in the lower frame (b) were calculated by summing over all contributing Gaussians of all Δ's in the system at the locations of the respective Δ's.

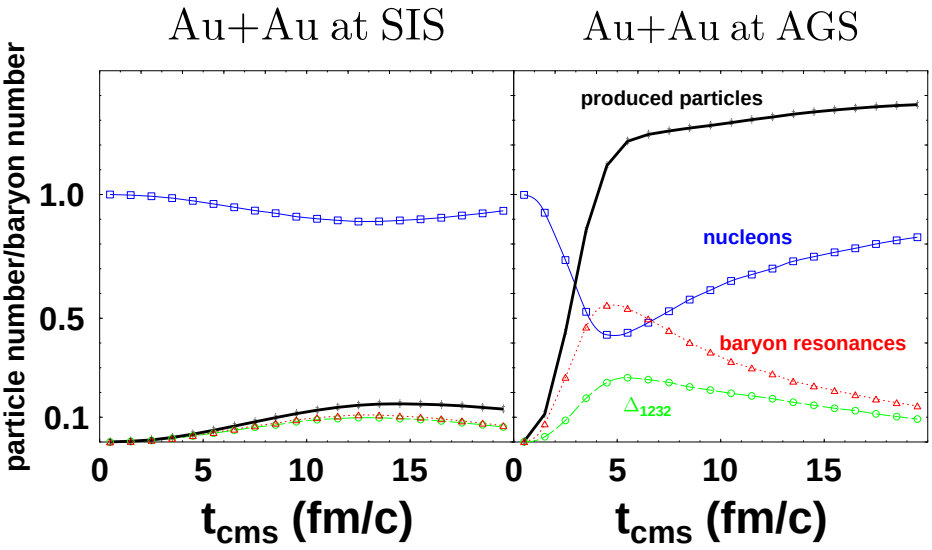

Figure 4.29: Time evolution of particle multiplicities (scaled with the number of incident nucleons) for central Au+Au collisions at 1 GeV/nucleon (SIS) and at 10.6 GeV/nucleon (AGS). At SIS energies, only about 10% of the nucleons are excited to resonances whereas at AGS energies the degree of excitation exceeds 50%. For a time-span of up to 10 fm/c the baryons are in a state of $\Delta-$matter. The figure has been taken from [254].

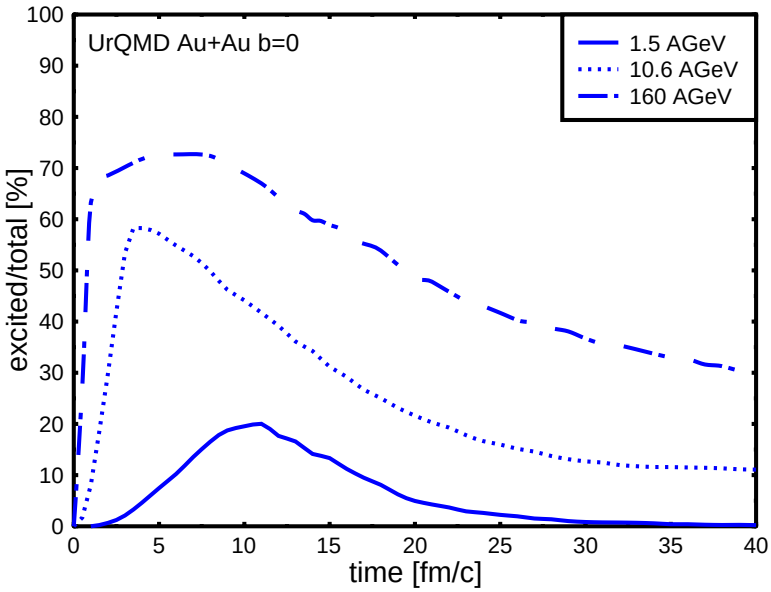

Figure 4.30: Fraction of excited resonances vs. time for central Au+Au collisions at SIS (solid line), AGS (dotted line) and SPS (dashed-dotted line) energies.

4.2.6 Antimatter and strange matter

As mentioned above, the dominant reaction mechanism in the early stage of a reaction is the excitation of collision partners to resonances or strings [37]. Then secondary interactions, i. e. the annihilation of produced mesons on baryons, lead also to the formation of s channel resonances or strings, which may explain the strangeness enrichment [184, 185, 160] and (for masses larger than $3m_N$) allow for $\overline{N}N$ creation [190]. It is clear, however, that any subsequent interaction of the newly produced particle can change the final yields and spectra, which has to be taken into account. E.g. the escape probability for $\bar{p}$'s from the exploding nuclear matter enters into microscopic models usually via the free $N\overline{N}$ annihilation cross section.

The two counter–acting effects (production vs. absorption) may be measured by the directed "antiflow" of antimatter. Varying the formation time τ, i. e. applying $\tau = 6$ fm/c instead of the default string fragmentation formation time ($\tau_{(\text{anti}-)\text{baryons}} \approx 1.5$ fm/c) reduces the absorption from ≈ 90 % to ≈ 50 % and the flow (to one half) for heavy systems.

The observable asymmetry for antimatter can be quantified by dividing the yields of the upper and lower hemispheres for target and projectile rapidity separately. The ratio $R = \frac{\phi^{\bar{\text{p}}} < 90^\circ|_{y<y_{\text{mid}}} + \phi^{\bar{\text{p}}} > 90^\circ|_{y>y_{\text{mid}}}}{\phi^{\bar{\text{p}}} > 90^\circ|_{y<y_{\text{mid}}} + \phi^{\bar{\text{p}}} < 90^\circ|_{y>y_{\text{mid}}}}$ then gives the probability for a *single* particle to follow the *collective* (directed) flow. The following table shows the sensitivity of the azimuthal asymmetry R and the antiflow–parameter (the mean p_x, integrated over the whole target or projectile rapidity) on the impact parameter for Au+Au reactions at 10.7 GeV/u within the RQMD model. The anti–flow of antiprotons appears to be strongest for semi-central collisions of $b \approx 5 - 7$ fm, while for protons the maximum p_x is at considerably smaller b–values. The latter is due to the pressure (i. e. the EoS), the former one due to absorption and geometry. A similar absorption mechanism is at work for all hadrons with valence anti-quarks, e.g. π's and anti-kaons, resulting in mesonic anti-flow as depicted in Fig. 4.31.

b[fm]	0	2.5	5.0	7.5	10.0	12.5	15.0
R	$\simeq$ 1:1	1:1.47	1:1.78	1:1.70	1:1.54	1:1.28	1:1.17
$< p_x^{\text{dir}} >$ [MeV/c]	$\simeq 0$	100	150	159	119	53	30

Now, let us turn to even more complex and sensitive observables, e.g. *clusters* of antinucleons. The antideuteron formation rate ($\overline{d}/\overline{p}^2$–ratio) in Si+Au collisions at the AGS is sensitive to the shape and size of the antinucleon source [257, 258]. It is different from the nucleon source. Annihilation strongly distorts a homogeneous coordinate space distribution of antibaryons. Asymmetric phase space distributions of anticlusters result for finite impact parameter b, visible as directed transverse anti–flow (fig. 4.32). Antimatter cluster formation is strongly suppressed.

In analogy to the deuteron case (see figure 4.12), the (anti-)deuteron formation is calculated by projecting the (anti-)nucleon pair phase space distribution on the (anti-)deuteron wave function via the Wigner–function method. The (anti-)deuteron Wigner–density ($\rho_{\overline{d}}^{\text{W}}$) is again given by the Wigner–transformed Hulthen wave function. Thus the recently measured Si(14.6AGeV)Au antideuteron data at the AGS [259] can be reproduced!

Fig. 4.33 shows the calculated coordinate space distribution of mid-rapidity antideuterons in a cut perpendicular to the reaction plane for the Au(10.7 AGeV)+Au, $b = 5$ fm reaction. Anti-matter is only emitted from the surface of the fireball – i.e. the region of hot and dense matter – in clear contrast to the source of baryons, which spreads over the whole reaction volume. This can be understood as a consequence of antibaryon absorption, which produces deep cuts in the momentum- and even more so in the coordinate space distribution of the antibaryons at freeze-out [190, 258]. $\overline{p}$'s in–plane are shadowed more effectively due to the presence of spectator matter. This leads to an antimatter cluster squeeze–out.

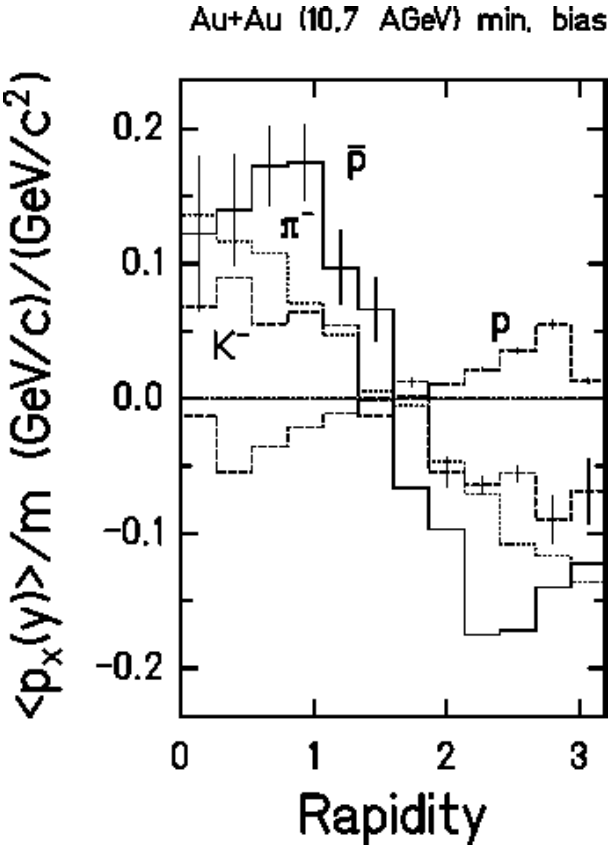

Figure 4.31: Mean directed transverse momentum (in–plane) of various hadrons in Au+Au collisions at 10 GeV/u as a function of rapidity (RQMD calculation). Fig. taken from [190].

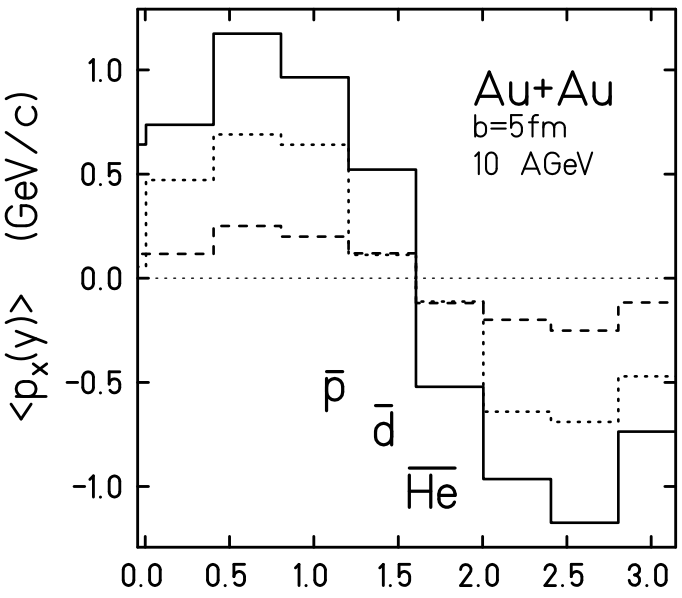

Figure 4.32: Mean directed transverse momentum (in–plane) of anti–clusters in Au+Au collisions at 10 GeV/u as a function of rapidity (RQMD calculation). Fig. taken from [256].

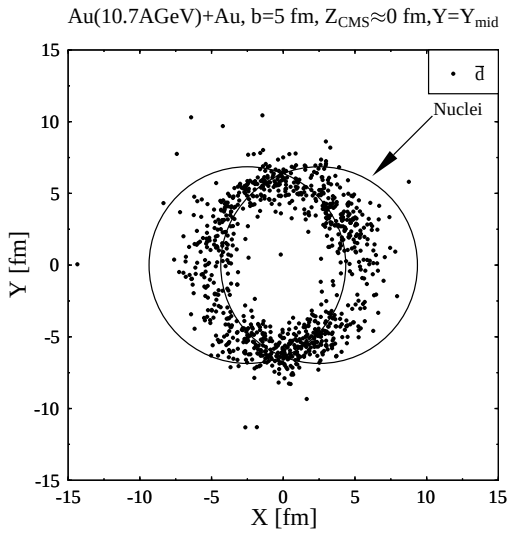

Figure 4.33: Coordinate space distribution of mid-rapidity anti-deuterons as obtained in RQMD calculations for the reaction Au(10.7 AGeV)+Au at freeze-out in a cut perpendicular to the reaction plane. (Fig. taken from [260])

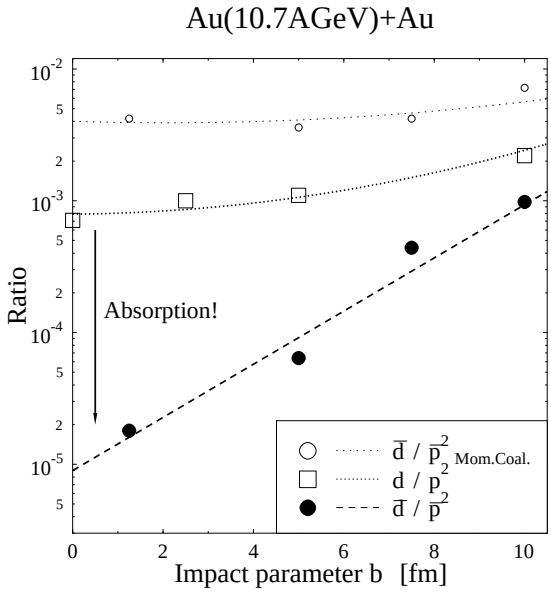

Figure 4.34: Impact parameter dependence of the anti-deuteron to the anti-proton ratio squared (full circles) and of the deuteron to the proton ratio squared (open squares) both at mid-rapidity. Open circles: the result of a simple momentum coalescence model. (Fig. taken from [260])

Let us explore the reaction volume dependence of the (anti-)deuteron formation by varying b as shown in fig. 4.34 ($\overline{d}/\overline{p}^2$-ratio, full circles). The deuteron formation rate (d/p^2-ratio, open squares) is proportional to V^{-1}. Those rates measure the average phase–space distance of N and $\overline{N}$'s, respectively.

In central collisions up to 95% of the initially produced antinucleons are reabsorbed.

The $\overline{d}$ formation rate is predicted to be roughly two orders of magnitude lower than the formation rate of deuterons. This difference vanishes when going to high impact parameters or small systems (like Si+Al). The assumption of the independent production of both antinucleons becomes less justified in very small systems. Calculating the antideuteron formation rate within a momentum coalescence model with a Δp–parameter of 120 MeV ($\overline{d}/\overline{p}^2$-ratio, open circles) one finds only small sensitivity to the chosen impact parameter. This proves the pure coordinate space nature of the effect.

Fig. 4.35 shows the azimuthal distribution of mid-rapidity $\bar{p}$, $\bar{d}$, $\bar{t}$ in peripheral Au+Au collisions. The momentum distribution of $\overline{p}$ in the $p_x - p_y$-plane is nearly isotropic. It reflects the geometry of the almond shaped reaction zone. In contrast the $\overline{d}$ distribution is shifted towards $\phi = 90°$ in line with the described coordinate space distribution of the $\overline{d}$. This looks like a squeeze-out effect. It is even more pronounced for $\overline{t}$.

The predicted reaction volume dependence and the squeeze-out of anti–fragments reflect the spatial distribution of antibaryons. This suppression of antideuterons may mask a possible antimatter cluster enhancement in a quark–gluon plasma event [261].

An enhancement of the production of anti-nucleons due to the presence of relativistic mean fields was predicted in [177, 262]. It has been calculated in the framework of RBUU [179, 180], QMD [181] and

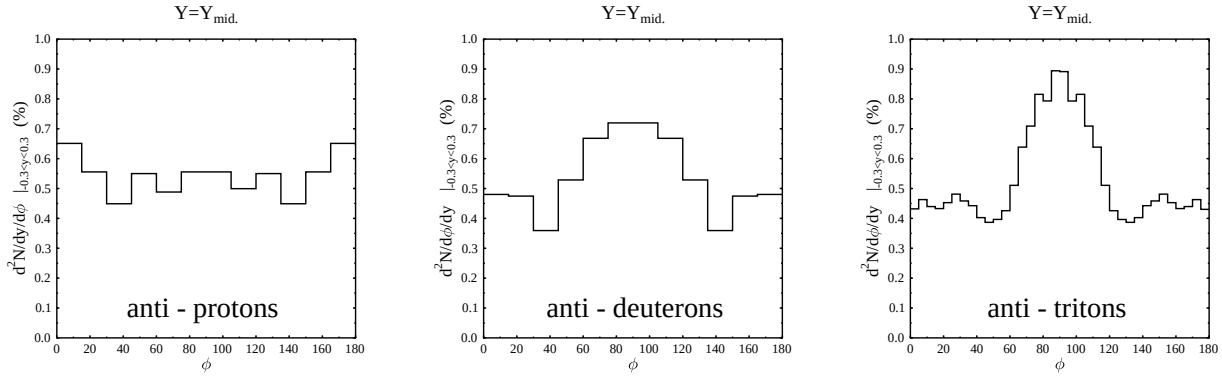

Figure 4.35: Correlations of antiprotons lead to a squeeze-out for $\overline{d}$ and $\overline{t}$ in peripheral Au(10.7AGeV)+Au reactions due to a higher anticluster formation probability at the ends of the almond shaped fireball (RQMD calculation). Fig. taken from [260].

RVUU [182] that enhanced antiproton production due to reduced effective masses may explain subthreshold antiproton measurements at SIS energies. On the other hand, these transport model calculations show that most of the additional anti-nucleons get reabsorbed. The absorption rate is much higher than in a cascade without mean fields [183], because this additional production mechanism is most effective in regions of high baryon density and because of the additional attractive interaction between nucleons and anti-nucleons.

Enhanced production of anti-nucleons due to mean fields or a quark-gluon plasma phase is conceivable at higher energies, i.e. at AGS and SPS, too. However, UrQMD calculations of a Si-Al collision at E_{lab} = 13.7 GeV/nucleon [263] without mean fields indicate that even at these energies, an enhanced production of anti-nucleons will be difficult to observe. Figure 4.36 shows the time evolution of 16 anti-nucleons ($8 \cdot \bar{p},\ 8 \cdot \bar{n}$) that are added by hand after 4 fm/c in the central region of the collision. One can see that nearly no anti-nucleon survives the further evolution of the system (less than 4%). In Au+Au collisions, where higher baryon densities are predicted, all additional anti-nucleons are reabsorbed after 1-2 fm/c.

We have learned that $\overline{N}$'s suffer strong final–state interactions. These interactions have in principle two components which can be related to the $\overline{N}$ self–energy in matter: collisions and annihilation on baryons[264] (imaginary part, semi-classically given by 2 Im $V = \sigma v \rho$) and a piece in the real part (Re$V = t_{\rm NN}\rho$ in the impulse approximation). In the semi-classical limit the real part of the self-energy can be approximated by potential–type interaction[265, 266] or a mean field.

Here we will focus on the effect of the real part. The motivation is that the long–range force of baryons acting on a $\bar{p}$ is expected to be stronger than for protons since the Lorentz–scalar and the Lorentz–vector parts of a meson exchange potential now have the same sign. The influence of baryonic mean–fields on baryons and mesons is well established. Therefore there should also be some influence on $\bar{p}$'s.

The strong *imaginary* part of the optical $\bar{N}N$–potential has been taken into account by using the geometric annihilation cross section. The *real* part may also be substantial [267]. However, it would be fatal to "improve" the description by just adding a mean field interaction, since a part of the real potential has already been taken into account by the (parameterized) free elastic and inelastic cross sections. Fig. 4.37

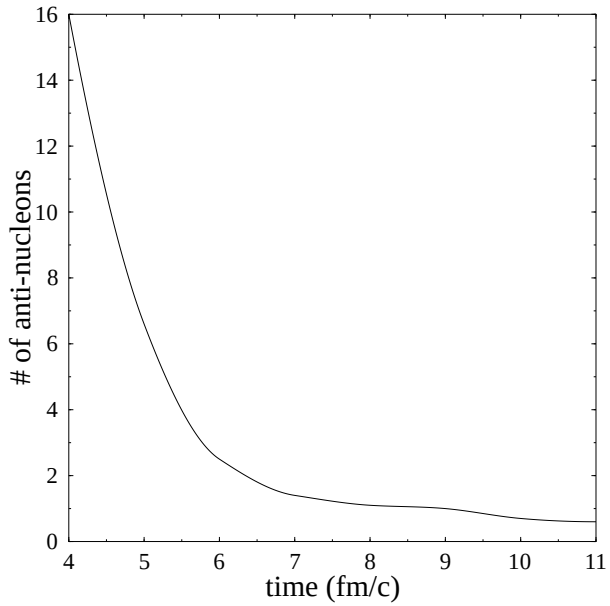

Figure 4.36: Time evolution of 16 anti-nucleons ($8 \cdot \bar{p},\ 8 \cdot \bar{n}$) in a Si-Al collision at $E_{lab} = 13.7$ GeV/nucleon calculated in the UrQMD-model (see text).

shows this effect for our model potential. Due to the strong attraction for the $\bar{B}B$ case, a reduced geometric annihilation cross section suffices to account for the measured free annihilation probability in binary $\bar{p}p$ reactions. To avoid the inevitable double counting in fully dynamical calculations this must not be neglected. In the case of a homogeneous nuclear medium the attractive potentials can partly cancel, leaving only the geometrical cross section effective for $\bar{N}$ annihilation. The importance of the real potential for the annihilation cross section results in an additional uncertainty of the $\bar{Y}$ and $\bar{\Delta}$ annihilation probabilities, since the real part of the self-energy is even less known than for $\bar{p}$'s. This should be taken into account for the analyses of (preliminary) reports of surprisingly high $\bar{\Lambda}/\bar{p}$ ratios at AGS and SPS experiments [268, 269, 270].

As a first step, we restrict our study on the residual potential interaction with its finite range to the dynamics *after* the hadronic freeze–out. The success of Dirac equation optical model calculations for pA scattering [271] leads us to using these relativistic potentials with Yukawa functions as interaction form factors— applying G–parity transformation — for the $\overline{p}$ case: The mass parameters are $\mu_V = 3.952$ fm^{-1} and $\mu_S = 2.787$ fm^{-1}, the coupling constants are $g_V = 2674.5$ MeV fm and $g_S = 2158.2$MeV fm. In line with [271] Gaussians are used as baryon profiles with a mean square radius of 0.8 fm. The central part of an effective Schrödinger equivalent potential (SEP) is constructed from the above potentials:

$$U_{\rm SE} = \frac{1}{2E}(2EU_V + 2mU_S - U_V^2 + U_S^2) \quad , \tag{4.6}$$

where E is the total energy of the incident particle.

For small $\overline{N}N$ distances the real potential should not show an effect, since the huge imaginary part absorbs the particular $\overline{p}$ anyhow. We have chosen 1.5 fm as cutoff distance corresponding to an averaged $\overline{p}p$-annihilation cross section of ≈ 70 mb.

The Schrödinger equivalent potential with the above parameters results in a mean $\overline{p}$-potential in nuclear matter of about -250 MeV ($p_{\overline{p}} = 0$ GeV/c), increasing with energy towards -170 MeV at $p_{\overline{p}} = 1$ GeV/c. The actual (averaged) SE-potential of the $\overline{p}$'s at freeze–out is about -70 MeV.

Due to the strong momentum dependence of the $\overline{p}p$-annihilation cross section, $\overline{p}$'s with low transverse momentum are suppressed in RQMD 1.07. Figure 4.38 shows the invariant multiplicity of $\overline{p}$'s with $p_t <$ 200 MeV for central collisions of Au+Au at 10.7 AGeV. Calculations with and without potentials are compared to preliminary data of the E878 collaboration[272]. Besides the proposed model interaction we calculated the effect for the same potentials, arbitrarily reduced by 50 %. Still the dip at mid-rapidity vanishes although the change is less pronounced.

Note that the p_t-integrated spectrum is not considerably affected by the potential interaction, but the final phase space distribution of the $\overline{p}$'s at low–p_t deviates substantially from the standard RQMD calculation: A clearly non-thermal spectrum with a dip at mid-rapidity for $p_t = 0$ gets distorted by the potential interaction during the last stage of the collision. Up to now, the possible influence on the formation of anti–clusters, which have just proved to be a delicate probe of the final phase–space distribution, is unclear.

Mean-fields are not only expected to influence the phase space distributions of hadrons, but also might have a strong impact on the production probabilities (see above). Relativistic meson-field models, which, at high temperature $T_{\rm C} \approx 180$ MeV qualitatively simulate chiral behavior of the nuclear matter, exhibit a transition into a phase of massless baryons [275]. Every (anti-)baryon species (hyperons included [25]) shows approximately the number density of normal nuclear matter ($\rho_0 \approx 0.16$ fm^{-3}) near $T_{\rm C}$. Thus, the fraction of (anti-)strange hyperons increases by 1-2 orders of magnitude at $T_{\rm C}$. Several hundred (anti-)baryons, the majority being (anti-)hyperons, may then fill the hot mid-rapidity region. Fig. 4.39 shows this transition for (anti-)nucleons and (anti-)hyperons at μ_q=100 MeV. Above $T_{\rm C}$ all effective masses

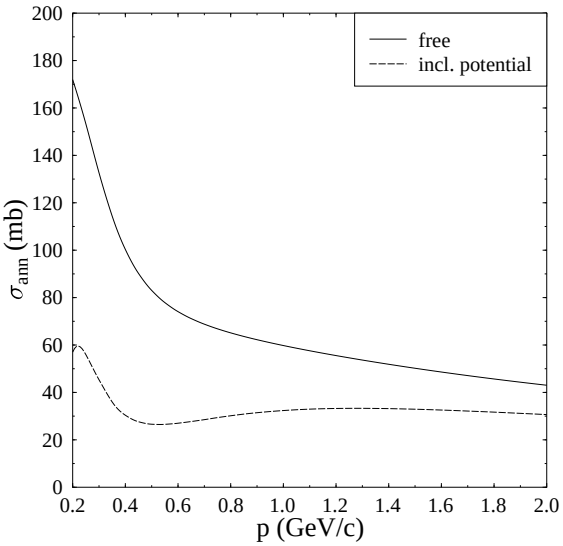

Figure 4.37: $\overline{p}p$ annihilation cross section as a function of the lab-momentum. Parameterization of the free measured cross section (full line) and the corrected value, if the described potential interaction is added (dashed line). (Fig. taken from [273])

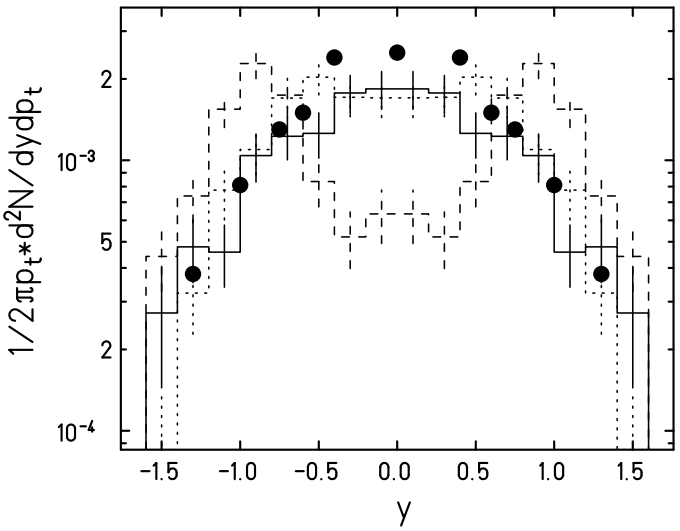

Figure 4.38: Invariant rapidity–distribution of the $\overline{p}$'s with $p_t < 200$ MeV for Au+Au ($b < 4$ fm) at 10.7 GeV/u. Shown is the RQMD calculation (dashed line), with the additional optical potential (full line) and the 50 % reduced potential (points). Preliminary data (full circles) from [272]. (Fig. taken from [274])

are small and the relative yields in the medium are dictated by the isospin degeneracy, thus favoring (anti-)hyperonic matter. This scenario could enhance the production probability of (anti–)hyperons. Even the formation of meta-stable exotic multi-strange objects (MEMO's [25]) is conceivable via this mechanism. However, the high temperature will suppress the formation of clusters of mass A by $e^{-A(m-\mu_B)/T}$.

It was speculated that strange matter might exist either as meta-stable exotic multi-strange objects (MEMO's [25]) or in form of *strangelets*. MEMO's are baryonic clusters which contain hyperons, thus constituting lumps of hypermatter. Strangelets, on the other hand, can be thought of as (meta-)stable multi-strange quark clusters [28, 29, 276].

The possible creation — in heavy ion collisions — of long-lived remnants of the quark-gluon-plasma, cooled and charged up with strangeness by the emission of pions and kaons, was proposed in [33, 277, 278, 279]. Strangelets can serve as signatures for the creation of a quark gluon plasma. The detection of strangelets would verify exciting theoretical ideas with consequences for our knowledge of the evolution of the early universe [30, 31], the dynamics of supernova explosions and the underlying theory of strong interactions. Currently, both at the BNL-AGS and at the CERN-SPS, experiments are carried out to search for MEMO's and strangelets, e. g. by the E864, E878 and the NA52 collaborations [280, 269].

The production of strangelets and anti-strangelets might be possible via the strangelet distillation mechanism [278, 279] if low values of the bag-constant $B^{1/4} \leq 180MeV$ are assumed. However hadronic ratios at SPS energies can be reproduced with the same hadronization model only under the assumption of a bag constant of $B^{1/4} \geq 230MeV$ [281] (see also [223, 224, 282]). This would exclude the formation of meta-stable strangelets within this model.

Be also reminded that the question, whether strangelets or MEMO's can exist as bound states at all, is very speculative and thus still a controversial point, on which we did not focus here. Special (meta-)stable candidates for experimental searches are the quark-alpha [32] with $A_B = 6$ and the H-Dibaryon with $A_B = 2$ [283].

4.2.7 Particle freeze-out

The previous sections have dealt with the description of the final state of heavy ion reactions. Different analyses of data at AGS and CERN/SPS energies have shown that the experimental results may be described as a transversally and longitudinally expanding chemically and thermally equilibrated hadron-gas [217, 220, 221, 284]. The assumption of a chemically and thermally equilibrated source, however, implies a uniform freeze-out for all particles; i.e. all particle species have the same freeze-out times, radii and densities. Such a scenario is easily tested in the framework of a microscopic calculation. This section therefore deals with the investigation of freeze out properties of different particle species in the framework of microscopic transport models and investigates model-independent methods to gain access to freeze-out information contained in the final state of the heavy ion reaction.

Figure 4.40 shows the time-evolution of the baryon density at the collision center and of the total strangeness per particle (i.e. the sum of $\bar{s}$ and s quarks per particle) for Au+Au reactions at 2, 10.6 and 160 GeV/nucleon. The time-axis has been scaled in order to synchronize the time-evolution to the time of maximum baryon-density. At 2 GeV/nucleon only about 50% of the total strangeness has been produced. It saturates first in the late stages of the reaction at $\approx 1.4\rho/\rho_0$. At AGS energies already 60% of the total strangeness has been produced at the point of maximum density – saturation again takes places at $\approx 1.5\rho/\rho_0$. Between SIS- and AGS-energies no significant differences are visible for the time-evolution of strangeness saturation. At SIS- and low AGS-energies the dominant production mechanisms for strangeness are multi-step excitation of heavy resonances and their subsequent decay into a hyperon and a kaon. At AGS-energies string excitation may also contribute to strangeness production, but is not

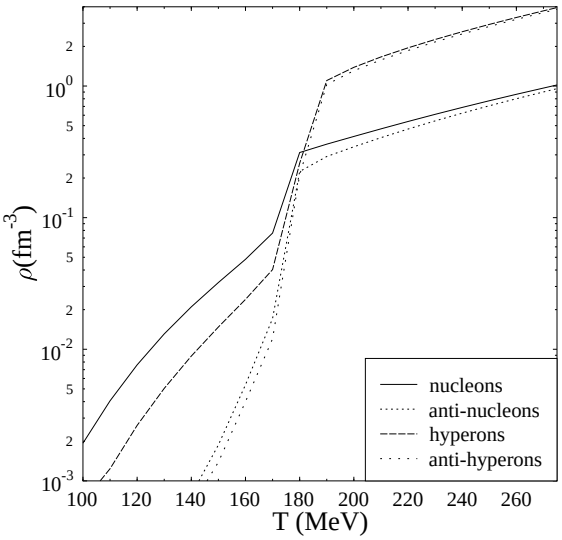

Figure 4.39: Densities of (anti–)nucleons and (anti–)hyperons as functions of temperature for fixed $\mu_q = 100$ MeV and strangeness fraction $f_s = 0$, calculated with a relativistic meson–baryon field theory (RMF) which implements hyperon–hyperon interactions (figure taken from [34]).

yet a dominant factor. The situation changes for SPS-energies: Here already 75% percent of the total strangeness is produced at the time of maximum baryon density and saturation takes place at $\approx 3\rho/\rho_0$. The dominant production mechanism for strangeness at SPS energies is string-excitation.

The time-evolution depicted in figure 4.40 characterizes the *chemical* freeze-out of strangeness in heavy collision systems. We shall now turn to the *kinetic* freeze-out, i.e. the time of the last interaction of the particle (i.e. scattering or its production via the decay of a resonance):

Freeze-out radii are closely correlated to freeze-out times. Although the latter are definitely not measurable (for the radii, two-particle correlation techniques may yield similar information) they are the cleaner observable for a transport model analysis. Freeze-out radii may be contaminated by low energy particles produced close to the geometric center of the reaction during the late dilute expansion stage – such particles would have small freeze-out radii but large freeze-out times.

The mass dependence of freeze-out times is studied in figure 4.41. It shows the freeze-out time distributions for π, η and ω mesons in central Au+Au reactions at 2 GeV/nucleon. The heavier the meson, the earlier its freeze-out. The reason for this correlation is that heavy mesons are solely produced by the decay of massive baryon-resonances which can only be excited in the early hot and dense reaction zone. Of course freeze-out times do not only depend on the mass of the produced particle, but also on its interaction cross section: Figure 4.42 shows freeze-out time distributions for K^+, K^- and hyperons. Despite their large mass difference, the freeze-out times for hyperons and K^- are very similar, whereas the K^+ freeze out much earlier. This is due to the different quark content of K^+ and K^-: Both, K^- and hyperons contain a s-quark and have relatively large hadronic interaction cross sections. The K^+, however, contains a $\bar{s}$-quark and has a far lower cross section.

So far, we have only studied the freeze-out behavior of mesons and hyperons at relatively low bombarding energies around 2 GeV/nucleon. In that domain, baryon-baryon and meson-baryon interactions

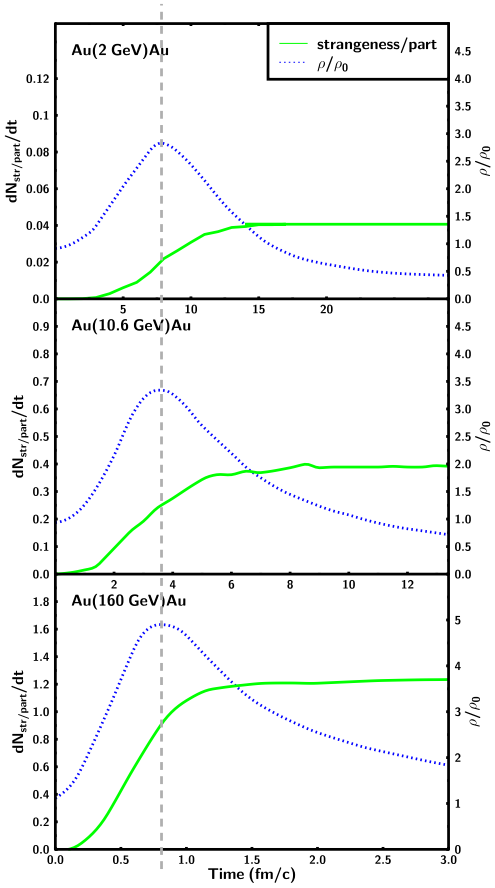

Figure 4.40: Time evolution of the mean baryon density and total produced strangeness per participant baryon (UrQMD calculation). The mean baryon density is defined as the average over the baryon densities computed at the locations of all individual baryons. The total strangeness is the sum of all produced quarks and antiquarks. The time axis has been rescaled in order to overlay the respective times of highest baryon density (dashed grey line).

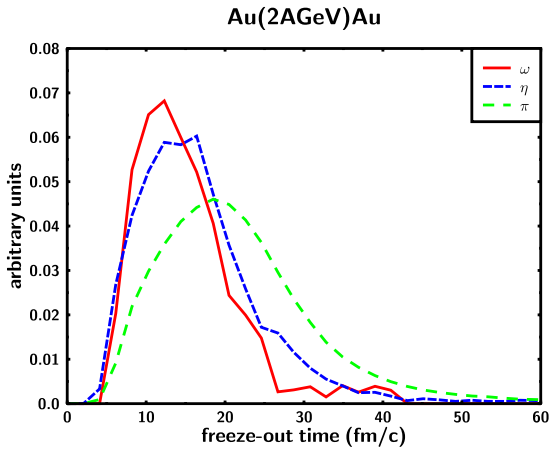

Figure 4.41: Normalized freeze-out time distributions for π, η and ω mesons in UrQMD central Au+Au reactions at 2 GeV/nucleon. Heavy mesons freeze out earlier than light ones.

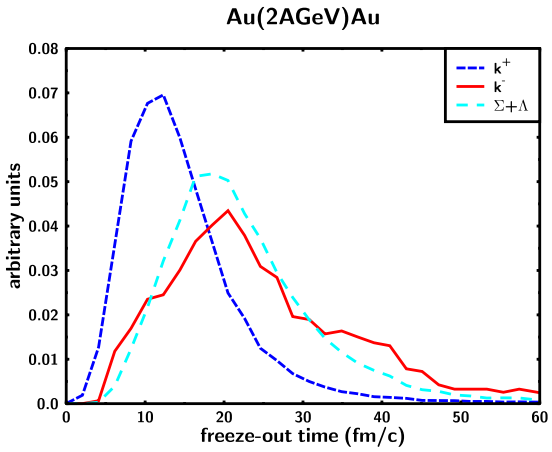

Figure 4.42: Normalized freeze-out time distributions for K^+, K^- and hyperons in UrQMD central Au+Au reactions at 2 GeV/nucleon. Particles with $\bar{s}$-quarks freeze out earlier than those with s-quarks.

are dominant and available phase-space may strongly influence the freeze-out behavior of the particles under investigation. Let us now turn to CERN/SPS energies – here meson production is so abundant that meson-meson and meson-baryon interactions dominate over baryon-baryon interaction and threshold or phase-space restrictions do not anymore apply.

Unfortunately, neither the freeze-out density, nor the freeze-out time is directly observable. However, figure 4.43 shows that we can establish a correlation between high transverse momenta and early freeze-out times, at least in heavy colliding systems. In figure 4.43 the freeze-out time of pions is plotted versus their transverse momenta for p+p, S+S and Pb+Pb reactions at SPS energies. Naturally, the proton-proton system does not show any correlation, whereas in the heavy Pb+Pb system a strong p_t-dependence of the freeze-out time is visible. Selecting particles with high transverse momenta thus yields a sample of particles with predominantly early freeze-out times and high freeze-out densities.

Do all hadron species exhibit a uniform freeze-out behavior – or does each species have its own complicated space-time dependent freeze-out profile, as observed at SIS-energies? Figures 4.44 and 4.45 show the freeze-out radius and freeze-out time distributions for pions, kaons, antikaons and hyperons at mid-rapidity in central Pb+Pb reactions at 160 GeV/nucleon. The distributions have been normalized in order to compare the shapes and not the absolute values. In contrast to the situation at 2 GeV/nucleon, all meson species show surprisingly the same freeze-out behavior – the transverse freeze-out radius and freeze-out time distributions all closely resemble each other. Only the hyperons show an entirely different freeze-out behavior. Whereas the common freeze-out characteristics of the mesons seem to hint at a thermalization, the hyperons show that even at SPS energies there exists no common global freeze-out for all hadron species.

Since the freeze-out distributions have a large width, the average freeze-out radius clearly does not define a freeze-out volume and therefore estimates of the reaction volume or energy density based on average freeze-out radii have to be regarded with great scepticism.

In this section we have investigated freeze-out properties of hadrons produced in relativistic heavy-ion

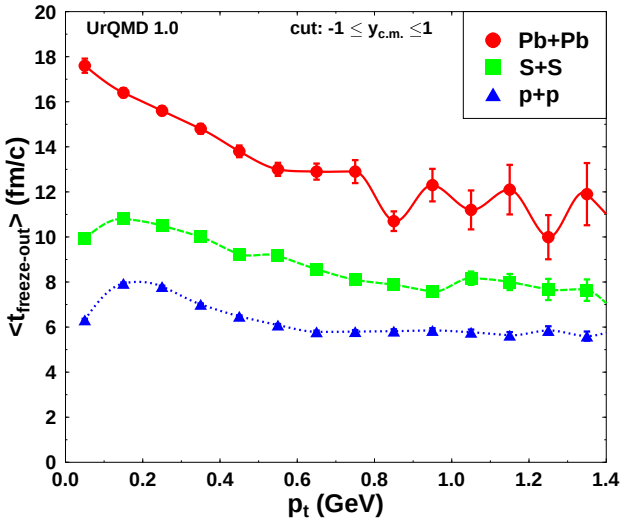

Figure 4.43: Freeze-out time of pions as a function of transverse momentum for p+p, S+S and Pb+Pb reactions at CERN/SPS energies. For heavy systems early freeze-out is correlated to high p_t.

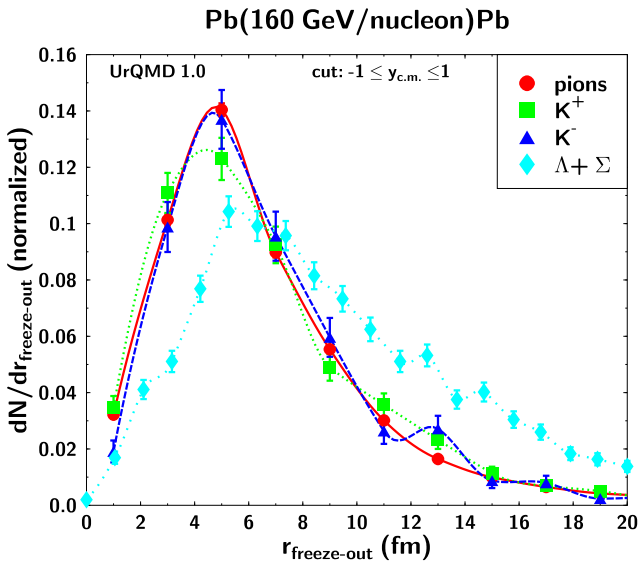

Figure 4.44: Normalized transverse freeze-out radius distribution for pions, kaons, antikaons and hyperons. Whereas all mesons show similar distributions, the hyperons freeze out at larger radii.

reactions. At SIS energies each particle species has its own complex freeze-out characteristics, governed by interaction cross sections, available phase-space and resonance lifetimes. At CERN/SPS energies, similar freeze-out distributions for various meson species hint at a system closer to thermal equilibrium. A comparison with the hyperon freeze-out distributions, however, indicates that no global thermalization and freeze-out has been achieved. Therefore, thermal model fits to hadron ratios and spectra – even though they work pretty well – may result in a misleading interpretation of the final state of a relativistic heavy ion reaction.

4.2.8 Dilepton production

One basic problem of heavy ion physics is actually *how* to investigate the hot and dense phase that is presumably formed in a collision of two relativistic nuclei. Since hadrons may interact several times, the intermediate stages are so to speak "shadowed" by the freeze-out distributions. Dileptons are of great interest, because they do not interact with the hadronic matter. Furthermore, they are emitted by various mechanisms at all stages of a heavy ion collision. Thus, the dilepton signal yields time *integrated* information on the reaction dynamics.

Dileptons were initially proposed as highly penetrating probes of the QGP state [286, 287, 288]. They can be produced via a virtual photon in $q\bar{q} \rightarrow \gamma^* g$ annihilations and in the QCD Compton process $gq \rightarrow \gamma^* q$. If one assumes the QGP to be an equilibrated gas, then dileptons (as well as real photons) can probe its thermodynamic conditions [289]. However, due to large background contributions of hadronic radiation at low masses and the Drell-Yan process [290] at high masses, dileptons stemming from the QGP will possibly be overshined.

Recent interest has focussed on low mass dileptons. They are emitted in hadronic decays and collisions.

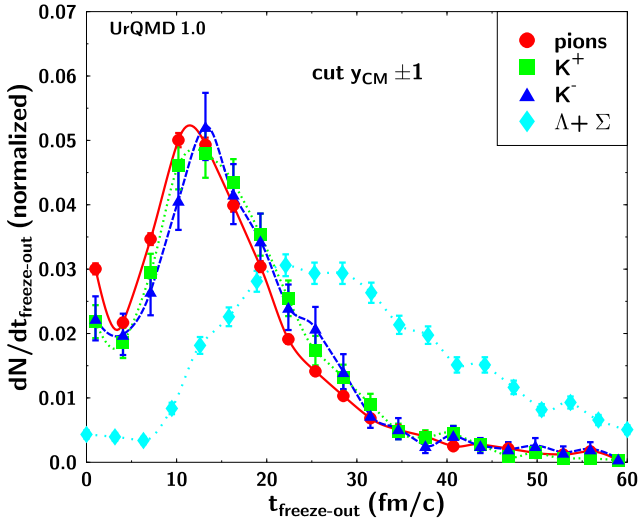

Figure 4.45: Normalized freeze-out time distribution for pions, kaons, antikaons and hyperons. As with the freeze-out radii, the times for the meson species are very similar. The hyperons again show a different behavior.

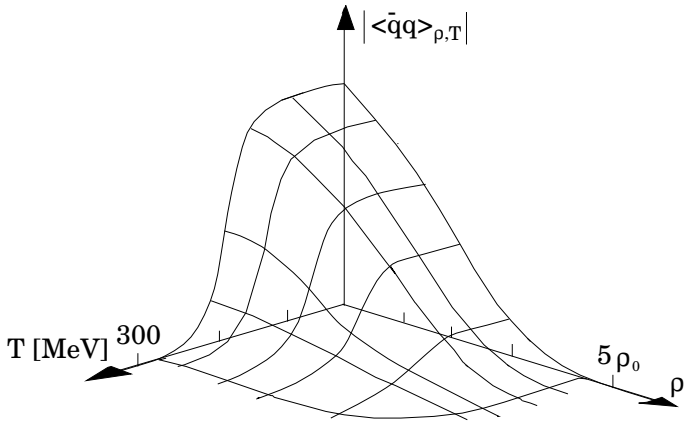

Figure 4.46: quark condensate $-\langle q\bar{q}\rangle$ as a function of temperature T and baryon density ρ/ρ_0. The figure has been adapted from [285].

Especially the Dalitz decays of light mesons and the direct decays of vector mesons are supposed to contribute significantly for invariant dilepton masses $M_{ll} < 1GeV$. In this mass region also various bremsstrahlung mechanisms might be important [81, 291, 292] as well as a number of direct production channels, e.g. $\pi\rho \rightarrow ll\pi$ [293]. Because the vector mesons have rather small life-times, they can supposedly resolve the rapid changes during the hot and dense phases of the collision. Their detection can proceed via low-mass dileptons.

In conjunction with the chiral symmetry restoration [285, 294, 295, 296], the QCD condensates (e.g. $\langle\bar{q}q\rangle$) should lower their values at high temperatures and/or densities. The dependence of $\langle q\bar{q}\rangle$ on the temperature T has been studied in the framework of lattice QCD [297] and chiral perturbation theory [298]. Up to 0.7 - $0.8T_C$, $\langle q\bar{q}\rangle$ remains nearly constant and then its absolute value decreases rapidly (see figure 4.46). The behavior of the quark condensate at finite baryon densities is described in a model independent fashion by the Hellman-Feynman-theorem [299]. A model calculation of the dependence of $\langle q\bar{q}\rangle$ on both, the baryon density ρ/ρ_0 and temperature T, can be seen in figure 4.46 – the drop of $\langle q\bar{q}\rangle$ with ρ and T is quite analogous to the temperature and density dependence of the nucleon effective mass in the $\sigma - \omega$ model as noted in [275].

The connection between the QCD condensates and phenomenological hadronic quantities (masses, width etc.) can be drawn via the QCD sum rule technique [300, 301, 302]. Under simplifying assumptions on the spectral function, such calculations find lowering vector meson masses as indicators of chiral symmetry restoration [303, 304]. More refined calculations, which try to evaluate the medium contributions to the self energy of the vector mesons, find broadening spectral functions in matter [86, 87, 88, 89, 90, 91].

Various experiments have focussed on low mass lepton pairs: the DLS spectrometer at the BEVALAC [305, 306], the CERES [307, 308] and HELIOS [309, 232] experiments at the SPS at CERN. The dilepton spectrometers HADES at SIS (GSI) [310] and PHENIX at RHIC (BNL) [311] are under construction.

Experiments at CERN have reported an enhanced production of dilepton pairs in nucleus-nucleus collisions over a broad invariant mass region around $M \sim 0.5\ GeV$ [312]. The enhancement is relative to the known sources as measured in pp or pA collisions after scaling to the nucleus-nucleus case (see l.h.s. of fig. 4.47). The data have been however reproduced by assuming density dependent masses of vector mesons as a consequence of partial chiral symmetry restoration [313, 314, 315, 316, 317] (r.h.s. of fig. 4.47).

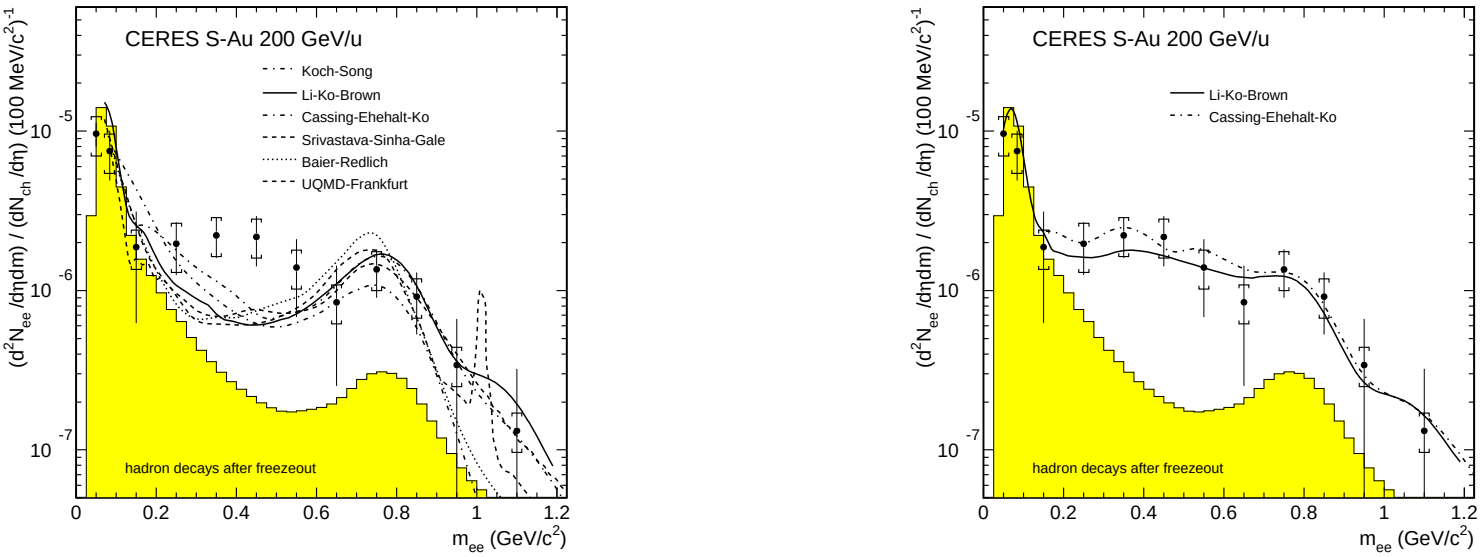

Figure 4.47: Inclusive e^+e^- mass spectra in 200 GeV/nucleon S+Au collisions as measured by the CERES collaboration [307]. The figures have been taken from [312]. The shaded area depicts hadronic contributions from resonance decays. The l.h.s. shows a comparison with calculations based on a purely hadronic scenario [317, 318, 313, 315, 319] whereas the r.h.s shows calculations including either a QGP phase transition or medium dependent vector meson masses [313, 315].

However, even bare hadronic transport model calculations, without any mass shift included, miss only the data in the 400 to 600 MeV bins (by 2 to 3 standard deviations) [316, 317]. Since hadronic transport models did – so far – neglect some contributions, e.g. from bremsstrahlung, it has yet to be determined whether partial restoration of chiral symmetry is the only possible explanation of these interesting new data. Calculations evaluating in-medium spectral functions, due to the coupling of the ρ with nucleon resonances and particle-hole excitations, also achieve a satisfactory reproduction of the CERES data [89], without requiring a dropping ρ-mass. One has to conclude that, up to now, comparisons of dilepton spectra with hadronic models do not give evidence for (partial) restoration of chiral symmetry [320]. Another, up to now neglected contribution to the low mass dilepton spectrum in nucleus-nucleus collisions, are secondary Drell-Yan processes, which are described in greater detail in the next sub-section.

The production of low mass dileptons is included in the UrQMD model via Dalitz decays of $\pi^0, \eta, \omega, \eta'$ mesons and of the $\Delta(1232)$ resonance, direct decays of neutral vector mesons and incoherent pn bremsstrahlung [321]. This approach has been used to analyze data of the DLS collaboration at the BEVALAC accelerator [305, 306]. The recent AA data all show a large enhancement as compared to model calculations (see fig. 4.48). The pd spectra imply a high $pn \rightarrow \eta X$ cross section, but TAPS data delimit this as an explanation for the enhancement. So far, these data resist any explanation by medium-dependent spectral functions [321, 322]. Note that the recent data strongly exceed earlier published measurements of the same collaboration [323] which have been reproduced by various transport

models [58, 324, 325, 322] and are also favored by the UrQMD model. A satisfying explanation of the recent DLS data is still missing.

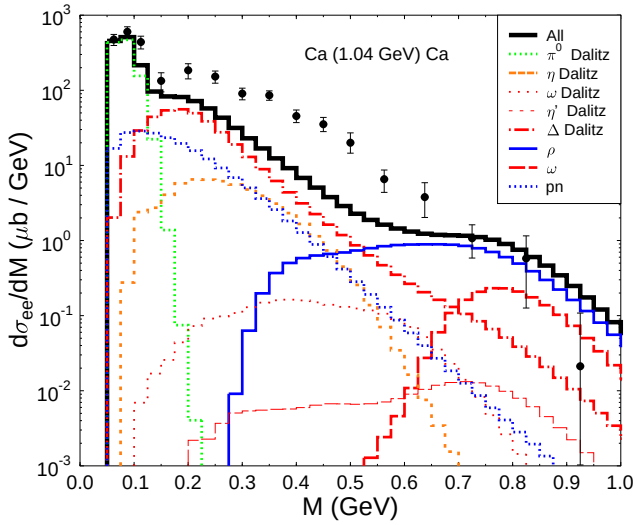

Figure 4.48: UrQMD dilepton cocktail plot for Ca+Ca in comparison to recent DLS data [305]. The upper solid curve is the sum of all contributions. The detector acceptance has been modeled with the DLS Filter 4.1 and a mass resolution of 10% is adopted.

Drell-Yan pairs from secondary collisions

Reports on intermediate mass muon pairs [328, 309, 326] produced in heavy ion collisions have recently attracted much attention. The measured spectrum is enhanced relative to the expected 'cocktail' dilepton sources (Fig. 4.49, left), one of them being the Drell-Yan pair production [290].

Rate estimates of this process (e.g. [329]) are essentially based on extrapolations of p+A reactions where a linear scaling with A is observed for the Drell-Yan production cross section [330]:

$$\sigma_{\mathrm{pA}} = \sigma_0 \ \mathrm{A}\,.$$

This linear scaling can be understood in the Glauber picture of the hadron-nucleus cross section, constructed at high energies using the AGK cutting rules [331].

But also the hot matter produced in ultrarelativistic heavy ion collisions contributes to the total dilepton radiation [332, 333, 334, 335, 336, 337]. It is shown that emission from thermal sources such as a quark-gluon plasma or hadron gas, whether in or out of equilibrium, cannot be neglected relative to nucleon-nucleon contributions to the Drell-Yan process for masses below the J/ψ peak — at least at higher energies than those presently available.

Another source of dileptons which may already play a role at SPS energies and could account for the observed intermediate mass dilepton enhancement has been proposed in [327]: Drell-Yan production by interactions involving produced, or secondary, hadrons. In order to investigate secondary dilepton production at SPS energies UrQMD has been employed to obtain a realistic collision spectrum of secondary hadrons. The differential Drell-Yan cross section is computed at leading order (LO) using the standard equation [338]:

$$\frac{\mathrm{d}^2\sigma}{\mathrm{d}m^2\mathrm{d}y}(\mathrm{AB}\to l\bar{l}X) = \frac{4\pi\alpha^2}{9m^2s}\sum_q e_q^2\left[q^{\mathrm{A}}(x_{\mathrm{A}},m^2)\overline{q}^{\mathrm{B}}(x_{\mathrm{B}},m^2)+\overline{q}^{\mathrm{A}}(x_{\mathrm{A}},m^2)q^{\mathrm{B}}(x_{\mathrm{B}},m^2)\right]\,, \tag{4.7}$$

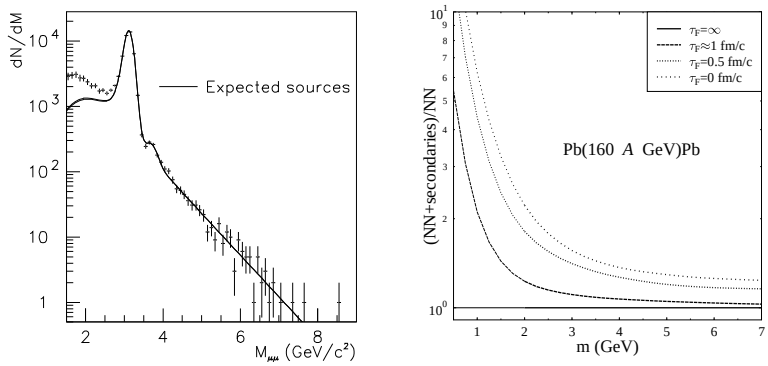

Figure 4.49: Left: Comparison of measured dimuon yield with expected sources in Pb+Pb collisions. Figure taken from [326]. Right: Calculation of secondary Drell-Yan processes based on a UrQMD simulation. Shown is the ratio between the total dilepton mass spectrum and the nucleon-nucleon scattering alone, at $y_{\rm cms} = 0.5$, for Pb+Pb at 160 A GeV assuming different hadronic formation times τ_F (Figure taken from [327].

where $q(x, m^2)$ and $\overline{q}(x, m^2)$ denote the quark and antiquark densities (according to [339, 340]), $\sqrt{s}$ is the center-of-mass energy of the colliding hadrons, m is the invariant mass of the lepton pair, $x_{\rm A} = \sqrt{\tau}\ e^{y}$ and $x_{\rm B} = \sqrt{\tau}\ e^{-y}$ with $\tau = m^2/s$, and y is the dilepton rapidity in the *cms* frame. The lepton pair production cross section is calculated for each hadron-hadron collision and weighted by the inverse of the total hadron-hadron cross section. The distributions from these elementary hh-collisions are then summed. It is clear that in pion-nucleon collisions, *valence* quark-antiquark annihilation can play a significant role in the Drell-Yan process. Pion-nucleon dilepton production cross sections are consequently higher than nucleon-nucleon cross sections, especially when $m/\sqrt{s} \gtrsim 0.1$. It is shown that these secondary collisions can serve as an important source of $m \sim 2$ GeV dileptons due to the availability of valence antiquarks in mesons and antibaryons (Fig. 4.49 right).

The standard Drell-Yan process corresponds to the interaction of fully formed hadrons. However, it was shown [341, 342, 343] that, during the early stages of the system evolution, partons can scatter and annihilate before they have come on mass-shell. To estimate the importance of these "primordial" or "pre-resonance" $q\bar{q}$ annihilations, the contribution of such processes have been calculated assuming that the asymptotic parton distribution functions are also valid for the primordial states. This is done very simply in the UrQMD calculation by decreasing the formation time of the produced hadrons within string excitations, τ_F, from the "default" value of around 1 fm/c.

The importance of this primordial (pre-resonance) contribution to the dilepton mass spectra is shown in Fig. 4.49 (right). The secondary dilepton yield for $\tau_F = 0$increases by a factor of ~ 5 at all masses compared to the calculations with the default $\tau_F \approx 1$ fm/c. With a value of $\tau_F = 0.5$ fm/c the enhancement in the range $1.5 < m < 2.5$ GeV shows quite good agreement with the mass data which are about a factor of two higher than naively expected [326, 328, 309].

4.2.9 Charmonium production and suppression

J/Ψ's, χ's and Ψ''s, consisting of a $c\bar{c}$ pair, are formed in pp-collisions by the fusion of two gluons, or to a larger extend by the annihilation of a quark-antiquark pair [345]. In a QGP of sufficiently high density and

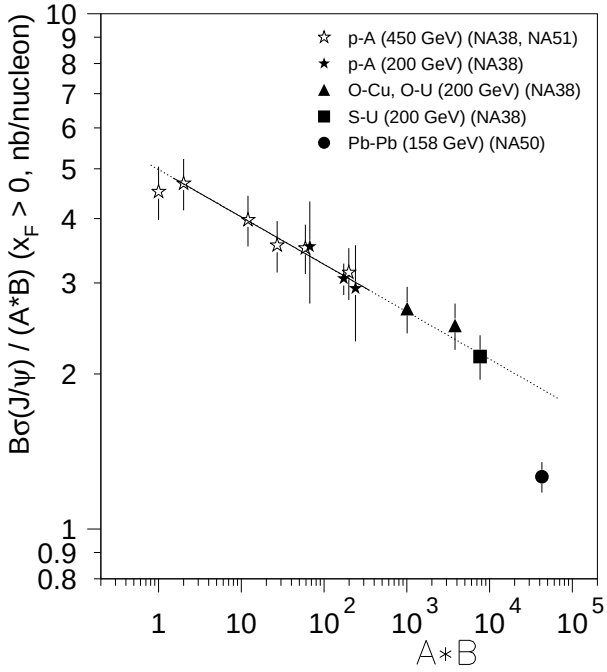

Figure 4.50: J/ψ production cross sections versus $A \times B$. Figure taken from [344].

temperature $c\bar{c}$ pairs cannot bind together – the presence of gluons and quarks in the plasma causes the color charge of quarks to be screened. Alternatively, hard gluons may be able to dissociate the $c\bar{c}$ pair (QCD photo-effect) in the QGP. Suppression of quarkonia-mesons has been suggested as a possible signature for deconfinement [346]. Lattice SU(3) gauge theory [347, 348] indicates that the necessary conditions for the screening are already fulfilled shortly above T_C (the screening length λ_D is inversely proportional to the temperature). Inclusion of dynamical fermions decreases the screening length [349, 350].

However, the suppression of quarkonia meson production is no unambiguous signal for deconfinement. They are no weakly interacting probes which can traverse hadronic matter unhindered. On the contrary, heavy quarkonia mesons suffer from low production cross sections and rather large hadronic dissociation cross sections. I.e. charmonium is already suppressed in pA-collisions, where the conditions for a QGP are not fulfilled. Figure 4.50 depicts the suppression of J/Ψ's in pA- and AB-collisions. The line shows the suppression due to the nuclear constituents of the projectile and target nuclei. One can see that this effect reproduces the data from pp- up to SU-collisions, but to explain the new lead on lead data one needs additional suppression. Purely hadronic scenarios have been suggested [264, 351, 352, 353, 354], which can explain J/Ψ and Ψ' suppression up to PbPb-collisions without the need for a deconfined phase. The most successful hadronic scenarios for J/Ψ and Ψ' suppression explicitly take interactions with produced particles into account and are referred to as *comover models* - the *comovers* being the produced mesons which are energetic enough to destroy a J/Ψ in the case of a collision. For the Ψ', all mesons can be *comovers*, but there is a threshold for the reaction $J/\Psi + X \rightarrow D\bar{D}$, because $2m_D - m_{J/\Psi} \approx 640$ MeV. So, "slow" pions (in the J/Ψ rest frame) cannot destroy a J/Ψ.

Hadronic transport model calculations which incorporate the full collision dynamics and go far beyond the commonly used simplified version of the Glauber theory yield conflicting results [355, 263]. These transport model calculations are very sensitive to certain input parameters such as the formation time of the J/Ψ and the comovers. The HSD transport model [355] can fully reproduce the NA50 lead data while assuming a fixed formation time of 0.7–0.8 fm/c for both, J/Ψ and comovers. A second calculation

with the HSD model using a formation time of 0 fm/c for the J/Ψ reproduces also the data [356]. The UrQMD model, however, uses for the comovers a variable formation time emerging from the Lund string fragmentation formalism (here the formation time depends on the hadron mass) and zero formation time for the J/Ψ. The assumption of zero formation time is valid if the J/Ψ is considered as a pre-resonance $c\bar{c}_8 - g$ state with a hadronic dissociation cross section of 7 mb. However, the UrQMD model does not reproduce the additional suppression of the Pb+Pb experiment [263]. The question of formation time might be a central issue since in the color octet model the dissociation cross section is actually higher during the lifetime of the pre-resonance $c\bar{c}_8 - g$ state [357, 358] than after hadronization. Furthermore the amount of comover-charmonium interaction will crucially depend on the formation time of the comovers.

One has to bear in mind, however, that hadronic transport models do not contain partonic degrees of freedom explicitly and are therefore incapable of correctly describing hard processes like charm production or the Drell-Yan process. From the measurements of Drell-Yan lepton pairs we know that the cross section in pA-collisions is proportional to A, as predicted by the Glauber model. Hadronic models on the other hand take into account the energy loss of incident nucleons due to the production of secondaries (which then could play an important role as comovers). If, however, the elementary hard scattering cross section is strongly energy dependent – as the charm production at SPS energies and below – the effect of nuclear stopping leads to a considerable underestimation of the AB cross section. So, at the moment it is not clear, how it is possible to include hard processes consistently in a hadronic transport model.

Another point under discussion is whether charmonium states might be created as a pre-resonance $c\bar{c}_8 - g$ state [343], which is not an eigenstate of the QCD Hamiltonian. Thus, one would expect a time evolution of this state and its cross section until it is a physical state, i.e a J/Ψ. The pre-resonance should evolve during the formation time which would lead to different effective absorption cross sections in small and heavy nuclei.

To summarize this section, we can say that the suppression of charmonium states in heavy ion collisions and even in proton-nucleus is not yet understood. Although, the assumption of a pre-resonance state with a constant cross section seems to reproduce the data, it contradicts principle ideas of quantum mechanics.

4.3 Collective flow

The excitation function of transverse collective flow is the earliest predicted signature for probing the formation of compressed nuclear matter [1, 150]. It has been shown that the excitation function of flow is sensitive to the EoS and can be used to search for abnormal matter states and phase transitions [15].

In the fluid dynamical approach the transverse collective flow is directly linked to the pressure of the matter in the reaction zone. With $P(\rho, S)$ being the pressure (depending on the density ρ and the entropy S) the generated collective transverse momentum can be written as an integral of the pressure over surface and time [359]:

$$P_\perp = \int_t \int_A P(\rho, S)\, \mathrm{d}A\, \mathrm{d}t\,, \tag{4.8}$$

where $\mathrm{d}A$ represents the surface element between the participant and spectator matters and the total pressure is the sum of the potential pressure and the kinetic pressure: The transverse collective flow depends directly on the equation of state, $P(\rho, S)$.

Collective flow has been predicted by nuclear fluid dynamics (NFD) [1, 150, 360, 361, 362, 16]. It is well established experimentally at the BEVALAC [363, 364, 365] for charged particles by the Plastic-Ball and streamer chamber collaborations and at GSI by the FOPI collaboration [366]. Microscopic models such as VUU (Vlasov-Uehling-Uhlenbeck) and QMD (Quantum Molecular Dynamics) have predicted smaller flow

than NFD. These models, however, show good agreement with the experimental findings [53, 152, 154, 202, 367]. One has to distinguish between different signatures of collective flow: The undirected *radial* flow which is best observed in ultracentral collisions and the *bounce–off* [360] of compressed matter *in the reaction plane* as well as the *squeeze–out* [361] of the participant matter *out of the reaction plane* in semi-central to semi-peripheral collisions.

The most strongly stopped, compressed matter around mid-rapidity is seen directly in the *squeeze–out* [71]. A strong dependence of these collective effects on the nuclear equation of state is predicted [202]. For higher beam energies, however, projectile and target spectator decouple quickly from the reaction zone, giving way to a preferential emission of matter in the reaction plane, even at mid-rapidity [368].

Apart from the above discussed *directed* flow, the so-called "radial", i.e. undirected, flow component can be used for simplicity (spherical symmetry) [197, 198]. It changes drastically the interpretation of particle spectra used for temperature extraction which may drop by as much as a factor of 2 (see the l.h.s. of figure 4.51). The mean (undirected) transverse velocity ($\langle\beta_t\rangle$) or momentum ($\langle p_t\rangle$) can be used as a measure for this undirected flow in central collisions. The r.h.s. of figure 4.51 shows a UrQMD excitation function for $\langle p_t\rangle$. Up to an incident beam energy of 2 GeV/nucleon, $\langle p_t\rangle$ rises steadily and then almost saturates. The inclusion of potentials does not play a major role for this observable. The saturation at 2 GeV/nucleon (which is also observed experimentally, see the l.h.s. of the figure) can be explained in the following scenario: Up to 2 GeV/nucleon the longitudinal momentum of the incoming nucleons is predominantly transferred into transverse degrees of freedom; particle production only accounts for a minor fraction of the total energy of the system at the end of the reaction. Above 2 GeV/nucleon, however, particle production gets more important and finally most of the energy of the final state is stored in produced particles, leading to a saturation in the amount of energy carried by the "primordial" constituents of the collision system, the nucleons. The increase of energy stored in produced particles can be seen on the r.h.s. of figure 4.51 - here the excitation function for total energy of all produced particles (diamonds) is plotted into the same frame as the $\langle p_t\rangle$ excitation function.

The origin of nuclear flow in ultrarelativistic heavy ion collisions can be seen in Fig. 4.52, where the time evolution of the longitudinal and the transverse pressure in the central region of Au(11GeV)Au (b=0), simulated with UrQMD, is depicted. A cylindrical volume of $r = 6$ fm and $\Delta z = 2$ fm in the center of the reaction is considered. The pressure is calculated according to the virial theorem:

$$VP^i = \frac{1}{\mathrm{N_{events}}} \sum_{\mathrm{n=1}}^{\mathrm{N_{events}}} \sum_{\mathrm{k=1}}^{\mathrm{N_{particles}}} p_k^i p_k^i / p_k^0 \quad ,$$

where $i = x, y, z$ denotes the three spatial directions. The contribution of this kinetic part and a part from quasi-potentials have been studied separately in the framework of RQMD [372]. It takes about 5 fm/c until the longitudinal pressure reaches its maximum value. The longitudinal pressure has decreased considerable at that time. Mainly not due to scattering and momentum transfer but due to the particles that simply have passed the central region and are therefore not considered any more. If *all* particles are taken into account, the ratio of transverse to longitudinal pressure does not exceed 0.5. This is in line with the observation of larger longitudinal than transverse flow after freeze-out.

4.3.1 Bounce–off: collective flow in the reaction plane

Due to its direct dependence on the EoS, $P(\rho, T)$, flow excitation functions can provide unique information about phase transitions: The formation of abnormal nuclear matter, e.g., yields a reduction of the collective flow [15]. A directed flow excitation function as signature of the phase transition into the QGP has been

proposed by several authors [7, 16]. A microscopic analysis showed that the existence of a first order phase transition can show up as a reduction in the directed transverse flow [71].

For first order phase transitions, the pressure remains constant in the region of the phase coexistence. This results in a vanishing velocity of sound $c_s = \sqrt{\partial p/\partial \varepsilon}$. The expansion of the system is driven by the pressure gradients, therefore expansion depends crucially on c_s^2. Matter in the mixed phase expands less rapidly than a hadron gas at the same energy density and entropy. In case of rapid changes in the EoS without phase transition, the pressure gradients are finite, but still smaller than for an ideal gas EoS, and therefore the system expands more slowly [374, 375].

This reduction of c_s^2 in the transition region is commonly referred to as *softening* of the EoS. The respective region of energy densities has been called the *soft region* [376, 377, 373, 378]. Here the flow will temporarily slow down (or possibly even stall). Consequently a *time delay* is expected in the expansion of the system. This prevents the deflection of spectator matter (the *bounce–off*) and, therefore, causes a reduction of the directed transverse flow [17, 18]. The softening of the EoS should be observable in the excitation function of the transverse directed flow of baryons (see figure 4.53).

The overall decrease of p_x seen in Fig. 4.53 for $E_{lab} > 2$ AGeV both for the hadronic and the QGP equation of state demonstrates that faster spectators are less easily deflected (because A and t in equation 4.8 are decreasing with E_{lab}) by the hot, expanding participant matter. For the QGP equation of state, however, these one-fluid calculations show a *local minimum* in the excitation function, at about 6 GeV/nucleon. This can be related to the QGP phase transition, i.e. to the existence of the *soft region* in the EoS.

However, one-fluid hydrodynamic calculations assume instantaneous thermalization. This becomes unrealistic for increasing beam energies since due to the average rapidity loss of only one unit per proton-proton collision, nucleons require several collisions for thermalization. A more realistic three-fluid calculation without a first order phase-transition, in which only local thermal equilibrium within each fluid is assumed, yields similar flow values as the one fluid model with a phase transition (solid squares in fig. 4.53) [379, 380]. The position of the minimum (the magnitude of the overall effect) therefore strongly depends on the degree of stopping (i.e. which type of fluid-dynamical model is employed) and on the details of the chosen EoS and phase transition parameters.

Moreover, for finite volumes, $V < 100$ fm^3, corresponding to expected plasma volumes in heavy ion collisions, there is a considerable rounding in the variables ϵ/T^4 and s/T^3 around T_C, even if there is a first-order phase transition for the infinite volume limit [281]. This is inferred, under simple assumptions, from basic thermodynamic considerations: Fluctuations of the two phases in a finite system lead to a smooth transition between the low temperature regime — where the hadronic phase dominates the system — and the high temperature regime — where the pure quark phase is most probable. Such a behavior has severe implications on the proposed signal as was shown in [378]: a smooth crossover transition within an assumed interval of $\Delta T = 0.1 T_C$ results in drastically reduced time delays as compared to a sharp transition.

Another effect is present if explicit finite size effects and the necessary requirement of exact color-singletness within the quark phase [381, 382] is included [281]. The model exhibits a barrier in the free energy between the two phases near the phase transition. This leads to a shift of the critical temperature to higher temperatures for finite volumes (see Fig. 4.54). The speed of sound is considerably increased in the mixed phase. The significance of the time delay signal for the experimental detection of a QGP phase in heavy ion collisions, in turn, becomes questionable.

A second order phase transition may not exhibit this minimum in the flow excitation function: The existence of a minimum in $p_{x,dir}(E_{lab})$ is rather a *qualitative* signal for a strong first order transition. If such a drop of $p_{x,dir}(E_{lab})$ is observed, it remains to be seen which phase transition caused this behavior: a

hadron–quark-gluon phase transition or, e.g., a nuclear matter to resonance matter transition in confined hadronic matter [249, 383].

What does the purely hadronic UrQMD model predict with respect to directed transverse flow? Figure 4.55 shows the averaged in plane transverse momenta for Ni+Ni and Au+Au in the 0.1 – 4 GeV/nucleon region which is accessible through experiments at SIS and AGS. Calculations employing a hard equation of state (full symbols) are compared to cascade simulations (open symbols). In the latter case only a slight mass dependence is observed. For the calculation with potentials the integrated directed transverse momentum push per baryon is more than twice as high for the heavier system which corroborates the importance of a non-trivial equation of state of hadronic matter.

For beam energies below 5 GeV/nucleon the amount of directed transverse momentum scales in the very same way as the total transverse momentum in the course of the reaction. Therefore the $\langle p_x \rangle$ versus rapidity divided by the $\langle p_t \rangle$ is identical for all beam energies in the range of scaling as can be seen in figure 4.56.

4.3.2 Squeeze–out: flow perpendicular to the reaction plane

The most strongly stopped, compressed matter at mid-rapidity is responsible for the *squeeze–out* [71]. A strong dependence on the nuclear equation of state for this collective effect is seen [202, 384].

Let us now show the dependence of the observed *squeeze–out* on increasing beam energy, transverse momentum and impact parameter. We define a *squeeze–out ratio* [71]

$$R_{out/in} = \left. \frac{\frac{dN}{d\varphi}(\varphi = 90^\circ) + \frac{dN}{d\varphi}(\varphi = 270^\circ)}{\frac{dN}{d\varphi}(\varphi = 0^\circ) + \frac{dN}{d\varphi}(\varphi = 180^\circ)} \right|_{y=y_{CM}} .$$

For values $R_{out/in} > 1$ neutrons are emitted preferentially perpendicular to the reaction plane.

The top frame of figure 4.57 shows $R_{out/in}$ for Au+Au collisions versus scaled transverse momentum p_t/p_{proj} for beam energies of 400, 600, 800 and 1000 MeV/nucleon with cuts on rapidity ($-0.15 \leq y_{CM} \leq 0.15$) and impact parameter ($3 \leq b\ [fm] \leq 9$). The ratio increases monotonously with the transverse momentum and is independent of the beam energy if the transverse momenta are scaled with the projectile momenta. Therefore, higher transverse momenta must be probed with increasing beam energy if a clean *squeeze–out* signal is to be isolated. Such a scaling behavior has already been extracted for the *in–plane bounce–off* in the hydrodynamic model [385]. It has been experimentally observed in the case of the neutron *squeeze–out* by the LAND collaboration [386]. The respective comparison between the IQMD model and LAND data (mid-rapidity, ERAT2 centrality criterion) is shown for 400 MeV/nucleon in the lower frame of figure 4.57. One should note, however, that in the IQMD calculation the reaction plane is always known, whereas the experimental determination of the reaction plane yields fluctuations which might underestimate the measured ratio by 15 to 30%. The p_t dependence of the squeeze-out ratio is even enhanced for heavier clusters, as can be seen in figure 4.59.

The dependence of the neutron *squeeze–out* on the momentum dependent interaction and the equation of state is shown in figure 4.58 (for Au+Au collisions at 1 GeV/nucleon): The upper frame shows the hard equation of state with and without momentum dependent interaction (mdi). With mdi, $R_{out/in}$ increases by 50% for large transverse momenta! A difference of 50% can also be observed by comparing the hard and soft equations of state (both including mdi) in the lower frame of figure 4.58: At high transverse momenta the hard equation of state with mdi exhibits a 50% higher *squeeze–out ratio* than the soft equation of state with mdi. The hard equation of state without mdi shows a $R_{out/in}$ vs. p_t dependence similar to the soft equation of state with mdi. It is important to note, however, that these differences are only seen for

high transverse momenta $p_t/p_{proj} \geq 1$. Analyzing p_t-integrated data will therefore severely diminish the sensitivity towards the nuclear equation of state and the momentum dependent interaction.

In fig. 4.60, the excitation function of the coefficient v_2 is shown representing the so-called elliptical flow. v_2 is extracted from a fit to the azimuthal distribution of nucleons according to $dN/d\phi = v_0[1 + v_1 \cos(\phi) + v_2 \cos(2\phi)]$. Positive values of v_2 correspond to a preferential in-plane enhancement of the emitted particles while negative values describe preferred emission perpendicular to the reaction plane.

Clearly, large differences are seen when comparing calculations with and without potentials. On the one hand, cascade calculations only show in-plane enhancement of the emitted particles. On the other hand, calculations including nucleonic potentials show a transition from in-plane to out-of-plane emission with increasing bombarding energy which is seen by current experiments of the EOS collaboration [387]. This big sensitivity to the model ingredients gives a handle to pin them down further.

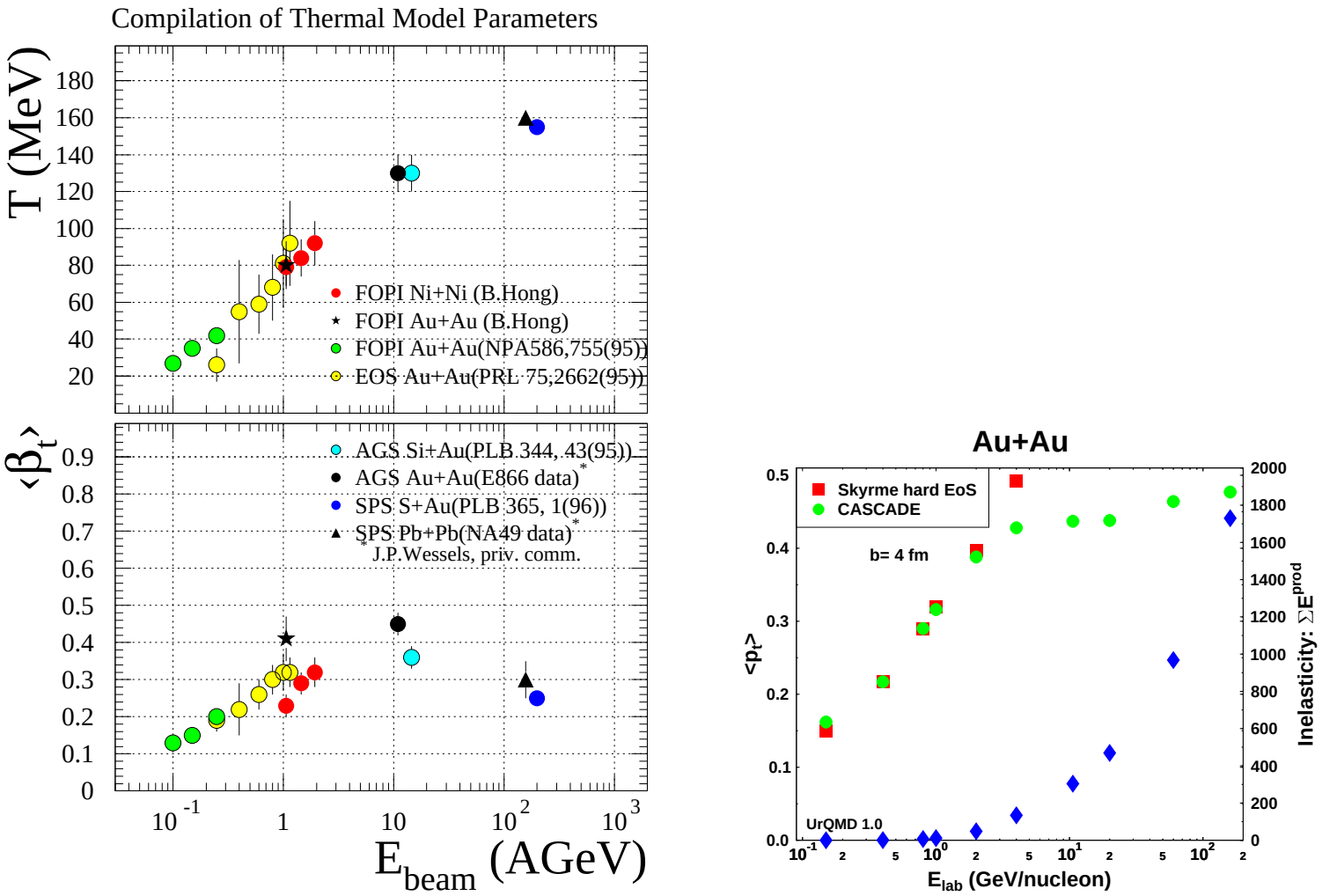

Figure 4.51: Left: Excitation function of temperature T and average transverse expansion velocity β_t. The figure has been taken from [366]. The data are from [369, 370, 371, 220, 221]. Right: Excitation function of the mean transverse momentum (squares and circles, left ordinate) in comparison with the total energy of produced particles (diamonds, right ordinate). Shown are the UrQMD results for Au+Au collisions with impact parameter $b = 4$ fm.

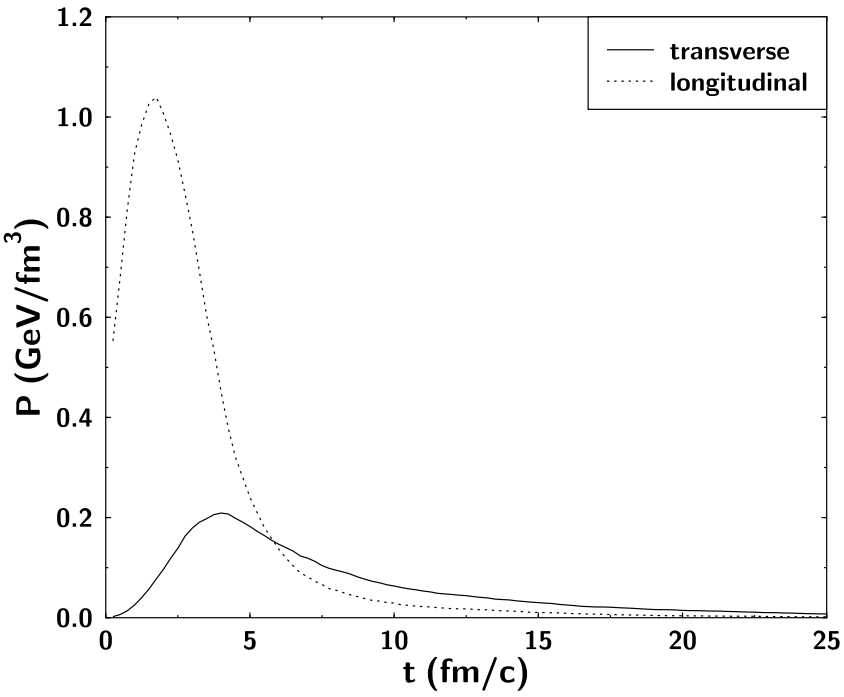

Figure 4.52: Time evolution of the longitudinal and the transverse pressure in the central region of a Au(11GeV)Au collision (b=0) calculated with UrQMD.

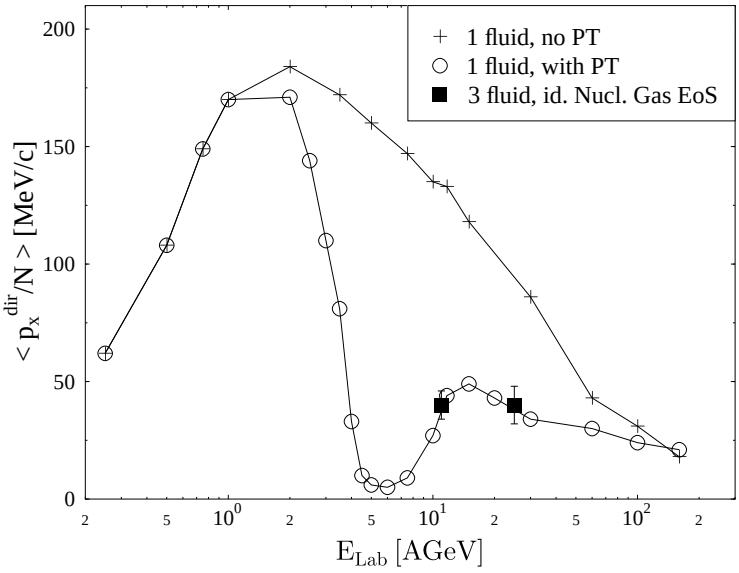

Figure 4.53: Excitation function of directed transverse flow, calculated in the framework of nuclear hydrodynamics [18, 373], with and without deconfinement phase transition. In the case of a phase transition a minimum in the excitation function is clearly visible. Solid squares correspond to a 3-fluid model calculation with ideal nucleon gas EoS.

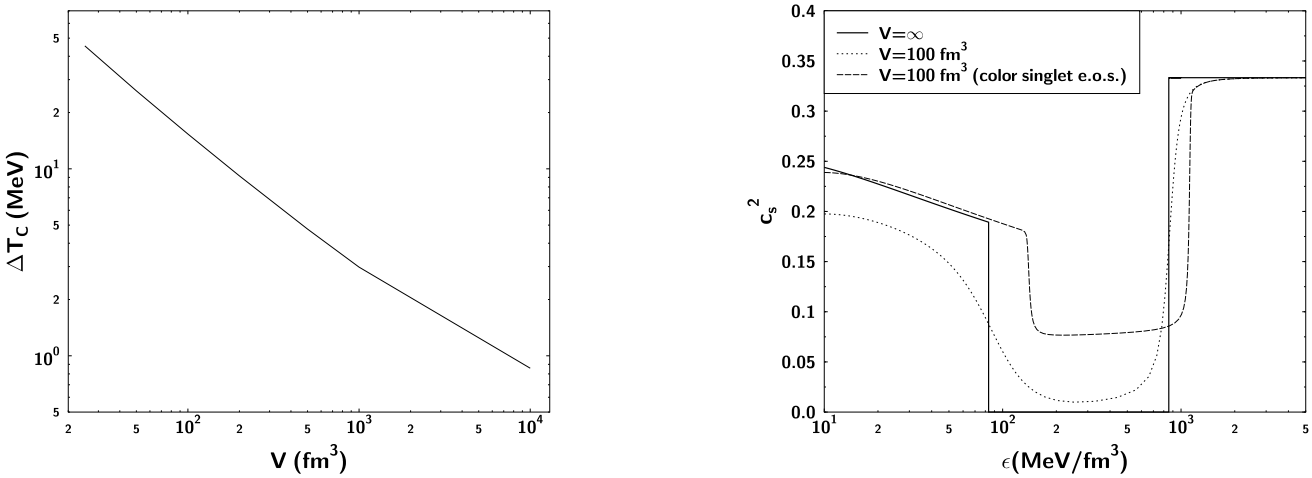

Figure 4.54: Left: Shift of the critical temperature ΔT_{C} vs. the systems size V. The bag constant is $B^{1/4} = 200$ MeV. The color singlet constraint is taken into account for the QGP equation of state. Right: Speed of sound (squared) c_s^2 as a function of energy density ϵ for three different cases:
1) infinite volume of the system (full line).
2) $V = 100\,\mathrm{fm}^3$ using the infinite matter EoS (dotted).
3) $V = 100\,\mathrm{fm}^3$ using the EoS with color singlet constraint (dashed).
Figures taken from [281]

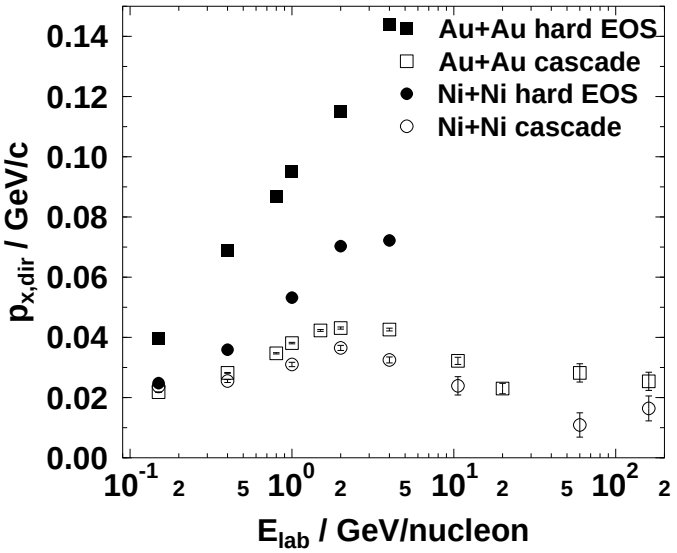

Figure 4.55: Excitation function of the total directed transverse momentum transfer p_x^{dir} for the Au+Au and Ni+Ni systems. UrQMD calculations including a hard equation of state (full symbols) are compared to UrQMD cascade calculations (open symbols).

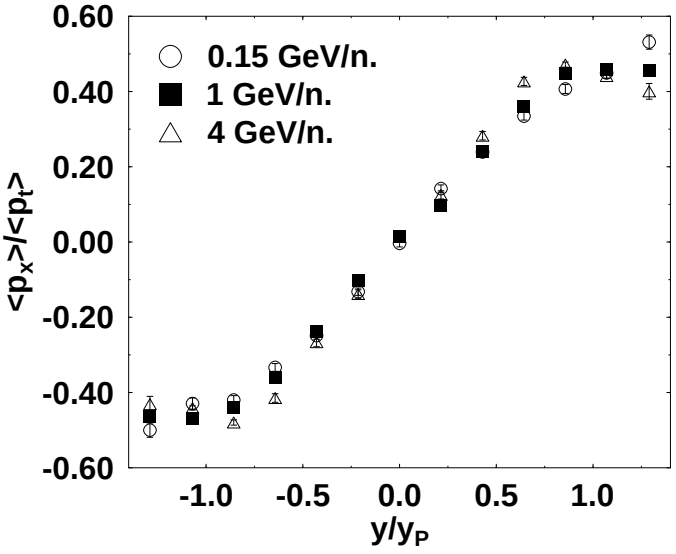

Figure 4.56: Mean directed transverse momentum as a function of the scaled rapidity for Au+Au at b=4 fm (UrQMD calculation). If the transverse flow is scaled with the mean transverse momentum, the sidewards does not depend on the bombarding energy.

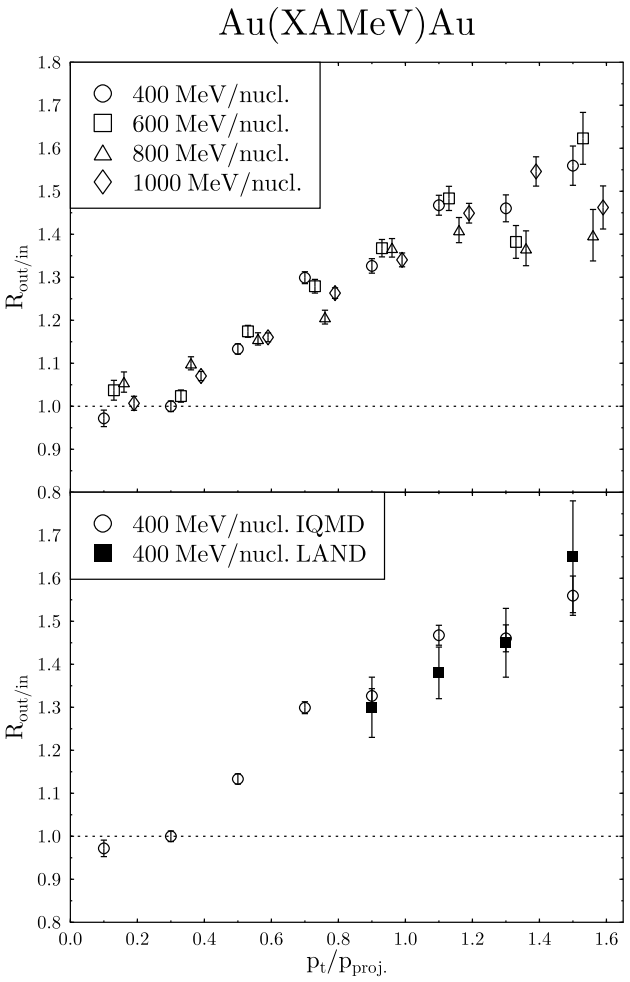

Figure 4.57: *Squeeze–out ratio* $R_{out/in}$ versus scaled transverse momentum p_t/p_{proj} for neutrons in Au+Au collisions at 400, 600, 800 and 1000 MeV/nucleon calculated with a hard equation of state without momentum dependent interaction (top) and a comparison between the IQMD calculation and data by the LAND collaboration for 400 MeV/nucleon (bottom). By scaling p_t with $p_{proj.}$ the ratio becomes independent of the incident beam energy (top). The binning is identical for all 4 energies, the symbols were shifted to increase the readability of the figure. The calculation shows good agreement with the data (bottom).

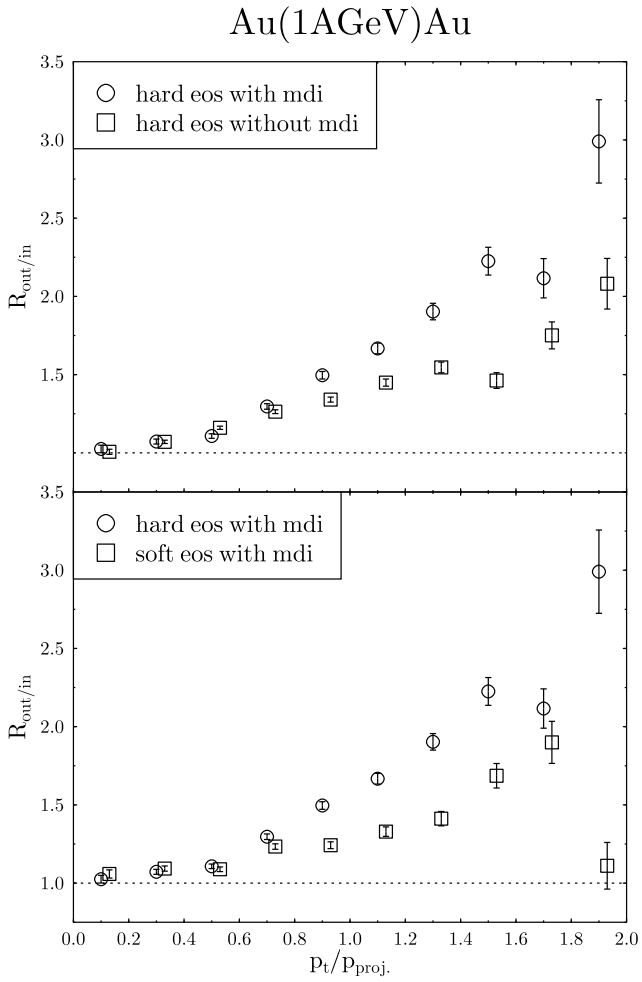

Figure 4.58: *Squeeze–out ratio* $R_{out/in}$ versus scaled transverse momentum p_t/p_{proj} for neutrons in Au+Au collisions at 1 GeV/nucl.. The upper frame shows a comparison between IQMD calculations with a hard equation of state with and without momentum dependent interaction (mdi). For large transverse momenta $p_t/p_{proj} \geq 1$ the calculation with mdi exhibits a 50% larger *squeeze–out ratio*. The lower frame shows a comparison between calculations with hard equation of state with mdi and soft equation of state with mdi: Again, for large transverse momenta $p_t/p_{proj} \geq 1$ the hard equation of state shows a 50% higher *squeeze–out ratio* than the soft equation of state.

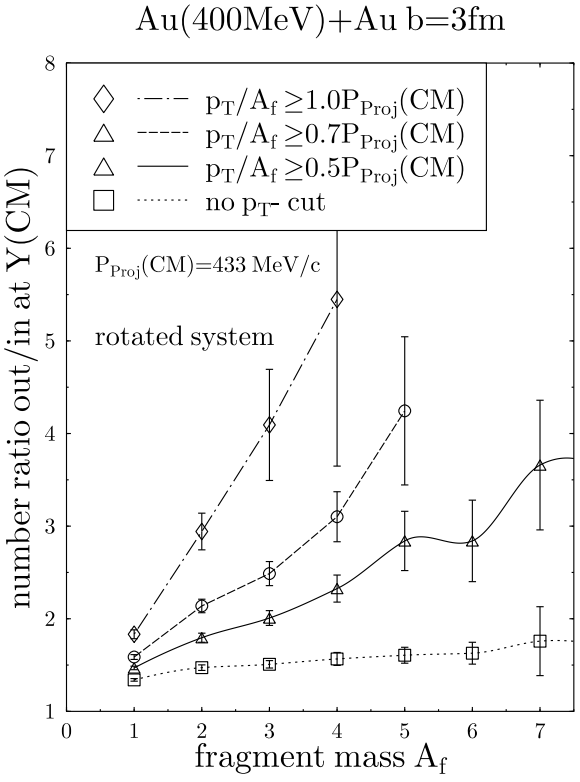

Figure 4.59: *Squeeze–out ratio* $R_{out/in}$ versus fragment mass A_f for Au+Au collisions at 400 MeV/nucleon (IQMD calculation). The system has been rotated by Θ_{flow} into the principal axis system, which enhances $R_{out/in}$. The rise of $R_{out/in}$ with increasing fragment mass is clearly visible, especially for high transverse momenta p_t/A_f. The figure has been taken from [384].

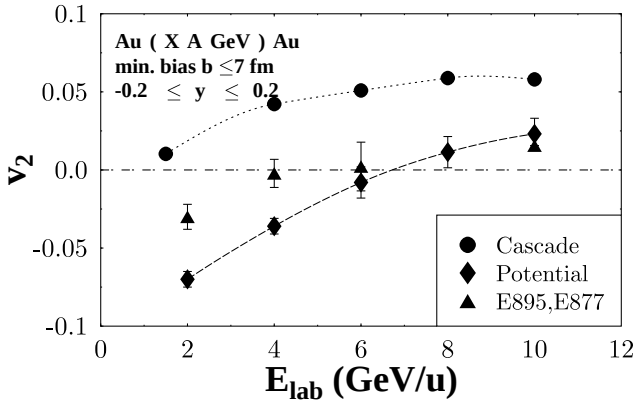

Figure 4.60: UrQMD calculation of the elliptical flow parameter v_2 for Au+Au collisions with (diamond) and without (circle) potentials. Also shown (triangle) are the preliminary data of the E877 and E895 collaborations [387].

Chapter 5

Summary and conclusions

This review has by no means covered the entire field of microscopic transport model applications to (ultra-)relativistic heavy ion collisions. To cover the entire field in one review is almost impossible due to its fast development pace and the width of applications which have been added in the last couple of years. Instead, we have selected a sample of topics which allow to elucidate different important features of microscopic non-equilibrium transport theory. Of course a "good" transport model must be able to come close to known correct data. It should predict the outcome of future experiments. However, it's usefulness must stretch far beyond that of a mere event-generator: it allows for the analysis of the underlying physics (the "input" of the transport model) and shows how the various components contribute to the final result of the calculation.

In chapter 2 the concepts of microscopic transport theory have been introduced and the features and shortcomings of the most commonly used ansatzes are discussed. For pedagogical reasons transport theory is first discussed extensively for the non-relativistic case and the relativistic extension is introduced in a subsequent section. An introduction to the Quantum Molecular Dynamics model concludes this chapter.

The UrQMD transport model has been described in great detail in chapter 3. Based on the same principles as QMD and RQMD it incorporates a vastly extended collision term with full baryon-antibaryon symmetry, 55 baryon and 32 meson species. Isospin is explicitly treated for all hadrons. The range of applicability stretches from $E_{lab} < 100$ MeV/nucleon up to $E_{lab} > 200$ GeV/nucleon, allowing for a consistent calculation of excitation functions from the intermediate energy domain up to ultrarelativistic energies. The UrQMD model as described in chapter 3 is no static structure. Its most important purpose is to serve as a framework into which new transport theoretical concepts and physics ideas can be incorporated, so that their effects on (ultra-)relativistic heavy ion reactions may be explored.

Among the tasks to be tackled in the near future are the implementation of a relativistic generalization of n-body forces, an improved treatment of the imaginary part of the relativistic hadron self-energy (off-shell propagation), medium-dependent cross sections, an improved treatment of resonance lifetimes and time-delays as well as the inclusion of partonic degrees of freedom. The latter is important for the extension and continued application of transport models at collider energies (RHIC and LHC). The intriguing role of color coherence phenomena (transparency and opacity) for fluctuations, stopping and charmonium production can be studied best at these energies. However, even at these high energies, hadronic degrees of freedom must not be neglected since hadronic interactions in the late reaction phase may considerably change the hadrochemical cocktail and phase space distribution of the system (e.g. via feeding).

Applications of transport models to (ultra-)relativistic heavy ion collisions have then been reviewed in chapter 4. The main topics under discussion have been stopping, particle production and collective flow. The main emphasis in the stopping section has been on the scaling behavior of the rapidity distribution

with respect to the incident beam energy and collision system mass as well as the dependence of the stopping behavior on the (di-)quark hadron cross section (i.e. the formation time dependence).

The section on particle production has carried the largest weight in this review: subthreshold production of antiprotons has been used as an example of subthreshold particle production in heavy ion collisions – the ideas and concepts being very similar for other particle species such as etas and kaons. Multi-step processes and the excitation of heavy resonances dominate this domain of particle production. Therefore subthreshold particle production is a sensitive probe for the investigation of in-medium cross sections and the nuclear equation of state. Single particle spectra have been discussed for protons, deuterons, tritons and pions. The proton and cluster spectra have been used to point out problems with the source temperature extraction from single particle spectra. Pion energy spectra show how different regions of the spectra may be sensitive to different sources and reaction stages.

Particle ratios have been used to discuss problems of temperature and chemical potential extraction via chemical equilibrium assumptions. The rapidity dependence of certain particle ratios may allow for the in-depth investigation of the baryon stopping mechanism in heavy ion collisions. The UrQMD exhibits the properties of a free hadron gas, however with a limiting temperature of approximately 140 MeV. The central cell in Au+Au reactions at AGS seems to be close to local thermal and chemical equilibrium.

The formation of resonance matter has been discussed in great detail. The fraction of excited matter in the collision system rises continuously from 20% at SIS up to 70% at CERN SPS energies. The properties and interactions of highly excited resonance matter is an important topic for further research. Creation of strange matter is discussed, although explicit *strangelet*-formation has yet to be included into microscopic transport model calculations. Hyperclusters and (anti-)deuterons have served as examples for the formation of composite particles. The main emphasis of the discussion has been on the phase space distributions of anti-deuterons and the sensitivity of the respective (centrality dependent) yields on parameters such as the formation time and the treatment of the baryon-antibaryon annihilation cross section.

Freeze-out distributions of mesons and hyperons at SIS and SPS energies show that global equilibration is not achieved in heavy ion reactions. The distributions indicate a complex non-equilibrium time evolution of the hadronic system. A thermal model although quite successful in fitting the data, may not be yielding the correct physics interpretation.

Electromagnetic probes allow for an unhindered view into the hot and dense reaction zone. This review focused on dilepton production (both at BEVALAC and SPS energies) and the creation of secondary Drell-Yan pairs at CERN/SPS energies, two of the most current topics. The latter offer a novel explanation for the observed dimuon excess in the intermediate mass range of $1.5 \leq m \leq 2.5$ GeV of the dimuon-spectrum. A brief discussion of charmonium production and suppression concludes the section on particle production.

The final section of chapter 4 deals with collective flow. The excitation function of the directed flow in the reaction plane can provide a signature for the hadron gas to quark gluon plasma phase transition. However, finite size effects may severely diminish the signal. Transport model calculations (which in most cases do not contain a phase transition) serve here again as an important smooth baseline to check the occurrence of possible QGP signatures, namely as irregularities in the excitation function, taken in small steps, $\Delta E \approx 5$ GeV or so. The sensitivity of flow perpendicular to the reaction plane to the nuclear equation of state is analyzed. Especially the squeeze-out excitation function seems to offer new possibilities for the investigation of the density dependence of the nuclear equation of state.

Microscopic transport models like UrQMD are a unique tool to further develop the general understanding of the dynamics of heavy ion collisions and interactions over a vast energy range from the Coulomb barrier (several MeV per nucleon) to the highest energies currently available or planned for the future. Their development is by far not complete. Nevertheless they allow for important insights into the field of hot, dense hadronic matter created in (ultra-)relativistic heavy ion reactions.

Bibliography

[1] W. Scheid, R. Ligensa, and W. Greiner, Phys. Rev. Lett. **21**, 1479 (1968).

[2] G. F. Chapline, M. H. Johnson, E. Teller, and M. S. Weiss, Phys. Rev. **D8**, 4302 (1973).

[3] E. V. Shuryak, Phys. Rep. **61**, 71 (1980).

[4] J. D. Bjorken, Phys. Rev. **D27**, 140 (1983).

[5] L. P. Csernai and J. I. Kapusta, Phys. Rep. **131**, 223 (1986).

[6] R. Stock, Phys. Rep. **135**, 261 (1986).

[7] H. Stöcker and W. Greiner, Phys. Rep. **137**, 277 (1986).

[8] R. R. Clare and D. Strottman, Phys. Rep. **141**, 179 (1986).

[9] B. Schuermann and W. Zwermann, Phys. Rep. **147** (1985).

[10] W. Cassing, V. Metag, U. Mosel, and K. Niita, Phys. Rep. **188**, 363 (1990).

[11] C. M. Ko and G. Q. Li, J. Phys. **G22**, 1673 (1996).

[12] J. Harris and B. Müller, Ann. Rev. Nucl. Part. Sci. **46**, 71 (1996), hep-ph/9602235.

[13] J. Pochodzalla *et al.*, Phys. Rev. Lett. **75**, 1040 (1995).

[14] H. Stöcker, W. Greiner, and W. Scheid, Z. Phys. **A286**, 121 (1978).

[15] J. Hofmann, H. Stöcker, U. Heinz, W. Scheid, and W. Greiner, Phys. Rev. Lett. **36**, 88 (1976).

[16] N. S. Amelin, L. P. Csernai, E. F. Staubo, and D. Strottman, Nucl. Phys. **A544**, 463 (1992).

[17] L. V. Bravina, N. S. Amelin, L. P. Csernai, P. Levai, and D. Strottman, Nucl. Phys. **A566**, 461c (1994).

[18] D. H. Rischke, Y. Pürsün, J. A. Maruhn, H. Stöcker, and W. Greiner, Heavy Ion Physics **1**, 309 (1995), nucl-th/9505014.

[19] M. Juric *et al.*, Nucl. Phys. **B52**, 1 (1973).

[20] D. H. Wilkinson, S. Lorant, D. Robinson, and S. Lokanathan, Phys. Rev. Lett. **3**, 397 (1959).

[21] A. S. Mondal, A. K. Basak, M. M. Kasim, and A. Husain, Nuovo Cim. **54A**, 333 (1979).

[22] S. Aoki *et al.*, Prog. Theor. Phys. **89**, 493 (1993).

[23] F. S. Rotondo *et al.*, Nucl. Phys. **A610**, 297c (1996).

[24] R. Klingenberg *et al.*, Nucl. Phys. **A610**, 306c (1996).

[25] J. Schaffner, C. Greiner, and H. Stöcker, Phys. Rev. **C46**, 322 (1992).

[26] A. J. Baltz *et al.*, Phys. Lett. **B325**, 7 (1994).

[27] D. D. Ivanenko and D. F. Kurdgelaidze, Astrophys. **1**, 251 (1965).

[28] A. R. Bodmer, Phys. Rev. **D4**, 1601 (1971).

[29] S. A. Chin and A. K. Kerman, Phys. Rev. Lett. **43**, 1292 (1979).

[30] E. Farhi and R. L. Jaffee, Phys. Rev. **D30**, 2379 (1984).

[31] E. Witten, Phys. Rev. **D30**, 272 (1984).

[32] F. C. Michel, Phys. Rev. Lett. **60**, 677 (1988).

[33] C. Greiner, P. Koch, and H. Stöcker, Phys. Rev. Lett. **58**, 1825 (1987).

[34] C. Spieles *et al.*, Phys. Rev. Lett. **76**, 1776 (1996).

[35] C. Greiner, K. Wagner, and P. G. Reinhard, Phys. Rev. **C49**, 1693 (1994).

[36] D. G. Currie, T. F. Jordan, and E. C. G. Sudarshan, Rev. Mod. Phys. **35**, 350 (1963).

[37] H. Sorge, H. Stöcker, and W. Greiner, Ann. Phys. **192**, 266 (1989).

[38] H. P. Duerr, Phys. Rev. **103**, 469 (1956).

[39] J. D. Walecka, Ann. Phys. **83**, 491 (1974).

[40] J. Schwinger, J. Math. Phys. **2**, 407 (1961).

[41] L. Kadanoff and G. Baym, *Quantum Statistical Mechanics* (W.A. Benjamin, New York, 1962).

[42] P. Danielewicz, Ann. Phys. **152**, 239 (1984).

[43] W. Botermans and R. Malfliet, Phys. Rep. **198**, 115 (1990).

[44] P. Martin and J. Schwinger, Phys. Rev. **115**, 1342 (1959).

[45] R. M. R. Brockmann, Phys. Rev. **C42**, 1965 (1990).

[46] L. Sehn and H. Wolter, Nucl. Phys. **A601**, 473 (1996).

[47] J. Jaenicke, J. Aichelin, N. Ohtsuka, R. Linden, and A. Faessler, Nucl. Phys. **A536**, 201 (1992).

[48] C. Fuchs, L. Sehn, and H. Wolter, Nucl. Phys. **A601**, 505 (1996).

[49] A. Vlasov, Zh. Eksp. Teor. Fiz. **8**, 291 (1938).

[50] L. Nordheim, Proc. Roy. Soc. London **A119**, 689 (1928).

[51] E. A. Uehling and G. E. Uhlenbeck, Phys. Rev. **43**, 552 (1933).

[52] E. A. Uehling and G. E. Uhlenbeck, Phys. Rev. **44**, 917 (1934).

[53] J. J. Molitoris, J. B. Hoffer, H. Kruse, and H. Stöcker, Phys. Rev. Lett. **53**, 899 (1984).

[54] H. Kruse, B. V. Jacak, and H. Stöcker, Phys. Rev. **C31**, 1770 (1985).

[55] G. Bertsch, S. D. Gupta, and H. Kruse, Phys. Rev. **C29**, 673 (1984).

[56] J. Aichelin and G. Bertsch, Phys. Rev. **C31**, 1730 (1985).

[57] C. Gregoire, B. Remaud, F. Sebille, and L. Vinet, Nucl. Phys. **A465**, 317 (1987).

[58] G. Wolf *et al.*, Nucl. Phys. **A517**, 615 (1990).

[59] P. Danielewicz, Phys. Lett. **B146**, 168 (1984).

[60] L. D. Landau, Zh. Eksp. Teor. Fiz. **30**, 1058 (1956).

[61] D. Pines and P. Nozieres*Theory of Quantum Liquids* Vol. 1 (Benjamin Inc., New York, 1966).

[62] J. P. Bondorf *et al.*, Phys. Lett. **B65**, 217 (1976).

[63] K. K. Gudima, H. Iwe, and V. D. Toneev, J. Phys. **C5**, 229 (1977).

[64] Y. Yariv and Z. Frankel, Phys. Rev. **C20**, 2227 (1979).

[65] J. Cugnon, Phys. Rev. **C22**, 1885 (1980).

[66] Y. Yariv and Z. Frankel, Phys. Rev. **C24**, 488 (1981).

[67] E. C. Halbert, Phys. Rev. **C23**, 295 (1981).

[68] G. M. Welke *et al.*, Phys. Rev. **C40**, 2611 (1989).

[69] J. Aichelin, Phys. Rep. **202**, 233 (1991).

[70] J. Aichelin *et al.*, Phys. Lett. **B224**, 34 (1989).

[71] C. Hartnack, H. Stöcker, and W. Greiner, Study of Observables from heavy ion data using vuu and qmd calculations, in *Proc. of the Nato Adv. Study Inst. on the Nucl. Equation of State (Peniscola, Spain)*, edited by W. Greiner and H. Stöcker, Plenum Press, 1990.

[72] C. Hartnack *et al.*, Nucl. Phys. **A538**, 53c (1992).

[73] P.-G. Reinhard, Rep. Prog. Phys. **52**, 439 (1989).

[74] K. Rutz, J. Maruhn, P.-G. Reinhard, and W. Greiner, Nucl. Phys. **A590**, 680 (1995).

[75] G. Mao *et al.*, Z. Phys. **A347**, 173 (1994).

[76] G. Mao, L. Neise, H. Stöcker, W. Greiner, and Z. Li, submitted to Phys. Rev. **C** (1997).

[77] J. Boguta and A. R. Bodmer, Nucl. Phys. **A292**, 413 (1977).

[78] A. R. Bodmer, Nucl. Phys. **A526**, 703 (1991).

[79] G. Mao, Z. Li, Y. Zhuo, and Y. Han, Phys. Rev. **C49**, 3137 (1994).

[80] W. Cassing and U. Mosel, Prog. Part. Nucl. Phys. **25**, 1 (1990).

[81] I. N. Mishustin, L. M. Satarov, H. Stöcker, and W. Greiner, (1997), hep-ph/9709384.

[82] K. Weber *et al.*, Nucl. Phys. **A515**, 747 (1990).

[83] C. Ko, Q. Li, and R. Wang, Phys. Rev. Lett. **59**, 1084 (1987).

[84] R. Cusson *et al.*, Phys. Rev. Lett. **55**, 2786 (1985).

[85] C. Fuchs and H. Wolter, Nucl. Phys. **A589**, 732 (1995).

[86] M. Asakawa, C. M. Ko, P. Levai, and X. J. Qiu, Phys. Rev. **C46**, R1159 (1992).

[87] M. Herrmann, B. Friman, and W. Nörenberg, Nucl. Phys. **A560**, 411 (1993).

[88] B. L. Friman and H. J. Pirner, Nucl. Phys. **A617**, 496 (1997).

[89] R. Rapp, G. Chanfray, and J. Wambach, Nucl. Phys. **A617**, 472 (1997).

[90] F. Klingl, N. Kaiser, and W. Weise, Nucl. Phys. **A624**, 527 (1997), hep-ph/9704398.

[91] W. Peters, M. Post, H. Lenske, S. Leupold, and U. Mosel, (1997), nucl-th/9708004.

[92] P. Danielewicz and G. F. Bertsch, Nucl. Phys. **A533**, 712 (1991).

[93] B. Andersson, G. Gustafson, G. Ingelman, and T. Sjoestrand, Phys. Rep. **97**, 31 (1983).

[94] B. Nilsson-Almquist and E. Stenlund, Comput. Phys. Commun. **43**, 387 (1987).

[95] H. Pi, Comput. Phys. Commun. **71**, 173 (1992).

[96] T. Sjoerstrand, Comp. Phys. Comm. **39**, 347 (1986).

[97] W. Ehehalt and W. Cassing, Nucl. Phys. **A602**, 449 (1996), hep-ph/9507274.

[98] K. Werner, Phys. Rep. **232**, 87 (1993).

[99] K. Geiger and B. Müller, Nucl. Phys. **B369**, 600 (1992).

[100] K. Geiger, Phys. Rep. **258**, 237 (1995).

[101] A. Capella, U. Sukhatme, and J. T. T. Van, Z. Phys. **C3**, 329 (1980).

[102] A. Capella, U. Sukhatme, C. I. Tan, and J. T. T. Van, Phys. Rep. **236**, 225 (1994).

[103] X. N. Wang and M. Gyulassy, Phys. Rev. **D44**, 3501 (1991).

[104] A. Shor and R. Longacre, Phys. Lett. **B218**, 100 (1989).

[105] K. Werner and J. Aichelin, Phys. Lett. **B308**, 372 (1993).

[106] H. Sorge, Phys. Lett. **B344**, 35 (1995).

[107] Y. Pang, T. J. Schlagel, and S. H. Kahana, Phys. Rev. Lett. **68**, 2743 (1992).

[108] J. Aichelin, A. Rosenhauer, G. Peilert, H. Stöcker, and W. Greiner, Phys. Rev. Lett. **58**, 1926 (1987).

[109] J. Aichelin and H. Stöcker, Phys. Lett. **B176**, 14 (1986).

[110] G. Peilert, A. Rosenhauer, J. Aichelin, H. Stöcker, and W. Greiner, Phys. Rev. **C39**, 1402 (1989).

[111] S. A. Bass, C. Hartnack, H. Stöcker, and W. Greiner, Phys. Rev. **C51**, 3343 (1995), nucl-th/9501002.

[112] S. Teis *et al.*, Z. Phys. **A356**, 421 (1997).

[113] G. Kortemeyer, W. Bauer, K. Haglin, J. Murray, and S. Pratt, Phys. Rev. **C52**, 2714 (1995).

[114] H. Feldmeier, Nucl. Phys. **A515**, 147 (1990).

[115] A. Ono, H. Horiuchi, T. Maruyama, and A. Ohnishi, Phys. Rev. Lett. **68**, 2898 (1992).

[116] H. Feldmeier and J. Schnack, Prog. Part. Nucl. Phys. **39**, 393 (1997).

[117] A. R. Bodmer and C. N. Panos, Phys. Rev. **C15**, 1342 (1977).

[118] L. Wilets, E. M. Henley, M. Kraft, and A. D. McKellar, Nucl. Phys. **A282**, 341 (1977).

[119] A. R. Bodmer, C. N. Panos, and A. MacKellar, Phys. Rev. **C22**, 1025 (1980).

[120] S. Kiselev and Y. Pokrovskil, Sov. J. Nucl. Phys. **38**, 46 (1983).

[121] C. Hartnack *et al.*, Nucl. Phys. **A495**, 303 (1989).

[122] N. Metropolis, A. Rosenbluth, M. Rosenbluth, A. Teller, and E. Teller, J. Chem. Phys. **21**, 1087 (1953).

[123] J. Konopka, Thesis, Goethe Universität, Frankfurt am Main, Germany (1996).

[124] T. Kodama, S. B. Duarte, K. C. Chung, R. Donangelo, and R. A. M. S. Nazareth, Rio De Janeiro Pesquisas Fis. **NF-83-026** (1983).

[125] Particle-Data-Group, Phys. Rev. **D54** (1996).

[126] M. Berenguer, Thesis, Goethe Universität, Frankfurt am Main, Germany (1993).

[127] V. Flaminio, W. G. Moorhead, D. R. O. Morrison, and N. Rivoire, CERN, Geneva Report No. CERN-HERA-84-01, 1984 (unpublished).

[128] M. Block and J. Jackson, Z. Phys. **C3**, 255 (1980).

[129] C. B. Dover, T. Gutsche, M. Maruyama, and A. Faessler, Prog. Part. Nucl. Phys. **29**, 87 (1992).

[130] B. Loiseau, Nucl. Phys. **A543**, 33c (1992).

[131] P. Koch and C. B. Dover, Phys. Rev. **C40**, 145 (1989).

[132] T. Elioff *et al.*, Phys. Rev. **128**, 869 (1962).

[133] P. Koch, B. Müller, and J. Rafelski, Phys. Rep. **142**, 167 (1986).

[134] K. Goulianos, Phys. Rep. **101**, 169 (1983).

[135] G. Mao, Z. Li, and Y. Zhuo, Phys. Rev. **C53**, 2933 (1996).

[136] P. Danielewicz and S. Pratt, Phys. Rev. **C53**, 249 (1996).

[137] J. Schwinger, Phys. Rev. **82**, 664 (1951).

[138] B. Andersson, G. Gustavson, and T. Sjoestrand, Nucl. Phys. **B197**, 45 (1982).

[139] B. Andersson, G. Gustavson, and B. Soederberg, Z. Phys. **C20**, 317 (1983).

[140] R. D. Field and R. P. Feynman, Phys. Rev. **D15**, 2590 (1977).

[141] R. D. Field and R. P. Feynman, Nucl. Phys. **B136**, 1 (1978).

[142] G. Charlton *et al.*, Phys. Rev. Lett. **30**, 574 (1973).

[143] T. Kafka *et al.*, Phys. Rev. **D16**, 1261 (1977).

[144] F. Becattini and U. Heinz, Z. Phys. **C76**, 269 (1997), hep-ph/9702274.

[145] M. Aguilar-Benitez *et al.*, Z. Phys. **C50**, 405 (1991).

[146] H. Kichimi *et al.*, Phys. Rev. **D20**, 37 (1979).

[147] M. Antinucci *et al.*, Lett. Nuovo Cim. **6**, 121 (1973).

[148] L. Frankfurt, G. Miller, and M. Strikman, Annu. Rev. Part. Sci. **44**, 501 (1994).

[149] L. Gerland, L. Frankfurt, M. Strikman, H. Stöcker, and W. Greiner, to be submitted for publication (1998).

[150] W. Scheid., H. Mueller, and W. Greiner, Phys. Rev. Lett. **32**, 741 (1974).

[151] W. Busza and A. S. Goldhaber, Phys. Lett. **B139**, 235 (1984).

[152] C. Hartnack, Diploma, Goethe Universitaet, Frankfurt am Main, Germany (1989).

[153] M. Berenguer *et al.*, J. Phys **G18**, 655 (1992).

[154] W. Schmidt *et al.*, Phys. Rev. **C47**, 2782 (1993).

[155] M. Gyulassy and W. Greiner, Ann. Phys. **109**, 485 (1977).

[156] L. Frankfurt and M. Strikman, Phys. Rev. Lett. **66**, 2289 (1991).

[157] J. Günther, Thesis (NA49 Coll.), Goethe Universität, Frankfurt am Main, Germany (1998).

[158] J. Baechler *et al.*, Phys. Rev. Lett. **72**, 1419 (1994).

[159] A. v. Keitz *et al.*, Phys. Lett. **B263**, 353 (1991).

[160] H. Sorge, M. Berenguer, H. Stöcker, and W. Greiner, Phys. Lett. **B289**, 6 (1992).

[161] S. A. Bass *et al.*, Urqmd - a new molecular dynamics model from ganil to cern energies, in *Proceedings of the International Conference on Nuclear Physics at the Turn of the Millenium: Structure of Vacuum and Elementary Matter, in Wilderness, South Africa, March 1996*, World Scientific Publishing Co., Singapore, 1996.

[162] J. Aichelin and K. Werner, Phys. Lett. **B300**, 158 (1993).

[163] B. Andersson, G. Gustavson, and B. Nilsson-Almquist, Nucl. Phys. **B281**, 289 (1987).

[164] B. Andersson *et al.*, Comp. Phys. Comm. **43**, 387 (1987).

[165] T. Sjoestrand, Comp. Phys. Comm. **82**, 74 (1994).

[166] S. Jeon and J. Kapusta, Phys. Rev. **C56**, 468 (1997).

[167] R. Glauber, *Lectures in Theoretical Physics* Vol. 1 (W.E. Britten and L.G. Dunham, New York, 1959).

[168] J. Hüfner and J. Knoll, Nucl. Phys. **A290**, 460 (1977).

[169] M. N. A. Leonidov and H. Satz, Z. Phys. **C74**, 535 (1997).

[170] J. B. Carroll *et al.*, Phys. Rev. Lett. **62**, 1829 (1989).

[171] A. Schröter *et al.*, Physica Scripta **48**, 184 (1993).

[172] A. Schröter *et al.*, Z. Phys. **A350**, 101 (1994).

[173] A. Shor, V. Perez-Mendez, and K. Ganezer, Nucl. Phys. **A514**, 717 (1990).

[174] A. Jahns, H. Sorge, H. Stöcker, and W. Greiner, Z. Phys. **A341**, 243 (1992).

[175] A. Jahns, H. Stöcker, W. Greiner, and H. Sorge, Phys. Rev. Lett. **68**, 2895 (1992).

[176] A. Jahns *et al.*, Phys. Lett. **B308**, 11 (1993).

[177] J. Schaffner, I. N. Mishustin, L. M. Satarov, H. Stöcker, and W. Greiner, Z. Phys. **A341**, 47 (1991).

[178] C. M. Ko and L. H. Xia, Phys. Rev. **C40**, 1118 (1989).

[179] S. Teis, W. Cassing, T. Maruyama, and U. Mosel, Phys. Rev. **C50**, 388 (1994).

[180] A. Sibirtsev, W. Cassing, G. Lykasov, and M. Rzyanin, submitted to Nucl. Phys. A Preprint nucl-th/9710044 .

[181] G. Batko, A. Faessler, S. W. Huang, E. Lehmann, and R. K. Puri, J. Phys. **G20**, 461 (1994).

[182] G. Q. Li, C. M. Ko, X. S. Fang, and Y. M. Zheng, Phys. Rev. **C49**, 1139 (1994).

[183] C. Spieles, A. Jahns, H. Sorge, H. Stöcker, and W. Greiner, Mod. Phys. Lett. **A8**, 2547 (1993).

[184] R. Mattiello, H. Sorge, H. Stöcker, and W. Greiner, Phys. Rev. Lett. **63**, 1459 (1989).

[185] H. Sorge, A. von Keitz, R. Mattiello, H. Stöcker, and W. Greiner, Nucl. Phys. **A525**, 95c (1991).

[186] C. Spieles, A. Jahns, H. Sorge, H. Stöcker, and W. Greiner, in *Proc. of the XXXII International Winter Meeting on Nuclear Physics, January 24–29 1994, Bormio/Italy* Vol. Supplemento N.97, p. 423, Ricerca Scientifica ed Educazione Permanente, 1994.

[187] R. Mattiello *et al.*, Cluster-flow and resonance-matter formation in ultra-relativistic heavy-ion reactions, in *Hot and Dense Nuclear Matter*, edited by H. S. W. Greiner and A. Gallmann Vol. NATO ASI Series B 335, p. 419, Plenum Press New York and London, 1993.

[188] W. Ehehalt, W. Cassing, A. Engel, U. Mosel, and G. Wolf, Phys. Rev. **C47**, 2467 (1993).

[189] S. A. Bass, M. Hofmann, C. Hartnack, H. Stöcker, and W. Greiner, Phys. Lett. **B335**, 289 (1994).

[190] A. Jahns, C. Spieles, H. Sorge, H. Stöcker, and W. Greiner, Phys. Rev. Lett. **72**, 3464 (1994).

[191] J. Gosset *et al.*, Phys. Rev. **C16**, 629 (1977).

[192] R. Hagedorn and J. Rafelski, Phys. Lett. **B97**, 136 (1980).

[193] N. Xu *et al.*, Nucl. Phys. **A610**, 175c (1996).

[194] M. Bleicher *et al.*, to be submitted for publication (1998).

[195] G. Roland and the NA49 collaboration, Talk at Quark Matter '97, December 1997, Tsukuba, Japan. Nucl. Phys. A (1998), in print. .

[196] K. S. Lee, U. Heinz, and J. Sollfrank, Z. Phys. **C48**, 525 (1990).

[197] P. Siemens and J. Rasmussen, Phys. Rev. **C42**, 880 (1979).

[198] H. Stöcker, A. Ogloblin, and W. Greiner, Z. Phys. **A303**, 259 (1981).

[199] J. Sollfrank, P. Koch, and U. Heinz, Phys. Lett. **B252**, 256 (1990).

[200] R. Mattiello, A. Jahns, H. Sorge, H. Stöcker, and W. Greiner, Phys. Rev. Lett. **74**, 2180 (1995).

[201] R. Mattiello, H. Sorge, H. Stöcker, and W. Greiner, Phys. Rev. **C55**, 1443 (1996), nucl-th/9607003.

[202] C. Hartnack, *Beschreibung von Flusseffekten und Teilchenproduktion in relativistischen Schwerionenstössen*, PhD thesis, Johann Wolfgang Goethe University, Frankfurt, Germany, 1992.

[203] O. Schwalb *et al.*, Phys. Lett. **321**, 20 (1994).

[204] S. Teis *et al.*, Z. Phys. **A359**, 297 (1997), nucl-th/9701057.

[205] B. A. Li, C. M. Ko, and G. Q. Li, Phys. Rev. **C50**, 2675 (1994).

[206] S. A. Bass, C. Hartnack, H. Stöcker, and W. Greiner, Phys. Rev. **C50**, 2167 (1994).

[207] B. A. Li, W. Bauer, and G. F. Bertsch, Phys. Rev. **C44**, 2095 (1991).

[208] B. A. Li and W. Bauer, Phys. Lett. **B254** (1991).

[209] C. Hartnack, H. Stöcker, and W. Greiner, Analysis of diogene's 4π data on δ, π^+, π^- using qmd, in *Proc. of the International Workshop on Gross Properties of Nuclei and Nuclear Excitation, XVI, Hirschegg, Kleinwalsertal, Austria*, edited by H. Feldmeier, 1988.

[210] M. Berenguer *et al.*, Confrontation of theoretical approaches and experimental data on high energy heavy ion collisions, in *Proc. of the Winter School on Nucl. Phys., Les Houches, France*, 1989.

[211] C. Spieles, H. Stöcker, and C. Greiner, Eur. Phys. J. **C**, in print (1998), nucl-th/9704008.

[212] D. Hahn and H. Stöcker, Nucl. Phys. **A476**, 718 (1988).

[213] D. Hahn and H. Stöcker, Nucl. Phys. **A452**, 723 (1986).

[214] J. Rafelski and B. Müller, Phys. Rev. Lett. **48**, 1066 (1982).

[215] J. Rafelski, Phys. Rep. **88**, 331 (1982).

[216] J. Letessier, A. Tounsi, U. Heinz, J. Sollfrank, and J. Rafelski, Phys. Rev. Lett. **70**, 3530 (1993).

[217] J. Letessier, J. Rafelski, and A. Tounsi, Phys. Lett. **B321**, 394 (1994).

[218] J. Sollfrank, M. Gadzicki, U. Heinz, and J. Rafelski, Z. Phys. **C61**, 659 (1994).

[219] J. Cleymans and H. Satz, Z. Phys. **C57**, 135 (1993).

[220] P. Braun-Munzinger, J. Stachel, J. P. Wessels, and N. Xu, Phys. Lett. **B344**, 43 (1995), nucl-th/9410026.

[221] P. Braun-Munzinger, J. Stachel, J. P. Wessels, and N. Xu, Phys. Lett. **B365**, 1 (1996), nucl-th/9508020.

[222] H. W. Barz, B. L. Friman, J. Knoll, and H. Schultz, Nucl. Phys. **A484**, 661 (1988).

[223] H. W. Barz *et al.*, Phys. Lett. **B242**, 328 (1990).

[224] H. W. Barz *et al.*, Nucl. Phys. (Proc. Suppl.) **B24**, 221 (1991).

[225] P. Braun-Munzinger and J. Stachel, Nucl. Phys. **A606**, 320 (1996), nucl-th/9606017.

[226] S. A. Bass *et al.*, nucl-th/9711032.

[227] M. Murray *et al.*, Nucl. Phys. **A566**, 589c (1994).

[228] M. Gazdzicki *et al.*, Nucl. Phys. **A590**, 197C (1995).

[229] J. T. Mitchell, Nucl. Phys. **A566**, 415C (1994).

[230] A. Iyono *et al.*, Nucl. Phys. **A544**, 415c (1992).

[231] J. Simon-Gillo *et al.*, Nucl. Phys. **A590**, 483c (1995).

[232] M. Masera *et al.*, Nucl. Phys. **A590**, 93c (1995).

[233] D. D. Bari *et al.*, Nucl. Phys. **A590**, 307c (1995).

[234] T. Alber *et al.*, Z. Phys. **C64**, 195 (1994).

[235] D. Röhrich *et al.*, Nucl. Phys. **A566**, 35c (1994).

[236] J. Günther *et al.*, Nucl. Phys. **A590**, 487c (1995).

[237] S. Abatzis *et al.*, Nucl. Phys. **A566**, 225c (1994).

[238] E. Andersen *et al.*, Phys. Lett. **B327**, 433 (1994).

[239] J. Barrette *et al.*, Phys. Rev. Lett. **73**, 2532 (1994).

[240] T. Peitzmann *et al.*, Proceedings of the International Workshop on Gross Properties of Nuclei and Nuclear Excitation XXV, *QCD Phase Transitions*, Hirschegg, Kleinwalsertal (Austria), January 1997 .

[241] A. Wagner *et al.*, nucl-ex/9712004.

[242] S. Barshay, G. Brown, and M. Rho, Phys. Rev. Lett. **32**, 787 (1974).

[243] G. D. Yen, M. I. Gorenstein, W. Greiner, and S. N. Yang, Phys. Rev. **C56**, 2210 (1997).

[244] M. Belkacem *et al.*, to be submitted for publication (1998).

[245] L. V. Bravina *et al.*, to be submitted for publication (1998).

[246] J. Barrette *et al.*, Phys. Rev. **C55**, 1420 (1997), nucl-ex/9610006.

[247] J. Boguta and H. Stöcker, Phys. Lett. **B120**, 289 (1983).

[248] J. Boguta, Phys. Lett. **B109**, 251 (1982).

[249] B. Waldhauser, J. A. Maruhn, H. Stöcker, and W. Greiner, Z. Phys. **A328**, 19 (1987).

[250] V. Metag, Prog. Part. Nucl. Phys. **30**, 75 (1993).

[251] W. Ehehalt, W. Cassing, A. Engel, U. Mosel, and G. Wolf, Phys. Lett. **B298**, 31 (1993).

[252] M. Hofmann, Diploma, Goethe University, Frankfurt am Main, Germany (1994).

[253] Y. Z. Zhuxia Li, Guangjun Mao and W. Greiner, Phys. Rev. **C56**, 1570 (1997).

[254] M. Hofmann, R. Mattiello, H. Sorge, H. Stöcker, and W. Greiner, Phys. Rev. **C51**, 2095 (1995).

[255] M. Brandstetter *et al.*, to be submitted for publication (1998).

[256] C. Spieles *et al.*, Nucl. Phys. **A590**, 271c (1995).

[257] M. Aoki *et al.*, Phys. Rev. Lett. **69**, 2345 (1992).

[258] S. Mrowczynski, Phys. Lett. **B308**, 216 (1993).

[259] J. L. Nagle *et al.*, Phys. Rev. Lett. **73**, 2417 (1994).

[260] M. Bleicher *et al.*, Phys. Lett. **B361**, 10 (1995).

[261] U. Heinz, P. R. Subramanian, H. Stöcker, and W. Greiner, J. Phys. G: Nucl. Phys. **12**, 1237 (1986).

[262] W. Greiner, Int. Journ. Mod. Phys. **E5**, 1 (1996).

[263] L. Gerland, Diploma, Goethe - Universitaet Frankfurt am Main (1996).

[264] S. Gavin and R. Vogt, Nucl. Phys. **B345**, 104 (1990).

[265] W. W. Buck, C. B. Dover, and J. M. Richard, Ann. Phys. **121**, 47 (1979).

[266] C. B. Dover and J. M. Richard, Ann. Phys. **121**, 70 (1979).

[267] V. Koch, G. E. Brown, and C. M. Ko, Phys. Lett. **B265**, 29 (1991).

[268] J. G. Lajoie and the E864 Collaboration, Proceedings of the *Conference on Heavy Ion Physics at the AGS* (HIPAGS '96) at Wayne State University, Detroit, USA (1996).

[269] T. A. Armstrong *et al.*, Phys. Rev. Lett. **79**, 3351 (1997).

[270] D. Röhrich, Talk presented at the Int. Workshop on Hadrosynthesis in Nuclear Collisions, April 7-12, Trento, Italy. (1997).

[271] L. G. Arnold, B. C. Clark, R. L. Mercer, and P. Schwandt, Phys. Rev. **C23**, 1949 (1981).

[272] B. S. Kumar *et al.*, Nucl. Phys. **A566**, 439C (1994).

[273] C. Spieles *et al.*, Phys. Rev. **C53**, 2011 (1996).

[274] C. Spieles *et al.*, Proc. Int. Conf.: Structure of Vacuum and Elementary Matter, 10-16 March 1996, Wilderness/George, South Africa, World Scientific Publ. Co., Singapore.
e-print nucl-th/9606027 and manuscript in preparation .

[275] J. Theis *et al.*, Phys. Rev. **D28**, 2286 (1983).

[276] J. D. Bjorken and L. McLerran, Phys. Rev. **D20**, 2353 (1979).

[277] H.-C. Liu and G. L. Shaw, Phys. Rev. **D30**, 1137 (1984).

[278] C. Greiner, D.-H. Rischke, H. Stöcker, and P. Koch, Phys. Rev. **D38**, 2797 (1988).

[279] C. Greiner and H. Stöcker, Phys. Rev. **D44**, 3517 (1991).

[280] Y. Akiba *et al.*, Nucl. Phys. **A610**, 139c (1996).

[281] C. Spieles, H. Stöcker, and C. Greiner, Phys. Rev. **C57**, 908 (1998), hep-ph/9708280.

[282] P. Braun-Munzinger and J. Stachel, J. Phys. G: Nucl. Part. Phys. **21**, L20 (1993).

[283] R. Jaffe, Phys. Rev. Lett. **38**, 195 (1977).

[284] J. Sollfrank, P. Koch, and U. Heinz, Z. Phys. **C52**, 593 (1991).

[285] W. Weise, Nucl. Phys. **A553**, 59c (1993).

[286] E. L. Feinberg, Nuovo Cim. **34A**, 391 (1976).

[287] E. V. Shuryak, Phys. Lett. **B78**, 150 (1978).

[288] G. Domokos and J. I. Goldman, Phys. Rev. **D23**, 203 (1981).

[289] J. Kapusta, P. Lichard, and D. Seibert, Phys. Rev. **D44**, 2774 (1991).

[290] S. D. Drell and T. M. Yan, Phys. Rev. Lett. **25**, 316 (1970).

[291] C. Gale and J. Kapusta, Phys. Rev. **C35**, 2107 (1987).

[292] K. Haglin and C. Gale, Phys. Rev. **C49**, 401 (1994).

[293] J. Murray, W. Bauer, and K. Haglin, (1996), hep-ph/9611328.

[294] M. C. Birse, J. Phys. **G20**, 1537 (1994).

[295] G. E. Brown and M. Rho, Phys. Rep. **269**, 333 (1996).

[296] W. Weise, Nucl. Phys. **A610**, 35c (1996).

[297] C. Bernard *et al.*, Phys. Rev. **D45**, 3854 (1992).

[298] P. Gerber and H. Leutwyler, Nucl. Phys. **B321**, 387 (1989).

[299] E. G. Drukarev and E. M. Levin, Nucl. Phys. **A511**, 679 (1990).

[300] M. A. Shifman, A. I. Vainshtein, and V. I. Zakharov, Nucl. Phys. **B147**, 385 (1979).

[301] L. J. Reinders, H. Rubinstein, and S. Yazaki, Phys. Rep. **127**, 1 (1985).

[302] T. D. Cohen, R. J. Furnstahl, D. K. Griegel, and X. Jin, Prog. Part. Nucl. Phys. **35**, 221 (1995).

[303] T. Hatsuda and S. H. Lee, Phys. Rev. **C46**, R34 (1992).

[304] T. Hatsuda, Y. Koike, and S. H. Lee, Nucl. Phys. **B394**, 221 (1993).

[305] R. J. Porter *et al.*, Phys. Rev. Lett. **79**, 1229 (1997).

[306] T. A. Armstrong *et al.*, Phys. Rev. Lett. **79**, 3612 (1997).

[307] G. Agakishiev *et al.*, Phys. Rev. Lett. **75**, 1272 (1995).

[308] G. Agakishiev *et al.*, (1997), nucl-ex/9712008.

[309] M. A. Mazzoni *et al.*, Nucl Phys. **A566**, 95c (1994).

[310] J. Stroth *et al.*, in *Dilepton spectroscopy with Hades at SIS, Proc. of the International Workshop on Gross Properties of Nuclei and Nuclear Excitation, XXII, Hirschegg, Austria*, edited by H. Feldmeier and W. Nörenberg, 1995.

[311] J. C. Gregory *et al.*, Nucl. Phys. **A566**, 287C (1994).

[312] A. Drees, Nucl. Phys. **A610**, 536c (1996).

[313] W. Cassing, W. Ehehalt, and C. M. Ko, Phys. Lett. **B363**, 35 (1995).

[314] W. Cassing, W. Ehehalt, and I. Kralik, Phys. Lett. **B377**, 5 (1996).

[315] G. Q. Li, C. M. Ko, and G. E. Brown, Phys. Rev. Lett **75**, 4007 (1995).

[316] C. M. Ko, G. Q. Li, G. E. Brown, and H. Sorge, Nucl. Phys. **A610**, 342c (1996).

[317] L. A. Winckelmann *et al.*, Nucl. Phys. **A610**, 116c (1996).

[318] D. K. Srivastava, B. Sinha, C. Gale, D. Pal, and K. Haglin, Nucl. Phys. **A610**, 350c (1996).

[319] V. Koch and C. Song, Phys. Rev. **C54**, 1903 (1996), nucl-th/9606028.

[320] J. Wambach and R. Rapp, nucl-th/9802001, talk at Quark Matter 97, December 1997, Tsukuba, Japan (1997).

[321] C. Ernst, S. A. Bass, M. Belkacem, H. Stöcker, and W. Greiner, (1997), nucl-th/9712069.

[322] E. L. Bratkovskaya, W. Cassing, R. Rapp, and J. Wambach, (1997), nucl-th/9710043.

[323] G. Roche *et al.*, Phys. Lett. **B226**, 228 (1989).

[324] L. Xiong, Z. G. Wu, C. M. Ko, and J. Q. Wu, Nucl. Phys. **A512**, 772 (1990).

[325] E. L. Bratkovskaya, W. Cassing, and U. Mosel, Phys. Lett. **B376**, 12 (1996).

[326] M. C. Abreu *et al.*, Nucl. - Phys. **A610**, 331c. (1996).

[327] C. Spieles *et al.*, Eur. Phys. J. **C**, in print (1998), hep-ph/9706525.

[328] C. Lourenço *et al.*, Nucl. Phys. **A566**, 77c (1994).

[329] R. Vogt, Atomic Data and Nuclear Table **50**, 343 (1992).

[330] D. Alde *et al.*, Phys. Rev. Lett. **64**, 2479 (1990).

[331] V. G. V. Abramovskij and O. Kancheli, Yad. Phys. **18**, 595 (1973).

[332] J. Kapusta, L. McLerran, and D. K. Srivastava, Phys. Lett. **B283**, 145 (1992).

[333] B. Kämpfer and O. P. Pavlenko, Phys. Lett. **B289**, 127 (1992).

[334] A. Dumitru, D. H. Rischke, H. Stöcker, and W. Greiner, Phys. Rev. Lett. **70**, 2860 (1993).

[335] L. A. Winckelmann, H. Sorge, H. Stöcker, and W. Greiner, Phys. Rev. **C51**, R9 (1995).

[336] K. Geiger and J. Kapusta, Phys. Rev. Lett. **70**, 1920 (1993).

[337] S. Gavin, P. McGaughey, P. Ruuskanen, and R. Vogt, Phys. Rev. **C54**, 2606 (1996).

[338] F. Halzen and D. Scott, Phys. Rev. **D18**, 3378 (1978).

[339] M. Glück, E. Reya, and A. Vogt, Z. Phys. **C53**, 651 (1992).

[340] M. Glück, E. Reya, and A. Vogt, Z. Phys. **C67**, 433 (1995).

[341] D. Kharzeev, Proceedings of the international school of physics, enrico fermi, in *Course 80: Selected Topics in Nonpertubative QCD*, p. 105, Varenna, Italy, 1996.

[342] H. Satz, Proceedings of the 32st. rencontres de moriond (cern-th/96-118), in *QCD and High Energy Hadronic Interactions*, p. 419, Less Arcs, France, 1996.

[343] D. Kharzeev, C. Lourenço, M. Nardi, and H. Satz, Z. Phys. **C74**, 307 (1997).

[344] C. Lourenço, Nucl. Phys. **A610**, 552c (1996).

[345] R. Baier and R. Rückl, Z. Phys. **C19**, 251 (1993).

[346] T. Matsui and H. Satz, Phys. Lett. **B178**, 416 (1986).

[347] T. DeGrand and C. DeTar, Phys. Rev. **D34**, 2469 (1986).

[348] K. Kanaya and H. Satz, Phys. Rev. **D34**, 3193 (1966).

[349] F. Karsch and H. Wyld, Phys. Lett. **B213**, 505 (1988).

[350] D. Blaschke, Nucl. Phys. **A525**, 269c (1991).

[351] S. Gavin, M. Gyulassy, and A. Jackson, Phys. Lett. **B207**, 257 (1988).

[352] R. Vogt, M. Prakash, P. Koch, and T. Hanson, Phys. Lett. **B207**, 263 (1988).

[353] S. Gavin and R. Vogt, Nucl. Phys. **A610**, 442 (1996).

[354] S. Gavin and R. Vogt, Phys. Rev. Lett. **78**, 1006 (1996), hep-ph/9606460.

[355] W. Cassing and C. M. Ko, Phys. Lett. **B396**, 39 (1996), nucl-th/9609025.

[356] W. Cassing and E. L. Bratkovskaya, Nucl. Phys. **A623**, 570 (1997).

[357] E. Braaten, Nucl. Phys. **A610**, 386c (1996).

[358] D. Kharzeev, Nucl. Phys. **A610**, 418c (1996).

[359] H. Stöcker and B. Müller, LBL-preprint 12471, unpublished .

[360] H. Stöcker, J. A. Maruhn, and W. Greiner, Phys. Rev. Lett. **44**, 725 (1980).

[361] H. Stöcker *et al.*, Phys. Rev. **C25**, 1873 (1982).

[362] G. Buchwald *et al.*, Phys. Rev. Lett. **52**, 1594 (1984).

[363] H. A. Gustafsson *et al.*, Phys. Rev. Lett. **52**, 1590 (1984).

[364] K. G. R. Doss *et al.*, Phys. Rev. Lett. **57**, 302 (1986).

[365] H. H. Gutbrod, A. M. Postkanzer, and H. G. Ritter, Rep. Prog. Phys. **52**, 1267 (1989).

[366] N. Herrmann *et al.*, Nucl. Phys. **A610**, 49c (1996).

[367] J. J. Molitoris and H. Stöcker, Phys. Lett. **B162**, 47 (1985).

[368] J. Y. Ollitrault, Phys. Rev. **D48**, 1132 (1993).

[369] B. Hong *et al.*, Phys. Rev. **C57**, 244 (1998).

[370] G. Poggi *et al.*, Nucl. Phys. **A586**, 755 (1995).

[371] M. A. Lisa *et al.*, Phys. Rev. Lett **75**, 2662 (1995).

[372] H. Sorge, Phys. Rev. Lett. **78**, 2309 (1997).

[373] D. H. Rischke and M. Gyulassy, Nucl. Phys. **A597**, 701 (1996).

[374] J. Kapusta, S. Pratt, L. M. Lerran, and H. v. Gersdorff, Phys. Lett. **B163**, 253 (1985).

[375] H. v. Gersdorff, Nucl. Phys. **A461**, 251c (1987).

[376] C. M. Hung and E. V. Shuryak, Phys. Rev. Lett. **75**, 4003 (1995).

[377] D. H. Rischke, S. Bernard, and J. A. Maruhn, Nucl. Phys. **A595**, 346 (1995).

[378] D. H. Rischke, Nucl. Phys. **A610**, 88c (1996).

[379] J. Brachmann *et al.*, Nucl. Phys. **A619**, 391 (1997).

[380] A. Dumitru, PhD Thesis, Goethe Universität, Frankfurt am Main, Germany (1997).

[381] H. T. Elze, W. Greiner, and J. Rafelski, Phys. Lett. **B124**, 515 (1983).

[382] H. T. Elze, W. Greiner, and J. Rafelski, Z. Phys. **C24**, 361 (1984).

[383] J. Boguta, Phys. Lett. **B109**, 251 (1981).

[384] C. Hartnack, J. Aichelin, H. Stöcker, and W. Greiner, Phys. Lett. **B336**, 131 (1994).

[385] A. Bonasera, L. Csernai, and B. Schürmann, Nucl. Phys. **A476**, 159 (1988).

[386] D. Lambrecht *et al.*, Z. Phys. **A350**, 115 (1994).

[387] *Quark Matter '97, Proceedings of the Thirteenth International Conference on Ultra-Relativistic Nucleus-Nucleus Collisions at Tsukuba, Japan*, 1997.